

Durham E-Theses

Designing a Fusion Power Plant with Superconducting Training Magnets

CHISLETT-MCDONALD, SIMON,BROOKE,LUKE

How to cite:

CHISLETT-MCDONALD, SIMON,BROOKE,LUKE (2022) *Designing a Fusion Power Plant with Superconducting Training Magnets*, Durham theses, Durham University. Available at Durham E-Theses Online: <http://etheses.dur.ac.uk/14404/>

Use policy

The full-text may be used and/or reproduced, and given to third parties in any format or medium, without prior permission or charge, for personal research or study, educational, or not-for-profit purposes provided that:

- a full bibliographic reference is made to the original source
- a [link](#) is made to the metadata record in Durham E-Theses
- the full-text is not changed in any way

The full-text must not be sold in any format or medium without the formal permission of the copyright holders.

Please consult the [full Durham E-Theses policy](#) for further details.

Designing a Fusion Power Plant with Superconducting Training Magnets



Simon Brooke Luke Chislett-McDonald

A thesis presented for the degree of

Doctor of Philosophy

Department of Physics

Durham University

United Kingdom

29th April 2022

To Mum, Dad and Charis

Designing a Fusion Power Plant with Superconducting Training Magnets

Simon Brooke Luke Chislett-McDonald

Abstract

Fusion power has the potential to revolutionise global energy production with a reliable, low CO₂ (not zero due to the use of steel, concrete etc. that typically produce CO₂ during manufacture), low radioactivity power supply, that is readily available at the point of need. The ITER and SPARC reactors are already under construction, with plans to begin full-power ($Q_{\text{fus}} \geq 10$) operation in the early 2030s; proving that fusion is a viable energy source. To see wide adoption however, reactors must be made as commercially attractive as possible. Here we present superconducting pilot reactor designs that have been optimised for minimum capital cost using the `PROCESS` systems code. Key design choices were made using technologies that are either available now or already in development; with concentrated effort these reactors could be built on 2030-2040 timescales. We focus primarily on the reactor from this set with the lowest overall capital cost, our “preferred” reactor: a 100 MW net electricity producing tokamak with REBCO superconducting toroidal field coils and central solenoid and Nb-Ti superconducting poloidal field coils. In addition, we have investigated using ductile, remountable Nb-Ti training coils (named after the training wheels of children’s bicycles) during the commissioning phase of a reactor to remove the risk of brittle failure of the full-power magnets during this stage. Such magnets would operate at lower field, but would enable thorough machine testing. Finally, we investigate and predict how advances in magnet technologies could effect our preferred reactor design and cost, and conclude that the effects of such advances do not justify waiting yet longer before beginning detailed reactor design and construction.

Supervisors: Prof. Damian Hampshire, Mr Michael Kovari, and Dr Elizabeth Surrey

Acknowledgements

I first wish to thank my principle supervisor Professor Damian Hampshire, who has been a fantastic guide and support from the first day of my PhD through to the finale. I also wish to thank my other supervisors Michael Kovari for his guidance and assistance with everything **PROCESS** and Liz Surrey for her wisdom, experience and encouragement. I thank too the members of the Durham Superconductivity Group, Mark Raine, Adel Nader, Paul Branch, Frank Ridgeon, Alex Blair, Jack Greenwood, Andy Smith, Charles Gurnham, Brad Din and Charles Haddon for their camaraderie and thought-provoking discussions - scientific or otherwise! I also wish to thank colleagues and friends at UKAEA: James Morris, Stuart Muldrew, Hanni Lux, Ian Jenkins, Jonathan Maddock, Seb Kahn, Alexander Pearce, Elizabeth Surrey, James Cook, Matti Coleman, Dan Short, Jonathan Naish and Anthony Turner for making me welcome at CCFE and for all of their technical and scientific experience and assistance. Finally, I wish to thank Mum, Dad, Charis and Eli, you've all been truly, fantastically supportive throughout my PhD and doubtless without your love and reinforcement I would never have finished!

This work is funded by EPSRC grant EP/L01663X/1 that supports the EPSRC Centre for Doctoral Training in the Science and Technology of Fusion Energy. This work has been carried out within the framework of the EUROfusion Consortium.

Contents

Declaration	xiii
Courses	xv
List of Figures	xvii
List of Tables	xxiii
Acronyms	xxix
1 Introduction	1
2 Superconductivity and Superconductors	7
2.1 Introduction	7
2.2 Bardeen-Cooper-Schrieffer Theory	8
2.3 Ginzburg-Landau Theory	10
2.3.1 The Ginzburg-Landau Equations	10
2.3.2 Coherence Length and Penetration Depth	11
2.3.3 Type I and Type II Superconductors	12
2.3.3.1 Type I Magnetic Behaviour	12
2.3.3.2 Type II Magnetic Behaviour	13
2.4 Critical Current Density	15

2.5	Technological Superconductors for Fusion Reactors	16
2.5.1	Niobium-Titanium	17
2.5.2	Niobium Tin (Nb_3Sn)	18
2.5.3	Rare-Earth Barium Copper Oxides	19
2.6	Conclusions	19
3	Nuclear Fusion	21
3.1	Introduction	21
3.2	Basic Principles of Magnetically Confined Fusion	22
3.3	Tokamaks	24
3.3.1	Primary Tokamak Systems	25
3.3.1.1	Magnetic Field coils	26
3.3.1.2	Auxiliary Heating and Current Drive	26
3.3.1.3	Divertor and Limiters	27
3.3.1.4	First Wall and Blanket	28
3.3.1.5	Neutron Shield and Vacuum Vessel	29
3.4	Reaching for the Stars	29
3.4.1	Physical Limits on Plasma Performance	30
3.4.2	Plasma Energy Confinement Time	31
3.5	Conclusions	32
4	PROCESS Systems Code Review	35
4.1	Rationale & Code Overview	35
4.2	Software and Hardware Requirements	37
4.3	Computational Methods	37
4.3.1	User Inputs	38
4.3.2	Code architecture	39
4.3.3	The Method of Lagrange Multipliers	41
4.3.4	The VMCON Sequential Quadratic Programming Solver (SQP)	43
4.4	1990 US\$ Capital Cost Model	47

4.4.0.1	1990 to 2021 US\$	48
4.4.1	Capital Cost	48
4.4.1.1	Direct cost	49
4.4.1.2	Indirect cost	49
4.4.1.3	Contingency	50
4.4.1.4	Capitalised financial costs	50
4.4.1.5	Total Capital Cost	51
4.5	Superconducting Coil Models	51
4.5.1	Winding Pack Geometries and Current Densities	51
4.5.2	TF Coil Peak Field	54
4.5.3	CS and PF Current Evolution and CS Peak Field	55
4.6	Personal Contributions to PROCESS	58
4.6.1	Updated Superconductor Critical Current Density Models	58
4.6.1.1	Durham Scaling Law	58
4.6.1.2	Nb-Ti Model	60
4.6.1.3	REBCO Model	61
4.6.2	Costing Superconductors in \$/kA m	63
4.7	Conclusions	64
5	Our Preferred REBCO Tokamak Pilot Power Plant Design	65
5.1	Introduction	65
5.2	Reactor Design Choices	69
5.2.1	Plasma Operation	69
5.2.1.1	Confinement Time and H_{98} -factor	69
5.2.1.2	Density, β and Safety Factor	70
5.2.2	Superconductor Operating Temperature	70
5.2.3	Tritium Breeding	74
5.2.4	Reactor Architecture	75
5.2.4.1	Divertor Constraints and Configuration	75
5.2.4.2	Number of Toroidal Field Coils	76

5.2.4.3	Coil Structural Support	76
5.2.4.4	Central Solenoid Use and Burn Time	77
5.3	Optimised Radiation Shielding	80
5.3.1	Neutronics - Thermal Load and Lifetime	80
5.3.1.1	Benchmarking Calculations	80
5.3.1.2	MCNP Calculation	85
5.3.2	Cryogenic flow - Benchmarking	89
5.4	Choosing the Optimal Superconductor	92
5.4.1	Nb-Ti	92
5.4.2	Nb ₃ Sn	92
5.4.3	REBCO	93
5.4.4	New fusion-focused high-field superconducting alloys	93
5.4.5	Critical Current Densities	94
5.4.6	Cost-Optimised Superconducting Reactor Comparison	97
5.4.7	The Cost-Optimal Field on Coil	103
5.4.8	Stress-limited, J_c -limited and B_{c2} limited Magnets	103
5.4.9	Graded and Sectioned Coils	105
5.5	Comments on Spherical Tokamaks	106
5.6	Comments on Aluminium/Copper Tokamak Power Plants	108
5.7	Reducing the Tritium Breeding Ratio and Required Net Electricity	114
5.8	Conclusions	114
6	Using Training Magnets to Reduce Reactor Risk	117
6.1	Introduction	117
6.2	Robotics, Remountable Magnets and Joints	119
6.3	Training Coils for REBCO Based Tokamak	123
6.4	Upgrade Coils for Nb-Ti Based Tokamaks	130
6.5	An Optimised Mid-21st Century Power Plant	136
6.6	Conclusions	139

7	Accounting for Future Advances in Magnet Technology	143
7.1	Introduction	143
7.2	Novel Support Architectures and Strengthened Steels	144
7.3	Reduced REBCO Cost	146
7.4	A Dreamer's Tokamak	146
7.5	Comments on Fusion-Specific REBCO tapes and Nb-Ti strands . . .	148
7.6	Discussion & Conclusions	149
8	Concluding Remarks & Future Work	151
8.1	Concluding Remarks	151
8.2	Future Work	153
	Bibliography	159
	Appendix A Example PROCESS Input File	193
	Appendix B Example PROCESS Output File Summary	203

Declaration

The work in this thesis is based on research carried out at Durham University Superconductivity Group, Department of Physics, University of Durham, England. No part of this thesis has been submitted elsewhere for any other degree or qualification, and it is the sole work of the author unless referenced to the contrary in the text.

Some of the work presented in this thesis has been previously published in journals and presented at conferences - the relevant publications and conferences are listed below.

Publications

“A roadmap for tokamak power plants: on upgrading and training superconducting magnet systems during a plant’s lifetime”, S. B. L. Chislett-McDonald, A. Turner, J. Naish, E. Surrey, M. Kovari, and D. P. Hampshire; (pending submission)

“The magnetic field, temperature, strain and angular dependence of the critical current density for Nb-Ti”, S. B. L. Chislett-McDonald, Y. Tsui, E. Surrey, M. Kovari, and D. P. Hampshire; *Journal of Physics: Conference Series* **1559** (2020)

“Could High H98-factor Commercial Tokamak Power Plants use Nb-Ti Toroidal Field Coils?”, S. B. L. Chislett-McDonald, E. Surrey, M. Kovari, and D. P. Hampshire; *IEEE Transactions on Applied Superconductivity* **29**(5) (2019)

Presentations

“Training and Upgrading Tokamak Power Plants with Remountable Superconducting Magnets” (Oral), S. B. L. Chislett-McDonald, A. Turner, J. Naish, M. Kovari, E. Surrey and D. P. Hampshire, *(virtual) European Conference on Applied Superconductivity* (September, 2021)

“How to train your tokamak: by swapping re-mountable superconducting magnets” (Oral), S. B. L. Chislett-McDonald, A. turner, J. Naish, M. Kovari, E. Surrey and D. P. Hampshire, *FuseNet PhD Event the “Virtualalternative”* (November, 2020)

“How to train your tokamak: by swapping re-mountable superconducting magnets” (Poster), S. B. L. Chislett-McDonald, M. Kovari, E. Surrey and D. P. Hampshire, *(virtual) Symposium on Fusion Technology* (September, 2020)

“The magnetic field, temperature strain and angular dependence of J_c for Nb-Ti wire” (Poster), S. B. L. Chislett-McDonald, Y. Tsui, M. Kovari, E. Surrey and D. P. Hampshire, *European Conference on Applied Superconductivity* Glasgow, UK (September, 2019)

“Could high H_{98} -factor commercial tokamaks use Nb-Ti in toroidal field coils?” (Poster), S. B. L. Chislett-McDonald, M. Kovari, E. Surrey and D. P. Hampshire, *Applied Superconductivity Conference* Seattle, USA (October, 2018)

29th April 2022

Simon Brooke Luke
Chislett-McDonald

Copyright © 2020 by Simon Brooke Luke Chislett-McDonald.

“The copyright of this thesis rests with the author. No quotation from it should be published without the author’s prior written consent and information derived from it should be acknowledged.”.

Courses

The Fusion CDT is comprised of a partnership between the University of Oxford, Durham University, the University of York, the University of Manchester, the University of Liverpool and the Culham Centre for Fusion Energy. Students on the course enjoy a number of lecture courses and hands-on laboratory experience delivered by world experts in particular aspects of fusion-related science. The aim of the courses is to give enrolled PhD students a firm and broad grounding in the physical, materials science and engineering concepts from which they can produce fruitful and contextual research. The programme is split into ‘materials science’ and ‘plasma physics’ strands, the author is a member of the former. The first 9 months of the PhD course are spent between the various partner institutions and require full-time study from students. An outline of the 2017/18 materials strand first year courses in the Fusion CDT is detailed in Table Table 1.

During their second year students embark on a collaboratory project at an institution of their choice within the broader fusion community. For this, the author spent six weeks with the École polytechnique fédérale de Lausanne (EPFL) superconductivity group at the Paul Scherrer Institut in Villigen, Switzerland, under the supervision of Dr Pierluigi Bruzzone. The project focused on the manufacture of a diffusion bonded copper joint between two "React & Wind" Nb₃Sn cables.

Course Name	Location	Dates
Introduction to Plasma Physics	York Plasma Institute	Oct 2017
Introduction to Materials	York Plasma Institute	Oct 2017
Computational Techniques	York Plasma Institute	Oct 2017
Material Applications in Fusion	Oxford University	Nov 2017
Radiation Damage	Oxford University	Nov 2017
Fusion Technology	York Plasma Institute	Jan 2018
Plasma-Surface Interactions	Liverpool University	Jan 2018
Analytical and Characterisation Techniques	Oxford University	Feb 2018
Finite Element Method and Design Codes	Manchester University	Mar 2018
Materials for Nuclear Power	Oxford University	Apr 2018
Integrated Systems and Project Management	Durham University	Apr 2018

Table 1: First year courses attended as part of the Fusion CDT.

List of Figures

2.1	Critical fields of Type I and Type II superconductors as a function of temperature. Type I superconductors have two states: Meissner and normal. Type II superconductors have three states: Meissner, mixed and normal. μ_0 is the permeability of free space. Adapted from [40]. . .	14
2.2	Whole strand/tape critical current densities as a function of applied field for superconductors available in long lengths [44].	16
3.1	Fusion reaction cross sections as a function of incident particle kinetic energy [72]	23
3.2	Primary systems of the ITER tokamak. Adapted from [5].	25
3.3	Comparison between a limited and a diverted tokamak plasma, showing the last closed flux surface (LCFS) and scrape off layer (SOL) in the limiter case [87].	28
3.4	A comparison between experimentally measured plasma energy confinement times from various tokamaks and the confinement time predicted by the IPB98(y,2) scaling law [99]. Figure adapted from [99]. The solid line is $H_{98} = 1.0$ dashed line is $H_{98} = 1.2$ and the dotted line is $H_{98} = 2.0$.	32
4.1	Flow chart of the overall PROCESS code architecture.	40

4.2	Contours of an objective function $f(x, y)$ and a single constraining function $g(x, y)$. The curvature of the functions is shown with arrows. At the constrained optimum value of $f(x, y)$ the gradients of the objective function and the constraint functions are parallel. [118]	42
4.3	Flow chart of the VMCON Optimiser used in PROCESS [115]. ifail = 1 denotes successful convergence, ifail \neq 1 denotes failed convergence at various stages during the computation. Taken from [115].	46
4.4	Flow chart of the capital cost estimation in PROCESS. Based on figure 3 in [119].	48
4.5	Definitions of the critical current density (the ratio between the critical current and the relevant cross-sectional area, CSA). Row 1: The total CSA of the cable is used i.e. $J_{c, \text{Total cable}} = I_c / \text{CSA}_{\text{Total cable}}$. Row 2: the total CSA of the whole strand or tape is used i.e. $J_{c, \text{Total Strand or Total Tape}} = I_c / \text{CSA}_{\text{Total Strand or Total Tape}}$. Row 3: Only the CSA of the non-copper region is used i.e. $J_{c, \text{Non-Cu}} = I_c / \text{CSA}_{\text{Non-Cu}}$. The CSA of the copper stabiliser is not included. Row 4: Only the CSA of the superconductor is used (either total filament CSA or CSA of the superconducting layer in a tape i.e. $J_{c, \text{superconductor}} = I_c / \text{CSA}_{\text{superconductor}}$. Micrographs for Nb-Ti, Nb ₃ Sn and images of CICC's [127, 128] for these materials, and REBCO [65] are given as examples.	53
4.6	Illustration of the inboard leg of a TF coil and conductor. Grey represents steel, black insulation and blue conductor (including superconductor, copper and helium). All parameters labelled may be input as fixed values or iteration variables. The number of cable turns is arbitrary in this illustration.	54
4.7	Example evolution of the current in the plasma, PF coils and CS coil of a 100 MW net electricity tokamak with a 100 second plasma burn time as calculated by PROCESS.	57

4.8	(a) $J_{c, \text{Total Strand}}(B, T)$ data from measurements performed on five ITER specification Nb-Ti strands (considered together as one data set) at zero strain. The solid lines are fits using equation 4.6.6. (b) Nb-Ti single strand critical current density as a function of applied strain at 4.2 K for different applied fields perpendicular to the direction of current flow. The solid lines are a fit using equation 4.6.7.	60
4.9	(a) Total strand critical current densities of Nb-Ti “alloys” with various values of $B_{c2}^*(0, 0)$ and $T_c^*(0)$ using equation 4.6.6 and table 4.1 at 4.2 K (b) Total strand/tape critical current density of ITER specification Nb-Ti and SuperPower REBCO tape at 4.2 K. using equation 4.6.6 and table 4.1. Critical current density from the old PROCESS Nb-Ti scaling law and literature REBCO data [62] at 4.2 K are shown for comparison.	62
5.1	Top: Total absolute central solenoid coil (CS) and poloidal field coil (PF) flux, central solenoid bore and thickness, and (Bottom:) plasma major radius and plant total capital cost as a function of plasma burn time, of 100 MW _e tokamak power plants with REBCO CS and TF coils and Nb-Ti PF coils (i.e. magnet materials as per the R ₁ BL reactor design) optimised for minimum capital cost. Note that R ₁ BL has a 7200 second plasma burn time.	79
5.2	Cross-sections and inboard mid-plane radial build of the preferred reactor R ₁ BL (a cost-optimised H ₉₈ = 1.2, 100 MW net electricity tokamak with REBCO toroidal field and central solenoid coils) with an optimised 25.0 cm neutron shield. Details of the layers can be found in the second column of table 5.5. The inboard blanket is 53 cm in radial thickness and based on the EU-DEMO helium-cooled pebble bed design [175], guaranteeing a tritium breeding ratio > 1.1.	83

5.3	<p>Nuclear heating in the TF coil system and number of full-power operation years until the Weber dose limit [205] is achieved for the preferred reactor R₁BL (a cost-optimised H₉₈ = 1.2, 100 MW net electricity tokamak with REBCO toroidal field and central solenoid coils) as a function of the thickness of its tungsten carbide neutron shield as calculated by MCNP (closed squares) and the benchmarking calculation (open diamonds). The material layers between the plasma and the TF coil are given in table 5.5. The dotted black lines indicate the minimum 40 year conductor lifetime limit (and corresponding minimum shield thickness as calculated by MCNP). The dotted red lines indicate the maximum 10 kW heating limit on the TF system (and corresponding minimum shield thickness as calculated by our benchmarking calculations).</p>	86
5.4	<p>Neutron and photon induced wall loading along the mid-plane within the preferred reactor R₁BL (a cost-optimised H₉₈ = 1.2, 100 MW net electricity tokamak with REBCO toroidal field and central solenoid coils) with an optimised 25.0 cm neutron shield. The radial positions of the central solenoid coil (light pink), toroidal field coil legs (blue), vacuum vessel (green), neutron shield (black) and blanket (deep pink) are shown.</p>	87
5.5	<p>MCNP calculated (a) fast neutron flux and (b) gamma ray flux through the poloidal cross-section of the preferred reactor R₁BL (a cost-optimised H₉₈ = 1.2, 100 MW net electricity tokamak with REBCO toroidal field and central solenoid coils) with an optimised 25.0 cm neutron shield detailed in the right hand column of table 5.5. (c) The neutron flux spectrum and (d) photon flux spectrum as a function of distance into inboard mid plane of R₁BL with an optimised 25.0 cm neutron shield. These spectra were converted to flux density per unit lethargy by multiplying the spectral histogram fluxes by the ratio between the energy bin average energies and the bin widths.</p>	88

5.6	Whole strand/tape critical current density of commercial ITER specification Nb-Ti (Comm. Nb-Ti), quaternary (Quat.) Nb-Ti, internal tin Nb ₃ Sn, and <i>REBa₂Cu₃O₇</i> (REBCO where <i>RE</i> :rare-earth) at 4.5 K, used in this work. Only quaternary Nb-Ti is not commercially available but could be optimised for fusion.	96
5.7	(a) Reactor power balance (where “Core Systems” includes the cryo-system (46 MW _e) and the tritium handling system (15 MW _e)); (b) direct capital cost breakdown of the preferred reactor R ₁ BL (a cost-optimised H ₉₈ = 1.2, 100 MW net electricity tokamak with REBCO toroidal field and central solenoid coils). Costs are in 1990 US M\$. . . .	101
5.8	The result of changing the field on plasma axis from the cost-optimum 5.36 T (of the preferred reactor R ₁ BL) on the cost-optimal TF coil design, reactor build and capital cost.	104
5.9	Toroidal magnetic field strength as a function of position within the R ₁ BL through the reactor mid-plane. TF coil outlines are shown in black.	107
6.1	Fusion power, gross electric power and net electric power as a function of operating H ₉₈ -factor for the two reactors R ₁ BL and R ₃ BL with REBCO CS and TF coils and Nb-Ti PF coils. R ₁ BL and R ₃ BL were optimised for minimum capital cost (open data points) at H ₉₈ -factors of H ₉₈ = 1.2 (red) and H ₉₈ = 1.6 (black) and produce 100 MW _e . Reactor builds were fixed. Reactors at higher or lower than expected H ₉₈ -factors were optimised to produce maximum net electricity (solid data points). The discontinuities in fusion power that occur between high and low H ₉₈ factors are due to a loss of energy confinement at H ₉₈ factors that are too low.	127
6.2	Artistic CAD model of the preferred reactor design R ₁ BL.	141

7.1	(a) Change in cost-optimal field on coil and (b) capital cost of a $H_{98} = 1.2$, 100 MW net electricity tokamak with REBCO toroidal field and central solenoid coils as a function of the allowable maximum of the shear stresses (as used for the Tresca yield criterion) on the central solenoid and inboard toroidal field coil mid-planes. Different data sets correspond to different costs of steel components (standard, $1.5 \times$ standard etc.), representative of either more expensive steels or larger steel volumes. Cost model uncertainties are $\approx 5\%$ for all data.	145
7.2	(a) Change in cost-optimal field on coil and capital cost of a $H_{98} = 1.2$, 100 MW net electricity tokamak with REBCO toroidal field and central solenoid coils as a function of REBCO cost in 1990 US \$. (b) The direct costs of REBCO, cable copper stabiliser, coil winding, TF casing, intercoil structure and gravity support as a fraction of the total TF costs. The two panels' have the same x axis . All costs are inclusive of (commercial) material and construction costs and have an error of $\pm 5\%$	147

List of Tables

1	First year courses attended as part of the Fusion CDT.	xvi
4.1	Parameters for the Durham scaling law for total strand critical current densities of ITER specification Nb-Ti strands and SuperPower REBCO tape. The commercial Nb-Ti parameters were found by extensive measurements taken at Durham university [53]. The value of A^* for REBCO was found by fitting to literature data [62], all other parameters were taken from measurements on REBCO tapes [132, 133]. Values of $u = 0.0$ and $w = 2.2$ were fixed.	62
5.1	Key design and performance parameters of PROCESS generated 100 MW and 500 MW net electricity (MW_e) capital-cost minimised plants (six baseline reactors and two additional reactors). Our preferred reactor is in bold . Also shown are: EU-DEMO [6], ARIES-ST [50], a PROCESS generated pulsed Cu reactor based on STPP [150], ARC [9], CFETR [10, 57], ITER [17, 54], SPARC [4, 151], JET [152, 153, 154], JT60-SA [155, 48], KSTAR [47, 156, 157], EAST [158, 159, 160], WEST [161, 162], MAST-U [13, 163] and SST-1 [164, 165]. Tokamaks have been grouped into: those in this work, demonstration reactors, proof of concept reactors and research tokamaks. Estimated parameters indicated with (*). Tokamaks with resistive primary magnets are indicated with (†).	68

5.2	Capital cost of the preferred reactor R ₁ BL and three other PROCESS generated, cost-optimised, 100 MW net electricity, H ₉₈ = 1.2 tokamak pilot plants. Right: R ₁ BL (with REBCO TF and CS coils); centre-right: R ₇ AD (with Nb ₃ Sn TF and CS coils); centre-left: R ₂ BL (with commercial Nb-Ti TF and CS coils); left: R ₈ AD (with quaternary Nb-Ti TF and CS coils). In all cases the PF coils are Nb-Ti. These costs are for simply building the plant without mitigating risk with training or upgrading coils. All costs are in 1990 M\$. This table is discussed in detail in section 5.4.6.	72
5.3	Power balance of the preferred reactor R ₁ BL and three other PROCESS generated, cost-optimised, 100 MW net electricity, H ₉₈ = 1.2 tokamak pilot plants. Right: R ₁ BL (with REBCO TF and CS coils); centre-right: R ₇ AD (with Nb ₃ Sn TF and CS coils); centre-left: R ₂ BL (with commercial Nb-Ti TF and CS coils); left: R ₈ AD (with quaternary Nb-Ti TF and CS coils). In all cases the PF coils are Nb-Ti.	73
5.4	Mean attenuation coefficients for (fast) neutrons of energy > 0.1 MeV of tokamak relevant materials. $\bar{\mu}_{TCA}$ are calculated from total neutron cross section data [204]. $\bar{\mu}_i$ calculated using data from MCNP calculations of neutron transmission through a 30 cm block of (ith) mono-material [202] except for Tungsten Carbide which is derived from the MCNP data in figure 5.3.	82
5.5	Thicknesses and material compositions (derived from the ITER radial build) of the layers between the first wall and the central solenoid at the inboard mid-plane for the initial 100 MW net electricity REBCO CS, TF and Nb-Ti PF reactor using a neutron shield thickness from the benchmarking calculations. As well as those for the preferred reactor R ₁ BL using a neutron shield thickness optimised using MCNP. Outboard dimensions are shown in brackets () where significantly different.	84

5.6	Above: Useful cryogenic materials properties under 5 bar pressure [214]. Below: (magneto)resistances of RRR = 1000 copper and RRR = 10000 aluminium [170, 215, 216].	90
5.7	Parameters for the Durham scaling law for the critical current density of quaternary Nb-Ti [229, 230] and internal tin Nb ₃ Sn [136]. Commercial Nb-Ti and REBCO scaling parameters shown again for convenience. . .	95
5.8	Magnet performance and reactor size of capital cost minimised, H ₉₈ = 1.2, 100 MW net electricity reactors. The different superconductors con- sidered are the high temperature superconductor <i>REBa₂Cu₃O₇</i> (RE- BCO where <i>RE</i> :rare-earth), commercial NbTi (Comm. NbTi) used in MRI scanners, and quaternary NbTi (Quat. NbTi) that is not yet avail- able commercially.	99
5.9	Iteration variables and bounds, for the reactor optimisation study. F- values are the allowable factor changes in values, e.g. an F-value of 1.2 would allow PROCESS to set a variable to 120 % of its predefined value. Note that this table does not cover input parameters (there are too many to list here), for a full list of all variables used see Appendix A.	102
5.10	Performance and cost of a steady-state H ₉₈ = 1.6, 100 MW _e reactor with copper TF, CS and PF coils (with minimised capital cost). Based on STPP [150].	110
6.1	Iteration variables and bounds used when modelling reactors with train- ing and upgrade coils. Note that there are no geometric engineering iter- ation variables: the modelled reactors' dimensions are limited by those of their corresponding baseline reactor. F-values are the allowable factor changes in values, e.g. an F-value of 1.2 would allow PROCESS to set a variable to 120 % of its predefined value. Note that this table does not cover input parameters (there are too many to list here), for a full list of all variables used see Appendix A.	122

6.2	Trained tokamaks designed for 100 MW net electricity and $H_{98} = 1.2$: Performance and cost data for the (preferred) tokamak optimised for REBCO toroidal field and central solenoid coils with minimised capital cost (*) and training magnets of different superconductors (with maximised net electricity yield). Also shown are the power values that would result, were a reduced $H_{98} = 1.0$ to occur in practice.	125
6.3	Trained tokamaks designed for 100 MW net electricity and $H_{98} = 1.6$: Performance and cost data for a tokamak optimised for REBCO toroidal field and central solenoid coils with minimised capital cost (*) and training magnets of different superconductors (with maximised net electricity yield). Also shown are the power values that would result, were a reduced $H_{98} = 1.0$ to occur in practice.	126
6.4	Trained tokamaks designed for 500 MW net electricity and $H_{98} = 1.2$: Performance and cost data for a tokamak optimised for REBCO toroidal field and central solenoid coils with minimised capital cost (*) and training magnets of different superconductors (with maximised net electricity yield). Also shown are the power values that would result, were a reduced $H_{98} = 1.0$ to occur in practice.	129
6.5	Upgraded tokamaks designed for 100 MW net electricity and $H_{98} = 1.2$: Performance and cost data for a tokamak optimised for Nb-Ti toroidal field and central solenoid coils with minimised capital cost (*) and upgraded magnets of different superconductors (with maximised net electricity yield). Also shown are the power values that would result, were a reduced $H_{98} = 1.0$ to occur in practice.	132

6.6	Upgraded tokamaks designed for 100 MW net electricity and $H_{98} = 1.6$: Performance and cost data for a tokamak optimised for Nb-Ti toroidal field and central solenoid coils with minimised capital cost (*) and upgraded magnets of different superconductors (with maximised net electricity yield). Also shown are the power values that would result, were a reduced $H_{98} = 1.0$ to occur in practice.	133
6.7	Upgraded tokamaks designed for 500 MW net electricity and $H_{98} = 1.2$: Performance and cost data for a tokamak optimised for Nb-Ti toroidal field and central solenoid coils with minimised capital cost (*) and upgraded magnets of different superconductors (with maximised net electricity yield). Also shown are the power values that would result, were a reduced $H_{98} = 1.0$ to occur in practice.	135

Acronyms

BCS	Bardeen–Cooper–Schrieffer
CS	Central Solenoid
DCLL	Dual-Cooled Lithium Lead
D-T	deuterium-tritium
ECCD	Electron Cyclotron Current Drive
ECRH	Electron Cyclotron Resonance Heating
ELM	Edge-Localised Mode
GL	Ginzburg-Landau
HCLL	Helium Cooled Lithium Lead
HCPB	Helium Cooled Pebble Bed
IBAD	Ion Beam Assisted Deposition
ICCD	Ion Cyclotron Current Drive
LHCD	Lower Hybrid Current Drive
MHD	Magnetohydrodynamics
MOCVD	Metal Organic Chemical Vapor Deposition
MW _e	Mega-Watts electricity
NBI	Neutral Beam Injection
PF	Poloidal Field
REBCO	Rare-Earth Barium Copper Oxide
RF	Radio Frequency
TF	Toroidal Field
WCLL	Water Cooled Lithium Lead
WCPB	Water Cooled Pebble Bed

Introduction

Climate change is an objective truth, and human society bears the brunt of the blame [1]. The 21st Century must see our civilisation turn away from the fossil fuels that they are built on and shift to cleaner and greener technologies for our power needs, both domestic and industrial. At the same time however, global power demand will continue to grow, and indeed must continue to grow to empower the developing world [2]. Access to energy is one of the primary tools to bring people out of poverty, and it would be morally bankrupt of us in the West to deny those in the most need, through a poor technical choice of power source. De-carbonising national electricity grids and power supplies whilst simultaneously increasing global energy capacity is however no mean feat. Fortunately, there are a number of novel and innovative technologies that have the capability to facilitate and accelerate this necessary achievement. Primary amongst these is nuclear fusion. Rather than splitting heavy atoms as is used in conventional nuclear fission, nuclear fusion harnesses the process that powers stars: fusing together light atoms, typically the hydrogen isotopes deuterium and tritium. The nuclear waste produced therefore has the very low lifetimes of 100-1000 years, much lower than fission's 100,000 years or more. Fusion is a "best of both" technology that combines the reliable power generation of fossil fuels and nuclear fission with the very low CO₂ footprint of renewable sources, without the need for expensive and low-energy density storage or specific environmental and geographical conditions. Fusion does still produce

large volumes of intermediate level nuclear waste (to to the neutron-activation of internal components), but none of the transuranic isotopes that makes fission waste so long lived. Indeed fusion neutron-activated materials can (eventually) simply be recycled [3]. The technology closest to realising fusion power on a commercial and global scale is the tokamak, a reactor that uses strong, helical magnetic fields to confine a super-heated hydrogen plasma to the $> 100,000,000$ °C necessary to maximise the deuterium-tritium (D-T) fusion reaction rate.

Superconducting magnets are an enabling technology for the next generation of tokamak reactors and it is testament to their incredible electromagnetic properties that they're used in MIT/CFS's SPARC [4], the international ITER reactor [5] and all tokamak demonstration plants designed to follow after them (e.g. EU-DEMO [6], JA DEMO [7], K-DEMO [8], ARC [9], CFETR [10], ST-135 [11]). Unlike resistive materials, when a DC current flows through a superconductor below its critical temperature it does so with zero resistance. The negligible resistance of technological superconductors means that the power required by the magnet cooling system is an order of magnitude lower (or more) than those of resistive magnets at the same field. Superconducting magnets can therefore produce large magnetic fields > 5 T over large areas of space > 25 m², far above what is practical with conventional resistive electromagnets. Historic practice has been to build superconducting magnets with the ductile, and comparatively cheap, niobium-titanium where fields are ≤ 6 T and to use the brittle intermetallic compound niobium-3-tin at higher fields. Rare-Earth barium copper oxide ("high temperature") superconductors are a relative newcomer to the arena of tokamak magnets, but offer the exciting possibility to generate fields significantly higher than those of Nb₃Sn at higher operating temperatures, further reducing cooling power. Fusion power scales as the fourth power of the magnetic field on plasma, so these higher fields can potentially be used to reduce plasma volume and reactor size.

It has taken more than 80 years of research and experiment to reach this point, but the 2020s promise to dispel the idea that "fusion is always 30 years away". The

ITER reactor [5] housed in Cadarache, France aims to begin operation in 2025 and a prototype REBCO magnet of the SPARC reactor has already been successfully tested [12]. Both of these tokamak reactors are designed to produce fusion plasmas with ≥ 10 times more power than is deposited in them, far exceeding break-even. We are tantalisingly close to seeing net fusion power. Building on these final “research” reactors, pilot and demonstration plants must take power generation a step further and produce electricity for the grid. The neutrons produced by fusion reactions are harnessed to generate tritium for fuel and heat for power. The heat is can be used to boil water to turn steam turbines, much in the same way as in fission or fossil fuel power plants. A pilot plant must demonstrate its ability to produce net electricity for sustained periods of time, as well as the ability to produce at least as much tritium as it uses. Fusion reactor designs vary greatly in requirements they attempt to satisfy, but most aim to produce one to a few hundred MW net electricity (MW_e), tritium self sufficiency and (if an intrinsically pulsed design) a plasma pule length $>$ two hours [6, 7, 9, 10, 11, 12, 13].

Whereas research reactors are necessarily flexible in their capabilities and designed to meet a specific scientific goal, an (expensive) pilot plant must be designed with clearly defined outcomes and ruthless economic efficiency; able to meet all the specifications of a pilot plant for the minimum capital cost. It is not enough that fusion is proven feasible on a large scale – it must also demonstrate and enable economic viability in a way that enables governments and private investors to actually build commercial reactors in future. That said, while it is essential for fusion to optimise its costs to be commercially competitive, it will be very difficult for a prototype to be commercially competitive both in costs and availability. Furthermore, fusion plant designs for a few hundred MW are expected to be too small to ever be commercially competitive due to their high parasitic load fraction in comparison to gross electric power [14]. In light of this, in this thesis we have used the world leading PROCESS systems code to produce reactor designs explicitly optimised with minimised capital cost. The designs meet all the specifications of a pilot power

plant and are based on technologies that are either available now, or already in development for other proposed reactors (such as EU-DEMO). We investigate the use of a range of different superconductors that culminates in our selection of our “preferred reactor”, which has the lowest capital cost of all options considered. With sustained effort, this reactor can be the last before commercialisation and built in the time frame of 2030-2040 (after which there is a risk that fusion power may miss the green energy boat [15]). It is our opinion that this is the reactor that should be built to demonstrate magnetically confined fusion’s capabilities and viability as the commercial bedrock of the post-carbon energy industry. As well as this design, we also propose a way to reduce reactor risk through the use of “training coils”: remountable ductile magnets that operate a lower field, but remove the risk of brittle failure of the higher field, full-power magnets during reactor commissioning whilst still allowing for thorough machine testing.

The thesis is presented in three parts: the background for the work (chapters 2 and 3), the `PROCESS` systems code with the author’s work to update `PROCESS` with superconducting modules (chapter 4) and the new `PROCESS` calculations and analysis (chapters 5-8). We begin in chapter 2 by detailing the primary theoretical models for superconductivity as well as describing technological superconductors in the context of magnets for fusion reactors. Chapter 3 is a discussion of nuclear fusion, from the basic principles to an overview tokamak design. Chapter 4 summarises the `PROCESS` systems code, its mathematical methods, use and models most pertinent to this research. In chapter 5 we explore the primary design optimisation options available to tokamak engineers. Beginning with the optimised neutron shield, we pass in turn through these key options and make our choice for each technology. We then decide upon which superconductor to use for the reactor coils, and converge upon the preferred reactor design (R_1BL). Chapter 6 builds upon this preferred reactor design and investigates the use of remountable “training magnets”; Nb-Ti magnets that are used in the reactor commissioning phase to reduce the risk of unforeseen damage to the brittle, full-power operating magnets.

An investigation into the likely effects of future, advanced, superconducting fusion magnet technologies on the preferred reactor design is provided in chapter 7. The thesis then concludes and avenues for future work are then presented in chapter 8.

Superconductivity and Superconductors

2.1 Introduction

A superconductor is defined as a material that exhibits zero DC electrical resistivity and perfect diamagnetism below a certain (critical) temperature. From these humble definitions, superconductors have become synonymous with high field magnets and have seen wide use around the globe. From nuclear magnetic resonance analysers [16] to fusion tokamaks [17] and stellarators [18] to the Large Hadron Collider [19], superconductors have enabled some of the worlds largest and most ambitious scientific projects. Perhaps most importantly to-date, superconducting magnets have been instrumental in the development of medical MRI, saving countless lives as a result.

From the first record of superconductivity in liquid helium cooled mercury 110 years ago by Onnes [20], myriad superconducting materials have been discovered. Initial study led to the discovery of superconductivity in other pure metals such as lead and niobium [21] and in the 1950s and 1960s in many metal alloys and intermetallic compounds (often to the great surprise of the discoverers). Of these earliest discoveries, perhaps the most important were Nb_3Sn by J. Kunzler et al.

[22] and Nb-Ti by T. Berlincourt et al. [23], both published in 1961. In the 80s the field was again astounded by the discovery of cuprate “high temperature superconductors” (HTS) with critical temperatures above the boiling point of liquid nitrogen [24].

The theoretical descriptions of superconductivity have been developed in tandem with the material discoveries. The earliest widely accepted theory was proposed by the brothers Heinz and Fritz London in 1935 [25], who formulated an expression for the depth an external magnetic field penetrates into a superconductor. Bardeen, Cooper and Schrieffer (BCS) [26] published their theory of superconductivity at the electron scale in 1957. This garnered wide acclaim within the community which culminated in the award of 1972 Nobel Prize in physics. First published in 1950 (but only widely regarded after Gor’kov’s demonstration that it was a limiting case of BCS theory in 1959 [27]) Ginzburg & Landau’s theory of superconductivity is arguably the most widely used theory today, forming the foundation of the critical current density scaling laws used for practical superconducting materials.

In this chapter we briefly detail the principles of superconductivity theory. The microscopic Bardeen-Cooper-Schrieffer theory is described section 2.2, followed by the phenomenological Ginzburg-Landau theory in section 2.3. We concentrate on the concepts of the superconductor critical temperature, critical field (thermodynamic, lower and upper) in these sections, and then critical current density in section 2.4. These parameters are of great importance for the technological application of superconducting materials for magnets. The chapter concludes with descriptions of fusion-relevant technological superconductors in section 2.5.

2.2 Bardeen-Cooper-Schrieffer Theory

Although unable to describe the behavior of high temperature superconductors [28, 29], Bardeen-Cooper-Schrieffer (BCS) theory provides valuable insight into the microscopic causes of superconductivity [26]. The theory builds on previous

work by Fröhlich, who proposed that superconductivity is due to electron coupling (that is, net attraction of two electrons) mediated by phonon exchange [30]. Qualitatively, if the thermal energy in the system is sufficiently low, an electron will deform the ion lattice within its locale, creating a body of net positive charge that another electron is then attracted to. This interaction can be described by the emission of a phonon (of wave number \mathbf{q} and energy $\hbar\omega_q$) by one electron (of momentum $\hbar\mathbf{k}$) and absorption of it by a second electron (of momentum $\hbar\mathbf{k}'$) [31]

$$V(\mathbf{k}, \mathbf{k}', \mathbf{q}) = \frac{g^2 \hbar \omega_q}{(\epsilon_{k+q} - \epsilon_k)^2 - (\hbar \omega_q)^2}, \quad (2.2.1)$$

where ϵ_i is the energy of electron state with wave number i and g is the electron-phonon coupling constant. For $|\epsilon_{k+q} - \epsilon_k| < \hbar\omega_q$ this is indeed attractive.

BCS extended this logic to a system of many electrons and assumed a simple square well potential with a constant attractive interaction potential V_0

$$V(\mathbf{k}, \mathbf{k}') = \begin{cases} -V_0, & \text{if } |\epsilon_k|, |\epsilon_{k'}| < \hbar\omega_D \\ 0, & \text{otherwise,} \end{cases} \quad (2.2.2)$$

where ω_D is the Debye frequency of phonons within the lattice. Solving the Schrödinger equation for a pair of electrons of opposite momentum in this potential, no matter how weak the interaction potential is, the electrons bind together (into “Cooper pairs”) with binding energy E_b

$$E_b = 2\hbar\omega_D \exp\left(-\frac{2}{N(0)V_0}\right), \quad (2.2.3)$$

where $N(0)$ is the electron energy density of states at the Fermi surface. Extending this to a system of electrons BCS showed that there is an energy gap, $\Delta(T)$, at the Fermi surface, between the normal and superconducting states

$$\Delta(0) = 2\hbar\omega_D \exp\left(-\frac{1}{N(0)V_0}\right), \quad (2.2.4)$$

(at $T = 0$) where $|\Delta| \ll \hbar\omega_D \ll \epsilon_F$. This energy gap is negative, and hence the formation of Cooper pairs is energetically favourable. These Cooper pairs act as composite bosons - and therefore all share the same momentum state. The

system-wide energy gap prohibits electron scattering, explaining how, within the superconducting state, there is zero (DC) resistance.

BCS theory predicts that a superconductors critical temperature depends on the strength of the energy gap as

$$3.52k_B T_c = 2\Delta(0) . \quad (2.2.5)$$

From equations 2.2.4 and 2.2.5 we can see that $T_c \propto \omega_D$. This is in clear agreement with the ‘Isotope effect’ [32] an empirical observation that $T_c \propto M^{-\alpha}$ where M is the lattice ion mass and $\alpha \approx \frac{1}{2}$, invoking the well-known relation $M \propto \omega_D^{-2}$.

2.3 Ginzburg-Landau Theory

2.3.1 The Ginzburg-Landau Equations

Ginzburg-Landau (GL) theory [33] is an extension of Landau’s foundational theory of second order phase transitions and describes the free energy of a superconducting system in terms of a spatially dependent complex order parameter, here denoted by ψ . This order parameter can be interpreted physically in relation to the density of super electrons, $n_s = |\psi|^2$ [34]. For small values of ψ (close to and below the critical temperature T_c) GL propose that the Gibbs free energy density of a superconductor, g_s , can be expressed as an expansion in powers of $|\psi(\mathbf{r})|^2$ and $|\nabla\psi(\mathbf{r})|^2$ as given in the excellent textbook by Tilley & Tilley [35]

$$g_s = g_n + \alpha |\psi(\mathbf{r})|^2 + \frac{\beta |\psi(\mathbf{r})|^4}{2} + \frac{|(-i\hbar\nabla - 2e\mathbf{A})\psi|^2}{2m_e} + \frac{\mathbf{B}^2}{2\mu_0} - \mathbf{H}_0 \cdot \mathbf{B} + \frac{\mu_0 \mathbf{H}_0^2}{2} , \quad (2.3.1)$$

where g_n is the Gibbs free energy density in the normal state (above T_c), \mathbf{B} is the magnetic field, \mathbf{H}_0 is an applied field strength, \mathbf{A} is the magnetic vector potential where $\mathbf{B} = \nabla \times \mathbf{A}$ and m_e is the electron mass. α and β are temperature dependent. We must also include a field energy term. The \mathbf{H}_0^2 term is added for convention

and $-\mathbf{H}_0 \cdot \mathbf{B}$ is a demagnetisation energy [35]. To ensure that ψ is zero above T_c and finite and singular below T_c , we define $\alpha = -\alpha_0(1 - T/T_c)$ and $\beta = \beta_0$ where α_0 and β_0 are positive constants. Minimising this free energy equation with respect to ψ we find the variation in the order parameter, minimising with respect to \mathbf{A} we find the variation in the magnetic field within the superconductor. In doing this we find the first and second Ginzburg Landau equations respectively

$$\alpha\psi + \beta|\psi|^2\psi + \frac{(-i\hbar\nabla - 2e\mathbf{A})^2\psi}{2m_e} = 0, \quad (2.3.2)$$

$$\mathbf{J} = \frac{\nabla \times \mathbf{B}}{\mu_0} = -\frac{ie\hbar}{m_e}(\psi^*\nabla\psi - \psi\nabla\psi^*) - \frac{4e^2}{m_e}\mathbf{A}\psi^*\psi. \quad (2.3.3)$$

2.3.2 Coherence Length and Penetration Depth

Although there is no general analytic solution to the GL equations, by use of appropriate limits it is possible to calculate the characteristic length scales of variation in the order parameter and magnetic field within a superconductor: the coherence length ξ and penetration depth λ , respectively.

In the absence of any magnetic field ($\mathbf{A} = 0$), equation 2.3.2 reduces to

$$\frac{-\hbar^2}{2m_e}\nabla^2\psi + \alpha\psi + \beta|\psi|^2\psi = 0. \quad (2.3.4)$$

At the boundary of the superconductor $\psi = 0$ by definition, and deep within the superconductor we can say that $\psi = \psi_\infty = \text{constant}$ in order for the superconducting state to indeed be a free energy minimum. Taking these limits yields the solution [35]

$$\psi = \psi_\infty \tanh\left(\frac{x}{\sqrt{2}\xi}\right), \quad (2.3.5)$$

where the temperature dependent coherence length is

$$\xi(T) = \left(\frac{\hbar^2}{2m_e|\alpha|}\right)^{\frac{1}{2}}. \quad (2.3.6)$$

Taking now equation 2.3.3 with the same consideration that $\psi = \psi_\infty = \text{constant}$ deep within the superconductor yields

$$\mathbf{J} = -\frac{4e^2}{m_e} \mathbf{A} |\psi|^2 . \quad (2.3.7)$$

By performing $\nabla \times \mathbf{J}$ and invoking Maxwell's equations $\nabla \times \mathbf{B} = \mu_0 \mathbf{J}$ and $\nabla \cdot \mathbf{B} = 0$ we find

$$\nabla^2 \mathbf{B} = \frac{\mathbf{B}}{\lambda^2} , \quad (2.3.8)$$

where the temperature dependent penetration depth is

$$\lambda = \left(\frac{m_e \beta}{4e^2 \mu_0 |\alpha|} \right)^{\frac{1}{2}} . \quad (2.3.9)$$

2.3.3 Type I and Type II Superconductors

The ratio between these two characteristic length scales gives rise to the two distinct classes of superconductors [35]

$$\begin{aligned} \kappa_{\text{GL}} = \frac{\lambda}{\xi} &\leq 1/\sqrt{2} \quad \text{Type I} \\ \kappa_{\text{GL}} = \frac{\lambda}{\xi} &> 1/\sqrt{2} \quad \text{Type II} \end{aligned}$$

Note that κ_{GL} is independent of temperature. We describe the magnetic behavior of these two classes of superconductors, Type I and Type II, in the subsections below.

2.3.3.1 Type I Magnetic Behaviour

In Type I materials cooled below their critical temperature, an applied field induces a supercurrent flow at the material surface which generates its own magnetic field which is equal and opposite to the applied field. This additional field screens the interior of the superconductor resulting in the Meissner effect [36]; the perfect diamagnetism that superconductors are famous for. There is a limit to the magnetic field strength that the surface supercurrents can generate however (the critical field

H_{cb}) above which the superconducting state is destroyed and the material is entirely normal.

For an isotropic superconducting bulk at $T = 0$ K, $B = 0$, $\psi = \text{const}$ the Gibbs free energy, G_s is given by [35],

$$G_s = V \left(g_n - \frac{|\alpha|^2}{2\beta} + \frac{1}{2}\mu_0\mathbf{H}_0^2 \right) \quad (2.3.10)$$

where the normal state Gibbs free energy G_n is

$$G_n = Vg_n . \quad (2.3.11)$$

At the transition they must be equal, yielding the critical field

$$H_{cb}^2 = \frac{|\alpha|^2}{\mu_0\beta} . \quad (2.3.12)$$

2.3.3.2 Type II Magnetic Behaviour

First described by Abrikosov in 1957 [37] Type II superconductors exhibit a second, stable ‘mixed’ superconducting state in which vortices of fixed magnetic flux $\phi_0 = h/2e$ penetrate into the bulk superconductor. The vortices have a characteristic radius of ξ and are surrounded by screening supercurrents with a characteristic radius of λ and typically arrange themselves into a triangular lattice [38]. Rather than a single critical field, Type II materials therefore have a lower critical field B_{c1} (defined as the field at which the first flux vortex enters the superconducting bulk) and an upper critical field B_{c2} (defined as the field at which the material is entirely comprised of overlapping flux vortices and is completely normal). These fields are shown in comparison with the Type I critical field in figure 2.1.

Similar to the case for the calculation of H_{cb} for a Type I superconductor, in order to find the lower critical field, H_{c1} , we can equate the free energies of the system in the Meissner state and in the situation where a single flux vortex has penetrated the bulk [39]

$$H_{c1} = \frac{\phi_0}{4\pi\mu_0\lambda^2} \ln \kappa_{GL} = \frac{H_{cb}}{\sqrt{2}\kappa_{GL}} \kappa_{GL} . \quad (2.3.13)$$

To find the upper critical field H_{c2} we must look to the first GL equation 2.3.2. Recognising that close to the normal state ψ is small, and by setting $\mathbf{A} = (0, x\mu_0 H_0, 0)$ equation 2.3.2 is reduced to the equation of a quantum harmonic oscillator

$$\frac{-\hbar^2}{2m_e} \frac{\partial^2 \psi}{\partial x^2} + \frac{1}{2m_e} \left(-i\hbar \frac{\partial}{\partial y} - 2ex\mu_0 H_0 \right)^2 \psi - \frac{-\hbar^2}{2m_e} \frac{\partial^2 \psi}{\partial z^2} = |\alpha| \psi, \quad (2.3.14)$$

and has solutions of

$$H_0 = \frac{m_e}{(2n+1)\hbar e\mu_0} \left(|\alpha| - \frac{\hbar^2 k_z^2}{2m_e} \right), \quad (2.3.15)$$

where k_z is the component of the wave vector in the z direction. The upper critical field is the highest valued of these fields (found for $k_z = 0$ and $n = 0$)

$$H_{c2} = \frac{m_e |\alpha|}{\hbar e\mu_0} = \frac{\phi_0}{2\pi\mu_0\xi^2} = \sqrt{2}\kappa H_{cb}. \quad (2.3.16)$$

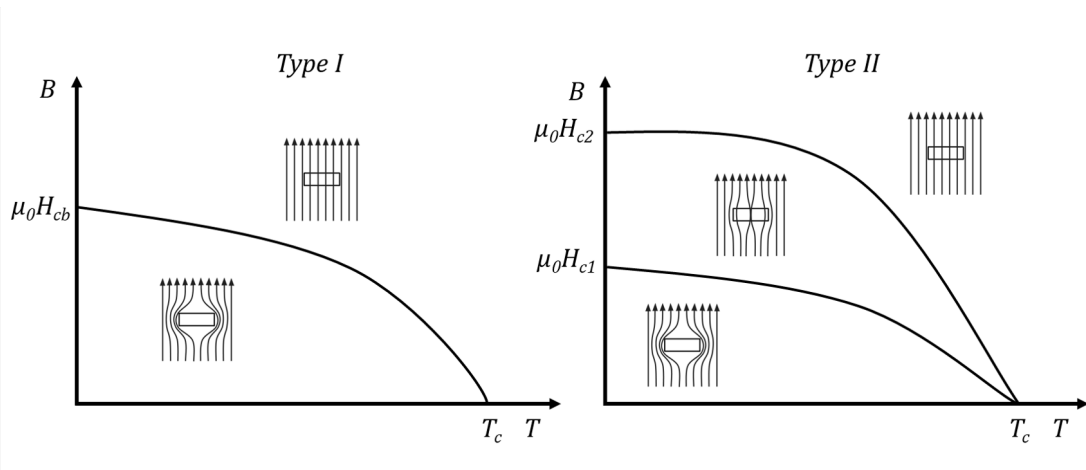


Figure 2.1: Critical fields of Type I and Type II superconductors as a function of temperature. Type I superconductors have two states: Meissner and normal. Type II superconductors have three states: Meissner, mixed and normal. μ_0 is the permeability of free space. Adapted from [40].

2.4 Critical Current Density

Current flowing through a bulk superconductor in the mixed state results in a Lorentz force $\mathbf{F}_L = \mathbf{J} \times \mathbf{B}$ on the flux vortices. In a perfectly homogeneous superconductor, this force causes the flux vortices to move, resulting in the generation of an electric field, resistance to current flow, heat, and ultimately the destruction of the superconducting state (a quench). Practical superconductors are therefore not perfectly homogeneous and contain normal regions within the material structure which act as energy wells for flux vortices, anchoring them in a fixed position [41] by exerting a pinning force \mathbf{F}_p . These normal regions are defects within the material lattice such as grain boundaries, impurities, substitutional atoms etc. They can be added during superconductor manufacture to increase the overall pinning force (so-called artificial pinning centres e.g. [42]) and can accrue during the superconductor operational lifetime due to e.g. exposure to neutron irradiation [43]. A large enough current density (the critical current density, J_c) will however overcome this pinning force - where the pinning force is defined by $\mathbf{F}_p = \mathbf{F}_L = \mathbf{J}_c \times \mathbf{B}$. J_c is a function of temperature, field and strain: changes in temperature affect the size of flux vortices through λ and ξ ; changes in field affect the spacing of flux vortices (in an ideal Abrikosov vortex, spacing $\propto 1/\sqrt{B}$ [37]); and changes in strain affect the superconductor microstructure and the location and form of pinning sites. The whole stand/tape critical current densities as a function of applied field for a number of superconducting strands and tapes are shown in figure 2.2 for reference.

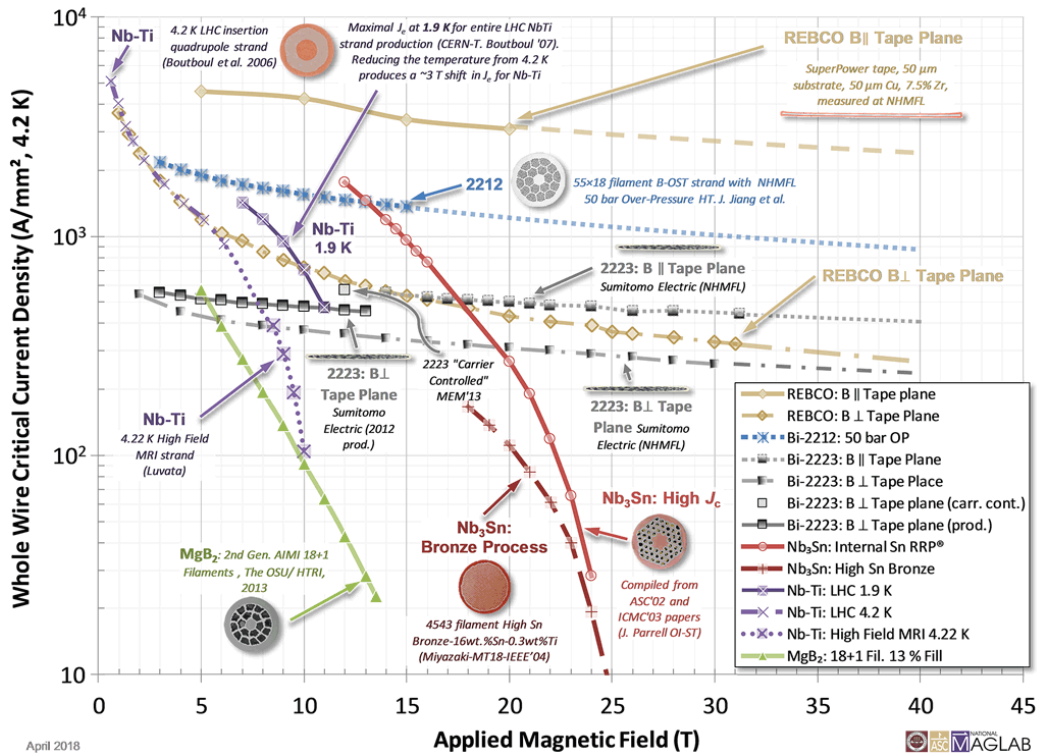


Figure 2.2: Whole strand/tape critical current densities as a function of applied field for superconductors available in long lengths [44].

2.5 Technological Superconductors for Fusion Reactors

Beginning with Tore Supra [45] (now WEST) in 1998, EAST [46] in 2006 and KSTAR [47] in 2008 superconductors are rapidly replacing copper as the material of choice for tokamak magnets. Within the next decade JT-60SA [48], DTT [49], SPARC [4], ITER [17] and CFETR are set for completion, and the 2030-40s will see the development of ARC [9] and DEMO [6]. This shift towards superconducting magnets is primarily driven by the drastically reduced power requirements of the magnet cooling system. For example, ARIES-ST (a proposed copper based tokamak reactor) would have total magnet system resistive losses of ≈ 550 MW [50] an order of magnitude larger than the ITER cryoplant's 39 MW installed power [51]. Indeed, it has become the broad opinion of the community that "...copper

coils would require too large an electric power to be acceptable for ITER as well as for a future reactor” [17]. To-date all superconducting tokamak magnets have been made with either Nb-Ti or Nb₃Sn. This is however set to change, as the rapidly advancing HTS industry has catalysed the development of tokamak designs with rare-earth-barium-copper-oxide (REBCO) based magnets, the first of which (SPARC and ST-135 [11]) are scheduled for construction within the next few years. We briefly discuss the applications and manufacture of these three materials, Nb-Ti, Nb₃Sn and REBCO in the following subsections.

2.5.1 Niobium-Titanium

Nb-Ti is the workhorse of the superconductivity industry, used in more than 90% of superconducting applications worldwide [23]. Originally developed for the Fermilab accelerator magnets, by far the most common commercially available alloy is Nb-46.5wt%Ti, which was optimised for maximum critical current density between \approx 5 T and 7 T. As a metal alloy Nb-Ti is highly workable and the depth and breadth of its application means that its properties are very well understood. Nb-Ti cables are formed of multiple Nb-Ti strands, which are themselves formed of thousands of filaments. These filaments are produced through a process of heat treatment (in order to produce the desired number of α -Ti ribbon pinning sites) followed by extrusion. Nb-Ti’s mechanical robustness and ductility make it innately suitable for pulsed field operation, and its strands are inexpensive to produce at only \lesssim 1\$/kA m (at 6.4 T, 4.2 K) [52]. Its relatively low upper critical field $B_{c2}(4.2\text{ K} \approx 10\text{ T})$ [53] however restricts its use to the poloidal field coils in ITER [54] and DEMO [6]. Lower field (research) tokamaks such as SST-1 [55] and the recently upgraded JT60-SA [48] do however have Nb-Ti toroidal and poloidal field coils.

2.5.2 Niobium Tin (Nb_3Sn)

The first material observed to maintain superconductivity beyond 8.8 T [22] Nb_3Sn has historically been the material of choice where > 10 T fields-on-conductor were required. It is used in the world's largest superconductivity application CERN's Large Hadron Collider [19], and in the magnets of important testing facilities such as SULTAN [56]. It will be used for the toroidal field and central solenoid coils of ITER[54] and CFETR [57] and is currently the material of choice for the magnets of EU-DEMO. Nb_3Sn itself is a brittle intermetallic compound and cannot be extruded into filaments once formed. The most common multifilamentary strand manufacturing processes are the bronze-route and internal-tin methods [22]. In the bronze route method, Nb rods are inserted into a bronze ingot in a hexagonal array which is then extruded. A number of these extruded composite rods are then stacked in first a tantalum tube (which acts as a diffusion barrier) and then a copper tube. These rods are then extruded a second time to form the final strand (though the work hardened bronze must be frequently annealed during extrusion). The strands are then heat treated at ≈ 675 °C for ≈ 200 hours, during which time the tin from the bronze reacts with the niobium, creating a Nb_3Sn ring around each niobium filament. In the internal tin method, the composite rods are instead made with copper instead of bronze and have a tin core, but the extrusion process is thereafter the same as in the bronze route method (without the requirement for anneals). Internal-tin strands have a two stage heat treatment. Firstly the copper and tin are reacted at ≈ 500 °C to form a high Sn-content bronze, followed by treatment at 650 °C to form Nb_3Sn . Like Nb-Ti, Nb_3Sn cables are formed from ≈ 1000 - 1500 strands. Nb_3Sn coils are wound from pre-heat treated cables ("React and Wind", which is only suitable for large magnets with large bending radii) or are wound from unreacted cables and then heat treated as a complete component ("Wind and React", which can result in wire degradation due to stresses during heat treatment [58][59]).

2.5.3 Rare-Earth Barium Copper Oxides

Typically made with the rare earths Yttrium or Gadolinium, REBCO cuprate compounds are a family of brittle superconductors with critical temperatures ≈ 90 K. REBCO materials also have very high upper critical fields; over 100 T at low temperature [60]. These properties make the application of REBCO much broader than for low temperature superconductors: it can be used in low field applications cooled with liquid nitrogen (such motors, transformers, transmission lines etc.) [29] and high field applications cooled with liquid helium (such as high field solenoids, accelerator and fusion magnets) [61]. As ceramic materials they cannot be drawn into strands, and conductors are therefore made of thin tapes produced through thin film deposition. The most common production technique is a combination of ion beam assisted deposition (IBAD) and metal organic chemical vapour deposition (MOCVD) [62]. The REBCO layer is typically only $1\mu\text{m}$ thick (1% of the whole-tape thickness) [63]. As a relatively new material, the optimal design of REBCO cables has not yet been decided. Recent designs for high field applications include CORC [64] where REBCO tapes are wrapped around a cylindrical copper core; slotted core cables [65, 66] where stacks of REBCO tapes wound into helical slots within a copper or aluminium core; and twisted stack cables [67, 68] where stacks of REBCO tapes are twisted, encased in copper and wound in a Rutherford pattern around a copper core.

2.6 Conclusions

In this chapter we have outlined the two most important theoretical models of superconductors, the microscopic BCS theory and the phenomenological Ginzburg-Landau theory. We have described three of the critical parameters for superconductors, the critical temperature, upper critical field and critical current density above which superconducting materials are driven normal and no longer superconduct. These critical parameters describe a surface in temperature-field-current

density space, the accurate and precise determination of which is paramount for optimal and controlled applications of superconducting materials. We briefly discussed the three types of superconductors used within the field of nuclear fusion magnets: Nb-Ti (a ductile and robust alloy best suited for use below ≈ 10 T), Nb₃Sn (a brittle intermetallic compound used in the toroidal field and central solenoid coils of ITER) and REBCO (a brittle ceramic oxide compound, under consideration for the next generation of tokamak reactors). In the next chapter we continue our discussion of nuclear fusion; perhaps the most exciting application for superconductors of all.

Nuclear Fusion

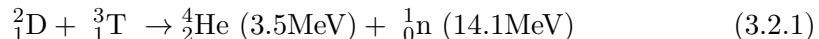
3.1 Introduction

How do we create a world free of fossil fuels? How do we create a global electricity economy powered completely by renewable energies? There are the obvious contenders: wind and solar power. But they are fundamentally unreliable and would require vast and inefficient energy storage to meet demand consistently (exacerbated by seasonal energy demand for heating) . There are also hydroelectric and tidal power. They are instead reliable, but can only be used under specific, relatively uncommon environmental conditions. Nuclear fission is another option, but we must then contend with the issue of high-level radioactive waste that lasts for hundreds of thousands of years. What then is the solution? We must look to the stars: nuclear fusion.

In this chapter we shall discuss the basic principles of technological nuclear fusion, beginning with the deuterium-tritium fusion reaction and the fusion triple product in section 3.2. We then describe the tokamak in section 3.3 before concluding with a description of the major tokamak plasma disruption limits and an overview of the empirically derived plasma energy confinement time scaling law in section 3.4.

3.2 Basic Principles of Magnetically Confined Fusion

The fusion reaction with the largest cross section (and therefore largest reaction rate) at attainable temperatures is the fusion between the two hydrogen isotopes deuterium and tritium:



D-T fusion has the highest cross section of any fusion reaction, with other reactions only reaching similar cross sections at 250 KeV (D-3He) (figure 3.1). Deuterium is abundant on Earth – accounting for $\approx 0.0154\%$ of the hydrogen in sea water. Tritium however is in limited supply, owing to its half-life of ≈ 12 years [69]. As we shall see later in this chapter, lithium is also very important for the generation of electricity from fusion power and can also be considered a ‘fuel’. It is not however in (absolute) short supply, making up ≈ 200 parts per million of the Earth’s crust [70].

The power density, p_{fus} , released by D-T fusion is given by [71]

$$p_{\text{fus}} = n_{\text{D}}n_{\text{T}}\langle\sigma v\rangle E = n^2/4\langle\sigma v\rangle E, \quad (3.2.2)$$

where n_{D} and n_{T} are the deuterium and tritium number densities, σ is the fusion cross-section, v the particle velocity and E the fusion energy (17.6 MeV for D-T). Neutrons’ neutral charge means that their energy is lost from the plasma, but the energy of the α -particles remains confined. Collisions between these helium nuclei and the surrounding D-T particles heat the plasma. In a power plant this alpha-power will dominate so-as to minimise the parasitic power load of auxiliary heating systems. However, to maintain control of the plasma, no power plant can operate with alpha-particle heating only.

In any real-world plasma there will be power losses to the surrounding environment defined in terms of a thermal confinement time, τ_{E} ,

$$P_{\text{loss}} = \frac{W}{\tau_{\text{E}}} \quad (3.2.3)$$

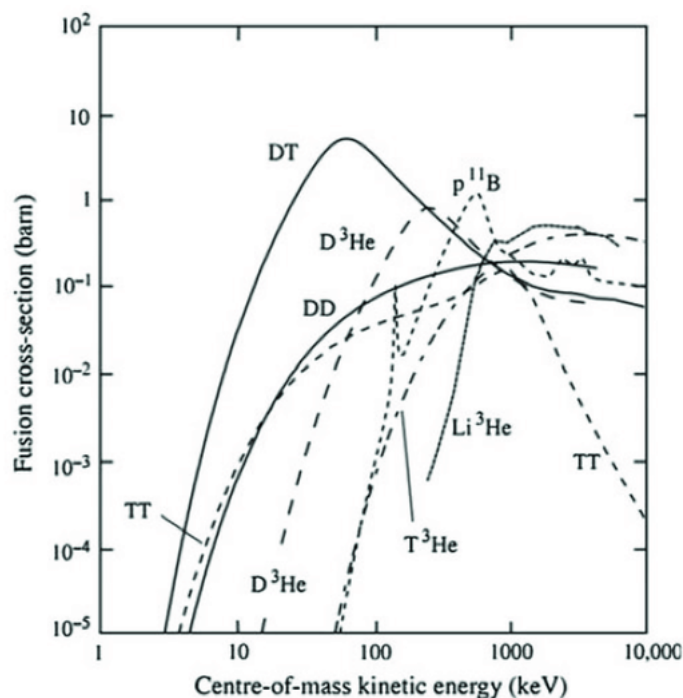


Figure 3.1: Fusion reaction cross sections as a function of incident particle kinetic energy [72]

where P_{loss} is the power loss to the environment per unit plasma volume, and W is the energy per unit plasma volume. In the case of an impurity free 50-50, D-T plasma with equal ion and electron temperatures, $W = 3nk_{\text{B}}T$. In order for a fusion plasma to be self-sustaining (an ‘ignited’ plasma), the α -particle self-heating must exceed power losses

$$\frac{n^2}{4} \langle \sigma v \rangle E_{\alpha} > \frac{3nk_{\text{B}}T}{\tau_{\text{E}}} \quad (3.2.4)$$

where E_{α} is the kinetic energy of a daughter α -particle immediately after a D-T fusion event. It is useful to rearrange this inequality to yield an equation in terms of tunable parameters, which yields the fusion triple-product

$$nT\tau_{\text{E}} \geq 12k_{\text{B}}T^2/E_{\alpha} \langle \sigma v \rangle, \quad (3.2.5)$$

where $\langle \sigma v \rangle \propto T^2$ at the minimum value of the triple product [73]. For an ideal D-T plasma, the minimum value the triple product must take, to achieve steady-state fusion conditions is then $nT\tau_{\text{E}} \approx 3 \times 10^{28} \text{ K s m}^{-3}$ (for a temperature of 1.5

$\times 10^8$ K) [74]. It is the goal of nuclear fusion reactors to maximise this condition, minimising the amount of external heat input and reducing the power consumption of the reactor itself, increasing reactor efficiency. An impurity free fusion plasma is however unrealistic as no heat exhaust solution has yet been found that does not require impurity seeding in the divertor region. Additionally, although a reactor will aim to maximise the triple product, it cannot be allowed to actually reach ignition (that is, be wholly alpha-heated) as heating is a powerful means of controlling the plasma.

3.3 Tokamaks

Tokamaks (the abbreviation of the Russian for “toroidal chamber with an axial magnetic field”) are widely regarded as the most advanced type of fusion reactor. During the next decade ITER [17] and SPARC [4], reactors designed to prove to feasibility of fusion power, are scheduled to begin operation. For these reactors, the primary figure of merit is achieving fusion power gain $P_{\text{fus}}/P_{\text{heating}} = Q_{\text{fus}} > 1$ and ideally $Q_{\text{fus}} \geq 10$. After these reactors have been proven successful, the next step is to prove the practicality of a fusion power plant and generate 100s MW net electricity (e.g. EU-DEMO [6], ARC [9], STEP [75]).

There is not a material known to science that can withstand the temperatures of order 100 million K of a fusing plasma. Given we do not have the luxury of strong gravitational confinement as occurs in stars, in order to confine a plasma, we must use ingenious methods not oft found in nature. The method discussed here is that of magnetic confinement: utilising the plasma particles’ charged nature in conjunction with strong magnetic fields arranged in a closed toroidal geometry.

A toroidal field alone cannot contain the plasma however. Magnetic drifts as a result of the curved magnetic field lines and the variable magnetic field strength across the torus minor radius inevitably lead to the plasma escaping confinement with deleterious effect [76]. In order to compensate for this, magnetic confinement

machines must also employ a poloidal field. The combination of the two fields results in helical particle motion. As a charged particle moves around the torus in the poloidal direction, the magnetic drift it experiences changes direction (from its reference frame). It experiences a downward drift at the top of the plasma and an upward drift at the bottom of the plasma resulting in zero net drift over the course of an orbit. In tokamaks, the poloidal field is generated inside the plasma by inducing a toroidal plasma current, which then in turn generates its own poloidal field (as well as through the action of the poloidal field coils and central solenoid).

3.3.1 Primary Tokamak Systems

In the following paragraphs we present the key systems of a tokamak reactor - it's magnetic field coils, auxiliary heating and current drive system, divertor and limiter, first wall and blanket and neutron shield and vacuum vessel. We omit reference to the power plant side of the machine (though of course this part is considered in our simulations), focussing only on the tokamak itself.

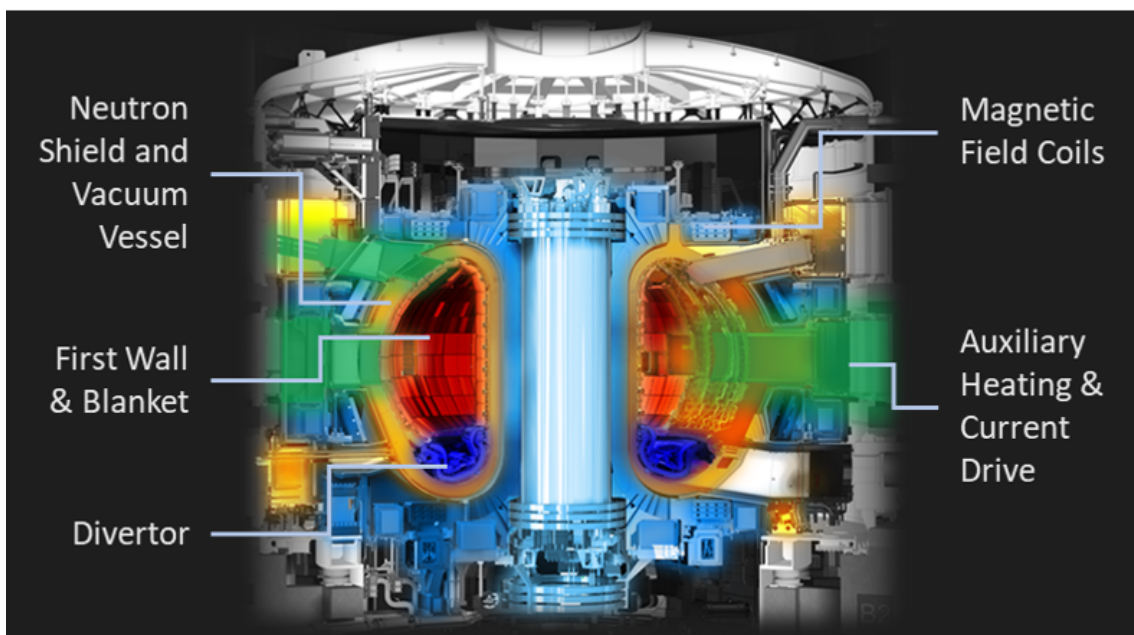


Figure 3.2: Primary systems of the ITER tokamak. Adapted from [5].

3.3.1.1 Magnetic Field coils

Tokamaks are typically built with three primary magnet systems: the toroidal field (TF) coils, the poloidal field (PF) coils and central solenoid (CS) [17]. The TF coils are typically D-shaped (in order to maintain constant tension in the coil during operation [77]) and are responsible for the generation of the toroidal magnetic field. The CS is located at the centre of the tokamak core and is typically responsible for both plasma start-up and for maintaining plasma current throughout the plasma pulse. The PF coils are usually located outside of the TF coils, though in spherical tokamaks can be within the TF magnet cage [78]. They are involved in plasma start-up and current drive, and assist with plasma shaping. Second order coils include divertor coils, responsible for shaping the plasma in the divertor region; error field correction coils, for fine tuned plasma shaping during operation; and edge localised mode (ELM) control coils for suppressing ELMs [79] (which can deposit up to 15% of the plasma stored energy on the first wall [80]).

3.3.1.2 Auxiliary Heating and Current Drive

As well as inductively, the plasma current can be induced and the plasma can be heated through externally driven auxiliary systems. These fall into two broad categories [81]: Radio Frequency (RF) systems and Neutral Beam Injection (NBI). RF systems where electromagnetic radiation is fired into the plasma at the resonance frequency of electron and/or ion Larmor motion, resulting in heating and electron/ion motion (i.e. current). Examples include electron cyclotron current drive (ECCD), ion cyclotron current drive (ICCD) and lower hybrid current drive (LHCD). In order for RF waves to penetrate into the plasma core their frequency must exceed the electron plasma frequency. For efficient absorption by electrons, the frequency must be close to the electron cyclotron frequency. Unfortunately, in many spherical tokamaks, the plasma frequency exceeds the resonance frequency so lower harmonics are missed (the frequencies that X-mode RF waves couple to the

best!). A way around this inefficiency is to excite "Electron-Bernstein" (EB) modes [82, 83]. Ordinary waves are fired through the plasma from the outboard side, are reflected from the inboard side as extraordinary waves. These X-waves then convert to EB waves at the at the change in plasma refractive index at the ultra high resonance and heavily damp even on higher EC harmonics thereby efficiently depositing energy into the plasma. NBI systems involve beams of high-energy neutral particles are fired into the plasma, imparting energy and momentum as the collide with the plasma ions - depositing heat and driving a current. A deuterium (although in principle tritium could also be used) plasma is formed and the ions are accelerated through a beam line with a strong electric field. They then pass through a gas cloud which neutralises the beam, without stripping away too much momentum. These neutral atoms are then released into the plasma core.

3.3.1.3 Divertor and Limiters

In order to prevent impurity build up in the plasma core, modern tokamaks employ divertor technology. The outermost magnetic field lines in the plasma remain open, ending at bespoke heat resistant plates. Material that falls into or is sputtered into the plasma is therefore diverted onto these plates, and does not contaminate the core plasma. These plates must be able to withstand very high heat fluxes (5 - 10 MW m⁻² [84]) and are therefore typically made from tungsten. The divertor is an area of highly active research: reactors such as MAST-Upgrade [78, 85] and the Divertor Test Tokamak [49, 86] have been designed specifically to determine the optimal divertor design for EU-DEMO and future tokamak power plants.

Limiters (and older technology) are sacrificial circumferential plates that jut out from the first wall into the plasma scrape-off layer. They prevent the plasma from interacting with the rest of the first wall (during normal operation) and act as "shock absorbers" of high heat loads during off-normal events. Limiters are also instrumental in many plasma start-up scenarios and ramp-down: the initial plasma is typically made to form around the limiters, and during ramp down the plasma is

guided to the limiters to prevent unwanted heating of other wall components. Older tokamak designs relied entirely upon limiters for heat exhaust, but sputtering of material into the plasma core is worse in a purely limited plasma (rather than a diverted one). A comparison between a a diverted and a limited tokamak plasma is shown in figure 3.3.

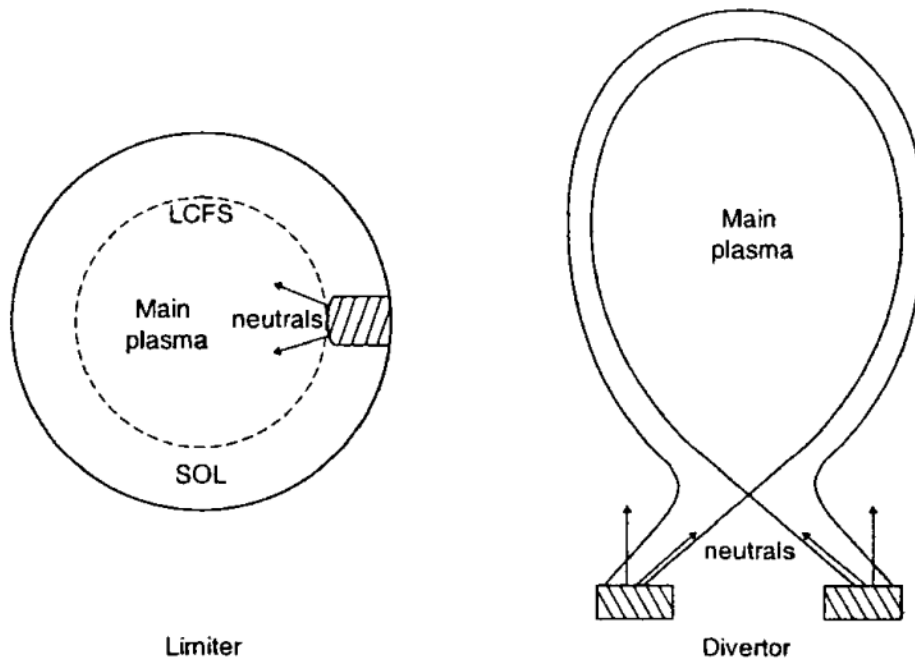
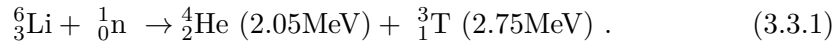


Figure 3.3: Comparison between a limited and a diverted tokamak plasma, showing the last closed flux surface (LCFS) and scrape off layer (SOL) in the limiter case [87].

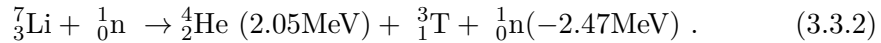
3.3.1.4 First Wall and Blanket

The first wall is the material that surrounds the plasma in the reactor core. It must be able to withstand heat fluxes $> 2 \text{ MW m}^{-2}$ and be resistant to sputtering (as to avoid cooling the plasma via parasitic radiation as a sputtered particle is ionised). Older tokamaks employed a graphite first wall, though these have fallen out of favour for tungsten and beryllium (primarily due to concerns of tritium retention [88]). Behind the first wall is the blanket. Here $> 99 \%$ incident fusion neutrons

are absorbed [89] and react with lithium-6 producing tritium and heat



The blanket lithium is enriched with Li-6, but also includes Li-7 which reacts with neutrons as



The tritium is then processed and passed back into the reactor as fuel, and the heat is used to power steam turbines for electricity generation. Proposed designs include lithium silicate and titanate pebble beds, liquid lithium-lead eutectic blankets and molten lithium salt blankets [90, 9].

3.3.1.5 Neutron Shield and Vacuum Vessel

The role of the neutron shield is to absorb the vast majority of the neutrons that remain after passing through the blanket [91]. Left unchecked these would damage delicate electronics, reduce the lifetime of superconducting magnets and significantly increase the power load on the magnet cryogenic cooling system. The neutron shield may be incorporated into the reactor vacuum vessel. For example in ITER, water and boronated steel plates are included within the vacuum vessel wall for this purpose [17]. The vacuum vessel itself is a barrier between the near vacuum conditions of the plasma chamber (with particle densities of $\approx 10^{-7} - 10^{-6} \text{ kg m}^{-3}$) and the reactor building. There is additional concrete “bioshield” between the reactor and personnel during operation. For example, in JET this shield is 2.5 m thick and is lined with 300 mm thick boronated concrete blocks [92],

3.4 Reaching for the Stars

In order to generate 100s MW to GWs, the goal of a commercial fusion tokamak power plant is to maximise fusion power [93, 94],

$$P_{\text{fus}} \propto \frac{\beta_{\text{N}}^2 B_{\text{T}}^4 R^3}{q^2 A^4} , \quad (3.4.1)$$

(where β_N is the normalised plasma beta, B_T is the toroidal field on plasma, R is the plasma major radius, q is the safety factor and A is the plasma aspect ratio) whilst simultaneously maximising fusion power gain [93, 94],

$$Q_{\text{fus}} = \frac{P_{\text{fus}}}{P_{\text{aux}}} \propto \frac{1}{\frac{q^{3.1} A^{3.53}}{H_{98}^{3.23} \beta_N^{0.1} R^{2.7} B_T^{3.7}} - \frac{1}{5}}, \quad (3.4.2)$$

where P_{aux} is the auxiliary power required to heat the plasma and H_{98} is the plasma H-factor. In the derivations of the above two equations, ITER-like confinement time scaling, a plasma temperature of 10-20 keV and $\beta_N \approx \beta_{95} A$ are assumed. From these equations we get an idea of the three schools of thought for tokamak power plant design: (i) ITER/DEMO-like reactors [6, 17] with large R and modest B_T and A , (ii) ARC-like reactors [9] with large B_T , small R and modest A and (iii) STEP-like reactors [75] with small A and modest B_T and R .

3.4.1 Physical Limits on Plasma Performance

Tokamak designers and operators must minimise the disruptivity of tokamak in order to generate fusion power for multiple hour pulses - an essential requirement of a base-load power plant. The most common causes of plasma disruptions are magnetohydrodynamic (MHD) instabilities [95]. Avoiding these disruptions requires respect of limits on q and β_N which are regrettably at odds with increasing P_{fus} and Q_{fus} .

The onset of kink instabilities sets a minimum of $q = 1$ throughout the entire plasma, where q is defined by [96]

$$q = \frac{aB_T}{RB_p} \propto \frac{a^2 B_T}{RI_P}, \quad (3.4.3)$$

where B_p is the plasma poloidal field and I_P is the plasma current. Most tokamaks operate with a safety factor at the 95 % poloidal flux surface of $q_{95} \geq 3$ for added security. The onset of ballooning instabilities sets a maximum of $\beta_N \approx 3.5$. β_N is defined as

$$\beta_N = \beta \frac{aB_T}{I_P}, \quad (3.4.4)$$

where β is the ratio between the plasma pressure and magnetic pressure

$$\beta = \frac{\langle nk_{\text{B}}T \rangle}{B_{\text{T}}^2/2\mu_0} . \quad (3.4.5)$$

Additionally, increasing the plasma density above the ‘Greenwald density’ [97]

$$n_{\text{GW}} = \frac{I_{\text{P}}}{\pi a^2} \quad (3.4.6)$$

leads to a disruption in almost all circumstances. Unfortunately, there has not yet been any theoretical model that fully describes the cause of this limit [98]. This limit can however be ‘exceeded’ by making use of ‘peaked’ plasma density profiles, where the core density is above n_{GW} but remains below it at the plasma edge. Such operation has become common-place in advanced reactors and will be used in DEMO [6] where $n_{\text{GW}}^{\text{edge}} = 0.8$, but $n_{\text{GW}}^{\text{line-avg}} = 1.1$.

3.4.2 Plasma Energy Confinement Time

Although not a hard, disruption based limit, empirical evidence from many thousands of plasma pulses across many tokamaks has identified a clear trend in plasma energy confinement time defined by the 1998 ITER Physics Basis ELMy H-mode scaling [99]

$$\tau_{\text{E}}^{\text{IPB98(y,2)}} = 5.26 \times 10^{-2} I_{\text{P}}^{0.93} B_{\text{T}}^{0.15} P_{\text{loss}}^{-0.69} n^{0.41} M^{0.19} R^{1.97} A^{-0.58} \kappa^{0.78} , \quad (3.4.7)$$

where M is the effective mass of the plasma ion species and κ is the plasma elongation. It should be noted that this is not the only scaling law available (e.g. [99, 100, 101]) though no others are used in this work. The ratio between the confinement time calculated with the ITER scaling law and the actual measured or expected confinement time defines the H_{98} -factor

$$H_{98} = \frac{\tau_{\text{E}}^{\text{measured or expected}}}{\tau_{\text{E}}^{\text{IPB98(y,2)}}} . \quad (3.4.8)$$

ITER is nominally designed with $H_{98} = 1.0$, though pulses with $H_{98} > 1.0$ have been observed in a number of existing tokamaks, e.g. DIII-D [102], and indeed ITER is

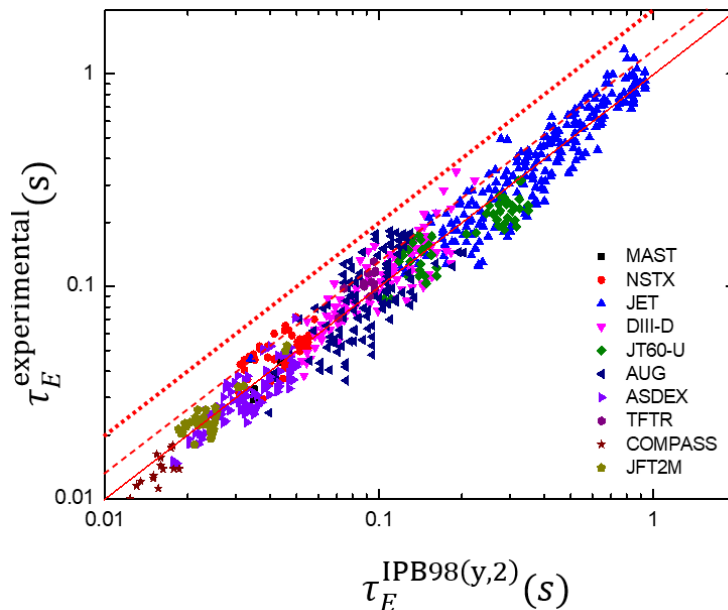


Figure 3.4: A comparison between experimentally measured plasma energy confinement times from various tokamaks and the confinement time predicted by the IPB98(y,2) scaling law [99]. Figure adapted from [99]. The solid line is $H_{98} = 1.0$ dashed line is $H_{98} = 1.2$ and the dotted line is $H_{98} = 2.0$.

expected to reach $H_{98} = 1.57$ in reversed-shear operation and $H_{98} = 1.2$ in hybrid operation [103]. Clearly too, taking a subset of the IPB98(y,2) data for different reactor geometries can yield quite different scaling laws and H_{98} -factors. For example, confinement times of spherical tokamaks appear to have much stronger field dependence [101, 104] than the IPB98(y,2) scaling e.g. $\tau_E^{\text{MAST}} \propto B_T^{1.4}$ in MAST [100].

3.5 Conclusions

Effectively harnessing nuclear fusion has the promise to change the world. Fusion reactors may deliver base-load power at the point of need, and may completely replace the conventional world fossil fuel electricity generation industry. Of the myriad fusion reactor designs, the tokamak is the closest to realising net electricity - and is hence the focus for the work presented in this thesis. In this chapter we have outlined the basic principles of nuclear fusion, the broad design of the tokamak

as well as the primary plasma physical limits on tokamak operation and design. Armed with this information, in the following chapter we outline the principles of the `PROCESS` systems code, the world's premier tokamak systems code - used throughout this work to optimise the design of all reactors studied.

PROCESS Systems Code Review

4.1 Rationale & Code Overview

Tokamak reactors are complex machines, consisting of many thousands of interweaving parts and parameters that are highly dependent on one another. Designing an optimised reactor is a monumental task. The first step of the modern reactor design process is to use a systems code to perform design consistency analysis and high-level optimisation [105]. PROCESS was developed by the UKAEA Technology Group [106, 107] and is a world-leading tokamak systems code, used for example in the development of the EU-DEMO baselines [6].

A Python wrapped, Fortran 90 code, PROCESS models all aspects of a tokamak reactor from the fusion reaction itself to the generation of net electricity; performing assessment of the physical, engineering and economic viability of a fusion reactor design. It allows users to give quantitative answers to intricate design questions such as:

“What is the lowest capital cost reactor for a given fusion power with arbitrary (or fixed) aspect ratio?”

“How does the superconducting magnet coolant temperature affect the minimum possible reactor major radius, or the shielding?”

“How do increases in plasma density affect the cost of electricity for a given reactor geometry?”

PROCESS has been comprehensively verified using higher resolution codes for many of its myriad systems and models. For example, its divertor model has been verified against the 2D SONIC code [108], its coil stress model has been verified against the MADMAX 3D finite element code [109] and its stellarator plasma physics model has been verified against W7-X data [110]. PROCESS is sufficiently highly regarded to be the code-of-choice for the verification and preliminary analyses of new reactor designs: HELIAS 5-B [111], SST-2 [112], CFETR [113] as well as EU-DEMO [114, 6] and now also STEP [75]. The overall accuracy of a reactor solution output by PROCESS can therefore be taken to be quite high; $\approx \pm 5\%$ is typical.

The code is comprehensive, and contains a great many models for each system of a tokamak reactor. Rather than reinvent the wheel and attempt to produce a description of the code in this document, the author recommends interested readers review the PROCESS Physics and Engineering papers by M. Kovari et al. [106, 107] and the PROCESS user guide [115] for greater detail on the models present. An exception for the reader has been made for key parts of the superconducting magnet models (which have been partially rewritten as part of this thesis work) and the 1990 US\$ capital cost model (which has not been widely reported on in the literature).

In the following sections we shall next review the PROCESS software and hardware requirements in section 4.2 and describe the code’s optimisation algorithm in section 4.3. Then, an overview of the PROCESS cost model is presented in section 4.4 and a broad description of the superconducting coil models is given in section 4.5. The chapter concludes in section 4.6 with a description of the author’s personal contributions to the PROCESS in the form of updated Nb-Ti and REBCO critical current density subroutines and a new \$/kA m superconductor cost model.

4.2 Software and Hardware Requirements

PROCESS is supported on Ubuntu20, Mac and Windows (through the use of Windows Subsystem for Linux, WSL1 or WSL2) operating systems. Its development is achieved collaboratively through an internal GitLab repository <https://git.ccfе.ac.uk/process/process> which natively upholds a high standard of version control. In order to install, compile and run PROCESS the following software must be installed: cmake 3.13.0 (or higher), python3-pip, gfortran and lcov as well as the numpy and pytest Python packages.

The hardware requirements for PROCESS are very low. Typical run times are only a few seconds on a single core modern computer [105]. Each VMCON solver iteration is completed in $\approx 0.1 - 1.0$ seconds (depending on the number of line searches required ((max. 10) - see section 4.3) and there are a maximum of 100 function calls (after which the PROCESS run exits and informs the user that convergence has not been met). User verification and analysis of the output is usually required as a final consistency and physicality check, though consistent reactor designs can be produced in a few hours to a few days depending on the novelty of the reactor in question and the experience of the code user.

4.3 Computational Methods

In this section we detail the PROCESS code user inputs and code structure in subsections 4.3.1 and 4.3.2. We then describe the method of Lagrange multipliers, used in PROCESS to solve the general non-linear optimisation problem in subsection 4.3.3 [115]. This method is performed numerically by the `fortran` sequential quadratic programming subroutine VMCON [116], the details of which are given in section 4.3.4.

4.3.1 User Inputs

As well as a figure of merit, the user of the code has control over three categories of parameters for each `PROCESS` calculation which are stored in either the `icc` array of constraint equations or the `ixc` array of iteration variables [115]:

- Constraint equations, of which there are two types: (1) equality constraints ensure self-consistency in the reactor design, e.g. `icc = 11 * tokamak radial build consistency` which ensures that the major radius of the machine radial build is the same as the plasma major radius (2) inequality constraints ensure that the limits on the governing physical and engineering limits are not exceeded, e.g. `icc = 31 * TF coil case stress upper limit` which ensures that the peak stress on the TF coil case does not exceed the limit set by the user. These constraints have default bounds, but the user is free to set additional manual bounds on the iteration variables.
- Iteration variables: parameters that are varied by `PROCESS` during a calculation in order to satisfy constraint equations and optimise a given figure of merit, e.g. `ixc = 29 * central solenoid bore` which allows `PROCESS` to vary the inner radius of the central solenoid coil. At each iteration step the solver calls the relevant physics and engineering subroutines after making small changes to these parameters, and determines the effect to the output as a result of these small changes (see section 4.3 for more detail). All iteration variables have default initial values, but the user is free to manually set them.
- Input parameters: fixed parameters that are not allowed to change during the calculations, e.g. `etath = 0.375D0 * thermal to electric conversion efficiency to 37.5 %` which fixes the turbine thermal to electrical power efficiency. Many of these variables can also be set as `scan` variables, where the user defines a number of values of a given parameter for `PROCESS` to use

in sequence, generating an optimised reactor design for each parameter (if possible).

An example `PROCESS` input file and output file summary are shown in Appendix A and Appendix B respectively (the full output file would be 34 pages long).

4.3.2 Code architecture

As a first step when running the `PROCESS` code, the initialisation module performs initial checks on the code inputs for inconsistencies and errors. Next, the scan module reads the input file and translates the constraint equations, iteration variables and input parameters into matrix form, readable by the optimisation algorithm `VMCON`. `VMCON` is then initialised, calls the relevant physics, engineering and cost modules and evaluates the figure of merit and constraint equations calculating the gradients of the figure of merit and constraint equations using the finite difference method. In doing this `VMCON` creates an initial estimate of the Hessian of the Lagrange function for the specific non-linear programming problem of the `PROCESS` run (see subsection 4.3.4). The code then iterates the iteration variables from the initial estimate until the convergence criterion is met (or failure-to-converge criteria are met) calling subroutines from the relevant modules as appropriate at each iteration. Once convergence is reached the code then produces multiple output files, perhaps most useful of which is the main ASCII file which gives full details of the computed reactor design.

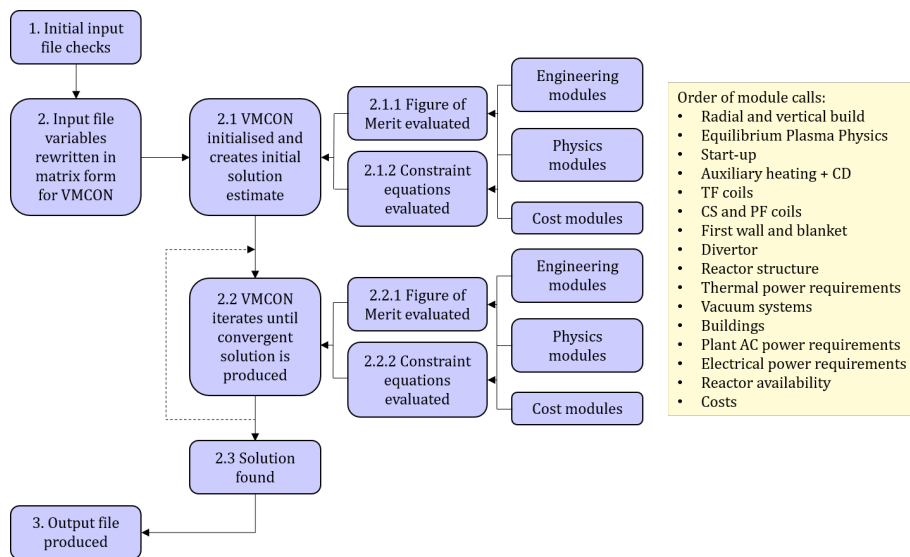


Figure 4.1: Flow chart of the overall PROCESS code architecture.

4.3.3 The Method of Lagrange Multipliers

Fundamentally, the problem of designing an optimised reactor is a specific case of the general non-linear optimisation problem. An optimised reactor must be consistent with the engineering and physical constraints of the system, and must minimise or maximise a given figure-of-merit. The general non-linear programming problem is defined as

$$\text{minimise } f(\mathbf{x}), \quad (4.3.1a)$$

$$\text{subject to } g_i(\mathbf{x}) = 0, i = 1, \dots, k \quad (4.3.1b)$$

$$\text{and } g_i(\mathbf{x}) \geq 0, i = k + 1, \dots, m \quad (4.3.1c)$$

where the solution vector \mathbf{x} is an n -dimensional array of real numbers, $f(\mathbf{x})$ is a figure-of-merit function (or “objective function”) and $g_i(\mathbf{x})$ are constraints of the system. This problem can be solved by the method of Lagrange multipliers. For simplicity, we shall begin by considering an objective function constrained by a single constraint $g_1(\mathbf{x})$. We can envisage contours of $f(\mathbf{x})$, where the contour with the (constrained) optimum value ($f(\mathbf{x}^*)$) must be tangential to the constraint at some optimal point \mathbf{x}^* . For ease of visualisation this is shown in figure ?? The gradients of two curves are parallel to each other at the point at which they are tangential, so

$$\nabla_x f(\mathbf{x}^*) = -\lambda \nabla_x g_1(\mathbf{x}^*) , \quad (4.3.2)$$

where λ is a constant known as the Lagrange multiplier (which is in fact equal to the rate at which the optimum value of the objective function changes as a function of a given constraint [117]).

The problem can be summarised with the Lagrange function

$$\mathcal{L}(\mathbf{x}, \lambda) = f(\mathbf{x}) - \lambda g_1(\mathbf{x}) , \quad (4.3.3)$$

Generalising to a system of m constraints, the gradient of the objective function at the optimum value of $f(\mathbf{x}^*)$ becomes a linear combination of the constraints' gradients at \mathbf{x}^*

$$\nabla_x f(\mathbf{x}^*) = - \sum_{i=1}^m \lambda_i^* \nabla_x g_i(\mathbf{x}^*) , \quad (4.3.4)$$

and we can write the general Lagrange function as

$$\mathcal{L}(\mathbf{x}, \boldsymbol{\lambda}) = f(\mathbf{x}) - \sum_{i=1}^m \lambda_i g_i(\mathbf{x}) . \quad (4.3.5)$$

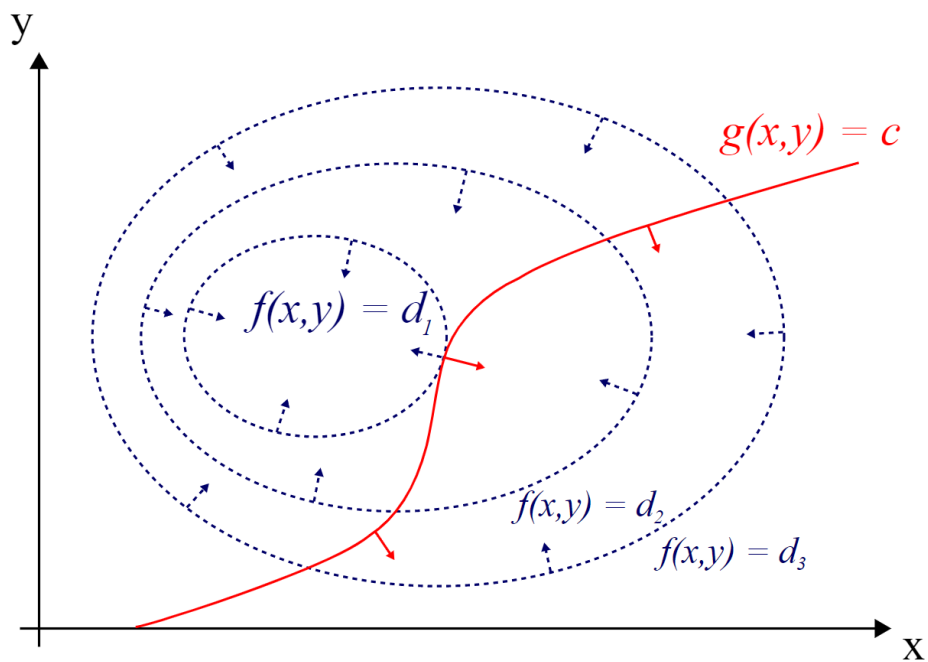


Figure 4.2: Contours of an objective function $f(x, y)$ and a single constraining function $g(x, y)$. The curvature of the functions is shown with arrows. At the constrained optimum value of $f(x, y)$ the gradients of the objective function and the constraint functions are parallel. [118]

In order for the Lagrange function of a particular problem to yield an optimum, the Karush–Kuhn–Tucker (KKT) conditions must be satisfied. These conditions are

$$\nabla_x \mathcal{L}(\mathbf{x}^*, \boldsymbol{\lambda}^*) = \nabla_x f(\mathbf{x}^*) - \sum_{i=1}^m \lambda_i^* \nabla_x g_i(\mathbf{x}^*) = 0, \quad (4.3.6a)$$

$$\lambda_i^* g_i(\mathbf{x}^*) = 0, i = 1, \dots, m, \quad (4.3.6b)$$

$$g_i(\mathbf{x}^*) = 0, i = 1, \dots, k, \quad (4.3.6c)$$

$$\lambda_i^* \geq 0, i = k + 1, \dots, m, \quad (4.3.6d)$$

$$g_i(\mathbf{x}^*) \geq 0, i = k + 1, \dots, m. \quad (4.3.6e)$$

In the special case of a continuously differentiable and convex objective function and constraints (and affine inequality constraints) the KKT conditions are sufficient for the calculation of the global optimum of the objective function. The PROCESS solver converges on a solution to the KKT conditions, but does not test whether such a solution is the global optimum. It is beholden on the user to verify that a global optimum has been found [115].

4.3.4 The VMCON Sequential Quadratic Programming Solver (SQP)

PROCESS uses the `fortran` routine VMCON (which itself is based on an algorithm formulated by Powell [116]) to solve the optimisation problem [115]. VMCON solves equation 4.3.1 iteratively, completing two major tasks in each iteration step: (1) a local positive definite quadratic sub-problem approximation to the general non-linear programming problem is solved; (2) a one-dimensional minimisation is performed, producing an estimate to \mathbf{x}^* [116] which either satisfies a user defined convergence criterion or is used as the starting point for the next iteration step. Typical of sequential quadratic programming methods, the complicated non-linear problem is reduced to solving local quadratic sub-problems of the same form as equation 4.3.1, but the objective function $f(\mathbf{x})$ is approximated by a second order

Taylor expansion of the Lagrange function (equation 4.3.5) with linear constraints about the current estimate of \mathbf{x}^* : \mathbf{x}^{j-1} . Equation 4.3.1 is thereby reduced to the expression

$$\text{minimise } Q(\boldsymbol{\delta}) = f(\mathbf{x}^{j-1}) + \boldsymbol{\delta}^T \nabla_x f(\mathbf{x}^{j-1}) + \frac{1}{2} \boldsymbol{\delta}^T \mathbf{B}(\mathbf{x}^{j-1}, \boldsymbol{\lambda}^{j-1}) \boldsymbol{\delta} \quad (4.3.7a)$$

$$\text{subject to } \boldsymbol{\delta}^T \nabla_x g_i(\mathbf{x}^{j-1}) + g_i(\mathbf{x}^{j-1}) = 0, i = 1, \dots, k \quad (4.3.7b)$$

$$\text{and } \boldsymbol{\delta}^T \nabla_x g_i(\mathbf{x}^{j-1}) + g_i(\mathbf{x}^{j-1}) \geq 0, i = k + 1, \dots, m \quad (4.3.7c)$$

where $\boldsymbol{\delta} = \mathbf{x} - \mathbf{x}^{j-1}$, the solution for a given iteration step j is $\boldsymbol{\delta}^j$ with Lagrange multipliers λ_i^j and $\mathbf{B}(\mathbf{x}^{j-1}, \boldsymbol{\lambda}^{j-1})$ is a positive definite approximation to $\nabla_{xx} \mathcal{L}(\mathbf{x}^{j-1}, \boldsymbol{\lambda}^{j-1})$, the Hessian of the Lagrange function. To prevent divergence from bad starting points $\boldsymbol{\delta}^j$ is not used directly as the next iteration variable. Instead, the next iteration variable is given by $\mathbf{x}^j = \mathbf{x}^{j-1} + \alpha^j \boldsymbol{\delta}^j$, where $\alpha^j > 0$ is the solution to the minimisation of

$$\Phi(\alpha) = f(\mathbf{x}) + \sum_{i=1}^k \mu_i |g_i(\mathbf{x})| + \sum_{i=k+1}^m \mu_i |\min(0, g_i(\mathbf{x}))|, \quad (4.3.8)$$

calculated by a line search algorithm, where $\mu_i > 0$ with weights of

$$\mu_i = \begin{cases} |\lambda_i^1| & \text{if } j = 1 (\text{first iteration}), \\ \max(|\lambda_i^j|, 1/2(\mu_i^{j-1} + |\lambda_i^j|)) & \text{if } j > 1 (\text{subsequent iterations}) \end{cases} \quad (4.3.9)$$

At every iteration of the line-search, l , a local one-dimensional quadratic approximation of $\Phi(\alpha)$ is created, $\Phi_l(\alpha)$

$$\Phi_l(\alpha) = \Phi(0) + \Delta\alpha + \frac{\Phi(\alpha_{l-1}) - \Phi(0) - \Delta\alpha_{l-1}}{\alpha_{l-1}^2} \alpha^2, \quad (4.3.10)$$

(with boundary conditions $\Phi_l(0) = \Phi(0)$, $\Phi'_l(0) = \Delta$ and $\Phi_l(\alpha_{l-1}) = \Phi(\alpha_{l-1})$) and minimised, yielding

$$\alpha_{min} = -\frac{\Delta\alpha_{l-1}^2}{2(\Phi(\alpha_{l-1}) - \Phi(0) - \Delta\alpha_{l-1})}, \quad (4.3.11)$$

and the next iteration variable is set to $\alpha_l = \min(\alpha_{min}, 0.1\alpha_{l-1})$. Convergence is tested after every line search iteration based on the criterion

$$\Phi(\alpha_l) - \Phi(0) < 0.1\Delta, \quad (4.3.12)$$

which ensures that the change in the function is small with respect to its derivative. After a solution has been converged upon, a revised estimate of the Hessian of the Lagrange function, \mathbf{B}_{new} , is calculated with the update of the iteration variable

$$\boldsymbol{\xi} = \mathbf{x}^j - \mathbf{x}^{j-1} , \quad (4.3.13)$$

and the update of the Jacobian of the Lagrange function

$$\boldsymbol{\gamma} = \nabla_x \mathcal{L}(\mathbf{x}^j, \boldsymbol{\lambda}^j) - \nabla_x \mathcal{L}(\mathbf{x}^{j-1}, \boldsymbol{\lambda}^j) , \quad (4.3.14)$$

using the Broyden-Fletcher-Goldfarb-Shanno (BFGS) quasi-Newton update.

$$\mathbf{B}_{new} = \mathbf{B} - \frac{\mathbf{B}\boldsymbol{\xi}\boldsymbol{\xi}^T\mathbf{B}}{\boldsymbol{\xi}^T\mathbf{B}\boldsymbol{\xi}} + \frac{\boldsymbol{\eta}^T\boldsymbol{\eta}}{\boldsymbol{\xi}^T\boldsymbol{\eta}} . \quad (4.3.15)$$

Rather than simply using $\boldsymbol{\gamma}$ in the formulation of \mathbf{B}_{new} , $\boldsymbol{\eta}$ is used where

$$\boldsymbol{\eta} = \theta\boldsymbol{\gamma} + (1 - \theta)\mathbf{B}\boldsymbol{\xi} , \quad (4.3.16)$$

to ensure that \mathbf{B}_{new} remains positive definite, where

$$\theta = \begin{cases} 1 & \text{if } \boldsymbol{\xi}^T\boldsymbol{\gamma} \geq 0.2\boldsymbol{\xi}^T\mathbf{B}\boldsymbol{\xi} \\ \frac{0.8\boldsymbol{\xi}^T\mathbf{B}\boldsymbol{\xi}}{\boldsymbol{\xi}^T\boldsymbol{\gamma}} & \text{if } \boldsymbol{\xi}^T\boldsymbol{\gamma} < 0.2\boldsymbol{\xi}^T\mathbf{B}\boldsymbol{\xi} \end{cases} \quad (4.3.17)$$

The initial estimate of $\nabla_{xx}\mathcal{L}(\mathbf{x}^{j-1}, \boldsymbol{\lambda}^{j-1})$ is typically the identity matrix \mathbf{I} but any constant multiple of \mathbf{I} can be used instead (and may be preferable for some problems [116]).

Finally, after the quadratic sub-problem has been solved a convergence test is made based on the criterion

$$\left| \nabla_x f(\mathbf{x}^{j-1})^T \cdot \boldsymbol{\delta}^j \right| + \sum_{i=1}^m \left| \lambda_i^j c_i(\mathbf{x}^{j-1}) \right| < \text{epsvmc} , \quad (4.3.18)$$

where `epsvmc` is a user defined error tolerance, the first term is the predicted change in the objective function after another line search is performed, and the second term is the amount by which equation 4.3.6b is unsatisfied (the ‘‘complimentarity error’’). If this sum is less than `epsvmc`, \mathbf{x}^{j-1} is accepted as the solution to equation 4.3.1. A flow chart of the VMCON optimiser is shown in figure 4.3.

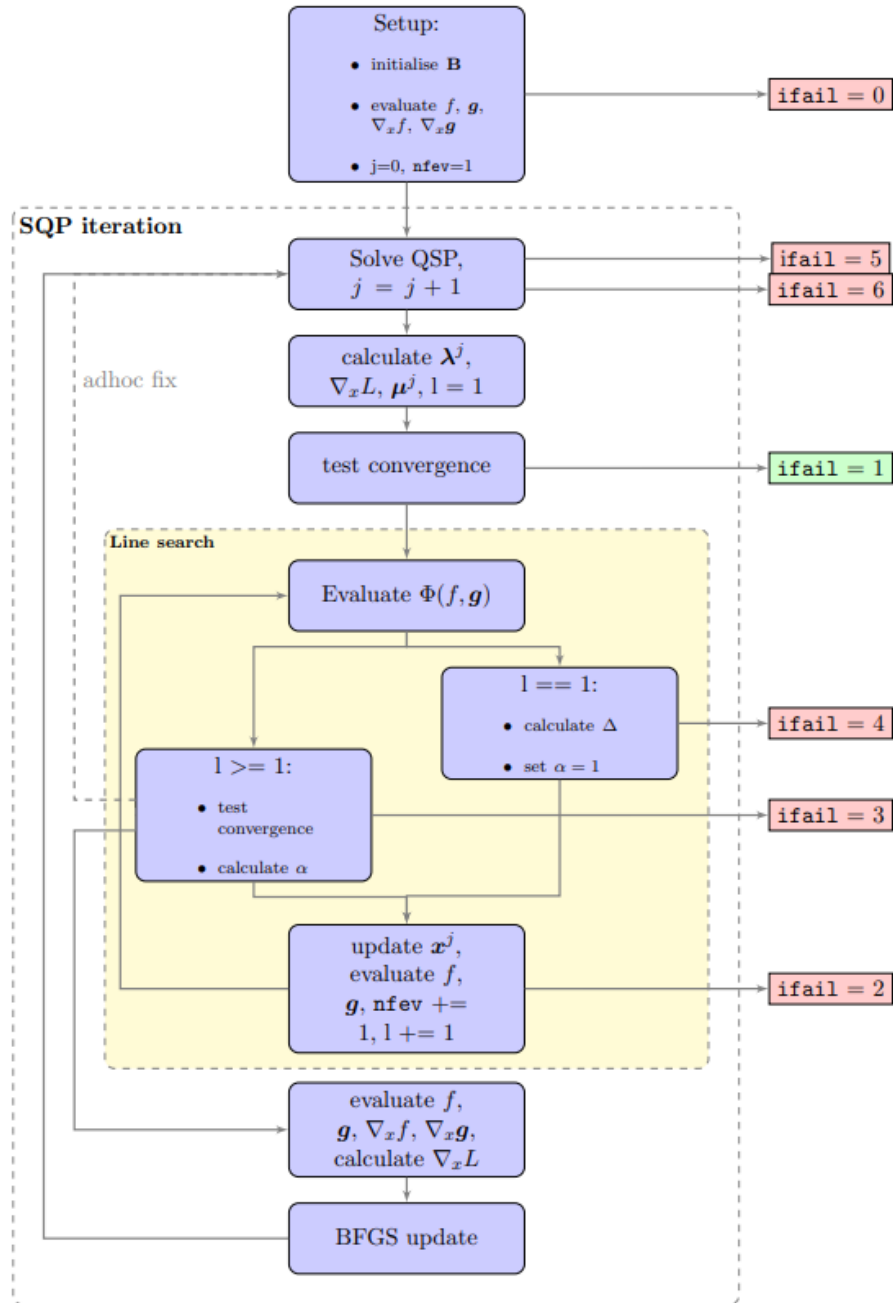


Figure 4.3: Flow chart of the VMCON Optimiser used in PROCESS [115]. ifail = 1 denotes successful convergence, ifail \neq 1 denotes failed convergence at various stages during the computation. Taken from [115].

4.4 1990 US\$ Capital Cost Model

The PROCESS 1990 US\$ cost model is a comprehensive tool that takes into account all of the components necessary to estimate the capital cost of a reactor, as well as the cost of electricity of a fusion power plant. The cost model is fully integrated into the PROCESS optimisation algorithm, and both the reactor capital cost and cost of electricity are available as figures-of-merit. It is based on the system presented in [119] wherein the numerous costs are broken down into discrete “accounts” each of which is associated with a particular tokamak subsystem. Individual components and materials have unit costs associated with them (e.g. unit cost for blanket lithium in \$/kg, unit cost for the electrical plant building in \$/m³ etc.). The author has not personally checked the unit costs present in the model and has taken it on good faith that they are representative of parts, components, materials and systems at the time of writing. The unit costs by default, correspond to first-of-a-kind costs, though the user is free to introduce a global “nth-of-a-kind” factor. Typical factors range from 0.5 to 0.8 [120]. Most components also have an additional cost factor dictated by the “level of safety assurance” (lsa) that can take one of four values. An lsa = 1 means that safety to personnel is achieved through entirely passive means of radioactive material release, whereas an lsa = 4 means that there are only active safety measures in place to prevent radioactive material release (this is the default - and the most expensive option) [121]. The resulting reductions in cost from a lower level of safety assurance depend on the particular subsystem in question.

It must be stressed that power plant and component system costs reported in later chapters should be viewed relatively - not absolutely. That is to say that it is valid to compare the relative costs of reactors produce in this work (or by PROCESS or similar design codes in previous work), but that the absolute costs should be considered with care. As a class 3 or class 4 cost analysis tool, PROCESS generated absolute costs have an error margin of -15 % to + 30 % (even class 1 cost analyses

have margins of -5 % to + 15 %) [122].

4.4.0.1 1990 to 2021 US\$

As its name suggests, the unit costs for the various materials, structures and equipment in the PROCESS cost model were collected in 1990. Extrapolating to present day (2021) costs can be difficult as the prices of different materials and services have grown at different rates with respect to standard inflation in the intervening years, and indeed can fluctuate by more than 50 % on the time scale of a few months [123]. For a broad gauge one can use the IHS-CERA index for nuclear fission power plant costs [124]. The index data were collected between 2000 and 2017; an extrapolation can be made using the consumer price index (CPI) to 1990 and 2021. Using this metric, 1 US \$ 1990 = 3.28 \$ in 2021 (when spent in the nuclear power sector).

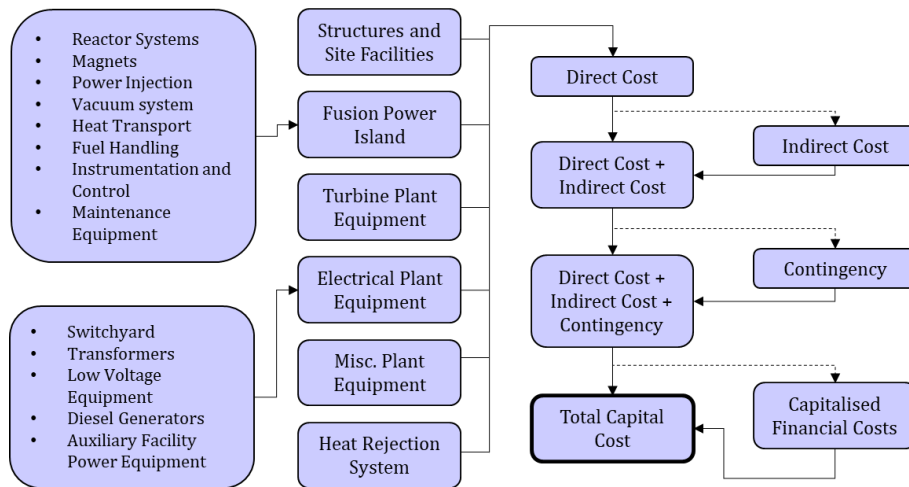


Figure 4.4: Flow chart of the capital cost estimation in PROCESS. Based on figure 3 in [119].

4.4.1 Capital Cost

The capital cost is defined as the total expenditure required to build an operational reactor. The capital cost of a tokamak reactor is made up of: direct costs, indirect

costs, contingency and capitalised financial costs (as shown in figure 4.4.

4.4.1.1 **Direct cost**

The direct cost is the cost of reactor construction, and all the costs of activities required to make the reactor operational. They include

- The raw material and equipment purchasing costs (including relevant taxes); the costs of shipment, insurance and handling of materials and equipment; R&D expenses in the development or qualification and testing for any materials and equipment specific to the reactor.
- Costs of site facilities, buildings and land.
- Labour costs of construction and component installation inclusive of payroll costs; travel and living allowances; supervision; contractor profit margins. Expenses towards management and technical direction; component and reactor inspection and testing

The direct cost assets are themselves split into six categories: structure and site facilities; fusion power island; turbine plant equipment; electric plant equipment; miscellaneous plant equipment; heat rejection systems. These categories are then further split into subcategories, for example the fusion power island category is comprised of: reactor costs (first wall, blanket, divertor etc.), magnet costs (TF, CS and PF coils inclusive of all winding costs, support structures etc.), power injection system costs, vacuum system costs, heat transport system costs, fuel handling systems costs, all instrumentation and control system costs and maintenance equipment costs.

4.4.1.2 **Indirect cost**

Included in the Indirect cost are the costs associated with supporting the activities whose costs are encompassed in the direct cost criterion. In **PROCESS** they are

calculated as: indirect cost = $0.2806 \times$ direct cost.

- Costs associated with the R&D and design of the reactor, power plant and all auxiliary components.
- Staff training costs, licensing fees, public relations exercises and advertising, legal fees, general management and administrative costs.

4.4.1.3 Contingency

No project runs exactly according to the plan. The contingency cost reflects additional expenditure as a result of unforeseen mitigating circumstances: acts of nature, supplier delays etc. They are accounted for as: contingency = $0.195 \times$ (direct costs + indirect costs).

4.4.1.4 Capitalised financial costs

The capitalised financial costs takes into account the additional expenditure due to loan repayments and the reduction in the purchasing power of the budget (as a result of inflation) over the course of reactor design and construction. Capitalised financial costs are inevitable and balance must be made between the two types; making more purchases up-front (typically) increases budget buying power, but means that larger loan repayments must be made. Capitalised financial costs are calculated as: capitalised financial costs = $0.165 \times$ (direct costs + indirect costs + contingency).

- Interest accrued on the debt portion of the reactor financing including equity charges and administration fees.
- Price escalation of plant construction, personnel salaries and other fees over the course of reactor construction.

4.4.1.5 Total Capital Cost

The total capital cost is the sum of the factors presented in sections 4.4.1.1 - 4.4.1.3

$$\begin{aligned} \text{Capital Cost} &= \text{Direct} + \text{Indirect} + \text{Temporal} + \text{Contingency} \\ &\approx 1.7828 \times \text{Direct} . \end{aligned} \tag{4.4.1}$$

4.5 Superconducting Coil Models

The PROCESS superconducting coil models are a broad, first order set of calculations that contain modules for all aspects of a superconducting coil: from the stress on the TF, CS coils (at the inboard mid-plane) and PF coils, to the critical current of the winding packs, to the power demand on the cryoplant. In this section, we will only detail parts of the models most pertinent to the work presented in later chapters, namely: a description of the winding pack geometry, calculations of the peak fields on the CS and TF coils and the current evolution in the CS and PF coils during a pulse. Descriptions of the other parts of the superconducting magnet models are described in [106, 107, 109, 125].

4.5.1 Winding Pack Geometries and Current Densities

PROCESS uses a simplified model of a coil, consisting of a winding pack made up of a number of superconducting cable turns, surrounded and supported by a steel case. In the TF coils there is a gap for insulation between the winding pack and the casing, in the PF and CS coils there is not. The CS and PF coil winding packs are rectangular in cross section, but the TF coil winding packs can have either a single rectangular, double rectangular (the default option) or trapezoidal cross-section. The superconducting cables are of a squared cable-in-conduit (CICC) design [126, 127, 128], comprised of a conductor made up of the superconductor,

copper stabiliser and a helium cooling channel (and additional void). The critical current of a single cable is given by

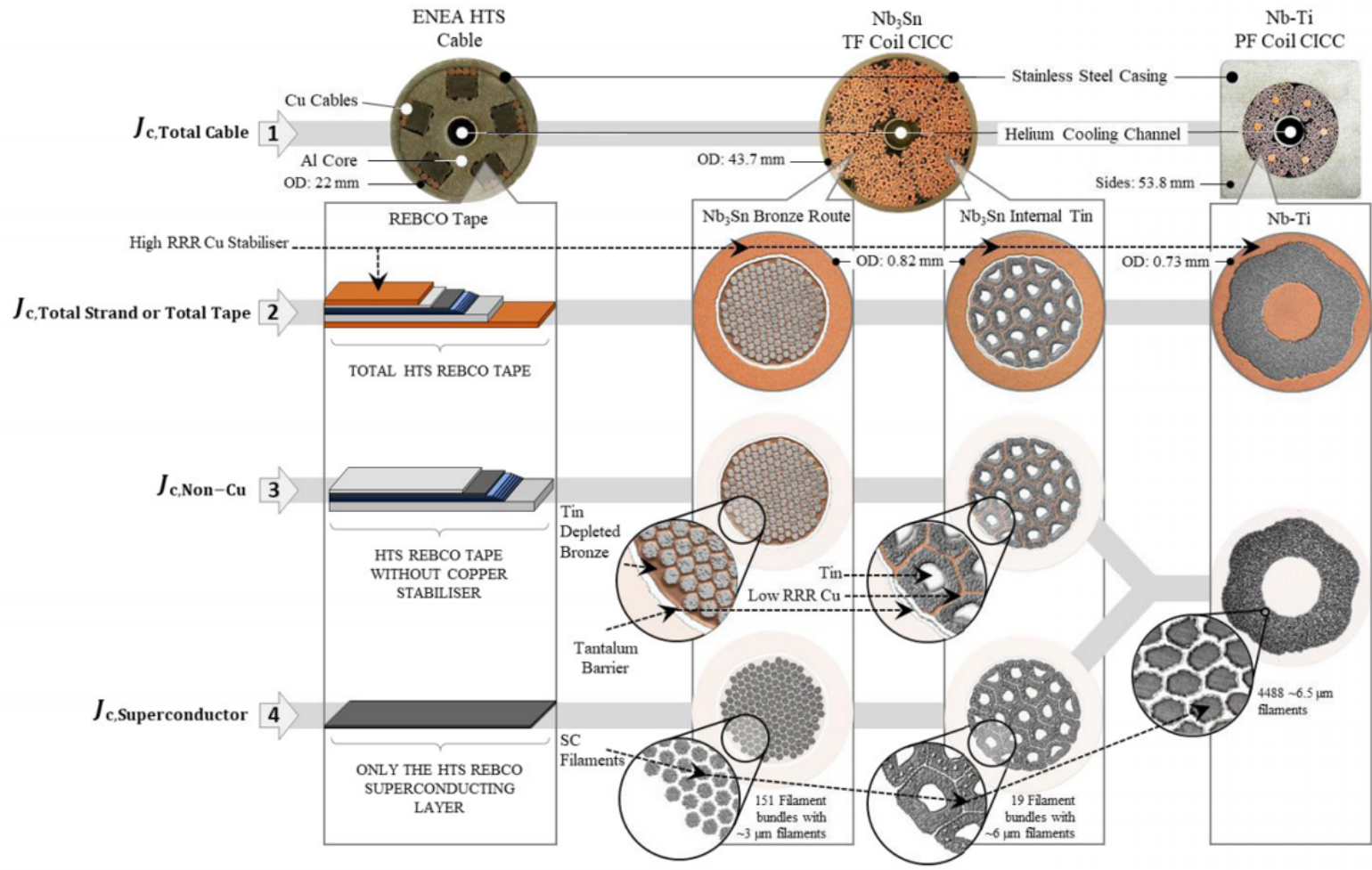
$$I_{c,cable} = J_{c,non-Cu}(1 - \text{Cu fraction})(1 - \text{He fraction}) , \quad (4.5.1)$$

where the non-copper critical current density of the superconducting strand or tape, $J_{c,non-Cu}$ is given by one of the many superconductor models (for example see section 4.6). $J_{c,non-Cu}$ is defined in figure 4.5. The cable steel and insulation fractions are taken into account at the winding pack level, the critical current of which is given by

$$I_{c,WP} = \frac{\text{No. Turns} \times I_{c,cable}}{\text{total (conductor area + conduit area + insulation area)}} . \quad (4.5.2)$$

All of the copper in the conductor is assumed to be in the strands or tapes. The copper and helium fractions of the cable and the dimensions and operating current per cable can either be set as fixed inputs or allowed to vary as iteration variables - though they are uniform for all cables in a given coil (and uniform for every coil in each system). All cables turns are modelled with inter-turn casing of uniform thickness, and the TF coils have additional inter-turn insulation of uniform thickness as shown in figure 4.6. The TF winding pack can be parameterised in three different ways

- The user defines the current in each superconducting cable (the default for TF and the only option for PF and CS coils).
- The size of the cable is defined by the user.
- The size of the conductor is defined by the user, **PROCESS** is free to vary the cable steel conduit thickness and inter-turn insulation thickness.



33

Figure 4.5: Definitions of the critical current density (the ratio between the critical current and the relevant cross-sectional area, CSA). Row 1: The total CSA of the cable is used i.e. $J_{c,Total\ cable} = I_c/CSA_{Total\ cable}$. Row 2: the total CSA of the whole strand or tape is used i.e. $J_{c,Total\ Strand\ or\ Total\ Tape} = I_c/CSA_{Total\ Strand\ or\ Total\ Tape}$. Row 3: Only the CSA of the non-copper region is used i.e. $J_{c,Non-Cu} = I_c/CSA_{Non-Cu}$. The CSA of the copper stabiliser is not included. Row 4: Only the CSA of the superconductor is used (either total filament CSA or CSA of the superconducting layer in a tape i.e. $J_{c,superconductor} = I_c/CSA_{superconductor}$. Micrographs for Nb-Ti, Nb₃Sn and images of CICC's [127, 128] for these materials, and REBCO [65] are given as examples.

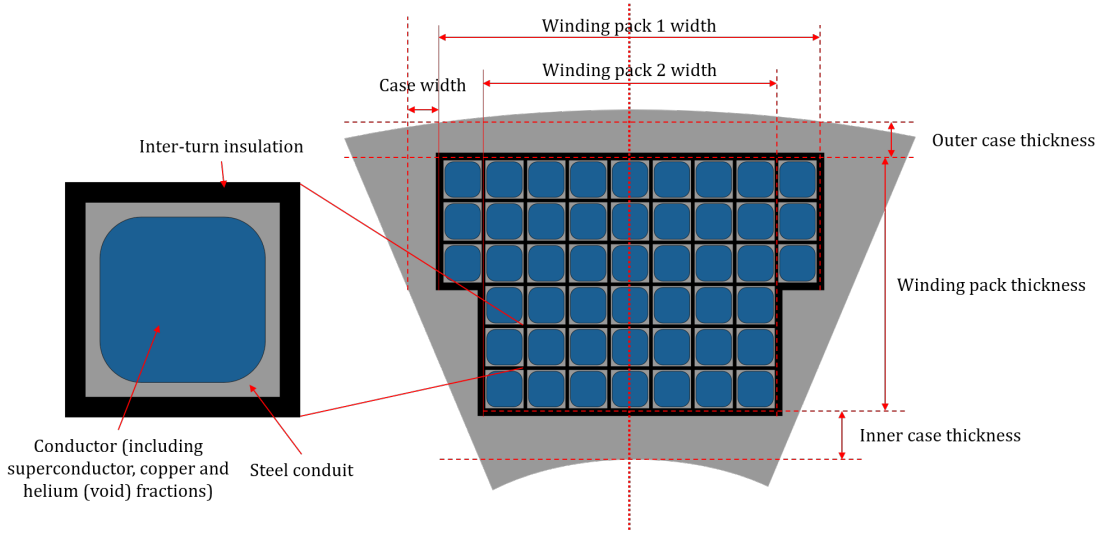


Figure 4.6: Illustration of the inboard leg of a TF coil and conductor. Grey represents steel, black insulation and blue conductor (including superconductor, copper and helium). All parameters labelled may be input as fixed values or iteration variables. The number of cable turns is arbitrary in this illustration.

The winding pack design options present in `PROCESS` do not include an explicit option for remountable coils (as is remarked upon later in chapter 8). `PROCESS` is a low-dimensionality, high-level design code, the small changes in winding pack design required for remountable magnets are design details of “resolution” beyond what the code models include. Ultimately all superconducting tokamak magnets have, and will joints - making coils remountable (in large part) is a design exercise in locating all joints of a winding pack together, appropriately shoeing them and making sure that the insulation prevents arcing after repeated mounting [61]. These are by no means easy tasks at the practical level, but they change little the overall first-order magnet design.

4.5.2 TF Coil Peak Field

In a perfectly toroidally symmetric system with the turns closely packed, the peak field on the TF coils would be given by Ampère’s law

$$B_{nominal,max}^{TF} = \frac{\mu_0}{2\pi} \frac{I_{TF}}{R_{B,max}}, \quad (4.5.3)$$

where I_{TF} is the total current in the TF coil and $R_{B,max}$ is the radial position of the peak field (i.e. the radius of the inner edge of the TF winding pack at the inboard mid-plane). However, the toroidal field on the plasma is produced by a finite number of coils, and hence the field produced by each individual coil must be increased in order to maintain the field-on-plasma in locations between TF coil limbs. In PROCESS this is calculated using the approximation

$$B_{max}^{TF} = B_{nominal,max}^{TF}(a_1 + a_2e^{-t} + a_3z + a_4zt) , \quad (4.5.4)$$

where

$$t = \frac{w}{w_{max}} , \quad z = \frac{\Delta r}{w_{max}} , \quad \text{for } w_{max} = 2(r_{in} - 0.5\Delta r)\tan\left(\frac{\pi}{N_{TF}}\right) , \quad (4.5.5)$$

where w is the toroidal width of the plasma facing side of the inboard TF leg, r_{in} is the radius of the centre of inboard TF winding pack leg, Δr is the winding pack radial thickness, and N_{TF} is the number of TF coils. For 16 TF coils: $a_1 = 0.3272$, $a_2 = 1.972$, $a_3 = -1.233$, $a_4 = 1.142$, for 18 TF coils: $a_1 = 0.3710$, $a_2 = 1.952$, $a_3 = -1.414$, $a_4 = 1.066$ and for 20 TF coils: $a_1 = 0.3030$, $a_2 = 2.027$, $a_3 = -1.135$, $a_4 = 1.019$. These values were derived by M. Kovari using MAGINT calculations on coil sets based on an EU DEMO case.

4.5.3 CS and PF Current Evolution and CS Peak Field

The total flux swing delivered by the CS and PF coil systems must be equal to the sum of resistive flux swing required during plasma start-up (which is initiated solely by inductive means in PROCESS) and current ramp, $\Delta\Phi_{res}$, the flux swing required due to the plasma self inductance, $\Delta\Phi_{ind}$ and the flux swing required during the plasma burn, $\Delta\Phi_{burn}$,

$$\Delta\Phi_{CS} + \Delta\Phi_{PF} = \Delta\Phi_{res} + \Delta\Phi_{ind} + \Delta\Phi_{burn} , \quad (4.5.6)$$

where

$$\Delta\Phi_{res} = C_E\mu_0 I_P R , \quad \Delta\Phi_{ind} = L_P I_P \quad \text{and} \quad \Delta\Phi_{burn} = V_{burn} t_{burn} , \quad (4.5.7)$$

where $C_E = 0.3 - 0.4$ (the Ejima constant [129]), I_P is the plasma current, L_P is the plasma self inductance, V_{burn} is the plasma loop voltage and t_{burn} is the plasma burn time. The total change in flux generated by the PF coils is

$$\Delta\Phi_{PF} = \sum_{i=PFcoils} L_{P,i} \frac{I_{i,eq}}{\text{no. turns}_i}, \quad (4.5.8)$$

where $L_{P,i}$ is the mutual inductance of PF coil i and the plasma and $I_{i,eq}$ is the total current required in PF coil i required to generate the vertical equilibrium field in the absence of the CS coil. The remaining flux swing generated by the CS coil affects the vertical field, so the currents in the PF coils (and subsequent flux generation) must be readjusted to counteract this. The total current swing in the CS coil is then calculated as

$$\Delta I_{CS} = \Delta\Phi_{CS} \times \frac{1}{\mu_0\pi} \left(\frac{2h}{R_{CS}^2 + (1/6)\Delta R_{CS}^2 + (1/2)\Delta R_{CS}R_{CS}} \right), \quad (4.5.9)$$

where R_{CS} is the CS inner bore, ΔR_{CS} is the CS thickness and h is half of the CS height.

Ultimately the pulse length is dictated by the maximum field that the CS coil can produce. The maximum field in the centre of the CS coil is given by

$$B_{\text{centre}}^{\text{CS}} = \mu_0 a J \beta \ln \left(\frac{\alpha + \sqrt{\alpha^2 + \beta^2}}{1 + \sqrt{1 + \beta^2}} \right), \quad (4.5.10)$$

where $\alpha = (R_{CS} + \Delta R_{CS})/R_{CS}$, $\beta = h/R_{CS}$ and J is the CS coil current density. The maximum field is at the innermost edge of the solenoid and is given for $\beta > 3$ (as is typically the case) by [106]

$$B_{\text{max}}^{\text{CS}} = \left(\frac{3}{\beta} \right)^2 B_{\text{centre}}^{\text{CS}} (1.007 + 0.0055(\alpha - 1)) + \mu_0 J \left(1 - \left(\frac{3}{\beta} \right)^2 \right) \Delta R_{CS}, \quad (4.5.11)$$

and for $\beta > 2$ by

$$B_{\text{max}}^{\text{CS}} = B_{\text{centre}}^{\text{CS}} ((1.025 - 0.018(\beta - 2)) + (\alpha - 1)(0.01 - 0.0045(\beta - 2))) . \quad (4.5.12)$$

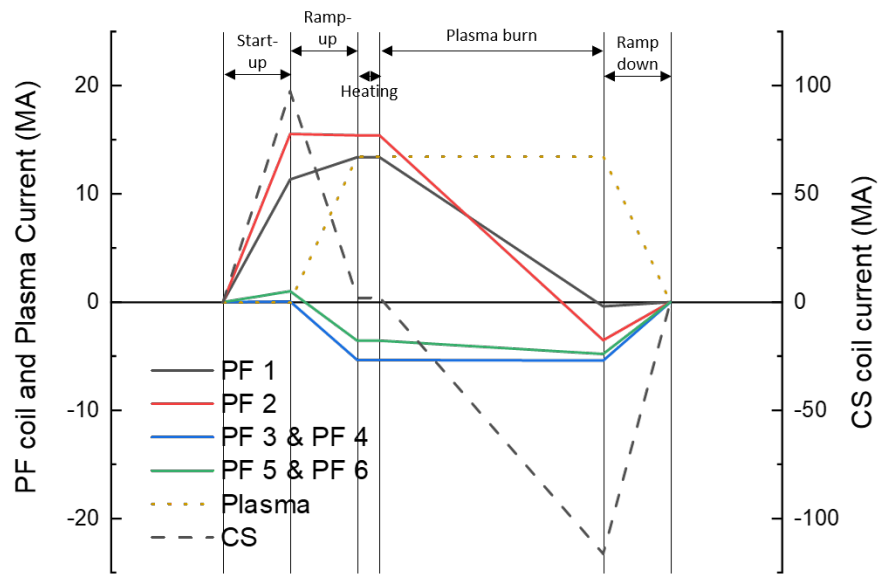


Figure 4.7: Example evolution of the current in the plasma, PF coils and CS coil of a 100 MW net electricity tokamak with a 100 second plasma burn time as calculated by PROCESS.

4.6 Personal Contributions to PROCESS

4.6.1 Updated Superconductor Critical Current Density Models

Through the course of the project it was discovered that PROCESS was lacking up-to-date scaling laws for either Nb-Ti or REBCO. The existing Nb-Ti critical surface model in PROCESS is based on an antiquated scaling law [130] that has not been used in the superconductivity field for at least three decades. It is overly simplistic and linear in $J_c(B)$ (for a fixed temperature), lacking accuracy in both the very high and low field regions: it under predicts J_c at low fields and over predicts both B_{c2}^* and J_c at high fields (see figure 4.9). The Nb-Ti strands that the law were fit to, were also made to a different specification to those used in ITER. As such, both the law itself and the fit have been revised using ITER specification Nb-Ti strand data and strain data from single filament Nb-Ti [53].

Additionally, the only existing REBCO model in PROCESS recommended for use was written expressly for modelling CROCO cables [68, 131] and did not allow for the investigation of different HTS cable designs (of which there are many, see section 2.5.3). Using the wealth of HTS tape characterisation data available at Durham University [132, 133], a revised REBCO model was written that was fully compatible with the existing cable in conduit superconducting model - allowing the user to tailor the cable copper fraction, helium fraction and conduit casing thickness as appropriate.

4.6.1.1 Durham Scaling Law

The Durham scaling law is derived from the well-known equation for the volume flux pinning force [134, 135, 136]

$$F_p = J_c B = A \frac{[B_{c2}^*(T, \varepsilon)]^n}{(2\pi\Phi_0)^{1/2} \mu_0 [\kappa_1^*(T, \varepsilon)]^2} b^p (1 - b)^q, \quad (4.6.1)$$

where n is a constant, Φ_0 is the flux quantum, ε is the strain, T is the system temperature, κ_1^* is the effective Ginzburg-Landau parameter [137] and $b = B/B_{c2}$ B_{c2} can be written as [41]

$$B_{c2}(T, \varepsilon) = \sqrt{2}\kappa_1^*(T, \varepsilon)B_{cb}(T, \varepsilon) . \quad (4.6.2)$$

From the two fluid model [35] it is known

$$B_{cb}(T) = B_{cb}(0)(1 - t^2) , \quad (4.6.3)$$

where $t = T/T_c$. From the BCS equation [41] $B_{cb}(0, \varepsilon) \propto T_c$, and extensive measurements have yielded

$$B_{c2}(T, \varepsilon) = B_{c2}(0, \varepsilon)(1 - t^\nu) , \quad (4.6.4)$$

for LTS and

$$B_{c2}(T, \varepsilon) = B_{c2}(0, \varepsilon)(1 - t)^s \quad (4.6.5)$$

for HTS. Substituting these equations into equation 4.6.1, we can write $J_{c,ENG}$ as

$$J_{c,ENG}(B, T, \varepsilon_I) = A^*(\varepsilon) \left[T_c^*(\varepsilon_I)(1 - t^2) \right]^2 [B_{c2}^*(T, \varepsilon_I)]^{n-3} b^{p-1} (1 - b)^q . \quad (4.6.6)$$

The strain dependencies are related through [136]

$$\frac{B_{c2}^*(0, \varepsilon_I)}{B_{c2}^*(0, 0)} = \left(\frac{T_c^*(\varepsilon_I)}{T_c^*(0)} \right)^w = \left(\frac{A^*(\varepsilon_I)}{A^*(0)} \right)^{w/u} , \quad (4.6.7)$$

and the (applied) strain, ε_a , can be written in terms of an intrinsic strain, ε_I where

$$\varepsilon_I = \varepsilon_a - \varepsilon_m , \quad (4.6.8)$$

and ε_m is the strain at which the peak in $J_{c,ENG}$ occurs. It has been comprehensively established that these strain scaling laws describe the current density of many different architectures of Nb₃Sn wires and we here extend their use to both other LTS, and HTS materials. One can relate the strain dependence of T_c to the strain dependence B_{c2} through a polynomial [136]

$$\frac{B_{c2}^*(0, \varepsilon_I)}{B_{c2}^*(0, 0)} = s(\varepsilon_I) = 1 + c_2\varepsilon_I^2 + c_3\varepsilon_I^3 + c_4\varepsilon_I^4 . \quad (4.6.9)$$

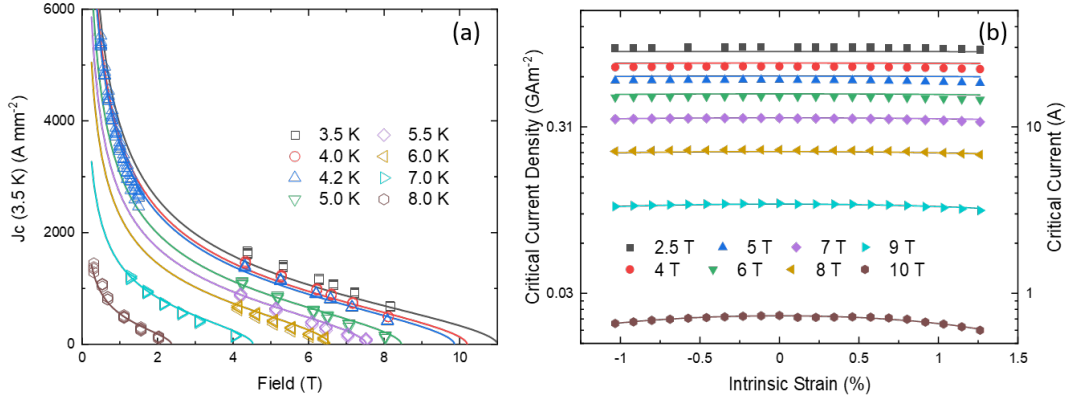


Figure 4.8: (a) $J_{c,\text{Total Strand}}(B, T)$ data from measurements performed on five ITER specification Nb-Ti strands (considered together as one data set) at zero strain. The solid lines are fits using equation 4.6.6. (b) Nb-Ti single strand critical current density as a function of applied strain at 4.2 K for different applied fields perpendicular to the direction of current flow. The solid lines are a fit using equation 4.6.7.

4.6.1.2 Nb-Ti Model

The fitting procedure began by fitting the variable temperature and field data shown in figure 4.8(a) to ascertain $A^*(0)$, $B_{c2}^*(0, 0)$, $T_c^*(0)$, p , q , n and ν . The Nb-Ti strands were produced by Chapetskiy Mechanical Plant (Glasov, Russia) for ITER PF6. Magnetisation measurements were performed on samples at 4.2 K (at low field). Transport measurements were performed at temperatures of 3.5 K, 4.0 K, 4.2 K, 5.0 K, 5.5 K, 6.0 K, 7.0 K and 8.0 K. Measurements were performed by Dr M. J. Raine. The solid lines are the best fit of the Durham scaling law to these data as calculated using the Python `scipy.optimize.curve_fit` function (with a root mean square error of 92.9 A mm^{-2}). The strands' diameters were $0.730 \pm 0.005 \text{ mm}$, and they had a copper volume fraction of 69%.

Variable strain measurements of $J_{c,\text{Total Strand}}$ at 4.2 K in high fields for the single filament Nb-Ti were made using a Walters spring [138]. For measurements on Nb_3Sn [139], the Nb_3Sn is wound on a mandrel that is shaped like the spring in its unreacted state and then reacted. It therefore fits onto the spring without

applying any strain to it. In a multifilamentary Nb-Ti wire considerable strain would be applied when winding and mounting it to a Walters spring. In such a sample, the filaments would be significantly compressed on the inboard side of the wire and significantly tensioned on the outboard side while soldering the wire to the spring. Such an effect is minimised by our choice to measure a small single filament wire because the filament lies on the neutral axis. Figure 4.8(b) shows transport measurements taken under various fields, temperatures and strains. The measurements were performed by Dr. Y. Tsui. The changes in $J_{c,ENG}$ are small but well above the uncertainties. These data were used to obtain c_2 , c_3 , c_4 and ε_m (with a root mean square error of 0.067 A).

Included in the model was the ability for the `PROCESS` user to vary Nb-Ti's upper critical field and critical temperature in the input file (rather than in the source code) in order to more easily run reactor simulations with different Nb-Ti alloys. Example critical current densities with $B_{c2}^*(0,0)$ s and $T_c^*(0)$ s are shown in figure 4.9(a).

4.6.1.3 REBCO Model

The value of A^* for REBCO was found by fitting to literature data [62], all other parameters were taken from data collected during an extensive measurement campaign at Durham university conducted by P. Branch [132, 133]. Strictly, this model should only be used within the interpolation range of the fit: $0 < B(\text{T}) < 14$ and $4.2 < T(\text{K}) < 60$. Indeed it is clear from figure 4.9 that the fit remains reasonably accurate for fields up to 30 T. The unphysical values of $B_{c2}^*(0,0)$ and $T_c^*(0)$ are due to large gradient of the REBCO flux pinning curve at low temperatures [133], though these data are not a concern so long as the fit is used within or close to the interpolation range. The Python utility `scipy.optimize.curve_fit` was used to perform the fits, with a root mean square error of 211.5 A mm^{-2} .

	$A^*(0)$ ($\text{Amm}^{-2}\text{K}^{-2}\text{T}^{3-n}$)	$T_c^*(0)$ (K)	$B_{c2}^*(0,0)$ (T)	p	q	n
Comm. Nb-Ti	3.42×10^2	9.04	14.86	0.49	0.56	1.83
REBCO	1.24×10^{-3}	184.98	138.97	0.45	1.44	3.33

	v	s	u	w	c_2	c_3	c_4	ε_m (%)
Comm. Nb-Ti	1.42	-	0.0	2.2	-0.0025	-0.0003	-0.0001	-0.002
REBCO	-	5.27	0.0	2.2	-0.0191	0.0039	0.00103	0.058

Table 4.1: Parameters for the Durham scaling law for total strand critical current densities of ITER specification Nb-Ti strands and SuperPower REBCO tape. The commercial Nb-Ti parameters were found by extensive measurements taken at Durham university [53]. The value of A^* for REBCO was found by fitting to literature data [62], all other parameters were taken from measurements on REBCO tapes [132, 133]. Values of $u = 0.0$ and $w = 2.2$ were fixed.

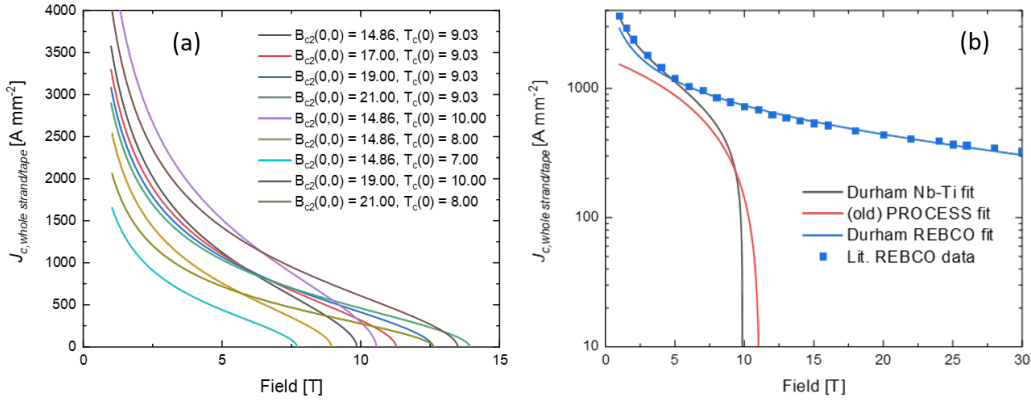


Figure 4.9: (a) Total strand critical current densities of Nb-Ti “alloys” with various values of $B_{c2}^*(0,0)$ and $T_c^*(0)$ using equation 4.6.6 and table 4.1 at 4.2 K (b) Total strand/tape critical current density of ITER specification Nb-Ti and SuperPower REBCO tape at 4.2 K. using equation 4.6.6 and table 4.1. Critical current density from the old PROCESS Nb-Ti scaling law and literature REBCO data [62] at 4.2 K are shown for comparison.

4.6.2 Costing Superconductors in \$/kA m

A new cost model for superconductors in \$/kA m was written as an alternative to the existing cost model based on bulk costs in \$/kg. This method of costing is more widely used within the superconductivity field [140] (allowing PROCESS developers to more accurately keep track of superconductor costs) and more accurately captures the cost of superconducting materials as a function of their operating conditions. Costs are typically derived under usual reference conditions for measuring the critical current of superconducting tapes and wires, namely 5, 6 or 20 T [52, 141], and 4.2 K or at self-field and 77 K [140] (though the latter temperature is relevant only for HTS). Costs under operating conditions can be derived using the simple relation

$$\text{Cost}(B, T) = \text{Cost}(B_{\text{ref}}, T_{\text{ref}}) \times \frac{J_c(B_{\text{ref}}, T_{\text{ref}})}{J_c(B, T)}, \quad (4.6.10)$$

where B_{ref} and T_{ref} are reference conditions at the which cost is quoted in the literature.

In the later chapters detailing PROCESS calculations of power plants, we use a (purchase) cost of 1.7 \$/kA m (6 T, 4.2 K) for both standard Nb-Ti and quaternary Nb-Ti, and 8.0 \$/kA m (6 T, and 4.2 K) for Nb₃Sn [142] (in 2021 costs). Currently, REBCO tapes are priced at ≈ 80 \$/kA m (6 T, 4.2 K) with the aim to reduce this to 30 \$/kA m (6 T, 4.2 K) in the near future [141]. Increased demand could reduce this even further to 10 \$/kA m (6 T, 4.2 K) [141, 140]. Here REBCO costs of 10 \$/kA m and 30 \$/kA m have been used for the $H_{98} = 1.6$ and $H_{98} = 1.2$ reactor studies respectively and are representative of the market prices of the superconducting strands/tapes, which are typically $10 \times$ [141] or even $20 - 35 \times$ the raw material costs [143]. All costs were converted from 2021 US\$ to 1990 US\$ (as required for use in the PROCESS cost module) using standard CPI inflation between now and 1990 of ≈ 2.13 [144, 145, 146]. We have used CPI here rather than the industrial index of section 4.4 as superconductors are a consumer product.

The `PROCESS` cost model requires that the costs of the superconducting strands and tapes are converted into \$/m

$$\text{cost in \$/m} = \text{cost in \$/kA m} \times \text{current in cable in kA} . \quad (4.6.11)$$

The operating currents are called from the superconducting TF, CS and PF coil routines at the same time as the critical current densities under operating conditions for equation 4.6.10.

The trustworthiness of this cost model was ascertained in three ways: (1) the cost model was applied to `PROCESS` test-cases (such as the 2018 EU-DEMO baseline model). (2) Runs were performed using the \$/kg model and then \$/kA m model. Typically, magnet costs from the new cost model differed from those of the original model by < 20 %, and were as expected in more extreme cases (such as for a REBCO cost of 0.025 \$/kA m as in section 7.3). (3) The relative costs between systems were compared to those from independent studies of other tokamaks (such as ARC [9], ITER and EU-DEMO [147]). Relative costs between plant components are broadly in line with what would be expected for the size of reactors investigated in later chapters.

4.7 Conclusions

In this chapter we have provided a description of the world-leading `PROCESS` systems code. Beginning with the rationale and necessity for the code, we have explored the mathematical methods `PROCESS` uses in order to optimise fusion reactor designs to a user defined figure of merit whilst respecting physical, engineering and cost constraints. We then detailed the `PROCESS` models most relevant to the work presented in the following chapters: key parts of the superconducting coil models; the 1990 US\$ cost model; as well as the superconductor critical current and \$/kA m cost models developed by the author. In the following chapters we shall see fruits of the `PROCESS` code calculations in the designs of capital-cost optimised fusion reactor power plants.

Our Preferred REBCO Tokamak Pilot Power Plant Design

5.1 Introduction

There are a number of road-maps [6, 15, 7] that focus on achieving a final build machine. It is now understood that both climate change and commercial imperatives mean that one simply can't wait 15 years for the optimum plasma performance to be identified and then wait another 15 years to develop the optimal superconducting technology [147]. To this end, in this chapter we present our "preferred" capital cost optimised power plant design using best-in-class technologies [53] available today (or in the near future) - reactor R₁BL. We have deliberately kept distance from so-called "advanced tokamak" designs [148] (which assume steady state operation and operate close to, or above plasma limits with normalised beta greater than 4 or Greenwald fractions of 1.0). We have based the design and scale of our reactor design on established engineering and physics already observed, or that to be implemented and designed for EU-DEMO. Reactor R₁BL uses REBCO magnets, which have very recently been demonstrated this year [12], with SPARC following in the next ten years [4, 66]. We are as confident as one can reasonably be that this reactor, presented in this (and the following chapter) could realistically be

built before the 2035-2040 deadline [15] (with concentrated, accelerated effort and generous R&D funding) for a demonstration power plant and that it can operate to specification. The above deadline is ambitious, but not unrealistic: EU-DEMO is envisioned to begin operation by 2050, but resources are diverted between different projects (STEP, SPARC, Tokamak Energy to name but a few), and the design philosophy does not allow for rapid deployment. If resources were pooled and firm nearer-term deadline set, it would not be unreasonable to suggest that it would be able to be met. The pace at which UKAEA and CFS developments are being made is evidence of this.

Section 5.2 details the rationale of key plasma physics and engineering design choices used across all of the superconducting tokamaks modelled in this chapter. Then, we optimise the radiation shield thickness for a pilot plant using detailed MCNP [149] calculations in section 5.3. Fusion reactors are a hostile environment for superconducting magnets, and they must be appropriately shielded to avoid damage and significant nuclear heating. After this we cost-optimize 100 MW_e, H₉₈ = 1.2 pilot power plant designs using TF and CS coils of REBCO (R₁BL), commercial Nb-Ti (R₂BL), Nb₃Sn (R₇AD) and quaternary Nb-Ti (R₈AD) and choose our preferred reactor design from the superconductor choice that leads to the lowest capital cost reactor of these options in section 5.4. We discover that this preferred reactor, R₁BL, has REBCO CS and TF coils, and Nb-Ti PF coils. Although we do not model any spherical tokamaks in this work, we briefly discuss them in section 5.5. In section 5.6 we compare our preferred superconducting tokamak (R₁BL) with an equivalently sized resistive tokamak power plant design where we swap the superconducting coils for either copper or cryogenic aluminium. We then conclude with a discussion on other possible cost-saving choices - to what degree reducing the required net electricity output or tritium breeding ratio would have a significant effect on the preferred reactor's cost and design in section 5.7.

We expand on this approach in chapter 6 where we consider swapping superconductors using two approaches: training and upgrading and assume that all magnets

will be fully remountable. With training magnets, the plant is cost-optimised for full power operation with REBCO but trained first using Nb-Ti coils. With the upgrading magnets approach, the plant is cost-optimised for Nb-Ti and then upgraded to REBCO coils. We have used the `PROCESS` systems code [106, 107] to find optimal designs, defined in all cases as minimised plant capital cost. For each of the training and upgrading approaches, we have considered three power plant designs which gives us six baseline tokamaks. The first two tokamaks (R_1BL and R_2BL) are the 100 MW_e, $H_{98} = 1.2$ preferred reactor and commercial Nb-Ti reactor which shall be initially discussed in section 5.4 of this chapter. The second two reactors (R_3BL and R_4BL) are designed for 100 MW_e and 1.6 and the final two reactors (R_5BL and R_6BL) produce 500 MW_e power plant and have $H_{98} = 1.2$. For each of these six baseline designs we have then investigated swapping superconductors out whilst maintaining the baseline reactors' architectures. Table 5.1 shows the key design and performance parameters for our preferred reactor, the other three 100 MW_e, $H_{98} = 1.2$ reactors from this chapter, and the additional four baseline reactors from chapter 6 together with the most important tokamaks that have operated, are operating or are planned.

	Tokamak	H ₉₈	R _{major} (m)	A	B _T (T)	B _{T,coil} ^{max} (T)	I _P (MA)	τ _{burn} (s)	P _{fusion} (MW)	P _{elec.} ^{net} (MW)	Reactor ID
Baseline	100 MW_e REBCO plant	1.2	6.75	3.15	5.36	12.50	13.6	7200	870	100	R₁BL
	100 MW _e Commer. Nb-Ti plant	1.2	7.93	2.42	3.38	9.16	18.9	7200	900	100	R ₂ BL
	100 MW _e REBCO plant	1.6	6.02	3.25	5.22	12.63	10.9	7200	840	100	R ₃ BL
	100 MW _e Nb-Ti plant	1.6	6.96	2.36	2.96	9.00	15.9	7200	870	100	R ₄ BL
	500 MW _e REBCO plant	1.2	7.48	2.39	4.18	11.85	25.2	7200	2110	500	R ₅ BL
	500 MW _e Nb-Ti plant	1.2	9.56	2.24	3.41	9.17	29.4	7200	2180	500	R ₆ BL
Add.	100 MW _e Nb ₃ Sn plant	1.2	7.21	2.99	5.16	12.1	14.6	7200	902	100	R ₇ AD
	100 MW _e Quater. Nb-Ti plant	1.2	7.28	2.93	4.94	11.7	14.9	7200	860	100	R ₈ AD
Demo.	EU-DEMO	1.1	9.00	3.10	5.90	12.50	18.0	7200	2000	500	-
	ARIES-ST†	1.5	3.20	1.60	2.10	7.40	29.0	∞	2980	1000	-
	STPP-Like†	1.6	3.42	1.68	2.50	7.56	19.4	7200	2110	100	-
	ARC	1.8	3.30	2.92	9.20	23.00	7.8	∞	525	190	-
	CFETR	1.4	7.20	3.27	6.50	14.70	13.8	∞	2190	740	-
P.o.C	ITER	1.0	6.20	3.10	5.30	11.80	15.0	400	500	-	-
	SPARC	1.0	1.85	3.25	12.20	20.00*	8.7	10	140	-	-
Research	JET†	0.5-1.3	2.96	2.40	3.45	7.40	4.8	1	16	-	-
	JT60-SA	1.1-1.3	2.96	2.50	2.25	6.40	5.5	100	41	-	-
	KSTAR	0.7-1.0	1.80	3.60	3.50	7.20	2.0	20	-	-	-
	EAST	0.5-1.2	1.75	4.38	3.50	5.80	1.0	1000	-	-	-
	WEST	1.0	2.50	5.00	3.70	9.00	0.6	1000	-	-	-
	MAST-U†	1.0-2.0	0.85	1.31	0.92	4.20	1.0	5	-	-	-
	SST-1	1.0-2.0	1.10	5.50	0.0	5.10	0.2	1000	-	-	-

Table 5.1: Key design and performance parameters of PROCESS generated 100 MW and 500 MW net electricity (MW_e) capital-cost minimised plants (six baseline reactors and two additional reactors). Our preferred reactor is in **bold**. Also shown are: EU-DEMO [6], ARIES-ST [50], a PROCESS generated pulsed Cu reactor based on STPP [150], ARC [9], CFETR [10, 57], ITER [17, 54], SPARC [4, 151], JET [152, 153, 154], JT60-SA [155, 48], KSTAR [47, 156, 157], EAST [158, 159, 160], WEST [161, 162], MAST-U [13, 163] and SST-1 [164, 165]. Tokamaks have been grouped into: those in this work, demonstration reactors, proof of concept reactors and research tokamaks. Estimated parameters indicated with (*). Tokamaks with resistive primary magnets are indicated with (†).

5.2 Reactor Design Choices

In this section, we consider the most important areas of tokamak development. We describe the choices and constraints that affect the design and cost-minimisation we have made in each area, explaining the reasoning for our choices. As a point of reference to quantify the reasoning behind these design choices, we often invoke the preferred reactor R₁BL.

5.2.1 Plasma Operation

5.2.1.1 Confinement Time and H₉₈-factor

We have primarily investigated H₉₈ = 1.2 as the most likely performance but in the following chapter shall also consider the much higher value of H₉₈ = 1.6 to quantify possible effects on costs in future from new advanced tokamak designs such as spherical tokamaks [11]. H₉₈-factor refers to the ratio between observed plasma energy confinement time, τ_E , and the τ_E predicted by the ITER Physics Basis ELMy H-mode IPB98(y,2) scaling law [99] which is derived from a vast array of tokamaks. Taking a subset of the IPB98(y,2) data for different reactor geometries can yield quite different scaling laws and H₉₈-factors. For example, confinement times of spherical tokamaks appear to have much stronger field dependence [104, 101, 166] than the standard $\tau_E^{\text{IPB98}(y,2)} \propto B_T^{0.15}$ e.g. in MAST $\tau_E^{\text{MAST}} \propto B_T^{1.4}$ [100]. Extrapolating this to stronger magnetic fields can result in H₉₈-factors upward of H₉₈ = 2.0. It is however not clear whether this strong field dependence extrapolates to power plant conditions. The field dependence is linked to strong τ_E scaling with plasma collisionality, ν_* , which itself depends on absolute ν_* [167]: at lower ν_* the confinement time scaling with ν_* is reduced. Thus in higher field tokamaks with reduced $\nu_* \propto B_T^{-4}$ it is unlikely that the strong field dependence will remain. Although ITER is nominally designed with H₉₈ = 1.0, H₉₈ > 1.0 have been observed in a number of existing tokamaks, e.g. DIII-D [102], and indeed ITER itself is

expected to reach $H_{98} = 1.57$ in reversed-shear operation and $H_{98} = 1.2$ in hybrid operation [103].

5.2.1.2 Density, β and Safety Factor

We have chosen a maximum Greenwald fraction at the plasma edge of $f_{GW}^{edge} = 0.67$ and a peaked density profile such that $f_{GW}^{line-avg} = 1.1$. The minimum plasma safety factor at the 95 % poloidal flux surface was set to $q_{95} = 3.45$. The normalised thermal beta, $\beta_N \approx 2.49$ for all reactors. These safety limit choices broadly follow the ARC and SPARC philosophies which have ($f_{GW}^{edge} = 0.67$, $q_{95} = 7.2$ and $\beta_N = 2.59$ [168] and $f_{GW}^{edge} = 0.37$, $q_{95} = 3.4$ and $\beta_N = 1$ [4], respectively) rather than the EU-DEMO philosophy which will operate closer to stability limits (with $f_{GW}^{edge} = 0.8$, $q_{95} = 3.25$, and $\beta_N = 2.50$ [6]). When we use the familiar expressions for fusion power [94] $P_{fus} \propto \beta_N^2 B_T^4 R^3 / q^2 A^4$, and safety factor $q \propto RB_T / A^2 I_P$ (for a fixed shaping factor); for a reactor design point with fixed P_{fus} : $\beta_N \propto 1 / I_P B_T \sqrt{R}$. Thus going to higher fields reduces β_N . q too scales positively with B_T , so larger fields would reduce further the probability of kink disruptions. In addition, I_P can be increased in tandem with B_T , increasing achievable plasma density (as the limiting density $n_G = I_P / \pi a^2$) whilst maintaining high q and further reducing β_N . Our calculations show that had we used the higher risk EU-DEMO safety limits for R₁BL, things don't change markedly. The capital cost decreases by 7.9 %, it decreases the major radius by 4.3 %, decreases the plasma current by 12.0 % and increases the field on plasma by 6.1 %. The findings of the following chapters are consistent should we have made this design choice.

5.2.2 Superconductor Operating Temperature

We have chosen 4.5 K as the operating temperature for all superconductors. As low temperature superconductors, Nb-Ti and Nb₃Sn coils demand liquid helium temperature operation. Even if a REBCO reactor could eventually be operated at

20 K, R₁BL operating at 4.5 K actually has a net capital cost ≈ 150 M\$ lower than at 20 K. Table 5.2 shows the capital cost of R₁BL operating at 4.5 K including the combined TF (130 M\$) and CS coils' (20 M\$) cable cost also at 150 M\$. Equivalent reactor power balances are shown in table 5.3. If operation were at 20 K REBCO's critical current density is $\approx 1.7 \times$ lower, which demands larger coils and a larger overall reactor volume, increasing direct costs by 84 M\$. On the other hand, modern cryoplant efficiency scales with temperature roughly as the ideal Carnot cycle (with a base temperature of about 2 K) [169]. The direct capital cost of cryoplant scales approximately linearly with cooling power and would be reduced from 88 \$M (as shown in table 5.2) to 20 \$M. Operation at 20 K does have the advantage of better REBCO quench mitigation due to the $\approx 3.0 \times$ greater thermal conductivity and $\approx 60 \times$ greater specific heat of RRR = 100 copper at 20 K than at 4.5 K [170]. Though, we expect that with rather modest advances in quench detection and mitigation technologies (e.g. fibre Bragg grating [171, 172], acoustic MEMS [173], stray capacitance change monitoring [174]) operation at 4.5 K using REBCO will be straightforward in future.

	R ₁ BL	R ₇ AD	R ₂ BL	R ₈ AD
Structures and site facilities	489	530	667	546
Reactor systems	39	45	61	47
Toroidal field coils	296	315	243	296
(TF cable)	(130)	(98)	(62)	(75)
Poloidal field coils and solenoid	163	159	181	153
(CS cable)	(20)	(19)	(20)	(17)
(PF cable)	(79)	(74)	(80)	(69)
First wall	63	73	107	77
Blanket	277	321	479	341
Divertor	33	38	59	41
Heating & current drive	10	10	10	10
Vacuum vessel	98	112	157	118
Power injection	88	88	88	88
Vacuum systems	16	16	16	16
Power conditioning	82	88	89	77
Heat transport system	130	139	130	127
(Cryogenics system)	(88)	(95)	(86)	(85)
Fuel handling system	120	127	147	129
Instrumentation and control	98	98	98	98
Maintenance equipment	195	195	195	195
Turbine plant Equipment	99	102	103	99
Electric plant equipment	32	34	38	34
Miscellaneous plant equipment	22	22	22	22
Heat rejection system	25	26	26	25
Plant direct cost	2373	2536	2915	2539
Constructed cost	3631	3881	4462	3885
Total Capital Investment (1990 M\$)	4231	4522	5198	4526

Table 5.2: Capital cost of the preferred reactor R₁BL and three other PROCESS generated, cost-optimised, 100 MW net electricity, H₉₈ = 1.2 tokamak pilot plants. Right: R₁BL (with REBCO TF and CS coils); centre-right: R₇AD (with Nb₃Sn TF and CS coils); centre-left: R₂BL (with commercial Nb-Ti TF and CS coils); left: R₈AD (with quaternary Nb-Ti TF and CS coils). In all cases the PF coils are Nb-Ti. These costs are for simply building the plant without mitigating risk with training or upgrading coils. All costs are in 1990 M\$. This table is discussed in detail in section 5.4.6.

		R ₁ BL	R ₇ AD	R ₂ BL	R ₈ AD
Raw Heat (MW)	Fusion power	865	889	902	860
	Blanket multiplication	165	169	172	164
	Injected power	50	50	50	50
	Ohmic heating	1	1	1	1
	Power from coolant pump	85	87	88	84
		1166	1196	1213	1158
Gross electric power (MW)	Power lost in conversion	-729	-747	-758	-724
		437	449	455	434
Net electric power (MW)	Heating and current drive	-125	-125	-125	-125
	Primary coolant pumps	-98	-100	-101	-97
	Vacuum pumps	-1	-1	-1	-1
	Tritium plant	-15	-15	-15	-15
	Cryoplant	-44	-50	-43	-42
	Toroidal field coils	-12	-12	-13	-8
	Poloidal field coils and solenoid	-1	-1	-1	-1
	Miscellaneous	-42	-45	-57	-47
		100	100	100	100

Table 5.3: Power balance of the preferred reactor R₁BL and three other PROCESS generated, cost-optimised, 100 MW net electricity, H₉₈ = 1.2 tokamak pilot plants. Right: R₁BL (with REBCO TF and CS coils); centre-right: R₇AD (with Nb₃Sn TF and CS coils); centre-left: R₂BL (with commercial Nb-Ti TF and CS coils); left: R₈AD (with quaternary Nb-Ti TF and CS coils). In all cases the PF coils are Nb-Ti.

5.2.3 Tritium Breeding

The blanket design in all reactors in this work based on the EU helium-cooled pebble bed (HCPB) [175] which has greatest breeding potential of the blanket designs under investigation for EU-DEMO [90]. We have used a minimum tritium breeding ratio (TBR) of 1.1 in all reactors. The TBR was set using the in-built PROCESS breeder ratios for given breeder blanket thicknesses as calculated by the FATI (Fusion Activation and Transport Interface) code [176] for EU-DEMO (to which our designs are similar, to first order, so the model is applicable here). We have chosen designs that require tritium self sufficiency as current tritium supplies could not maintain multiple pilot plant reactors at once [177]. The TBR cannot be too large, as to avoid an excessive tritium inventory and issues of tritium permeation throughout the reactor. $TBR = 1.1$ is the widely accepted ratio for a power plant: “enough but not too much”.

If the global tritium inventory were markedly increased, a cheaper pilot plant could be built with a lower intermediate $TBR = 0.9$, which is probably the lower limit to de-risk the tritium breeding technology for investors [15]. Our detailed MCNP calculations in section 5.3.1.2 (cf figure 5.5) that the 0.53 m thick blanket and 0.25 m thick neutron shield in R₁BL, each reduce the neutron flux by about two orders of magnitude. Due to the exponential nature of neutron absorption (the first 15 cm or so of shielding absorbs 90 % of the dose) and as calculated by extrapolating from FATI code tritium breeding calculations on an EU DEMO design. A TBR of only 0.9 can therefore be generated with a smaller inboard blanket of ≈ 0.20 m and outboard blanket of ≈ 0.35 m only. However, to maintain the same nuclear heating in the magnets, the neutron shield would need to be thicker by ≈ 0.17 m leading to a net reduction in capital cost of ≈ 24 % which is large but does not justify losing tritium self-sufficiency (which will be required by future tokamaks and must therefore ultimately be demonstrated).

Other breeding blankets are being developed: A water-cooled lithium lead blanket

(WCLL) design [178, 179] is under consideration for EU-DEMO. The WCLL provides greater neutron shielding than the HCPB (due to neutron capture by the water coolant) whereas the latter has greater breeding potential (due to the inclusion of Be neutron multiplier modules). Other helium-cooled and dual-cooled lithium lead concepts are also under consideration [90]. A FLiBe molten salt blanket is being developed in the USA which includes a coolant outlet temperature of up to 930 °C [9], higher than either the HCPB (650 °C) or WCLL (330 °C) and may therefore eventually lead to more efficient electricity production.

5.2.4 Reactor Architecture

5.2.4.1 Divertor Constraints and Configuration

The divertor architecture in all the simulated reactors here is based on the single-null ITER design [84] [108], which is currently the baseline option considered for EU-DEMO [6]. The steady-state heat flux onto the divertor set to $< 6 \text{ MW/m}^2$, below the maximum steady-state heat flux of $\approx 10 \text{ MW/m}^2$ expected in ITER [84] and we consider this an easily achievable conservative choice, manageable with techniques such as divertor impurity seeding (e.g. in EAST which maintains high H_{98} [180]) or moving the divertor strike points (e.g. in SPARC [4]). In our PROCESS simulations we have allowed the argon impurity fraction to vary, to facilitate reduced power to the divertor through argon ionisation and bremsstrahlung. Other advanced techniques developed for much smaller machines with commensurately much higher fluxes are also potentially available including long legged [181, 182] or snowflake divertors [183] but they require additional plasma shaping coils which are exposed to large neutron fluxes, or raise demands (and costs) on the existing coil system [184, 185] (e.g. in ITER, the current through the upper-most and lower-most solenoid modules would have to be increased by more than a factor of 10 [186] in order to produce a snowflake). In the large, capital-cost minimised machines considered the primary limiting factor preventing smaller sized reactors was the yield

stress of the magnet support structural material rather than the heat flux to the divertor; these divertor configurations were therefore not needed. A hard limit of $P_{\text{separatrix}}/R_{\text{major}} = 20 \text{ MW/m}^{-1}$ was set, similar to the values of $P_{\text{separatrix}}/R_{\text{major}} = 17$ and 30 MW/m^{-1} expected for EU-DEMO and J-DEMO respectively [187]. We found that increasing the $P_{\text{separatrix}}/R_{\text{major}}$ limit had negligible effect on our cost-optimal designs because they are predominantly magnet stress limited.

5.2.4.2 Number of Toroidal Field Coils

All reactors in this work have 18 toroidal field coils and a maximum field ripple at the plasma outboard mid-plane of 6 % (in following with EU-DEMO designs). Ripple cannot be avoided, but must be kept low in order to reduce ripple-induced drift of trapped particles and associated energy losses [188]. **PROCESS** runs were performed to ascertain the cost-optimal number of coils for each reactor run in this chapter and for the baseline reactors in the following chapter. In all cases 18 was the optimum amount. The difference in total capital cost between a given reactor with 18 or 20 TF coils was typically quite small: for R₁BL the difference was only 0.3 %. Having a greater number of coils reduces the peak field that each coil must produce (due to the coils be closer together, and the field between them ‘dipping’ less), thereby slightly reducing the coil size and overall reactor volume. Each added coil however increases the cost of the magnet system.

5.2.4.3 Coil Structural Support

The maximum allowable shear stress (used for the Tresca yield criterion in **PROCESS**) was set to 660 MPa for both the CS and TF coils, 2/3 of the yield stress of standard fusion relevant, high strength structural steels [189]. A bucked and wedged (B&W) coil support structure [77, 190] has been incorporated in all reactors studied here. Performing dedicated **PROCESS** runs, we found that a B&W support structure reduces R₁BL’s CS coil bore by 13.7 % (27.9 cm), TF coil thickness by 13.4 % (10.9

cm) major radius by 5.6 % (40.7 cm) and capital cost by 400 M\$ compared to a conventional wedged support structure that isolates the TF coils from the CS coil (as in ITER [17]). In the B&W support structure, stresses are shared throughout the whole support structure, rather than constrained to the supports of individual coils, reducing the size of the steel support structure required. The TF coils are wedged in a circular vault which bucks onto a low-friction bucking cylinder which itself is in contact with the central solenoid. Such an architecture does however require the use of a bespoke low-friction interfacial material [77] and comes at the cost of reduced plasma shaping flexibility, and additional cyclic loading on the TF coils [191] which reduce the fatigue-limited lifetime of the TF coil casing and has not been accounted for in our calculations.

5.2.4.4 Central Solenoid Use and Burn Time

We have chosen to include both a central solenoid coil and auxiliary heating system for current drive, start-up and plasma heating. To minimise the size of the central solenoid, a large 50 MW ECRH auxiliary heating current drive was used. This ECRH power follows EU-DEMO [6], which would already be the largest ever built and limits any further reduction in the blanket volume (as auxiliary heating systems take up valuable first wall surface area) and hence the tritium breeding ratio and electricity generated. The 50 MW ECRH system produces 10 – 15 % of the plasma current. It was taken to have a power conversion efficiency $\mu_{\text{CD,conv}} = 0.4$, and normalised current drive efficiency of $\gamma_{\text{CD}} = 0.3$ - taken from the PROCESS DEMO 2018 baseline values and slightly more conservative than assumed for EU-DEMO [192]. PROCESS was then given freedom to vary the inductive and non-inductive current fractions and yielded an inductive (CS and PF coil driven) current fraction of ≈ 50 % (the exact fractions depend on the reactor in question) and a bootstrap current fraction of ≈ 40 %. Each coil system produced \approx half of the total magnetic flux at all times.

A number of novel plasma start-up techniques have been developed that could in

principle reduce the demand on the CS coil, and therefore reduce its size and cost. Helicity injection is a promising family of technologies and have seen implementation in a number of smaller tokamaks [193]. The most powerful system under construction is NSTX-U [194] which is predicted to produce > 400 kA. Merging compression (MC) has seen some success in spherical tokamaks [195, 196, 197] and is expected to be used in Tokamak Energy's ST-40 reactor [198] and produce a 2 MA current. To date MC magnets have been inside the vacuum vessel which brings with it huge neutron fluxes and the requirement for frequent replacement, reducing reactor availability. Designs that improve the location of the MC magnets will be developed, but we consider this approach too high risk at this time. Up to 200 kA current has also been achieved inductively using the PF coil systems in JT60-U (with supplementation from the lower hybrid current drive system) with 1.9 Wb flux [199], but higher currents must be demonstrated before this technique becomes a practical solution for reactors of the scale considered in this work.

A radio frequency (RF) current drive was chosen for the auxiliary current drive system as it is cheaper, requires less neutron shielding, and consumes a smaller blanket volume than the alternative neutral beam injection system [200] [201]. In principle the ECRH system could be exchanged for a different 50 MW RF current drive option without changing the overall reactor design should ion cyclotron or lower hybrid current drive systems prove more efficient or reliable in future. For an EU-DEMO-like reactor, at present ECRH has the most flexible power deposition which gives the highest current drive efficiency [192].

For both the 100 MW_e and 500 MW_e reactors considered here, the cost is not very sensitive to burn-time so we have chosen to adopt the EU-DEMO standard of 2 hours [6]. The variation in the cost-optimal central solenoid bore, thickness and flux generation as a figure of required plasma burn time and resulting reactor capital cost are shown in figure 5.1.

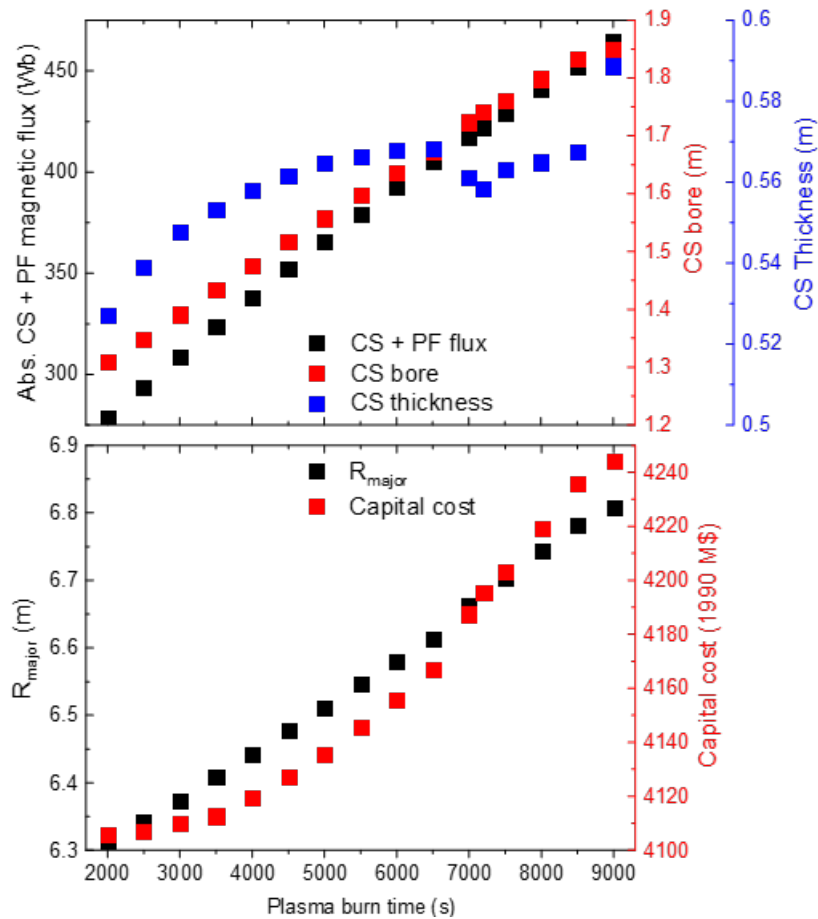


Figure 5.1: Top: Total absolute central solenoid coil (CS) and poloidal field coil (PF) flux, central solenoid bore and thickness, and (Bottom:) plasma major radius and plant total capital cost as a function of plasma burn time, of 100 MW_e tokamak power plants with REBCO CS and TF coils and Nb-Ti PF coils (i.e. magnet materials as per the R₁BL reactor design) optimised for minimum capital cost. Note that R₁BL has a 7200 second plasma burn time.

5.3 Optimised Radiation Shielding

In this section we optimise the thickness of the radiation shield made from tungsten carbide (considered the primary candidate for neutron shielding in tokamak power plants [91, 202]). A thinner shield is cheaper and enables more compact reactor designs. However, the shield must be thick enough for both the lifetime of the tokamak to be sufficiently long, and the cryogenic load to be sufficiently small. We start by using state-of-the-art MCNP [149] calculations for the flux spectrum at the first wall for a cost-optimised, $H_{98} = 1.2$, 100 MW REBCO CS and TF and Nb-Ti PF tokamak. Then we use MCNP attenuation coefficients derived for neutron flux attenuation through slab geometries, to provide empirical attenuation coefficients for what we call in this thesis ‘benchmarking calculations’. We have used them here to calculate the lifetime and cryogenic load for a range of simplified tokamak designs using different radiation shield thicknesses. These quick calculations provide a broad brush insight into how changes in the component parts and size of the shield affects the tokamak’s performance. Then we progress to MCNP [149] calculations that include the full complexity of the tokamak geometry, and optimise the neutron shield thickness more accurately. These calculations finalise the shield thickness of our preferred reactor R₁BL (see section 5.4.7) and the other tokamaks in this and the following chapters. We go on to use the properties for the optimised shield in our cryogenics analysis to calculate the helium coolant mass flow rate required.

5.3.1 Neutronics - Thermal Load and Lifetime

5.3.1.1 Benchmarking Calculations

The incident neutron flux density spectrum at the first wall (FW) for R₁BL $I_{FW,RT}(E)$ ($\text{n cm}^{-2} \text{s}^{-1}$) was calculated using MCNP in terms of i different energy bins of width dE_i and average energy \bar{E}_i (and the 175 Vitamin-J energy bin width size distribution [203] - a choice which does not significantly affect any results in this work).

For all other tokamaks under consideration, the flux density in any i th energy bin was then simply given by

$$I_{\text{FW}}(\overline{E}_i) = \frac{P_{\text{Total}}}{P_{\text{RT}}} I_{\text{FW,RT}}(\overline{E}_i) , \quad (5.3.1)$$

where the flux density has simply been scaled by ratio of the total fusion power of the tokamak under consideration to the total fusion power of the cost-optimised REBCO tokamak $P_{\text{Total}}/P_{\text{RT}}$.

We then take the thermal load onto the TF coils after passing through all the walls (the first wall, blanket, neutron shield, vacuum vessel and thermal shield) to be

$$P_{\text{TF}} = A \sum_{\text{Bins}} g I_{\text{FW}}(\overline{E}_i) \times \overline{E}_i \left\{ \prod_i^{\text{Walls}} \exp[-a\mu_i x_i] \left(1 - \prod_i^{\text{TF Coils}} \exp[-a\mu_i x_i] \right) \right\} . \quad (5.3.2)$$

where A is the surface area of the first wall. We have introduced two geometrical factors: g which accounts for only a fraction of the flux reaching the cryogenic system where $g = (R_{\text{major}} - R_{\text{minor}}) / R_{\text{major}}$ (i.e. the cryogenic system unlike say the shielding, does not cover the entire surface of the toroid), and a which accounts for the volume of a curved surface being smaller (and therefore attenuating less (on the inner leg of the important TF coils) than a slab where $a = 1 - t_{\text{All Walls}} / 2 \cdot r_{\text{All Walls}}$. For R₁BL, $R_{\text{major}} = 6.750$ m and $R_{\text{minor}} = 2.145$ m. Also $t_{\text{All Walls}} = 1.238$ m taken for the first wall, breeder blanket, neutron shield and vacuum vessel given in Table 5.5 and $r_{\text{All Walls}} = 3.383$ m from Figure 5.2, so $g = 0.682$ and $a = 0.817$. Because these corrections appear in exponential functions, they significantly improve the agreement between the benchmarking calculations and the MCNP calculations provided below. The empirical attenuation coefficients used were those calculated using MCNP for neutron transmission through 30 cm blocks of mono-material [202] and averaged for all fast neutron flux ($E > 0.1\text{MeV}$). This approach ignores the complexity of the multiple nuclear interactions (discussed below) and simply associates the reduction in energy and flux with a single attenuation coefficient. Table 5.4 lists the empirical values for the attenuation coefficients as well as those derived using established total nuclear cross sections for comparison.

Material	$\bar{\mu}_{\text{TCA}}(E > 0.1\text{MeV})$ (m^{-1})	$\bar{\mu}_i(E > 0.1\text{MeV})$ (m^{-1})
Tungsten	42.71	19.55
304B7 Boronated Steel	39.92	16.44
316 Stainless Steel	40.06	15.31
Copper	34.71	14.98
Niobium	34.77	13.73
Beryllium	39.97	14.61
Tin	15.75	12.06
Zirconium	26.26	11.87
Gadolinium	19.85	12.63
Titanium	15.75	13.01
Water	13.73	8.15
Aluminium	21.43	13.53
Lithium	13.16	10.72
Helium (liquid)	4.56	9.45
Hydrogen	1.94	2.45
Tungsten Carbide	23.06	18.9

Table 5.4: Mean attenuation coefficients for (fast) neutrons of energy > 0.1 MeV of tokamak relevant materials. $\bar{\mu}_{\text{TCA}}$ are calculated from total neutron cross section data [204]. $\bar{\mu}_i$ calculated using data from MCNP calculations of neutron transmission through a 30 cm block of (ith) mono-material [202] except for Tungsten Carbide which is derived from the MCNP data in figure 5.3.

To calculate the lifetime of the tokamak, we note that neutron flux density initially increases J_c in superconductors, due to an increase in the density of fluxon pinning sites [43], but eventually causes a sharp decrease after a fluence of $\approx 3.9 \times 10^{22}$ fast neutrons m^{-2} , for $E_{\text{neutron}} > 0.1$ MeV. We have used this fluence threshold (also known as the Weber dose limit [205]) to calculate the magnet lifetime of the toroidal field (TF) coils τ_{TF} (s), where

$$\tau_{\text{TF}} = \frac{3.9 \times 10^{22}}{\sum_{\text{Bins}} g I_{\text{FW}}(\bar{E}_i) \left\{ \prod_i^{\text{Walls}} \exp[-a\mu_i x_i] (1 - \prod_i^{\text{TF Coils}} \exp[-a\mu_i x_i]) \right\}}. \quad (5.3.3)$$

To validate these benchmarking calculations, we input the radial build dimensions and fusion power for ITER [17] and compared the values obtained to more detailed neutronics calculations [206]. With $P_{\text{ITER},\text{fus}} = 500$ MW, a first wall surface area of 610 m^2 , $R_{\text{ITER},\text{major}} = 6.20$ m, $R_{\text{ITER},\text{minor}} = 2.00$ m, $t_{\text{ITER},\text{All Walls}} = 0.808$ m and $r_{\text{All Walls}} = 3.817$ m (as shown in Table 5.1), our benchmarking calculations

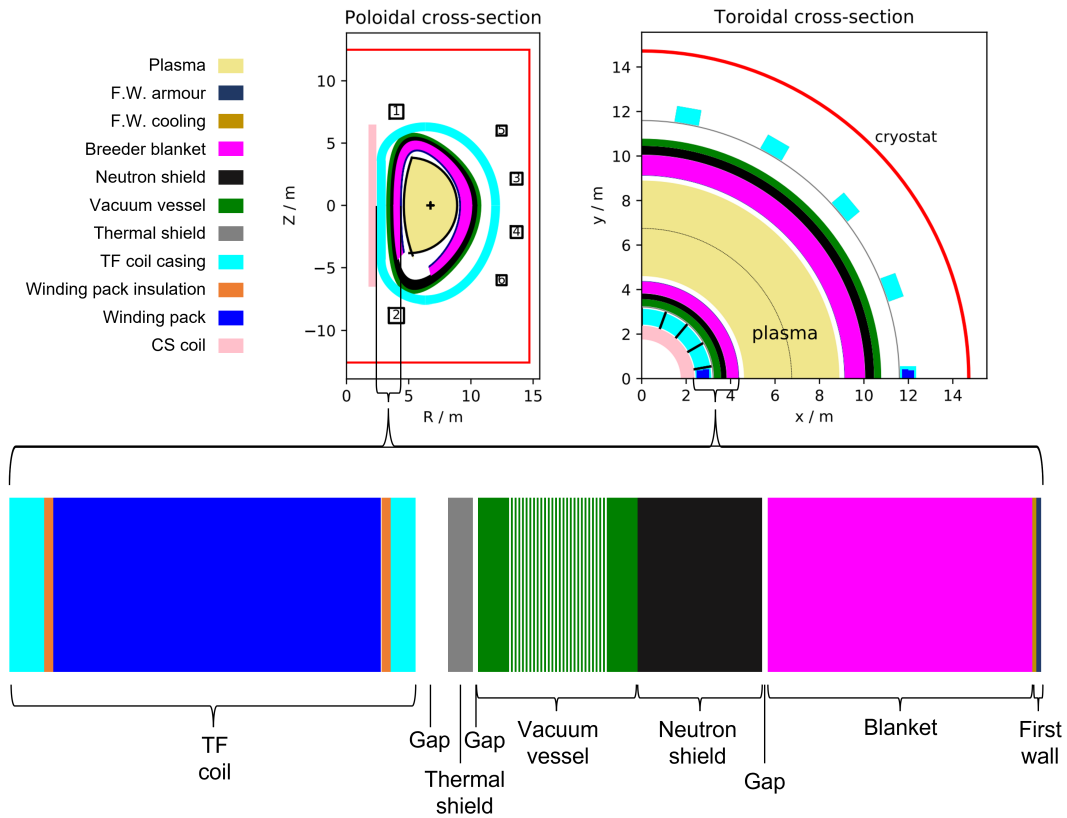


Figure 5.2: Cross-sections and inboard mid-plane radial build of the preferred reactor R₁BL (a cost-optimised $H_{98} = 1.2$, 100 MW net electricity tokamak with REBCO toroidal field and central solenoid coils) with an optimised 25.0 cm neutron shield. Details of the layers can be found in the second column of table 5.5. The inboard blanket is 53 cm in radial thickness and based on the EU-DEMO helium-cooled pebble bed design [175], guaranteeing a tritium breeding ratio > 1.1 .

yield a TF coil nuclear heating of 32.8 kW, within a factor of two of the expected range of 14 - 18 kW [206]. The calculated magnet lifetime for ITER is 23.6 full-power years. After this we changed the neutron shield to be tungsten carbide and used PROCESS to vary the thickness of the components of the radial build and found the first approximate design of the preferred tokamak (the data for this initial design are listed in table 5.5). Having found the first approximate design for the preferred tokamak, MCNP was then used to finalise the shield thickness.

5.3.1.1. Benchmarking Calculations

Section	Layer	Material composition	initial component thicknesses (m)	preferred design thicknesses (m)
First wall	Armour	Tungsten	0.010	0.010
	Cooling	90% Glidcop, 10% water	0.008	0.008
Breeder blanket		37.5% TiBe ₁₂ 37.5% Li ₂ SiO ₄ 9.7% 316 stainless steel 15.3 % He	0.530 (0.910)	0.530 (0.910)
Gap		Air	0.010	0.010
Neutron shield		Tungsten Carbide	0.214	0.250
Vacuum vessel	Wall	316 stainless steel	0.060	0.060
	Interior	60% 304 stainless steel with 2% Boron 40% water	0.200 (0.350)	0.200 (0.350)
	Wall	316 stainless steel	0.060	0.060
Gap		Air	0.010	0.010
Thermal shield		316 stainless steel	0.050	0.050
Gap		Air	0.065 (0.75)	0.065 (0.75)
TF coil	TF coil casing	316 stainless steel	0.050	0.052
	Insulation	45% Fibreglass tape	0.018	0.018
		45% Kapton tape 10% epoxy resin		
	Winding pack	<1% REBCO 51% Copper 28% Hastelloy 20% He	0.460	0.550
	Insulation	45% Fibreglass tape	0.018	0.018
		45% Kapton tape 10% epoxy resin		
TF coil casing	316 stainless steel	0.070	0.070	

Table 5.5: Thicknesses and material compositions (derived from the ITER radial build) of the layers between the first wall and the central solenoid at the inboard mid-plane for the initial 100 MW net electricity REBCO CS, TF and Nb-Ti PF reactor using a neutron shield thickness from the benchmarking calculations. As well as those for the preferred reactor R₁BL using a neutron shield thickness optimised using MCNP. Outboard dimensions are shown in brackets () where significantly different.

5.3.1.2 MCNP Calculation

The MCNP code is a dedicated numerical solver that considers the progressive creation and loss of approximately 4000 isotopes, via decay and nuclear reactions. These calculations include the complexity of flux in all directions, and the geometry of the component structures of the tokamak under consideration [207, 208]. It is used here to calculate the changes in the neutron flux and gamma flux as they pass through the component walls and magnets of the tokamak. The calculations do not include changes in composition or microstructure that affect mechanical properties, such as embrittlement or swelling [209, 210], nor do they include changes in transport properties, such as thermal or electrical conductivity [211], or magnetic properties. The MCNP calculations presented in this section were conducted by Anthony Turner and Jonathan Naish of the CCFE Neutronics group.

Having used the benchmarking calculations to identify the first approximate broad optimal design for a cost-optimised REBCO tokamak, we repeated the nuclear heating and superconductor lifetime calculations using MCNP near the optimal shield design. The space for the tungsten carbide radiation shield was set as a 30 cm block and split into six, 5 cm thick sections. The sections were successively set as void regions starting from the plasma facing side, and the neutron and photon flux density spectra were calculated for materials throughout the entire tokamak together with the lifetime and cryogenic load on the TF coil system, which are shown in figure 5.3. The MCNP calculated lifetimes and TF coil nuclear heating as a function of shield thickness are $\approx 3\text{-}4 \times$ and $\approx 4 \times$ lower than the corresponding benchmarking values for a given neutron shield thickness. This is as expected, as the simple attenuation approach results in a larger > 10 MeV neutron flux but lower $0.1 - 10$ MeV neutron flux at the magnets. Thus the total fast neutron flux is lower (resulting in a longer superconductor lifetime) but the total power deposited in the magnets is larger (resulting in a larger nuclear heating).

The optimal tungsten carbide neutron shielding thickness was calculated to be

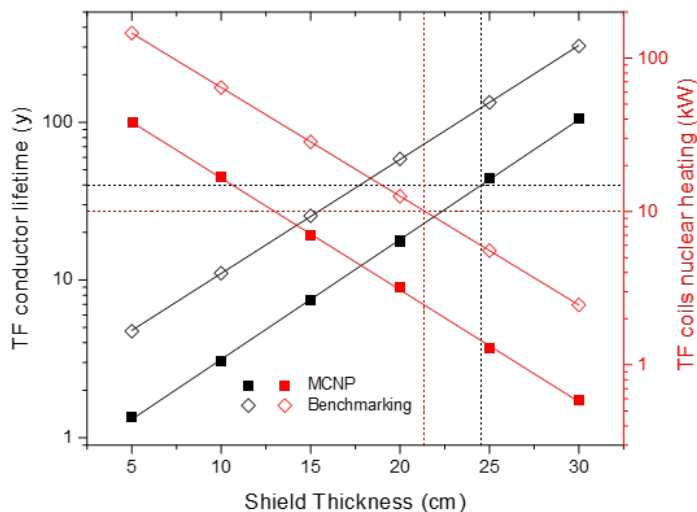


Figure 5.3: Nuclear heating in the TF coil system and number of full-power operation years until the Weber dose limit [205] is achieved for the preferred reactor R₁BL (a cost-optimised H₉₈ = 1.2, 100 MW net electricity tokamak with REBCO toroidal field and central solenoid coils) as a function of the thickness of its tungsten carbide neutron shield as calculated by MCNP (closed squares) and the benchmarking calculation (open diamonds). The material layers between the plasma and the TF coil are given in table 5.5. The dotted black lines indicate the minimum 40 year conductor lifetime limit (and corresponding minimum shield thickness as calculated by MCNP). The dotted red lines indicate the maximum 10 kW heating limit on the TF system (and corresponding minimum shield thickness as calculated by our benchmarking calculations).

24.5 cm, based on a 40 year superconductor lifetime criterion. With this shield the combined nuclear heating on the TF coils was only ≈ 1.4 kW. We note that if we had chosen to reduce the lifetime to just 3 years, the shielding would have reduced to 9.8 cm, but at the price of the nuclear heating increasing to a large value of 17.2 kW and the cost reducing by less than 5 %. We did not pursue this option further. A 25.0 cm shield was then employed for all of the further PROCESS calculations. A breakdown of the resulting R₁BL reactor radial build (with this 25 cm shield) is shown in table 5.5 and figure 5.2. The approach we have adopted here has identified the important properties of our preferred reactor using state-of-the-art MCNP calculations. The benchmarking data in Table 5.4 demonstrates that the neutron flux typically reduces by an order of magnitude every 15 cm or so.

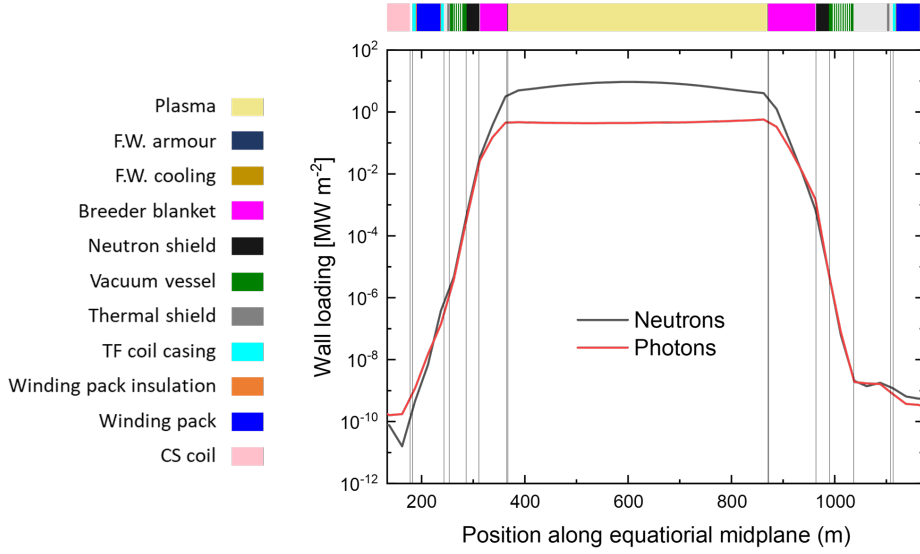


Figure 5.4: Neutron and photon induced wall loading along the mid-plane within the preferred reactor R_1BL (a cost-optimised $H_{98} = 1.2$, 100 MW net electricity tokamak with REBCO toroidal field and central solenoid coils) with an optimised 25.0 cm neutron shield. The radial positions of the central solenoid coil (light pink), toroidal field coil legs (blue), vacuum vessel (green), neutron shield (black) and blanket (deep pink) are shown.

This makes clear that (unless frequent replacement of the magnets is envisioned) the range of wall thicknesses available to the fusion engineer is relatively small for any reasonable lifetime and thermal power load into the magnets.

Neutron and photon wall loading data are shown in figure 5.4. The neutron and photon spectra as a function of depth into the R_1BL reactor wall at the inboard mid-plane are shown in figure 5.5. The data are presented as flux density per unit lethargy (i.e. flux density in the i th bin, divided by the i th energy bin width, and multiplied by the average energy in the bin) versus energy. This form of the data is independent of the details of how the bins are discretised and enables comparison with for example Weber [205] who finds a peak value of $\approx 4 \times 10^{12} \text{ n m}^{-2} \text{ s}^{-1}$ at the magnet location, that is similar to the peak flux of $2.3 \times 10^{12} \text{ n m}^{-2} \text{ s}^{-1}$ incident on the TF coils shown in figure 5.5. We note that the gamma flux is similar to the neutron flux although to our knowledge there are no confident reports of how this may affect the lifetime of the superconductors.

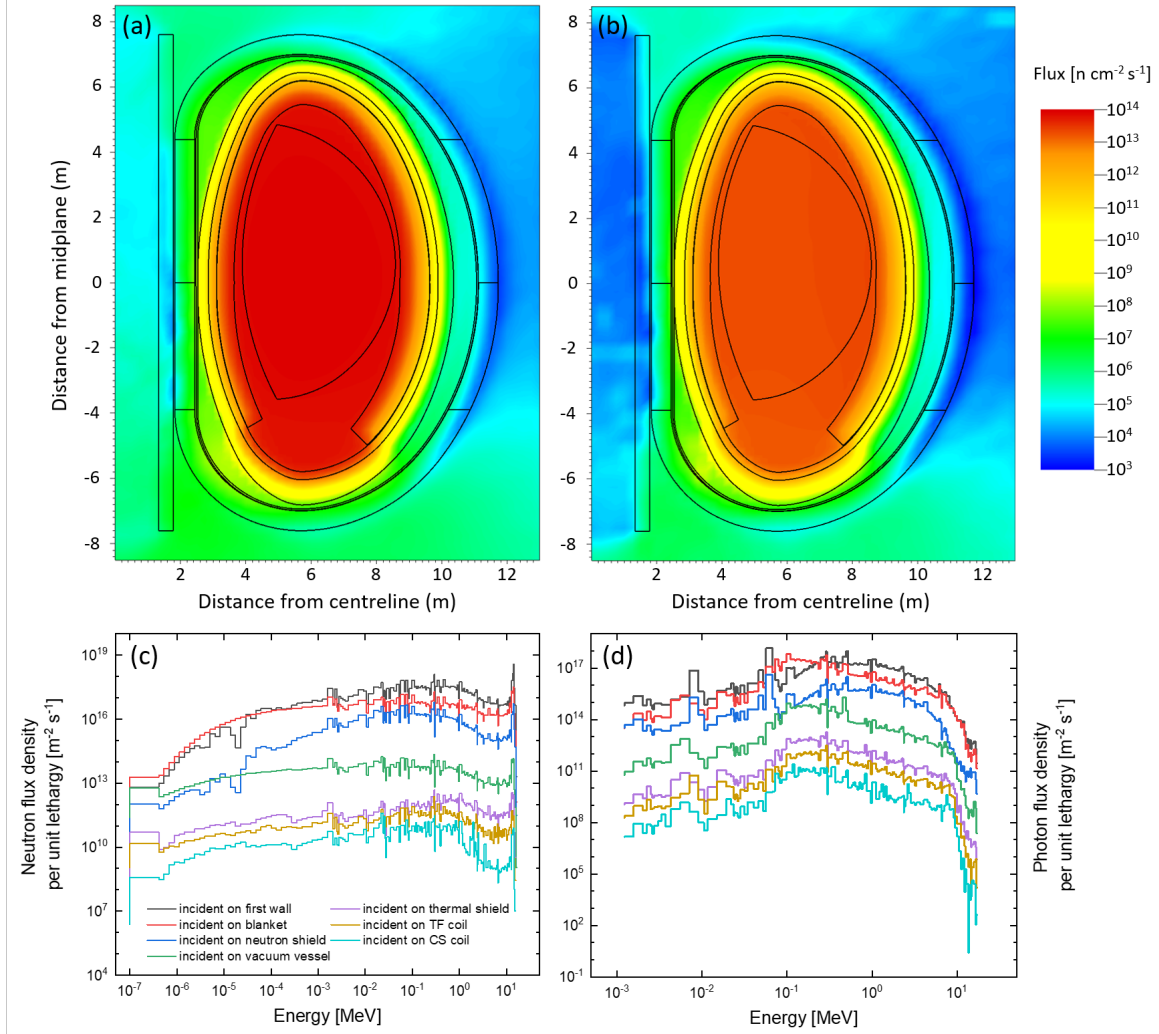


Figure 5.5: MCNP calculated (a) fast neutron flux and (b) gamma ray flux through the poloidal cross-section of the preferred reactor R₁BL (a cost-optimised $H_{98} = 1.2$, 100 MW net electricity tokamak with REBCO toroidal field and central solenoid coils) with an optimised 25.0 cm neutron shield detailed in the right hand column of table 5.5. (c) The neutron flux spectrum and (d) photon flux spectrum as a function of distance into inboard mid plane of R₁BL with an optimised 25.0 cm neutron shield. These spectra were converted to flux density per unit lethargy by multiplying the spectral histogram fluxes by the ratio between the energy bin average energies and the bin widths.

5.3.2 Cryogenic flow - Benchmarking

In this work, we assume that the cryogenic heat load is broadly constant throughout a plasma pulse and distributed evenly throughout each cooling channel. The benchmarking thermal calculations only consider the TF coils (whereas the detailed PROCESS calculations consider the entire magnet system - TF, CS and PF coils). The temperature of the superconductor can be estimated using Newton's law of cooling [212]

$$T_{sc}(x) = T_{coolant}(x) + \Delta T_{coolant-sc} = \left(T_{coolant}^{inlet} + \frac{Qx}{\dot{m}L_{channel}c_p} \right) + \frac{Q}{W_p L_{channel} h} , \quad (5.3.4)$$

where $\Delta T_{coolant-sc}$ is the difference between the temperature of the coolant and that of the superconductor, Q is the heating load (in Watts) in each cooling channel, $L_{channel}$ is the cooling channel length, W_p is the cooling channel wetted perimeter, \dot{m} is the coolant mass flow rate, x is the distance along the cooling channel, $c_p(T)$ is the coolant specific heat capacity per unit mass, and the heat transfer coefficient, $h(T, p)$, can be derived from the Dittus-Boelter equation, written in terms of the Nusselt number, Nu , [213];

$$Nu = \frac{hD_h}{\kappa} = 0.023Re^{0.8}Pr^{0.4} , \quad (5.3.5)$$

where D_h is the cooling channel hydraulic diameter, $\kappa(T, p)$ is the coolant thermal conductivity, $Re(T, p) = \dot{m}D_h/\mu(T, p)A_{coolant}$ is the coolant Reynolds number, $A_{coolant}$ is the coolant cross section, $Pr(T, p) = \mu(T, p)c_p(T, p)/\kappa(T, p)$ is the coolant Prandtl number and $\mu(T, p)$ is the coolant dynamic viscosity. From the maximum pressure drop allowed, the maximum mass flow rate can be calculated using the Darcy-Weisbach equation [213]

$$\Delta P(x) = \frac{f_d x \rho_V \langle v \rangle^2}{2D_h} \quad (5.3.6)$$

where ρ_V is the density, $\langle v \rangle = \dot{m}/\rho A_{coolant}$ is the mean coolant flow velocity and the Darcy friction factor f_d can be expressed in terms of the Reynolds number and

	c_p (J kg ⁻¹ K ⁻¹)	κ (W m ⁻¹ K ⁻¹)	ρ (kg m ⁻³)	μ (MPa.s)
Water (293 K)	4183	0.598	998	1005
N ₂ (65 K)	1165	0.174	861	282
Ne (30 K)	2009	0.138	1156	89
He (30 K)	5312	0.034	8	5
He (20 K)	5472	0.027	12	4
He (4.5 K)	3955	0.021	143	4

	Cu Resistivity (Ω m)	Al Resistivity (Ω m)
293 K, 0 T	1.7×10^{-8}	2.7×10^{-8}
65 K, 0 T	1.5×10^{-9}	1.1×10^{-9}
65 K, 6 T	9.9×10^{-9}	2.9×10^{-9}
20 K, 0 T	2.8×10^{-11}	9.0×10^{-12}
20 K, 6 T	3.1×10^{-10}	6.8×10^{-11}

Table 5.6: Above: Useful cryogenic materials properties under 5 bar pressure [214]. Below: (magneto)resistances of RRR = 1000 copper and RRR = 10000 aluminium [170, 215, 216].

void fraction in the cable - $V_{coolant}$ as [213]

$$f_d = \frac{19.5/Re^{0.7953} + 0.0231}{V_{coolant}^{0.742}} . \quad (5.3.7)$$

We validate this benchmarking approach by considering the JT60-SA tokamak and the materials properties used in table 5.6. Using $A_{coolant} = 1.27 \times 10^{-4} \text{m}^2$, $D_h = 4.57 \times 10^{-4} \text{m}$, $\dot{m} = 3.5 \text{g s}^{-1}$, $V_{coolant} = 0.32$, $T_{coolant}^{\text{inlet}} = 4.4 \text{K}$, an inlet pressure of 5 bar, $L_{\text{channel}} = 123.3 \text{m}$ (5 double pancakes per TF coil, each of length 296 m [155] and 12 cooling channels per TF coil [213]), the time averaged heat load on each coolant channel is 12.1 W. Equations 5.3.4 - 5.3.7 yield a pressure drop of 0.9 bar and helium outlet temperature for each cooling channel of 5.2 K, which compares favourably to more detailed calculations of 1.1 bar and $\approx 4.8 \text{K}$ [213].

For our preferred choice reactor R₁BL, PROCESS gave 18 TF coils with a total cable cross section of 39.6 cm² and an inner (square) cross section of 23.6 cm². We have set the number of cooling channels per TF coil to be 10 (note JT-60SA has 12

and ITER has 14), which given there are 100 turns per TF coil each of 36.4 m, leads to $L_{\text{channel}} = 364$ m. A 20 % conductor void fraction [217] then sets the cooling channel hydraulic diameter in the superconducting cable to be 2.45 cm (with $V_{\text{coolant}} = 1.0$ within this channel). Setting the inlet temperature to 4.5 K, inlet pressure to 5 bar and limiting the pressure drop along the coolant pipe to no more than $\Delta P = 1.0$ bar sets an upper limit on the fluid mass flow rate of ≈ 132 g s^{-1} (much larger than in JT-60's 3.5 g s^{-1} because the channel is much wider and is unobstructed by conductor strands, with commensurately less drag). Assuming similar TF coil winding pack circulator work, AC losses and static heat loads to those in ITER, the TF coil coolant outlet temperature is 4.6 K. Hence we conclude that the cryoplant performance required by R₁BL is straightforward using existing tokamak cryoplant systems.

It is interesting to consider whether, if operation were required at 30 K, a different cryogen, would be preferred. Here we rule out hydrogen and oxygen mixes to avoid unnecessary additional safety considerations and just consider neon. Under 5 bar pressure, supercritical helium at 30 K has ≈ 6 % of its density and ≈ 120 % of its dynamic viscosity at 4.5 K [214]. If we maintain the 1.0 bar pressure drop, the mass flow rate reduces to 30 g s^{-1} resulting in an outlet temperature of 30.3 K. At 30 K and 5 bar, liquid neon has a density $\approx 9 \times$ greater and a dynamic viscosity $\approx 25 \times$ greater than He at 4.5 K. A 1.0 bar pressure drop leads in this case to a mass flow rate of 380 g s^{-1} and an outlet temperature of 30.1 K. Hence, at at 30 K liquid neon only slightly outperforms supercritical helium as cryocoolant and so is not required/considered further.

5.4 Choosing the Optimal Superconductor

5.4.1 Nb-Ti

The Nb-47wt.%Ti alloy [218] is the most important commercial superconducting material. It has been optimised for maximum critical current density between ≈ 4 T and 6 T for MRI and accelerator magnet applications [23]. Its relatively low upper critical field ($B_{c2}(4.2\text{ K}) \approx 10$ T [53]) means that it has only been used for the poloidal field coils in next generation fusion reactors such as ITER [54] and EU-DEMO [6] (though it is being used for the TF coils in JT60-SA [48]).

5.4.2 Nb_3Sn

Nb_3Sn is a brittle intermetallic compound with $B_{c2}(4.2\text{ K}) \approx 20$ T [219] which has long made it the material of choice for applications when > 10 T fields are required. The Nb_3Sn superconducting matrix can also include tantalum and titanium [220] (to increase the upper critical field) or hafnium [221] dopants (for improved J_c at fields above 15 T). Nb_3Sn cables are broadly produced in one of two ways: Wind & React where unreacted cables are jacketed and wound into a coil which then undergoes heat treatment; or React & Wind where the cables are heat treated and then wound into a coil [222, 223]. When using the former process one has to be careful about the fracture of the Nb_3Sn filaments and consequent degradation of the cables' critical current during manufacture [58, 59] due to the different thermal expansions of the cable jacket and superconducting filaments. The latter method avoids this issue, but the reacted cable can only be used to produce magnets with large bending radii. Nb_3Sn is not considered in detail in this work because we have found almost always that a cost minimised Nb_3Sn reactor has a larger capital cost than an equivalent REBCO reactor, as shown in table 5.2. However as discussed below in section 5.4.9, Nb_3Sn could still have a role to play in cost optimising

graded coils where different superconductors are used within the same winding pack.

5.4.3 REBCO

REBCO high temperature superconductors present an exciting possibility to operate with high magnetic fields (> 20 T on coil) and at elevated temperatures (20 K and above). REBCO's ≈ 90 K critical temperature [133] allows for large temperature margins in cable design and higher operation temperature that reduces cryo-power requirements. However it is a ceramic oxide material, that is prone to brittle fracture under tensile strain $> 0.3 - 0.7$ % [224, 225] and tape delamination under cyclic loading [61, 226]. Although stable against quenches, quench protection and detection are more demanding than in low temperature superconductors due to REBCO's low normal zone propagation velocities [227] and the low thermal conductivity in the tapes ($\approx 100 - 600$ W m $^{-1}$ K $^{-1}$ at 20 K and zero field [228]). Nevertheless, the exciting new results from MIT which achieved a field of > 20 T [12] demonstrate REBCO cables are on a fast track to fusion applications [66].

5.4.4 New fusion-focused high-field superconducting alloys

Other Nb-Ti based alloys have been produced with larger upper critical fields than commercial Nb-Ti. Indeed the record upper critical field at 4.2 K is held by a quaternary alloy Nb 38.5%wtTi 6.1%wtZr 24.3%wtTa with $B_{c2}(4.2 \text{ K}) \approx 13$ T [229, 230]. Although the alloy is not produced commercially, its higher B_{c2} and ductility make it a obvious candidate material to optimise for future high-field fusion coils. In this work we have completed cost calculations using both the commercially available Nb-Ti used in ITER, and quaternary Nb-Ti (with the implicit assumption that fusion on an industrial scale would provide the commercial driver for quaternary Nb-Ti if required, at a similar cost to current commercial Nb-Ti). These calculations demonstrate that in fusion magnets, unlike accelerator mag-

nets, it is the low resistance rather than the high J_c values that is required. This points to future work (beyond the scope of this thesis) developing fusion-focused high B_{c2} superconductors that may be new alloys, or perhaps exploit reduced dimensionality to produce high B_{c2} [231] in say artificial multilayer alloys that bring the potential advantages of more straightforward robotic handling, higher radiation tolerance and higher strength than brittle materials and hence could displace high temperature superconductors.

5.4.5 Critical Current Densities

All superconductors were modelled using the previously derived Ginzburg-Landau scaling law for critical current density, equation 4.6.6, shown again here for convenience:

$$J_{c,ENG}(B, T, \varepsilon_1) = A^*(\varepsilon) \left[T_c^*(\varepsilon_1)(1 - t^2) \right]^2 [B_{c2}^*(T, \varepsilon_1)]^{n-3} b^{p-1} (1 - b)^q .$$

An applied strain of -0.5 % (equivalent to an intrinsic strain of -1.0%) was fixed for all conductors, representative of typical cryogenic pre-strain (a compressive strain of -0.58% is expected for ITER conductors [232]). Quaternary Nb-Ti has not been commercialised or produced in wire form. Here we have addressed its potential by using the literature values of $B_{c2}(4.2 \text{ K})$ and T_c for bulk materials reported in [229, 230]. All other fitting parameters for this quaternary material were assumed to be the same as for commercial Nb-Ti. The scaling parameters for the critical current densities of all superconducting strands and tapes modelled in the PROCESS calculations are given in table 5.7 and are shown at 4.5 K in figure 5.6. When modelling the low temperature superconductors using PROCESS, the cable conductor fraction of copper is 69 % and of superconductor is 31 %. The cable conductor helium void fraction is 33 % (similar to the ITER cables [233]). For REBCO, we have assumed the cable is fabricated with stacked tapes (similar to [217]) and has a helium void fraction of 20 %. The operating current was in all cases set to 100 kA and limited to 50 % of the cable critical current in all cases.

	$A^*(0)$ ($\text{Amm}^{-2}\text{K}^{-2}\text{T}^{3-n}$)	$T_c^*(0)$ (K)	$B_{c2}^*(0,0)$ (T)	p	q	n		
Quat. Nb-Ti	3.42×10^2	8.30	21.13	0.49	0.56	1.83		
Nb ₃ Sn	2.45×10^7	16.89	28.54	0.47	1.53	2.34		
Comm. Nb-Ti	3.42×10^2	9.04	14.86	0.49	0.56	1.83		
REBCO	1.24×10^{-3}	184.98	138.97	0.45	1.44	3.33		

	v	s	u	w	c_2	c_3	c_4	ε_m (%)
Quat. Nb-Ti	1.42	-	0.0	2.2	-0.0025	-0.0003	-0.0001	-0.002
Nb ₃ Sn	1.45	-	-0.06	1.94	-0.7697	-0.4913	-0.0538	0.279
Comm. Nb-Ti	1.42	-	0.0	2.2	-0.0025	-0.0003	-0.0001	-0.002
REBCO	-	5.27	0.0	2.2	-0.0191	0.0039	0.00103	0.058

Table 5.7: Parameters for the Durham scaling law for the critical current density of quaternary Nb-Ti [229, 230] and internal tin Nb₃Sn [136]. Commercial Nb-Ti and REBCO scaling parameters shown again for convenience.

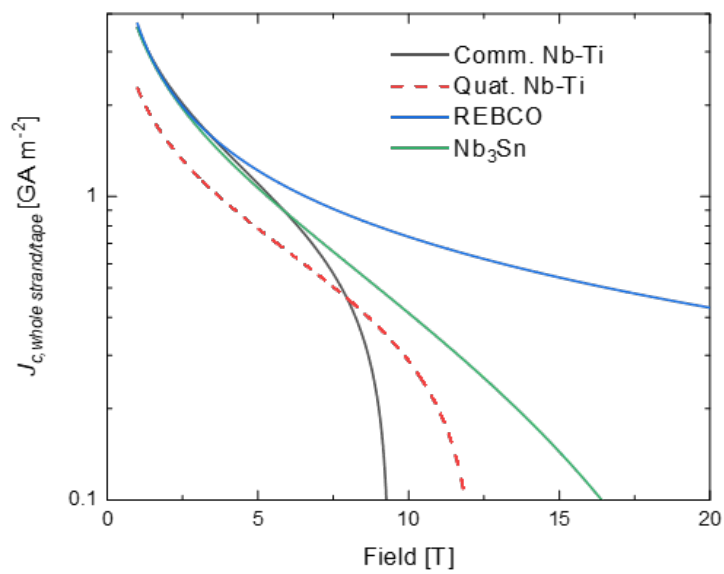


Figure 5.6: Whole strand/tape critical current density of commercial ITER specification Nb-Ti (Comm. Nb-Ti), quaternary (Quat.) Nb-Ti, internal tin Nb₃Sn, and $REBa_2Cu_3O_7$ (REBCO where RE :rare-earth) at 4.5 K, used in this work. Only quaternary Nb-Ti is not commercially available but could be optimised for fusion.

5.4.6 Cost-Optimised Superconducting Reactor Comparison

From table 5.2, we can see that R₁BL with REBCO CS and TF coils is of a lower capital cost than one with either Nb₃Sn or Nb-Ti (at the REBCO unit cost of 30 \$/kA m (6 T, 4.2 K)). The Quaternary Nb-Ti, REBCO and Nb₃Sn reactor (R₈AD, R₁BL and R₇AD respectively) error margins on capital cost ($\approx 5\%$ - see section 4.1) do overlap. At the resolution that PROCESS can provide they are effectively the same cost. The reactor with commercial Nb-Ti TF and CS coils is the most expensive (and is statistically distinct from the other three reactors, taking the 5% error margin) but R₈AD and R₇AD are essentially equal in capital cost. This highlights the great benefit of increasing the B_{c2} of Nb-Ti alloys for fusion purposes. If quaternary Nb-Ti could be manufactured at the scales required for fusion power then the data suggest that it could perhaps supersede Nb₃Sn: for roughly the same capital cost a reactor could be built with a ductile superconductor!

Taking the results in table 5.2 at face value, and ignoring the error 5% error: it is not surprising that a REBCO reactor would be cheaper to build than a Nb-Ti reactor given Nb-Ti's low B_{c2} (for example, see [234]), but it is interesting that it would also be cheaper than a Nb₃Sn reactor (should REBCO prices drop this low). This cost reduction is due to the smaller overall reactor volume: R₁BL has a device centre to outer-surface-of-the-TF-outer-leg width of 12.3 m and height of 14.6 m compared to the 13.3 m and 15.7 m height of R₇AD. The drivers for this larger size are the cost-optimal specifications of the CS and TF coils: The REBCO CS coil has an overall outer width of 2.38 m with a peak field of 14 T, and its TF coils are 0.71 m thick with a peak field of 12.6 T producing a field on plasma axis of 5.36 T; compared to the Nb₃Sn reactor's CS coil outer width of 2.52 m and peak field of 11.5 T and TF coil thickness of 0.75 m and peak field of 12.1 T producing a field on plasma axis of 5.16 T. The critical current densities of the REBCO cables in the CS and TF at peak operating conditions were approximately double those of the Nb₃Sn cables, hence the smaller central solenoid and thinner TF coils, despite

the higher fields. The $\approx 4\%$ lower toroidal field of the Nb₃Sn reactor demands a comparatively large increase in plasma volume of $\approx 16\%$ to achieve an equivalent fusion power (see table 5.8). Therefore, the R₇AD has a larger cost-optimal plasma minor radius of 2.41 m and elongation (at the 95 % flux surface) of 1.60 compared to the R₁BL's 2.15 m minor radius and 1.58 elongation. Note that this explains why a REBCO reactor could be cheaper - but such a conclusion cannot necessarily be drawn here, as the error margins on R₁BL's and R₇AD's capital costs overlap (if only just).

In summary, R₇AD's coils are thicker and its plasma volume is larger, resulting in $\approx 21\%$ larger volume and 7 % larger cost, despite its 25 % cheaper total superconducting cable cost. Minimum capital cost is our primary figure of merit in this work, so our preferred reactor must be the 100 MW_e reactor with REBCO CS and TF coils and (commercial) Nb-Ti PF coils, R₁BL. The capital cost and power balance of this reactor are displayed in figure 5.7. The recirculating power fraction of the reactors in this section is far too high for “true” power plants: more power is recirculated than net electricity produced! These reactors are not full-scale power plants however, they are pilot power plants - designed to demonstrate the viability of all integrated technologies for a power plant [15], for the lowest capital cost (not the minimum recirculating power fraction or cost of electricity). Increasing the net electrical output of a reactor significantly reduces the recirculating power fraction, as evidenced by a drop in cost of electricity [142]:

$$\text{Cost of electricity} \propto \text{Net electric output in GW}^{-0.6} . \quad (5.4.1)$$

Although it is not advisable to do so (as stated in section 4.4) converting the reactor capital costs in table 5.2 to 2021 US \$ yields a range between ≈ 14 Bn\$ and 17.5 Bn\$, less than ITER's 20 – 65 Bn\$. We suggest that this mismatch is due to the fundamental difference in design philosophy between the reactors in this work and ITER. Here, we have categorically sought to minimise capital cost.

Reactor ID	TF s.c.	CS s.c.	TF (CS) peak field (T)	Field on plasma (T)	TF (CS) steel %	Plasma current (MA)	Capital cost (1990 M\$)	R _{major} (m)	R _{minor} (m)	Plasma volume (m ³)
R ₁ BL	REBCO	REBCO	12.5 (14.0)	5.4	52.8 (80.4)	13.6	4230	6.75	2.15	1020
R ₇ AD	Nb ₃ Sn	Nb ₃ Sn	12.1 (11.5)	5.2	52.7 (70.7)	14.6	4520	7.21	2.41	1350
R ₂ BL	Commer. Nb-Ti	Commer. Nb-Ti	9.2 (8.1)	3.4	45.2 (63.9)	18.9	5200	7.93	3.27	2860
R ₈ AD	Quat. Nb-Ti	Quat. Nb-Ti	11.7 (10.6)	4.9	51.6 (70.1)	14.9	4530	7.28	2.49	1460

Table 5.8: Magnet performance and reactor size of capital cost minimised, $H_{98} = 1.2$, 100 MW net electricity reactors. The different superconductors considered are the high temperature superconductor $REBa_2Cu_3O_7$ (REBCO where RE :rare-earth), commercial NbTi (Comm. NbTi) used in MRI scanners, and quaternary NbTi (Quat. NbTi) that is not yet available commercially.

The reactors here are not science experiments with multiple possible operating modes, plasma shapes, pulse lengths etc. They have one mode of operation and a much-reduced specification as a result. Additionally, ITER's construction is deliberately diffuse: different countries (often multiple countries in parallel) build and test components before shipping them across the world to Cadarache. Taking the TF coils as an example: the conductors were manufactured in Japan, China, the US, Russia and Europe; the TF cases were manufactured in Japan; and the TF coils were assembled in Italy and Japan. The philosophy has been one of maximum collaboration (and maximum bureaucracy) to enable all stakeholders to build their own demonstration power plant post-ITER – not one of minimised costs, where the reactor would be built by a single body, at, or close to, the final site.

The parameters that PROCESS was given the freedom to vary in all of the reactor simulations in this chapter are shown in the table of iteration variables: Table 6.1.

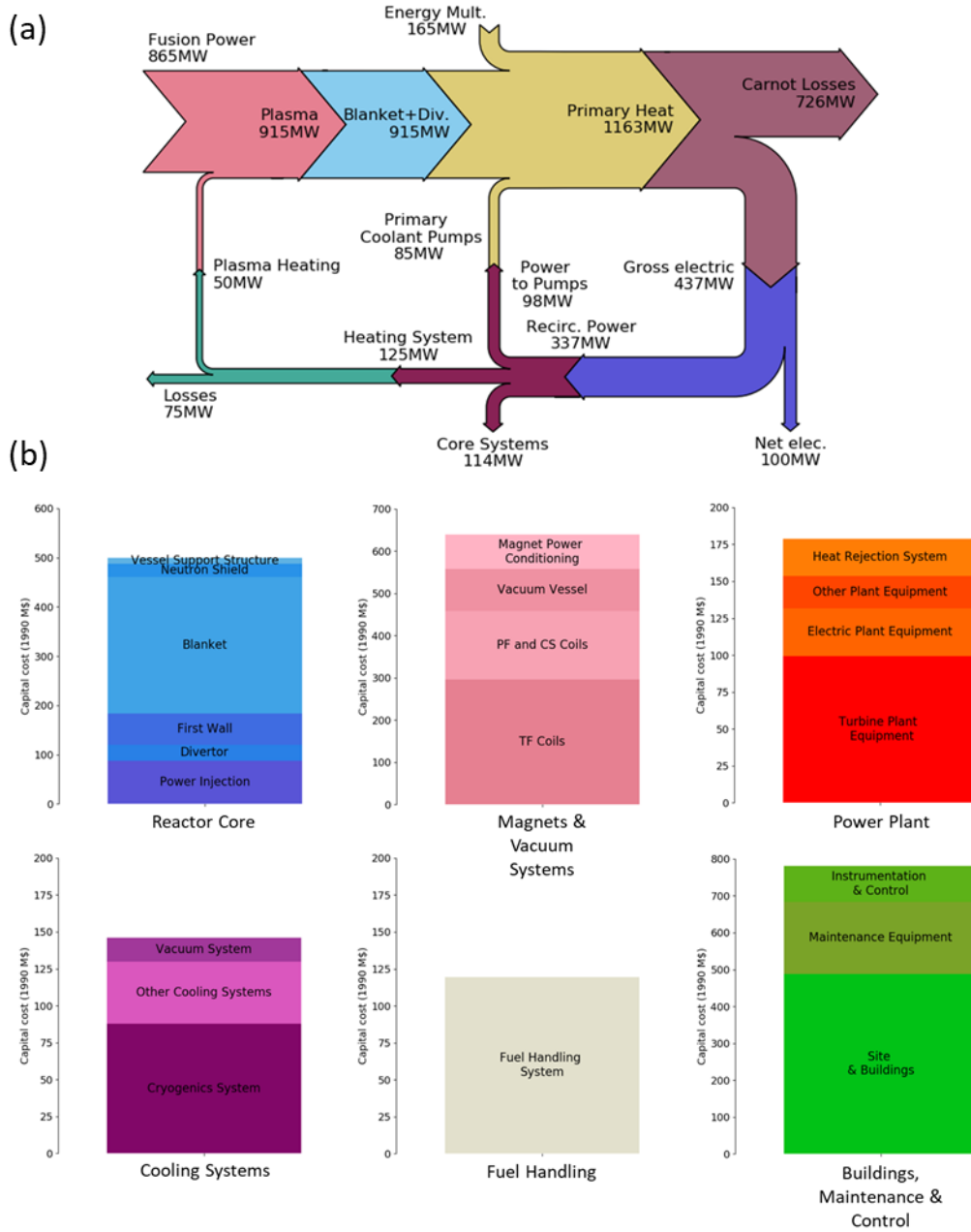


Figure 5.7: (a) Reactor power balance (where “Core Systems” includes the cryo-system (46 MW_e) and the tritium handling system (15 MW_e)); (b) direct capital cost breakdown of the preferred reactor R_1BL (a cost-optimised $H_{98} = 1.2$, 100 MW net electricity tokamak with REBCO toroidal field and central solenoid coils). Costs are in 1990 US M\$.

Figure of merit:	Minimum capital cost	
Iteration Variable	Upper Bound	Lower Bound
Aspect ratio	-	-
Toroidal field on axis (T)	-	-
Plasma major radius (m)	-	-
Volume averaged electron temperature (keV)	-	-
Total plasma beta (%)	-	-
Electron density ($\times 10^{19} \text{ m}^{-3}$)	-	-
F-value for density limit	1.1	-
Inboard TF coil thickness (m)	-	-
F-value for maximum wall load	-	-
Central solenoid thickness (m)	-	-
Safety factor at 95 % flux surface	50	3.45
F-value for the net electrical power generated	-	-
CS bore (m)	-	-
F-value for beta limit	-	-
CS overall current density at EOF (MA m^{-2})	-	19
F-value for CS current at EOF	0.5	-
F-value for CS current at BOP	0.5	-
Ratio of CS overall current density at EOF & BOP	-	-
Non-inductive plasma current fraction	-	-
F-value for TF coil case stress	-	-
F-value for TF coil conduit stress	-	-
F-value for TF coil operating current	0.5	-
F-value for dump voltage	-	-
Max voltage across TF coil during quench (kV)	10	-
F-value for TF coil winding pack current density	-	-
Dump time for TF coil (s)	100	30
Inboard TF coil case outer thickness (m)	-	-
F-value for power through the separatrix	0.8	-
TF coil conduit case thickness (cm)	-	-
F-value for L-H power threshold	-	-
F-value for CS coil Tresca stress limit	-	-
F-value for radiation wall load limit	-	-
Fraction of steel in CS	-	-
F-value for max Z_{eff}	-	-
Argon impurity f-value	-	-
TF coil Winding pack radial thickness (m)	-	-

Table 5.9: Iteration variables and bounds, for the reactor optimisation study. F-values are the allowable factor changes in values, e.g. an F-value of 1.2 would allow PROCESS to set a variable to 120 % of its predefined value. Note that this table does not cover input parameters (there are too many to list here), for a full list of all variables used see Appendix A.

5.4.7 The Cost-Optimal Field on Coil

Despite having REBCO magnets, the cost-optimal field of R₁BL at 12.6 T is somewhat lower than the ≥ 20 T on-coil fields proposed for SPARC and ARC [4, 9, 151]. We suggest that this is because of the explicit use of capital cost as the figure of merit in the PROCESS (rather than maximum field, or minimum radius). The field on coil can be increased above this, but the resulting cost-optimal reactor has a larger overall volume (despite having a lower plasma volume) and is ultimately more expensive (see figure 5.8). As we shall discuss in more detail in the following subsection, the primary cost-limiting factor is the yield strength of the steel support architecture. Increasing the toroidal field increases the required thickness of the TF support casing, which demands an increase in the major radius of the reactor. For example (allowing PROCESS to vary reactor design parameters) if the field on plasma axis of R₁BL is arbitrarily increased from 5.36 T to 6.5 T, the plasma volume falls to 820 m³ from 1020 m³, but the major radius increases to 6.94 m from 6.75 m - driven by the 27 cm thicker TF coils - and the capital cost increases to 4320 M\$ from 4230 M\$. More advanced structural support architectures may delay this cost increase, a topic we discuss in more detail in chapter 7.

5.4.8 Stress-limited, J_c -limited and B_{c2} limited Magnets

In general, superconducting magnets can be: stress-limited, in which case the Lorentz force induced stresses are close to the yield-stress of the component magnet material; J_c -limited, where the current density in the superconductor is sufficiently high to overcome flux pinning and the material may become resistive. Here we also consider a type of J_c -limited, that we call B_{c2} -limited. In this case, the operating field is close to the upper critical field of the superconductor so the description makes clear that increasing B_{c2} will significantly affect the operating field achievable equivalent to the critical current density being low because of the superconductor's bulk critical properties rather than the strength of flux pinning per se. The limit-

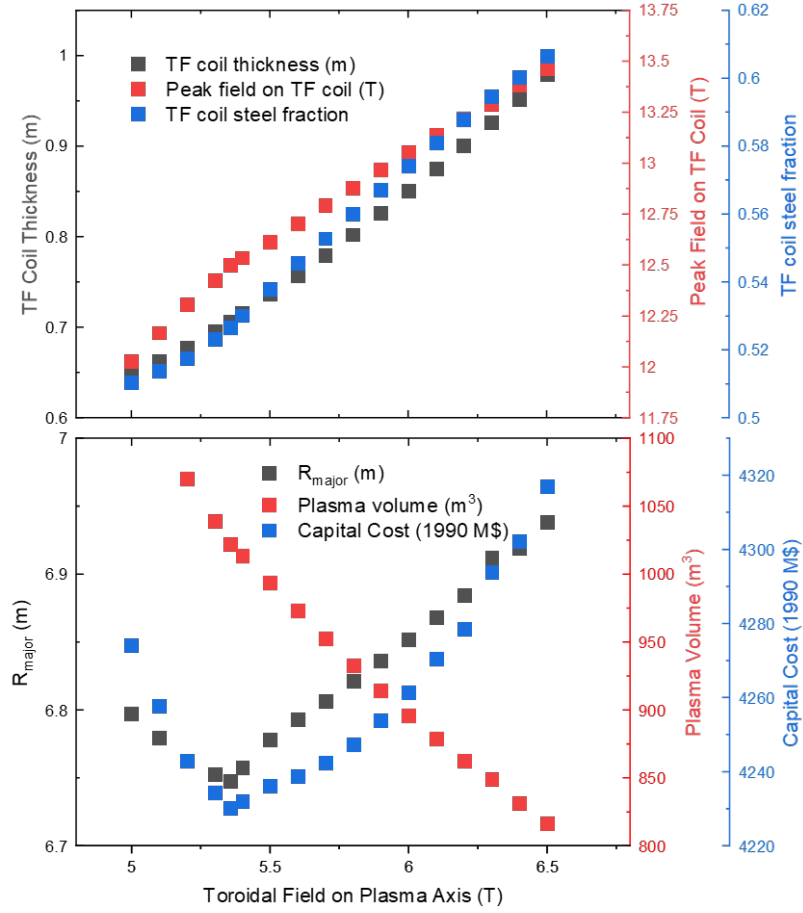


Figure 5.8: The result of changing the field on plasma axis from the cost-optimum 5.36 T (of the preferred reactor R_1BL) on the cost-optimal TF coil design, reactor build and capital cost.

ing factors for magnets can be understood with reference to the hoop stress in a magnet approximated by [41]

$$\sigma_{\text{hoop}} = B_{\text{magnet}} J R_{\text{magnet}}, \quad (5.4.2)$$

where these are averaged properties over the magnet, and B_{magnet} is the magnetic field, J is the magnet current density, and R_{magnet} is the radius of the magnet.

In commercial, small bore superconducting accelerator magnets such as those at CERN, the operating current density of the component superconductors is close to the critical current density of 10^9 A m^{-2} at the operating field of 16 T and the magnets are J_c -limited. In contrast, the huge bore, R_1BL reactor has $B_{\text{coil}} = 12.5$

T and a leg-centre to leg-centre distance at the mid-plane of 9.2 m. At $\sigma_{\text{hoop}}^{\text{max}} = 660$ MPa the operating current density in the TF coil winding pack is $\approx 2.3 \times 10^7$ A m⁻², two orders of magnitude lower than that in accelerator magnets or that in the whole tape critical current density of REBCO at 12 T, 4.5 K (see figure 5.6). It is important to distinguish whether a magnet is stress limited or J_c limited. If the magnet is J_c limited improvements in J_c directly increase the field the magnet can produce, whereas in a stress-limited magnet where say only a few percent of the cross-section of the coil is superconductor, improvements in J_c only allow marginal increases in the steel volume content whereas it is improvements in stress limits (or design) that are markedly more beneficial because they increase the space for more superconductor and hence increase the operating field. If the magnet is B_{c2} -limited, increases in the superconductor upper critical field are most effective in increasing the cost-optimal field on-coil. These considerations demonstrate that in conventional aspect ratio tokamaks magnets are stress-limited and the overall current density in the cable is far from the operating J_c limits of REBCO, and that current superconductors are far from optimised for fusion applications. REBCO magnets are stress-limited and cable design benefits most from improvements of structural material, as it is the yield stress of the material (and the design of the magnets, discussed below) that primarily determines operational limits and cost. Likewise increasing the upper critical field of Nb-Ti (e.g. via the use of a higher B_{c2} alloy) would significantly improve its use in fusion magnets.

5.4.9 Graded and Sectioned Coils

In this thesis, we have used the most straightforward winding pack design which uses the same superconductor cross section along the entire cable length (as determined at the peak field on coil) [235]. In lower field regions the superconductor operates well below its critical current density. However one can consider graded coils in which the cross section of the cables are better tailored to the operating current. In the lower field regions the the cross-section of the cables is reduced

[223, 236]. Further cost reductions follow when cheaper superconductors are used in the outer parts of the winding pack e.g. Nb-Ti in the low field regions, Nb₃Sn in the middle of the winding pack and REBCO in the high field regions [237]. Taking the example of the solenoid coil in [238] and using a REBCO cost of 30 \$/kA m (6 T, 4.2 K), we calculate the graded multi-superconductor solenoid has a materials cost ≈ 21 % lower than the ungraded REBCO-only solenoid. There is a clear case for grading even with TF coils. The inboard side of a tokamak TF coil outer leg sees fields 50 % weaker than the maximum on-coil field (at the outboard side of the TF inner leg), and the outboard leg sees fields 25 % weaker or less. The toppling forces are also localised, meaning that grading the cable conduit thickness is also viable.

As well as traditionally graded coils, the field-on-coil data of figure 5.9 show that given we need remountable magnets to enable timely repair, we can also consider sectioned coils, perhaps with a half-phi design: coils where the inner and outer coil limbs are based on different superconductors [234, 239]. For the R₁BL reactor TF coils, the field on the outer limb is below 8 T, making Nb-Ti the obvious choice. Nb-Ti at 8 T has a cost in \$/kA m $\approx 16 \times$ lower than that of REBCO at 12.5 T, so adopting Nb-Ti outer limbs would reduce the R₁BL's TF coil direct cost by ≈ 16 % (reducing the reactor's overall capital cost by ≈ 2 %).

5.5 Comments on Spherical Tokamaks

Spherical tokamaks have several advantages over conventional aspect ratio tokamaks and are being considered for pilot fusion power plants [75, 11]. Spherical tokamaks operate at higher beta (of up to 40 % [240]) and at higher safety factors (e.g. $q_{95} = 8.9$ in FNSF [13]) than conventional reactors, meaning that their plasmas are inherently more stable (and disruptions less likely) for a given field on plasma axis [240, 241, 242]. Proposed spherical tokamak pilot plants designs are also compact, with major radii > 3.5 m [11, 150, 50, 13] (in principle redu-

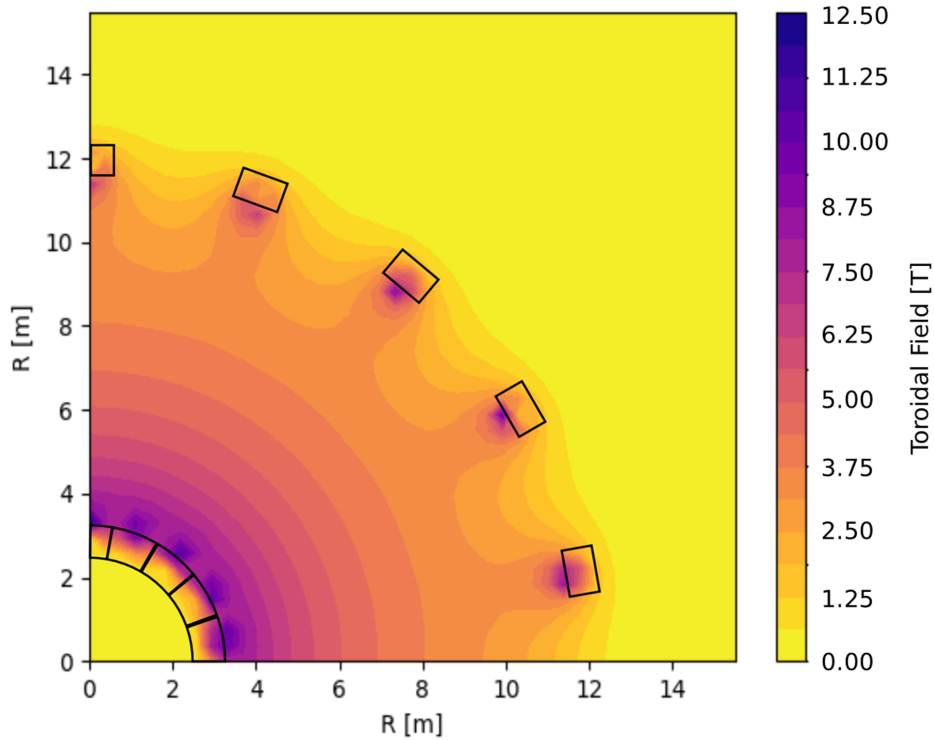


Figure 5.9: Toroidal magnetic field strength as a function of position within the R₁BL through the reactor mid-plane. TF coil outlines are shown in black.

cing construction costs and time [243]) whilst producing fusion power gain ≈ 30 [11, 244].

Spherical tokamaks' compact size however also increases average neutron wall loading, above 3.5 MW m^{-2} in some proposed pilot plant designs [150, 50], more than three times that of EU-DEMO [6]. This very high flux necessitates thick neutron shielding (or breeding blanket) of $\approx 60 \text{ cm}$ for the central column [13] (reducing the field on coil for a fixed reactor major radius), or frequent remote replacement of the central column magnets (on the order of every 3 years [50]). The small size also increases the power through the separatrix (above 30 MW m^{-1} in some designs [150, 50]) necessitating the use of advanced divertor configurations [245] which would either make use of sacrificial, resistive, inboard coils (that are part of a higher order reactor design than that discussed in this work) or require heavily distorted TF coil architectures [184, 185]. As stated in the previous chapter, tokamaks design studies have shown the cost of electricity is lower for large tokamaks,

scaling proportionally to the electric power of the tokamak raised to the power -0.59 (i.e. increasing the electric power by a factor 10 reduces the cost of electricity by about 4) [142] and ultimately means that large fusion power plants will probably be most cost competitive. Nevertheless compact spherical tokamaks may offer the opportunity for lower capital costs to demonstrate fusion energy is commercially viable - it is beyond the scope of this thesis on ITER-like aspect ratio machines to assess to what degree these reductions are offset by the specific technical challenges of spherical tokamaks, and hence how effectively they provide a short-cut to demonstrating commercial fusion energy is cost-effective.

5.6 Comments on Aluminium/Copper Tokamak Power Plants

Copper [246, 247] and aluminium [248] have the best combination of high strength and high electrical conductivity to have been the choices for magnets in experimental fusion reactors. Resistive magnets for tokamaks are typically operated at 300 – 400 K and do not suffer the same cut-off in current carrying capacity with neutron fluence as superconductors, meaning that shielding requirements are reduced and reactors can (in principle) be made more compact. However, the (magneto-)resistivity of these materials is unchanged for many decades and can be contrasted with developments in superconductivity where large scale projects such as ITER and CERN continue to drive improvements in materials with higher current density, and one can expect commercial fusion to drive the development of the more neutron tolerant materials (e.g. high-field alloys). Resistive tokamaks have indisputably helped drive our understanding of, and encouraged new designs for, high-field fusion plasma physics. For example, ARIES-ST [50] which was designed with only a 20 cm ferritic steel centre-post shield leading to a predicted nuclear heating of 164 MW and total magnet system losses of $\approx 730 \text{ MW}_e$, an order of magnitude more than the cryopant power and magnet system losses for

the superconducting reactors in table 5.3.

Proposed resistive reactors however have very low plasma burn times (e.g. FIRE [249] (a prototype reactor) with a 20 s plasma burn and ≈ 3 h repetition time) or rely on non-inductive start-up mechanisms and assume large $H_{98} \gtrsim 1.5$ (e.g. ARIES-ST [50] and STPP [150]). Even the small size of proposed resistive tokamaks would not obviously reduce their capital cost compared to superconducting reactors. Both ARIES-ST's cost of ≈ 4200 M\$ (1990 \$) and our PROCESS generated capital costs for a 100 MW_e STPP-like reactor (with minimised capital costs) of 5200 (1990) M\$ shown in 5.10 are similar to (and larger than) the cost of the $H_{98} = 1.2$ R₁BL, and in fact larger than the $H_{98} = 1.6$ R₃BL. The reduced costs due to smaller size are counterbalanced by cost increases in coil bussing and power conditioning. It has been argued that high temperature superconductors are an essential technology that will enable commercial fusion power [168]. We broadly concur that the scarce resources for commercialisation of fusion are best focussed on de-risking and up-skilling in commercialising the unprecedently large superconducting magnets required, rather than resistive ones.

R_{major}	A	κ	δ	Field on TF coil (T)	Field on plasma (T)	TF steel fraction (%)	Plasma current (MA)	Capital cost (1990 M\$)	$H_{98} = 1.6$		$H_{98} = 1.0$	
									Fusion power (MW)	Net. elec. (MW)	Fusion power (MW)	Net. elec. (MW)
3.42	1.40	3.20	0.55	7.56	2.50	5	19.4	5200	1670	100	530	-370

Table 5.10: Performance and cost of a steady-state $H_{98} = 1.6$, 100 MW_e reactor with copper TF, CS and PF coils (with minimised capital cost). Based on STPP [150].

Using a similar validation process to the one in section 5.3.2, we first confirm the reliability of our PROCESS calculations by comparing them with some simple benchmark calculations and with JET experimental results. Our approach was to compare the maximum current per resistive magnet turn to the maximum current per superconducting magnet turn in a tokamak with space allocated to the magnets equal to that in R₁BL. Making explicit our use of Ampere's law [250], we can write:

$$I_{\text{turn}}^{\text{resistive}}/I_{\text{turn}}^{\text{R}_1\text{BL}} = B_{\text{T}}^{\text{resistive}}/B_{\text{T}}^{\text{R}_1\text{BL}} \quad (5.6.1)$$

where $I_{\text{turn}}^{\text{resistive}}$ and $I_{\text{turn}}^{\text{R}_1\text{BL}}$ are the coils' currents per turn on the resistive reactor and R₁BL and $B_{\text{plasma}}^{\text{R}_1\text{BL}}$ and $B_{\text{plasma}}^{\text{resistive}}$ are the magnetic fields on plasma axis of R₁BL and resistive reactor respectively. The maximum current per resistive magnet turn was calculated using

$$Q_{\text{cooling}}^{\text{max}} = (I_{\text{turn}}^{\text{resistive}})^2 \frac{\rho_n L_{\text{turn}}}{(A_{\text{turn}} - \pi(D_h/2)^2)} \quad (5.6.2)$$

where ρ_n is the conductor resistivity, L_{turn} is the length of each turn and A_{turn} is the cross-section of each turn. The maximum cooling power per turn $Q_{\text{cooling}}^{\text{max}}$ is given by

$$Q_{\text{cooling}}^{\text{max}} = \dot{m} c_p \Delta T_{\text{turn}} \quad (5.6.3)$$

where \dot{m} is calculated from equation 5.3.6 noting that for $\dot{m} \approx 0.1 \text{ kg s}^{-1}$ $f_d \approx 0.0231/V_{\text{coolant}}^{0.742}$.

In each of JET's 32 TF coils [152, 251, 92], there are 24 turns of length 15 m, and average turn cross section of $\approx 32 \text{ cm}^2$. Each turn has its own cooling channel with a cooling channel hydraulic diameter of $D_h = 1.5 \text{ cm}$, an inlet over-pressure is 5 bar and $\Delta P = 0.5 \text{ bar}$. The temperature of the coolant is $T_{\text{coolant}}^{\text{inlet}} = 293 \text{ K}$ and $\Delta T_{\text{turn}} = 75 \text{ K}$. We have set the average copper magnetoresistivity over the temperature range (and typical field $\approx 6 \text{ T}$) to be $2.20 \times 10^{-8} \text{ } \Omega \text{ m}$ (see table 5.6 [252, 170]) and used the well-known properties of water for the coolant (rather than the anticorrosion fluid Galden HT55 used in practice). The simple benchmarking equations above yield a current per turn of 63.4 kA, very close to the JET current

per turn of 66 kA and resistive losses for the TF magnet system of 497 MW, close to the JET power requirements of 700 - 1375 MW [92, 253].

Turning to use the geometry of R₁BL, there are 18 TF coils each with 100 turns each of length 38.1 m and a cross-section for each cable of 39.6 cm². Following JET, we consider resistive copper magnets operating at room temperature where each turn has its own cooling channel. The inlet pressure was set to that of JET with 5 bar and $\Delta P = 1$ bar, as well as the temperature of the coolant, $T_{\text{coolant}}^{\text{inlet}} = 293$ K and $\Delta T_{\text{turn}} = 75$ K. The cooling channel hydraulic diameter was optimised and found to be at 56 % of the cross-section (i.e. $D_h = 5.3$ cm). Equations (5.6.1 - 5.6.3) then yield a maximum current per turn of 57.1 kA compared to R₁BL which has 100 kA per turn. Not surprisingly for resistive magnets, we find a huge power consumption of 3 GW. We now consider whether running resistive magnets at cryogenic temperatures is more viable and calculate the performance of cryogenically cooled resistive aluminium magnets cooled to 65 K using liquid nitrogen as the coolant, and then at 20 K using supercritical helium. Aluminium and copper have similar room temperature resistivity ($\approx 2.7 \times 10^{-8}$ Ω m and $\approx 1.7 \times 10^{-8}$ Ω m respectively), but it is cheaper to make high-purity high-strength aluminium than copper, so aluminium is generally preferred at low temperatures for cryocooled resistive magnets. Ensuring the nitrogen doesn't solidify or become gaseous requires setting $T_{\text{coolant}}^{\text{inlet}} = 65$ K and $\Delta T = 15$ K. Averaging over the temperature range, at 6 T and RRR = 10000, Al has a resistance of $\approx 3 \times 10^{-9}$ Ω m [215, 216]. Using the benchmarking calculations we find the current in each turn is only 35.6 kA which is lower than the 100 kA in R₁BL. Of greater concern commercially (also found below for 20 K) is that the required resistive heating is 148 MW which even with ideal Carnot losses require cryocooler work of 520 MW:

$$(\text{ideal}) \text{ cryocooler work} = \text{heat at } 65 \text{ K} \times \frac{T_h - T_c}{T_c} . \quad (5.6.4)$$

Turning to 20 K operation with $\Delta T = 20$ K and using supercritical helium: averaging over the temperature range, at 6 T and RRR = 10000, Al has a resistance of $\approx 10^{-10}$ Ω m [215, 216]. Under these conditions, the current in each turn is higher

than the superconductor by about 50 % (were it not to be stress limited), however the resistive losses of the Al magnet system would be ≈ 90 MW at 20 K equivalent to huge cryocooler work 1.23 GW_e. Our calculations show why superconductivity is a disruptive technology for fusion: resistive magnets in a fusion power plant would consume most of the power (and sometimes more) than the plant would produce. At room temperature, huge levels of power are needed to drive the magnets themselves. At cryogenic temperatures, equally huge levels of power would be required to drive the cryoplant.

Finally we note that plasma control is more demanding with resistive magnets compared to superconducting ones. When the current changes in a resistive magnet, along with the magnetic field changing, the temperature and the size of the magnets change because of the thermal expansion of the various components. In the superconducting case, the current does not substantially heat the magnets so the differential thermal properties of the component parts of the tokamak play little role. We also remind the reader that we have not included any calculations for the cost of robotic replacement of resistive parts, which will almost certainly be cheaper than removing and installing brittle superconducting components. However, we have not proceeded any further with calculations for resistive magnets given their huge power demands, and that we feel the magneto-resistance of copper and aluminium is well enough understood that no significant reduction in the magneto-resistivity is likely. Our calculations, table 5.10, show that even if we could find some way for the plasma to perform well beyond current expectations at $H_{98} = 1.6$, we might get a little electricity. However given that resistive magnets are a very mature technology and the lessons from history about what inevitably happens to technologies that can't evolve if they compete with a continuously improving disruptive technology - superconductivity, we basically set aside considering large resistive magnets in the tokamak for the rest of the thesis.

5.7 Reducing the Tritium Breeding Ratio and Required Net Electricity

It is useful to consider at this stage if there are any expensive technologies that could be eliminated or reduced in scale from R₁BL to reduce its capital cost. Primary amongst these are the breeding blanket and the power plant, so here we chose to focus on a reducing the tritium breeding ratio, and the net electricity output of the reactor. As discussed briefly in section 5.2.3, a capital cost reduction of $\approx 24\%$ can be made by setting $TBR = 0.9$. This does not just reduce the cost of the blanket (which makes up $\approx 12\%$ of R₁BL's direct cost, see table 5.2) but also reduces the the reactor volume by 28% (by reducing the inboard and outboard blanket modules' thicknesses by 64%) and hence leads to a cost reduction A further reduction to $\approx 69\%$ of R₁BL's capital cost can be made by designing the tokamak to break-even rather than produce 100 MW_e . The reduced necessary blanket size would allow for a more compact $R_{\text{major}} = 6.2\text{ m}$, operating with a field on plasma of 6.1 T and field on TF coil of 12.5 T . Such a tokamak would need to produce $\approx 560\text{ MW}$ fusion power. Investors may be concerned that either of these $TBR = 0.9$ tokamaks wouldn't actually demonstrate or de-risk a potential integrated commercial technology: Commercial tokamak power plant must be self-sufficient in tritium [177], and if a pilot plant is to demonstrate all necessary technologies for a commercial reactor, then it follows that it too must show $TBR = 1.1$. We conclude that there are no foreseeable substantial cost reductions for building a practical tokamak on the timescales of the 2030-2040 deadline.

5.8 Conclusions

Using the `PROCESS` systems code we have modelled and minimised the capital cost of 100 MW_e superconducting tokamaks with Nb-Ti PF coils, and TF and CS coils of either commercial Nb-Ti, quaternary Nb-Ti, Nb₃Sn or REBCO. Superconducting

magnets must be shielded from the fusion neutron radiation to reduce the nuclear heating on the magnet system to manageable levels (below 10 kW) and to reduce damage to superconducting materials themselves (which have a lifetime neutron fluence of $\approx 3.9 \times 10^{22}$ neutrons m^{-2}). A capital cost optimised shield will be as thin as possible (whilst meeting the above specification) and we have employed dedicated MCNP calculations to calculate the thickness of this shield for a 100 MW_e reactor: 25 cm tungsten carbide.

We also discussed the major design choices for all of our tokamaks: the plasma energy confinement time; plasma β , density and safety factor; superconductor operating temperature; tritium breeding ratio; divertor constraints and configuration; coil structural support; central solenoid use and burn time. Our intention was that the reactors in this work could be realistically built within the next 20 years, and hence we have chosen components and operating conditions that have either already been proven, or are “in the works” for ITER or EU-DEMO (granted EU-DEMO is envisioned to begin operation around 2050, but with concentration of effort around the single goal of completion - reducing the timescale by 10 years is not unreasonable). Of those components we chose those most likely to yield a lower capital cost reactor.

The chapter culminates in the presentation of our preferred reactor: a 100 MW_e REBCO CS and TF and Nb-Ti PF reactor. It is interesting to note that should REBCO’s price fall to the predicted 30 \$/kA m (6 T, 4.2 K) this reactor would have a capital cost ≈ 300 M\$ (1990 US\$) lower than a Nb₃Sn reactor. We expand on this reactor design in the next chapter, where we investigate the use of Nb-Ti training coils. If the reactor is built with remountable magnets, we can ask: can we use robust Nb-Ti (rather than brittle REBCO) during the commissioning stage of the tokamak lifetime (thereby reducing risk of damage to the REBCO magnets), and how effective would those training magnets be?

Using Training Magnets to Reduce Reactor Risk

6.1 Introduction

The high temperature field superconductors REBCO and the low temperature superconductor Nb₃Sn are the candidate high field materials for the toroidal field (TF) and central solenoid (CS) coils for fusion reactors. The ITER [17] and SPARC [4] reactors use these materials and are expected to operate with fusion power gain $Q_{\text{fus}} \geq 10$, as will other pilot fusion power plant reactors that will eventually generate 100s MW net electricity (e.g. EU-DEMO [6], STEP [75], ARC [9]). During the commissioning phase after construction, in addition to the high stresses that occur in magnets during standard operation, unexpected, powerful disruptions can also occur in the plasma such as vertical displacement events and associated halo currents. In the JET reactor, such uncontrolled events induce forces of order 4 MN, that have lifted the entire vessel by 9 mm [254, 255]. These disruptions are expected to be an order of magnitude greater in ITER [256]. More than half of all unintentional disruptions in JET were not due to physics instabilities, but were attributed to, for example, failure of one of the sub-systems, control errors or human error. Fewer disruptions predominantly followed better technical operation

of JET. In short, operating a tokamak properly requires completion of a ‘learning curve’ that does not require full plasma power operation [95]. These uncontrolled events would bring with them the risk of permanent and irreparable damage to a tokamak with expensive brittle superconducting magnets. In ITER, were a TF coil failure to occur before nuclear operation starts, one can reasonably expect it to take 4 years to replace the coil (using an available spare). Once nuclear (i.e. tritium) operation has begun, the activation in the reactor vessel would be so high that, given there is no robotic control of magnet replacement, it would probably not be cost-effective to replace a TF coil [257]. Unfortunately all the very high field superconductors that we need in full operation for optimal (profitable) commercial fusion are brittle, and the largest Nb₃Sn fusion magnets ever produced to date (by size or weight) were resistive from origin [258]. In this thesis, we propose using Nb-Ti during the critical commissioning and testing phase because although it has poorer high field performance, it is ductile and so is robust against mechanical or brittle failure. We therefore (re)define “training coils” as remountable ductile magnets that operate a lower field, but remove the risk of brittle failure of the higher field, full-power magnets during reactor commissioning whilst still allowing for thorough machine testing.

In this chapter we primarily consider the utility of these training coils in our preferred 100 MW_e REBCO CS, TF Nb-Ti PF reactor, R₁BL, from the previous chapter. We do however also investigate the utility of swapping superconducting coils more generally, and so have adopted two approaches: (a) using Nb-Ti training magnets during the commissioning stage of a reactor cost-optimised with REBCO magnets; (b) upgrading a reactor cost-optimised with Nb-Ti coils with REBCO upgrade magnets. As well as the modelling cost-optimised reactors at the 100 MW_e, H₉₈ = 1.2 scale as in the previous chapter, we also optimise the designs of 100 MW_e, H₉₈ = 1.6 and 500 MW_e, H₉₈ = 1.2. For each of these ‘baseline’ reactors, the geometry was fixed and the superconducting materials used in the TF and CS coils were replaced with either REBCO, commercial Nb-Ti or quaternary Nb-Ti.

By “reactor geometry”, we mean the reactor’s physical build (e.g. the location of the coils, thickness of blanket, location of the first wall, etc.) - the plasma shape was allowed to vary. Where the materials in both magnet systems were replaced the mutual size of CS and TF coils were allowed to vary so long as the overall reactor radius and height changed by less than 1 % (equivalent to re-optimising the cable dimensions and construction, but keeping the reactor radius and height fixed) - note that this is beyond the accuracy of the **PROCESS** outputs. In all cases the reactors were then re-optimised for maximum net electricity yield in order to maximise the swapped magnets’ performance. For each reactor geometry the effect of a reduction from the designed-for operating H_{98} -factor to $H_{98} = 1.0$ was calculated (with a fixed reactor build) in order to assess the resulting drop in fusion power and net electricity generation should plasma quality not meet the higher values hoped for. All costs within this section are quoted in 1990 US\$. We are making the simplifying assumption that the use of training coils does not affect overall reactor architecture and that remountable magnets are the same cost as conventional (non-remountable) magnets, to first order.

We begin by highlighting the important issues concerning remote handling and remountable coils in section 6.2. We then present the results for avenue (a): the training coils for three baseline REBCO reactors (R_1BL , R_3BL and R_5BL) in section 6.3. The results from avenue (b) the upgrade coils for three baseline Nb-Ti reactors (R_2BL , R_4BL and R_6BL) are presented in section 6.4. We conclude by reaffirming our preferred reactor R_1BL as the optimal design for a mid 21st century pilot power plant, ultimately recommending the use of Nb-Ti training coils in section 6.5.

6.2 Robotics, Remountable Magnets and Joints

In high aspect ratio reactors of the type considered here (and similar to ITER and DEMO), conventional robotics/crane systems can be employed to extract the

CS and TF coils if they become damaged because they see little neutron flux due to thick radiation shielding. The requirements on remote handling (RM) for coils alone, are therefore not particularly demanding in the designs considered in this work. However, maintenance of the first wall, blanket and the other internal reactor components will be extremely challenging due to the high radiation levels of order 100 - 600 GBq kg⁻¹ remaining 4 weeks after shutdown [3], similar to those found in the core container of a fission reactor 8 years after shutdown [259]. Specialised radiation hard RM systems as found in ITER's/EU-DEMO's internal RM system [260, 261] will be required (and have not been included in the costs for replacing a damaged irradiated magnet in this work). The economic damage of a damaged or destroyed non-remountable magnet would be unjustifiable: it would put a power plant out of action for years. This risk is simply unacceptable for a commercial plant, and is the reason why (in the author's opinion) "life-time component" magnets will not be permitted in future reactors.

Commercial reactors will require availabilities as large as possible (70% or higher). Magnet failure forces the reactor to shut down, and repairs and replacements must be made as swiftly as possible. Remountable magnets and joints will be required to enable magnet replacement without having to cut open the vacuum vessel and the shielding - and exposing the irradiated core. Remountable joints for both low temperature superconductors [262, 239] and high temperature superconductors [9, 263, 264, 265] have been designed, though to-date none have been incorporated into working tokamaks. Indeed there is no published work (at time of writing) demonstrating full-scale remountable joints. There have been preliminary works on cable-to-cable remountable joints [66, 266] and there are no reasons why such joints couldn't simply be scaled to a full winding pack [61]. With concentrated effort however, we are confident that full-scale, reactor ready remountable joints are feasible by 2035-2040: non-remountable joints in superconducting magnets are commonplace in large-scale magnets; multiple institutions are working together and competitively to build them [66, 61, 266]; remountable joints are already present in

resistive magnet tokamaks e.g. MAST-U. Remountable joints introduce additional thermal load on the reactor cryo-system, though the required wall plug cryoplant power to manage this is ≈ 1 MW [9] and has been omitted from the PROCESS calculations here as it is small compared to the pre-existing cryogenic power demand of order 40 - 50 MW. For example, soldered REBCO joints have resistances of $\approx 50 \text{ n}\Omega \text{ cm}^{-2}$ [267], which for an ITER TF coil system gives a total thermal load of ≈ 600 W and is only about 1 % of the existing heat load (and far below the ≈ 5 % accuracy of PROCESS models) .

In the current final development phase for commercial fusion, one would not want to use brittle REBCO magnets in the commissioning phase for the reactor when the risk of damaging the magnets is not well-known. Indeed, operating with Nb-Ti training magnets may be required as part of regulatory licensing of the construction prior to operation [268]. After the reactor has operated successfully for several years and completed all its commercial requirements, in the post-demonstrator research reactor phase one may reuse the Nb-Ti magnets as part of trialling new technologies and component designs, because the risk of disruptions during such trials may again be high.

During the commissioning of the reactor, the full-power REBCO coils must of course be tested and commissioned themselves. Indeed the reactor will have to itself be recommissioned at full power. The training coils will allow the operational team to iron out the majority of user error and manufacturing error related disruptions and unexpected events which could destroy the brittle REBCO magnets, before they are installed. Plasma will be generated, power plant systems will be able to be tested etc. – simply not at full capacity, but close enough to full capacity to discover and significantly reduce the risk of magnet-destruction-capable events. Experience has shown that the majority of disruptions occur at the beginning of reactor life [95] - using training coils therefore puts the brittle full-power magnets at much less risk.

Figure of merit:	Maximum net electricity yield	
Iteration Variable	Upper Bound	Lower Bound
Toroidal field on axis (T)	-	-
Volume averaged electron temperature (keV)	-	-
Total plasma beta (%)	-	-
Electron density ($\times 10^{19} \text{ m}^{-3}$)	-	-
F-value for density limit	1.1	-
F-value for maximum wall load	-	-
Safety factor at 95 % flux surface	50	3.45
F-value for the net electrical power generated	-	-
F-value for beta limit	-	-
CS overall current density at EOF (MA m^{-2})	-	19
F-value for CS current at EOF	0.5	-
F-value for CS current at BOP	0.5	-
Ratio of CS overall current density at EOF & BOP	-	-
Non-inductive plasma current fraction	-	-
F-value for TF coil case stress	-	-
F-value for TF coil conduit stress	-	-
F-value for TF coil operating current	0.5	-
F-value for dump voltage	-	-
Max voltage across TF coil during quench (kV)	10	-
F-value for TF coil winding pack current density	-	-
Dump time for TF coil (s)	100	30
F-value for power through the separatrix	0.8	-
F-value for L-H power threshold	-	-
F-value for CS coil Tresca stress limit	-	-
F-value for radiation wall load limit	-	-
Fraction of steel in CS	-	-
F-value for max Zeff	-	-
Argon impurity f-value	-	-

Table 6.1: Iteration variables and bounds used when modelling reactors with training and upgrade coils. Note that there are no geometric engineering iteration variables: the modelled reactors' dimensions are limited by those of their corresponding baseline reactor. F-values are the allowable factor changes in values, e.g. an F-value of 1.2 would allow PROCESS to set a variable to 120 % of its predefined value. Note that this table does not cover input parameters (there are too many to list here), for a full list of all variables used see Appendix A.

6.3 Training Coils for REBCO Based Tokamak

In this section we present reactor calculations for approach (a): reactors are cost-optimised using REBCO CS and TF coils and training coils of either commercial or quaternary Nb-Ti are swapped-in for the REBCO magnets and re-optimised for maximum net electricity production in order to maximise their field yields. The capital costs of the reactors with training coils were calculated as the cost of the full-power reactor together with the cost of the training magnets alone. We have assumed that other plant components can simply operate with reduced capacity, so using training magnets would not incur any additional costs other than the cost of the magnets themselves (including installation).

Table 6.2 shows that for R_1BL , the use of commercial Nb-Ti TF and CS training magnets during the training phase (R_1T_3) reduces fusion power to ≈ 60 MW from 860 MW, and results in a electricity deficit of ≈ -180 MW. Despite the less energetic plasma and the lower peak fields on TF coils (70 %) and CS coil (66 %) that commercial Nb-Ti training magnets would generate, such coils would nevertheless allow rather thorough machine testing during the plant commissioning phase. Interestingly, quaternary Nb-Ti TF training magnets are almost able to match the field of the full-power REBCO TF coils (93 %) when REBCO is used for the CS coil (R_1T_2). These large percentages are because the high B_{c2} quaternary Nb-Ti coils are able to produce a large fraction of the stress limited cost-optimal field and provide a *prima facie* case for the fusion community to develop new high B_{c2} ductile low temperature superconductors specifically for fusion, but with J_c values that by the standards of other applications are (undemandingly) very low. At $H_{98} = 1.6$ (Table 6.3, R_3BL) the lower plasma current requirement (due to the higher intrinsic plasma quality) reduces the peak field on the REBCO CS coil, so commercial Nb-Ti CS coil produces 77 % of the CS coil peak field and the quaternary Nb-Ti coil produces 87 %.

Similarly due to the higher H-factor, the CS training coils also do not have to

produce as high a magnetic flux. The commercial Nb-Ti CS and PF system in R_3T_3 delivers only 105 Wb compared to the 261 Wb of R_1T_3 (note that the plasma current fractions of the respective baseline reactors are however approximately equal at 62 % at $H_{98} = 1.6$ for R_3BL and 66 % at $H_{98} = 1.2$ for R_1BL). Given the peak field on the CS remains 9.2 T in both cases and the number of turns falls by only 10 %, the lower flux requirement allows a larger proportion of the available CS-TF space to be occupied by the TF coils resulting in a 32 % larger TF conductor cross-section - allowing for the production of the larger toroidal field. The quaternary Nb-Ti case R_3T_4 is similar.

Reactor ID	TF s.c.	CS s.c.	TF (CS) peak field (T)	Field on plasma (T)	TF (CS) steel % (%)	TF (CS) peak stress (MPa)	Plasma current (MA)	$H_{98} = 1.2$		$H_{98} = 1.0$		
								Capital cost (1990 M\$)	Fusion power (MW)	Net. elec. (MW)	Fusion power (MW)	Net. elec. (MW)
R ₁ BL	REBCO*	REBCO*	12.5 (14.0)	5.4	52.8 (80.4)	660 (660)	13.6	4230	860	100	20	-190
R ₁ T ₁	Commer Nb-Ti	REBCO	8.7 (14.0)	3.7	38.5 (80.4)	390 (450)	9.5	4580	90	-170	30	-190
R ₁ T ₂	Quat. Nb-Ti	REBCO	11.6 (14.0)	5.0	47.1 (80.4)	600 (660)	12.6	4630	530	-20	30	-190
R ₁ T ₃	Commer Nb-Ti	Commer Nb-Ti	8.8 (9.2)	3.7	44.9 (42.0)	560 (620)	8.6	4540	60	-180	30	-190
R ₁ T ₄	Quat. Nb-Ti	Quat. Nb-Ti	11.0 (9.9)	4.7	47.1 (69.4)	660 (620)	11.0	4620	130	-150	40	-170

Table 6.2: Trained tokamaks designed for 100 MW net electricity and $H_{98} = 1.2$: Performance and cost data for the (preferred) tokamak optimised for REBCO toroidal field and central solenoid coils with minimised capital cost (*) and training magnets of different superconductors (with maximised net electricity yield). Also shown are the power values that would result, were a reduced $H_{98} = 1.0$ to occur in practice.

Reactor ID	TF s.c.	CS s.c.	TF (CS) peak field (T)	Field on plasma (T)	TF (CS) steel % (%)	TF (CS) peak stress (MPa)	Plasma current (MA)	$H_{98} = 1.2$			$H_{98} = 1.0$	
								Capital cost (1990 M\$)	Fusion power (MW)	Net. elec. (MW)	Fusion power (MW)	Net. elec. (MW)
R ₃ BL	REBCO*	REBCO*	12.6 (11.9)	5.2	52.0 (81.2)	660 (660)	10.9	3610	830	100	30	-190
R ₃ T ₁	Commer Nb-Ti	REBCO	9.1 (11.2)	3.7	41.3 (81.2)	410 (240)	7.4	3920	140	-150	20	-190
R ₃ T ₂	Quat. Nb-Ti	REBCO	11.8 (11.6)	5.0	48.5 (81.2)	590 (550)	9.2	3950	420	-50	30	-190
R ₃ T ₃	Commer Nb-Ti	Commer Nb-Ti	9.3 (9.2)	4.0	52.3 (34.1)	450 (550)	7.3	4060	180	-130	30	-180
R ₃ T ₄	Quat. Nb-Ti	Quat. Nb-Ti	11.9 (10.3)	5.1	48.9 (73.2)	650 (580)	9.4	4010	560	0	20	-190

Table 6.3: Trained tokamaks designed for 100 MW net electricity and $H_{98} = 1.6$: Performance and cost data for a tokamak optimised for REBCO toroidal field and central solenoid coils with minimised capital cost (*) and training magnets of different superconductors (with maximised net electricity yield). Also shown are the power values that would result, were a reduced $H_{98} = 1.0$ to occur in practice.

The effect of a range of different H_{98} -factors ($H_{98} = 1.2$ and $H_{98} = 1.6$) for the two REBCO 100 MW_e reactors R₁BL and R₃BL are shown in figure 6.1. For increases in H_{98} factor above design expectations the fusion power is not greatly increased. However, if the actual H_{98} factor achieved is below the design specification, the plasma loses energy faster than it is supplied, energy confinement is lost [269] and the plasma burn cannot be maintained for the required 2 hours. As a result the fusion power collapses, resulting in negative net electricity production. It is therefore critical that tokamak power plant designs are conservative with regard to H_{98} -factor and that they do meet plasma quality expectations, since the consequences of unexpectedly poor performance are quite severe.

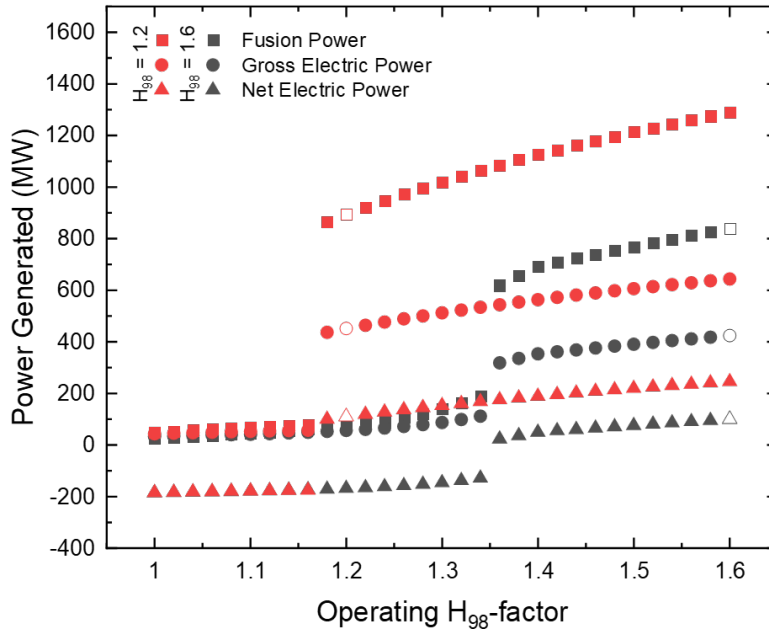


Figure 6.1: Fusion power, gross electric power and net electric power as a function of operating H_{98} -factor for the two reactors R₁BL and R₃BL with REBCO CS and TF coils and Nb-Ti PF coils. R₁BL and R₃BL were optimised for minimum capital cost (open data points) at H_{98} -factors of $H_{98} = 1.2$ (red) and $H_{98} = 1.6$ (black) and produce 100 MW_e. Reactor builds were fixed. Reactors at higher or lower than expected H_{98} -factors were optimised to produce maximum net electricity (solid data points). The discontinuities in fusion power that occur between high and low H_{98} factors are due to a loss of energy confinement at H_{98} factors that are too low.

Considering the 500 MW_e REBCO design R₅BL, the commercial Nb-Ti TF and CS training magnets of R₅T₃ are able to generate 78 % field on TF (Table 6.4). This larger percentage than in R₁T₃ is because the TF coils of R₅BL reactor have larger radii (11.1 m from leg centre to leg centre at the mid-plane compared to the 9.2 m of R₁BL) which reduces the optimal field on TF for the baseline design due to the larger stresses (equation 5.4.2). The larger plasma current requirement for the larger fusion power means that the poloidal field coils generate a larger proportion of the magnetic flux (it is more cost-beneficial to increase the output of the Nb-Ti poloidal field coils than it is to increase the size of the REBCO CS and overall reactor volume as a result). In R₅BL the PF system delivers 51 % of the total magnetic flux, compared to 43 % of the flux in R₁BL. The flux requirement when the commercial Nb-Ti training coils are used drops from 446 Wb to 321 Wb, so the (unchanged) PF system delivers 66 % of the flux, reducing the flux demand on the CS, and its necessary size, allowing for larger TF coil thickness. This larger thickness leads to a 24 % larger conductor cross section (in comparison to the R₁BL case) and the generation of an additional ≈ 0.5 T on-coil. Commensurately, a full quaternary Nb-Ti set of training coil in R₁T₄ can generate a TF coil field of nearly 97 % of that of REBCO with a field on coil of 11.5 T. All three baseline reactors in Tables (6.2 - 6.4), R₁BL, R₃BL and R₅BL, operate with TF and CS coil stresses of 660 MPa as this uses the minimum amount of steel and thereby results in the lowest capital cost. Taking the case of R₁BL, when only commercial Nb-Ti TF training coils are used (R₁T₁), operation close to the upper critical field demands a larger superconducting fraction and reduces TF coil steel fraction from 52.8 % to 38.5 %. Operation below the designed-for field reduces stress on the TF by 270 MPa and CS by 210 MPa. When both TF and CS training coils are used (R₁T₃) the steel fraction must also decrease (from 80.4 % to 42 %) in order to maximise the CS superconductor fraction and magnetic flux the coil can generate. The peak stresses rise closer to the 660 MPa limit as the mutual variation between the TF and CS coil thicknesses allows for better optimisation of the coil steel fractions.

Reactor ID	TF s.c.	CS s.c.	TF (CS) peak field (T)	Field on plasma (T)	TF (CS) steel %	TF (CS) peak stress (MPa)	Plasma current (MA)	$H_{98} = 1.2$			$H_{98} = 1.0$	
								Capital cost (1990 M\$)	Fusion power (MW)	Net. elec. (MW)	Fusion power (MW)	Net. elec. (MW)
R ₅ BL	REBCO*	REBCO*	11.9 (12.8)	4.2	51.9 (89.4)	660 (660)	25.3	5890	2120	500	1490	290
R ₅ T ₁	Commer Nb-Ti	REBCO	9.1 (11.9)	3.2	52.7 (89.4)	260 (360)	179.5	6340	440	-70	220	-150
R ₅ T ₂	Quat. Nb-Ti	REBCO	11.8 (12.6)	4.2	51.2 (89.4)	660 (660)	25.1	6460	2080	490	1490	290
R ₅ T ₃	Commer Nb-Ti	Commer Nb-Ti	9.3 (9.1)	3.3	43.2 (52.2)	590 (660)	19.8	6490	1060	150	620	-10
R ₅ T ₄	Quat. Nb-Ti	Quat. Nb-Ti	11.5 (11.0)	4.0	51.3 (72.8)	660 (660)	24.3	6500	1920	440	1250	210

Table 6.4: Trained tokamaks designed for 500 MW net electricity and $H_{98} = 1.2$: Performance and cost data for a tokamak optimised for REBCO toroidal field and central solenoid coils with minimised capital cost (*) and training magnets of different superconductors (with maximised net electricity yield). Also shown are the power values that would result, were a reduced $H_{98} = 1.0$ to occur in practice.

6.4 Upgrade Coils for Nb-Ti Based Tokamaks

In this section we present reactor calculations for approach (b): reactors are cost-optimised using commercial Nb-Ti CS and TF coils and upgrade coils of either quaternary Nb-Ti or REBCO are swapped-in for the commercial Nb-Ti magnets and re-optimised for maximum net electricity production in order to maximise their field yields. The capital costs were calculated as the cost of the respective baseline reactor combined with the cost of the new magnets and costs associated with increasing the scale of additional plant components (enhanced generator capacity, heat transport, fuel handling etc.). In all cases as noted above, we have not added cost associated with making the magnets remountable or the design and operational costs associated with robotic handling.

Table 6.5 shows that upgrading tokamaks is a significantly more expensive approach than the training approach (compare the 6470 M\$ of R₂U₂ in Table 6.5 compared to the 4540 M\$ R₁T₃ in Table 6.2). Although swapping the CS and TF coils for REBCO (R₂U₂), or the CS coil for REBCO and the TF coil for quaternary Nb-Ti (R₂U₄) produces more electricity (i.e. $\approx 280 \text{ MW}_e$) and swapping all coils for quaternary Nb-Ti (R₂U₃) yields more electricity (i.e. $\approx 230 \text{ MW}_e$), we feel these increases do not significantly better de-risk fusion energy production for commercialisation (and are only slightly statistically different from each other when considering PROCESS' model accuracy of 5 %).. In the former case, the CS and TF coils are stress limited, so although in principle the REBCO upgrade coils could produce higher fields on the plasma and in the CS coil, they are prevented from doing so by the thickness of the steel support required to resist the greater magnetic forces in the limited space available. In the latter case, the limiting factor is the critical current density of the quaternary Nb-Ti cable in the CS coil. Just swapping the centre solenoid alone for REBCO, while keeping the original commercial Nb-Ti TF coils (R₂U₁) offers no benefit, as the TF coils in the baseline design are already B_{c2} limited. The H₉₈ = 1.6 commercial Nb-Ti case R₄BL, shown in table 6.6, is

very similar to the $H_{98} = 1.2$ case. The larger fields produced by the upgraded magnets are due to the higher H_{98} -factor which leads to a smaller major radius, and the stresses on the TF coils are consequently lower for a given field-on-coil.

Reactor ID	TF s.c.	CS s.c.	TF (CS) peak field (T)	Field on plasma (T)	TF (CS) steel % (%)	TF (CS) peak stress (MPa)	Plasma current (MA)	$H_{98} = 1.2$		$H_{98} = 1.0$		
								Capital cost (1990 M\$)	Fusion power (MW)	Net. elec. (MW)	Fusion power (MW)	Net. elec. (MW)
R ₂ BL	Commer.* Nb-Ti	Commer.* Nb-Ti	9.2 (8.1)	3.4	45.2 (63.9)	660 (660)	18.9	5200	900	100	60	-200
R ₂ U ₁	Commer. Nb-Ti	REBCO	9.2 (9.1)	3.4	45.2 (79.0)	660 (660)	19.3	5280	900	100	60	-200
R ₂ U ₂	REBCO	REBCO	10.1 (13.2)	3.7	47.5 (91.5)	660 (660)	20.8	6470	1410	280	920	100
R ₂ U ₃	Quat. Nb-Ti	Quat. Nb-Ti	9.7 (10.3)	3.6	46.8 (79.2)	660 (660)	20.0	6150	1250	230	630	-40
R ₂ U ₄	Quat. Nb-Ti	REBCO	10.1 (13.0)	3.7	47.5 (91.6)	660 (660)	20.8	6350	1400	280	900	100

Table 6.5: Upgraded tokamaks designed for 100 MW net electricity and $H_{98} = 1.2$: Performance and cost data for a tokamak optimised for Nb-Ti toroidal field and central solenoid coils with minimised capital cost (*) and upgraded magnets of different superconductors (with maximised net electricity yield). Also shown are the power values that would result, were a reduced $H_{98} = 1.0$ to occur in practice.

Reactor ID	TF s.c.	CS s.c.	TF (CS) peak field (T)	Field on plasma (T)	TF (CS) steel %	TF (CS) peak stress (MPa)	Plasma current (MA)	$H_{98} = 1.2$		$H_{98} = 1.0$		
								Capital cost (1990 M\$)	Fusion power (MW)	Net. elec. (MW)	Fusion power (MW)	Net. elec. (MW)
R ₄ BL	Commer.* Nb-Ti	Commer.* Nb-Ti	9.0 (7.3)	3.0	45.5 (58.8)	660 (660)	15.9	4470	870	100	20	-200
R ₄ U ₁	Commer. Nb-Ti	REBCO	9.0 (7.2)	3.0	45.5 (69.5)	660 (660)	15.9	4530	870	100	20	-200
R ₄ U ₂	REBCO	REBCO	10.2 (14.4)	3.3	46.7 (90.8)	660 (660)	18.1	5280	1190	210	30	-200
R ₄ U ₃	Quat. Nb-Ti	Quat. Nb-Ti	9.7 (10.9)	3.2	45.8 (71.0)	660 (660)	17.3	5180	1070	170	30	-200
R ₄ U ₄	Quat. Nb-Ti	REBCO	10.2 (14.2)	3.4	46.7 (90.7)	660 (660)	18.1	4890	1200	210	30	-200

Table 6.6: Upgraded tokamaks designed for 100 MW net electricity and $H_{98} = 1.6$: Performance and cost data for a tokamak optimised for Nb-Ti toroidal field and central solenoid coils with minimised capital cost (*) and upgraded magnets of different superconductors (with maximised net electricity yield). Also shown are the power values that would result, were a reduced $H_{98} = 1.0$ to occur in practice.

For the larger 500 MW_e tokamak (R₆BL, Table 6.7), upgrading the reactor with a REBCO CS coil and either REBCO (R₆U₂) or quaternary Nb-Ti (R₂U₄) TF coils results in an increase in net electricity output of $\approx 36\%$. The smaller percentage increase in this larger machine is due to the more stringent stress limits in the larger radius coils. Indeed, a fully quaternary Nb-Ti upgraded reactor (R₂U₃) would only generate 8 % more electricity as the current in the CS coil is limited by the critical current density of the conductor.

The cost-optimised upgraded tokamaks again operate with 660 MPa stresses on the TF and CS coils in order to minimise the amount of steel support used. Focusing on R₂BL, when REBCO TF and CS coils are used (R₂U₂), the peak fields on coil increase by 9 % and 63 %, the current densities increase by 1 % and 14 % and the coil radii decrease by 0 % and by 6 % respectively. The resulting change in stress (equation 5.4.2) necessitates increases in the TF and CS coil steel fractions by 2.3 % and 27.6 %. The same is true of quaternary Nb-Ti upgrade coils in R₂U₃, though the increases in steel fractions are more modest due to the lower increases in field.

Reactor ID	TF s.c.	CS s.c.	TF (CS) peak field (T)	Field on plasma (T)	TF (CS) steel %	TF (CS) peak stress (MPa)	Plasma current (MA)	$H_{98} = 1.2$		$H_{98} = 1.0$		
								Capital cost (1990 M\$)	Fusion power (MW)	Net. elec. (MW)	Fusion power (MW)	Net. elec. (MW)
R ₆ BL	Commer.* Nb-Ti	Commer.* Nb-Ti	9.2 (8.7)	3.4	48.3 (81.6)	660 (660)	29.4	7730	2180	500	1500	270
R ₆ U ₁	Commer. Nb-Ti	REBCO	9.2 (9.3)	3.4	48.3 (93.4)	660 (660)	29.6	7910	2220	510	1570	290
R ₆ U ₂	REBCO	REBCO	10.0 (11.9)	3.6	48.8 (92.2)	660 (660)	32.2	9790	2730	680	1730	340
R ₆ U ₃	Quat. Nb-Ti	Quat. Nb-Ti	9.4 (9.1)	3.4	47.8 (83.3)	660 (660)	30.1	9180	2290	540	1560	290
R ₁ U ₄	Quat. Nb-Ti	REBCO	10.0 (9.4)	3.6	48.8 (92.2)	660 (660)	32.2	9600	2730	670	1730	340

Table 6.7: Upgraded tokamaks designed for 500 MW net electricity and $H_{98} = 1.2$: Performance and cost data for a tokamak optimised for Nb-Ti toroidal field and central solenoid coils with minimised capital cost (*) and upgraded magnets of different superconductors (with maximised net electricity yield). Also shown are the power values that would result, were a reduced $H_{98} = 1.0$ to occur in practice.

6.5 An Optimised Mid-21st Century Power Plant

The scientific evidence for global warming [1] and the damage it is causing is now sufficiently clear [270, 271] that there is a global commitment to zero carbon [272]. For example, the UK Government has banned the sale of new cars powered solely by petrol or diesel from 2030 [273] and a legally binding commitment to “at least” zero carbon by 2050 [274]. Cheap intermittent solar and wind resources are the natural place to start. However the decarbonisation commitments to replace the carbon fuels used both in power stations and in transportation in the UK, will require several orders of magnitude more green electricity than is currently planned for. Unfortunately, unlike other renewable energy sources, although a relatively small power plant can de-risk the holistic integration and operation of the key-technologies for commercial fusion, cost of electricity will eventually drive commercial fusion power plants to be large [142]. To what degree fusion power will be used to provide base-load electricity directly [275], rather than produce synthetic fuel [276] for say aviation , or conversion of carbon dioxide back into carbon black [277]) is an open question that will depend on the particular commercial realities of global warming when commercial fusion energy arrives - whether for example we will need it to reverse global warming.

Fusion energy is clearly a huge-risk huge-return investment that only a relatively small group of wealthy Governments [75, 15, 278, 10] or philanthropic billionaires [279] can lead. Much more work is needed to bring the scientists, policy makers, investors, defence interests, and public together to de-risk fusion power and make it commercial as quickly as possible. Even the excellent texts that deal with the science of renewable energy [280] or the economic opportunity (or green premium) it presents [281], hardly mention fusion at all. Fusion technology is quite different from other renewable technologies in that the scale of investment required to make meaningful commercial advances is much larger. Of course there have been huge projects in the past including, putting the first man on the moon [282] or the devel-

opment of fission power. Those projects had straightforward aims and well-defined competitive environments, but crucially, did not have to broadly operate in the free-market. Commercialising fusion is far more complex. The green revolution and changes that have followed were not driven by the free-market, but by an unprecedented alignment of public social awareness and enlightened policy. However in order for the commercialisation of fusion energy to be a success, it must roll-out across the developed world on a huge scale. It therefore needs the resources and skills of the markets with commensurate and proper financial returns for investors.

The approach for designing, financing and building the last fusion tokamak before commercialisation requires very careful planning. There are precedents for Governments simply outsourcing everything, and it leads to poor management [283]. Managing the process to commercialise fusion energy will require an approach that is more than that of just an ‘intelligent business’ that knows what it needs. Experience suggests that an ‘intelligent customer’ will be needed that includes an extremely capable in-house capability, that can manage procurement, understand opportunities and potential innovation on the horizon, as well as integrate the programme into (changing) overall policies and structures [284]. Of course the scientific challenges addressed in this thesis and required to develop commercial fusion are huge. But perhaps as challenging is developing an in-house management environment to roll-out fusion that attracts the required calibre of personnel with the relevant scientific, financial and administrative skills, and that provides a clear career development path for early career staff while retaining and developing its in-house expertise over a very protracted capital-rich period of investment [283].

It is in this context that in this work we focus on our ‘preferred choice’ 100 MW_e REBCO TF,CS and Nb-Ti PF tokamak R₁BL with a fusion gain $Q_{\text{fus}} = 17$, a net gain $Q_{\text{net}} = 1.3$. In a competitive commercial environment, the best machine must be sufficiently close to market to de-risk all the key technologies, provide a working prototype and a cost for producing fusion energy that the markets could rely on. Breakdowns of the power balance and direct capital cost for R₁BL are shown in

figure 5.7. The magnets are a single-point of failure for the entire project so we have mitigated damage to the brittle and expensive magnets by recommending the use of Nb-Ti training coils for the preferred choice reactor in R₁T₃. Such training coils would increase overall preferred reactor capital cost by only < 10%, and would allow for the thorough testing of the reactor (at 70 % field on TF coil 66 % field on CS coil) - reducing the risk of damage to the full-power REBCO magnets. These considerations hold for machines both with higher H₉₈ = 1.6 and for the 500 MW_e scale. The cost of electricity is expensive from R₁BL at 550 \$ MW⁻¹ h⁻¹, compared to 50-100 \$ MW⁻¹ h⁻¹ for fossil fuels or solar/wind (converted into 1990 US \$ [285]). However, the primary aim of this thesis is to minimise the capital cost of de-risking commercial fusion technology, not produce cheap electricity. The 500 MW_e machine produces electricity at a lower cost of 290 \$ MW⁻¹ h⁻¹, a fusion gain $Q_{\text{fus}} = 41$, a net gain $Q_{\text{net}} = 1.9$, demonstrating the benefits of large scale plants [142].

One can ask whether the Nb-Ti training coils would be sufficient to meet our aims were the HTS magnets not to perform to specification. Reviewing tables 5.1 and 6.2 shows the field on the plasma axis would be 3.7 T, close to the ≈ 3.5 T field of JET and substantially larger than the 2.25 T of JT60-SA. The plasma current would be much larger than existing tokamaks' at 8.6 MA and almost identical to the 8.7MA proposed for SPARC. It would also reach a plasma pulse length of 7200 seconds – orders of magnitude longer than those achieved in existing tokamak reactors. Although its $Q_{\text{fus}} = 1.2$ is low, it would have a fusion power gain between those of JET or ITER. It is clear that the primary aims of the power plant are to de-risk a holistic demonstration of all the relevant fusion technologies, and show what is possible commercially and technologically. In this context, the exciting very high field values for the ARC and SPARC tokamaks (noted in Table 5.1) remind us that we have focused on derisking a cost-optimised plant closest to a commercial power plant. Alternatively one can focus more on what is possible by increasing the maximum field (and improving the safety margins) and cost of the power plant.

We suggest that discussion of the relative merits of these two approaches would need consideration of the possible potential developments in fusion-focused high B_{c2} alloys, as well as whether or not large fusion power plants are inevitably the commercial endgame.

6.6 Conclusions

In this chapter, motivated by the 4 year downtime should an ITER TF coil require replacement, we argued that remountable superconducting coils will be a necessary component of commercial tokamaks in order to realise the high availability required of a power plant. Expanding from this axiom, we have investigated the utility of “training coils”: TF and CS coils made from ductile Nb-Ti that are used prior to full-power, higher field brittle REBCO magnets in a reactor. Primarily these coils would be used in the commissioning phase of a reactor’s lifetime, when disruptions that could damage brittle magnets are more likely due to manufacturing flaws, design errors or simply operator inexperience. The training coils could however also be used as testing coils for new equipment or regimes or indeed as a final step in the eventual reactor assembly line.

At first glance, it is not obvious whether cost-minimising a REBCO reactor and using training coils within its architecture is cheaper than cost-minimising a Nb-Ti reactor and using upgrade coils within its architecture - so we have investigated both avenues. Primarily we are interested in investigating pilot power plants, so have focused on training coils the preferred reactor from the previous chapter R_1BL : an $H_{98} = 1.2$, 100 MW_e reactor with REBCO CS, TF and Nb-Ti PF coils. For the second avenue we have investigated upgrading the $H_{98} = 1.2$, 100 MW_e reactor R_2BL with Nb-Ti CS, TF and PF coils, also from the previous chapter. In order to more generally assess the utility of training and upgrade coils, we also considered REBCO and Nb-Ti based reactors with $H_{98} = 1.6$ (R_3BL and R_4BL) and those that produce 500 MW_e (R_5BL and R_6BL). We also considered the use of quaternary

Nb-Ti for both training and upgrade coils.

The addition of Nb-Ti training coils for commissioning the preferred reactor increases costs by $< 10\%$ and would allow for thorough reactor testing (generating 70 % field on TF, 66 % field on CS of the preferred reactor). These conclusions hold at the $H_{98} = 1.6$ and 500 MW_e scales. Of the two avenues, cost-minimising a REBCO reactor first and using Nb-Ti training coils is the lower overall cost route. For example, a 500 MW_e REBCO reactor (including the cost of its training coils) costs 6490 M\$, very close to the 6470 M\$ of a 100 MW_e Nb-Ti reactor that's been upgraded with REBCO coils, though the latter is only able to produce 280 MW_e .

In light of this we refocus on our preferred reactor design R_1BL - this is indeed the cost optimal reactor and Nb-Ti training magnets are an attractive technology that would enable thorough reactor testing before full-power operation, significantly reducing risk to the REBCO magnets - and all for a modest increase in overall capital cost of under 10 %. The REBCO preferred reactor design is cheaper and has a more robust power balance than a tokamak with resistive magnets, or indeed any other tokamak with superconducting magnets and is the pilot plant that we recommend companies and countries should strive to build. It fully demonstrates all necessary technologies for a full scale power plant [15]: large scale superconducting magnets, net electricity production of 100 MW, 2 hour burn time, tritium self sufficiency and high availability for the lowest capital cost. And, with training Nb-Ti training coils (R_1T_3), is low-risk.

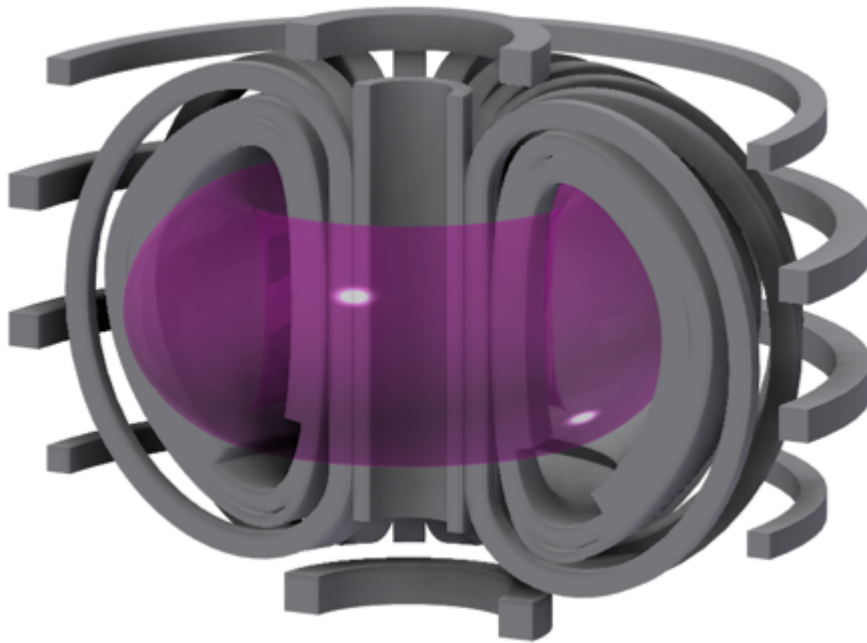


Figure 6.2: Artistic CAD model of the preferred reactor design R₁BL.

Accounting for Future Advances in Magnet Technology

7.1 Introduction

Superconducting fusion magnet technology is a rapidly evolving field. In chapter 5 we investigated whether there would be any key technologies that could be removed from our preferred reactor R₁BL to reduce its cost whilst remaining in keeping with all the requirements of a tokamak pilot power plant (and came to the conclusion that there were not). In this chapter we seek to expand on this analysis, and consider to what extent possible advances in fusion superconducting magnet technology would affect the design and capital cost of R₁BL.

We focus on two areas of advancement in particular: the development of novel magnet structural support architectural design (as in ARC [9]) and further decreases in REBCO cost below 30 \$/kA m [140]. In doing this we seek to determine whether these technological advances are ‘low-lying fruit’ that enable substantial cost reductions to the R₁BL reactor design in the future, beyond the 2030-2040 timescales considered so far. We also briefly discuss the utility of producing fusion specific high B_{c2} ductile alloys as well as the areas of development that should be prioritised for fusion specific REBCO tapes.

7.2 Novel Support Architectures and Strengthened Steels

In practice the highest of the shear stresses (as used for the Tresca yield criterion) cannot justifiably be increased much beyond 660 MPa (2/3 yield strength of 316LN steel [189]), though external support structures such as those proposed for the ARC reactor [9], would reduce the stress at the TF coil for a given field. For example the ARC support rings at the top and bottom of the TF coils would resist both toroidal and vertical forces, leading to an increased cost-optimal field. This has been accounted for in figure 7.1, where data is included for inflated costs of complete structural steel components; representative of increased cost of enhanced steels or increased volumes of steel used in advanced support architectures. Relaxing the TF and CS coils' stress limit to 1000 MPa in R₁BL increases the cost-optimal field on coil to 14.4 T ($B_T = 6.3$ T) and reduces R_{major} to 6.36 m (6 % reduction) and the capital cost to 3920 M\$ (7 % reduction), assuming steel costs do not change. With larger allowed stresses the field increases further, plateauing by ≈ 2000 MPa (due to the $P_{\text{sep}}/R_{\text{major}} = 20$ MW/m⁻¹ limit) with a field on coil of 16.8 T ($B_T = 7.7$ T), R_{major} of 5.99 m (11 % reduction) and capital cost of 3690 M\$ (13 % reduction). These results are in line with our findings in the previous chapters that the cost-optimal field produced by REBCO magnets is limited by the yield stress of steel support structure rather than by the critical current density of the superconductor: increasing the effective yield stress increases the cost-optimal field on coil. What however is perhaps surprising is how little an effect this has on the resulting capital cost of the reactor, even with a stress limit of 2000 MPa the capital cost only falls by 13 % with respect to R₁BL.

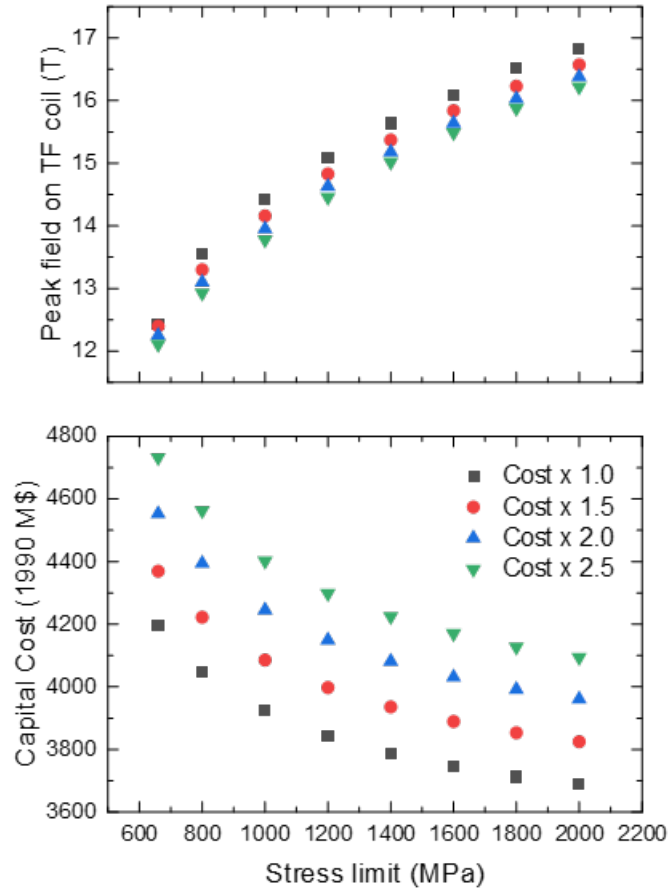


Figure 7.1: (a) Change in cost-optimal field on coil and (b) capital cost of a $H_{98} = 1.2$, 100 MW net electricity tokamak with REBCO toroidal field and central solenoid coils as a function of the allowable maximum of the shear stresses (as used for the Tresca yield criterion) on the central solenoid and inboard toroidal field coil mid-planes. Different data sets correspond to different costs of steel components (standard, $1.5 \times$ standard etc.), representative of either more expensive steels or larger steel volumes. Cost model uncertainties are $\approx 5\%$ for all data.

7.3 Reduced REBCO Cost

Fusion power plants represent a multi-billion-dollar market for high temperature superconductors - nevertheless supply must rise to meet demand. Precedent for rapid growth in superconductor manufacturing capacity exists however in ITER [126]. Requiring ≈ 600 tons Nb_3Sn strands [233], ITER's demand transformed annual global production from < 2 ton/year in the early 1990s to 100 tons/year today [286]. REBCO tapes have seen a substantial decrease in production cost in the two decades [141] and it is likely that they will continue to see a price reduction as global demand increases. Maintaining our preferred reactor design choices, the REBCO cost was reduced from 30 $\$/\text{kA m}$ (6 T, 4.2 K) to 0.025 $\$/\text{kA m}$ (6 T, 4.2 K) (note that doubling superconductor J_c has the same effect as halving cost in $\$/\text{kA m}$, see equation 4.6.10) resulting in a capital cost minimised reactor with an increased toroidal field of 12.7 T and a capital cost of 4000 M\$. It is noteworthy that this increase in cost-optimal field and reduction in capital cost from the 30 $\$/\text{kA m}$ case is less than that obtained by relaxing the steel stress limits even to 1000 MPa. R₁BL's REBCO magnets are limited by the yield stress of the steel casing - as we saw in chapter 5. A reduced REBCO cost therefore only reduces the capital cost of the TF coils - it does not increase the cost-optimal field and decrease reactor volume (as it would, if the magnets were J_c limited or B_{c2} limited). Figure 7.2 shows that a reduction in REBCO cost beyond those presented in [141] would therefore not offer much benefit for reactor cost-reduction purposes as the cable cost is dominated by non-superconducting components.

7.4 A Dreamer's Tokamak

Paymasters inevitably ask whether there may be any developments in the future that are likely to substantially reduce costs. To answer this for magnetic technology which is the primary driver for the tokamak size and hence cost, the maximum

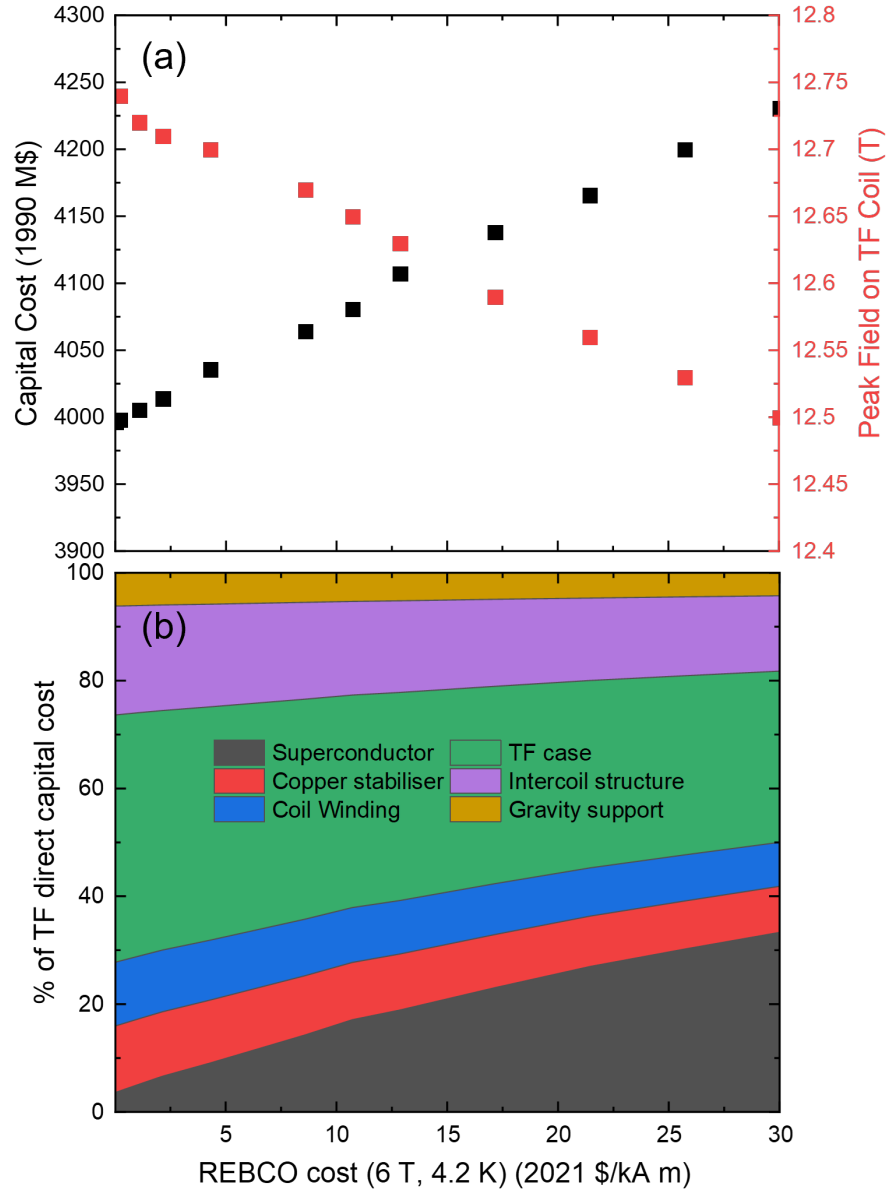


Figure 7.2: (a) Change in cost-optimal field on coil and capital cost of a $H_{98} = 1.2$, 100 MW net electricity tokamak with REBCO toroidal field and central solenoid coils as a function of REBCO cost in 1990 US \$. (b) The direct costs of REBCO, cable copper stabiliser, coil winding, TF casing, intercoil structure and gravity support as a fraction of the total TF costs. The two panels' have the same x axis . All costs are inclusive of (commercial) material and construction costs and have an error of $\pm 5\%$.

yield stresses on the TF and CS coils was set unrealistically high to 1000 MPa, the REBCO cost unrealistically low to 0.025 \$/kA m, the H-factor set to $H_{98} = 1.8$ and the limit on the power through the separatrix was increased to $P_{\text{sep}}/R = 25$ MW. All other constraints from R₁BL were retained. Under these conditions, the optimised reactor has a field on plasma of 5.7 T, field on TF coil of 14.0 T, peak field on CS coil of 12.4 T, plasma current of 9.7 MA, major radius of 5.37 m, aspect ratio of 3.36 and a capital cost of 3400 M\$. This leads to a cost only 19.5 % lower than R₁BL.

7.5 Comments on Fusion-Specific REBCO tapes and Nb-Ti strands

REBCO cables have been, and are being designed and optimised explicitly for high-field tokamak applications (e.g. CORC [64], slotted core cables [66, 65] and twisted-stack cables [67, 68]). The superconducting strands and tapes used in these cables however, are not explicitly optimised for the coming generation of tokamaks. A primary aim of the REBCO industry is to develop higher J_c tapes (at reduced cost), though as we have seen in sections 5.4 and 7.2, the limiting factor on the REBCO winding pack current density is not the critical current density of the superconductor, it is the yield stress of the magnet support structure. Indeed, the critical current density of the REBCO tapes is two orders of magnitude larger than current density of the winding pack. This begs the question, are high J_c REBCO tapes truly necessary for tokamak magnets? It would be more prudent to use lower cost, lower J_c tapes (that are already available) and to focus more on other important issues such as quench mitigation and brittle fracture prevention at the tape level, rather than seek to increase critical current density ever further: using higher J_c tapes would serve no substantial cost reductive purpose so long as the critical current density remains stress-limited.

The Nb47%wt.Ti alloy used in ITER, on the other hand, was developed for the

MRI/accelerator market to maximise J_c between 4-6 T. These designed-for conditions do not mirror those of the coming generation of tokamaks. For Nb-Ti, the limiting factor on the cost-optimal field of Nb-Ti TF and CS coils and on the field produced by Nb-Ti training and upgrade coils is the superconductor B_{c2} . Nb-Ti has unfortunately been left at the wayside in favour of Nb₃Sn and REBCO for the higher-field TF and CS magnets for the coming generation of tokamaks. It is certainly true that a reactor with commercial Nb-Ti TF and CS coils would be more expensive than a reactor built to the same net electricity specification using REBCO or Nb₃Sn (see chapter 5.4). As we have shown in section 5.4 however, a higher B_{c2} quaternary alloy would compete favourably with Nb₃Sn magnets in terms of cost whilst having the benefit of being ductile. Additionally, our model quaternary Nb-Ti training magnets would produce a 10 - 20 % larger field fraction (of corresponding REBCO based full-power magnets) than conventional Nb-Ti in all cases investigated - an increase driven solely by the alloy's larger upper critical field. It is the author's opinion that we should give the workhorse of the superconducting world its dues and seek to develop a fusion specific alloy, rather than contenting ourselves that commercially available Nb-Ti would not be a wise choice with which to design a tokamak magnet system - despite the fact that the alloy was never designed with tokamak operating fields in mind.

7.6 Discussion & Conclusions

The calculated cost reductions as a result of foreseeable advancements in superconducting magnet technology are relatively small. Reductions in REBCO costs below the 30 \$/kA m (6 T, 4.2 K) stipulated in [141] do not significantly reduce the overall cost-optimised reactor cost. A drop in price to the negligible cost of 0.025 \$/kA m (6 T, 4.2 K) only reduces the overall reactor capital cost by ≈ 5.5 %. This is what we would expect: we know from previous chapters that the cost-optimal field is limited by the yield stress of steel, increases in the field actually increase

the overall reactor capital cost. Therefore reductions in REBCO cost only serve to decrease the cost of the TF coils, even then the benefits are limited. REBCO at 30 \$/kA m (6 T, 4.2 K) makes up approximately 30 % of the total TF coil capital cost, so the TF coil costs cannot fall below 70 % of the costs of those of R₁BL.

Increases in the steel yield stress limit (here used as a proxy for advanced magnet support structures) do have a more significant impact on capital cost, though it too is not substantial. Increasing the stress limit to 1000 MPa increases the cost-optimal field by 15 % and reduces the plasma major radius by 6 %, reducing capital cost by 7 % overall. By 2000 MPa the cost reduction plateaus at about 15 % - limited by the $P_{\text{sep}}/R = 20$ MW limit.

It is only once we combine these advancements with more liberal plasma physics assumptions of $H_{98} = 1.8$ and power through the separatrix of $P_{\text{sep}}/R = 25$ MW that the capital cost falls by as little as 19.5 %. This is less than the cost reduction achieved than by reducing the tritium breeding ratio to 0.9 (see section 5.7). The relatively low cost reduction lends strength to the idea that we as a community and civilisation should aim to build a tokamak pilot power plant on the timescale of 2030-2040, rather than wait for for a “silver-bullet” magnet technology to drastically reduce reactor capital cost. Indeed in this chapter we have shown that no obvious silver bullet exists. We recommend our preferred reactor R₁BL described in the previous chapters for this role.

Concluding Remarks & Future Work

8.1 Concluding Remarks

Pilot fusion reactors aim to reliably and consistently produce net electricity of at least 100 MW_e with plasma burn times of at least 2 hours [15], as well as demonstrate a commercial viability that proves fusion is a practicable option for large scale decarbonisation of global electricity production. To this end, in this thesis we have used the PROCESS systems code to minimise the capital cost of superconducting tokamak pilot plants using best-in-class technologies available on the time scales of 2030-2040. Should the cost of REBCO continue to fall and reach the expected 30 \$/kA m (6 T, 4.2 K) [141], our preferred reactor R₁BL which uses REBCO CS and TF coils and Nb-Ti PF coils has a lower capital cost than a reactor with Nb₃Sn CS and TF coils, or an entirely Nb-Ti reactor. This reactor has $R_{\text{major}} = 6.75$ m, $A = 3.15$, $P_{\text{fusion}} = 870$ MW, $Q_{\text{fusion}} = 17$, $B_T = 5.4$ T and $B_{\text{t,coil}}^{\text{max}} = 12.5$ T and total capital cost of 4230 M\$ (US 1990 \$). We find the cost-optimal winding pack current density and field on coil is limited by the yield stress of the steel support structure and not the critical current density of the REBCO superconductor.

In order to achieve the necessarily high availability of a base-load power plant, motivated by the 4 year downtime should an ITER TF coil fail we argue that commercial tokamaks must have remountable magnets, and hence pilot reactors must also demonstrate them. Remountability offers the possibility of easily swapping superconductors at different stages during a reactor lifetime. Here we have focused on using robust Nb-Ti training coils during plant commissioning in order to protect the brittle REBCO magnets from powerful disruptions as a result of operator inexperience, manufacturing errors etc. The full power magnets would then be mounted for full-power operation. The addition of Nb-Ti training coils (R_1T_3) for reactor commissioning increases the capital cost of R_1BL by $< 10\%$ and would allow for thorough reactor testing (generating 70 % field on TF, 66 % field on CS of R_1BL). Additionally, higher B_{c2} alloys would be superior to commercial Nb-Ti for fusion magnets [229, 230].

We conclude: the cost of building the human resources, engineering processes, supply chains, and capital-intensive last-before commercialisation power plant will not change significantly over the next few decades against inflation - no ‘silver-bullet’ magnet technology exists that will make fusion significantly cheaper. The very broad design for a superconducting tokamak is provided here in sufficient detail using *PROCESS* to address the challenge of holistically building a state-of-the-art tokamak which includes all the key technologies; the imperatives of net zero carbon require huge base-load electricity globally [287]. This power requirement has an obvious solution using nuclear power.

Finally we investigated how advances REBCO magnet technology such as reduced REBCO cost and the use of advanced support structures (proxied with higher yield strength steels) would affect the preferred reactor design. We concluded that advances in these areas would only decrease the reactor capital cost by only 19.5 % and are therefore not worth waiting for. As a civilisation we should commence building tokamak power plants with existing technologies today. The cost of delaying is far greater than the rewards of waiting.

8.2 Future Work

A timely path for future work would be to repeat the study for spherical tokamak pilot plants. The question of whether spherical or conventional aspect ratio tokamaks are superior for pilot or power plants is by no means decided within the fusion community and there are clear advantages and disadvantages for reducing the reactor aspect ratio below 2.0 (see section 5.5). Regardless, spherical tokamaks are devices of interest, and optimising their designs for minimum capital cost (and maximum commercial success) is a worthwhile endeavour. In principle repeating the calculations presented in this work for spherical tokamaks (including an investigation of the utility of training coils) would be a relatively straight forward task for a competent PROCESS systems modeller with good experience of superconducting fusion magnets. The superconducting magnet module has recently been made compatible with the spherical tokamak module for the UK STEP project, so there would likely be only limited necessary source code development. The major difficulty is likely to be in generating a first-of-a-kind input file that reaches convergence. Example input files exist for superconducting conventional aspect ratio reactors (e.g. EU-DEMO), and resistive magnet spherical tokamaks (e.g. FNSF) but not for a spherical tokamak with superconducting magnets; there is not a clear and firm foundation to work from (outside of the input files used for STEP - which are not publicly accessible).

Regarding the ARC reactor resign [9], the magnet support structure is somewhat different from the wedged TF coil structure used in ITER or the bucked and wedged TF and CS structures used in this work. The TF coils are half-Phi (Φ) shaped, are not only bucked and wedged, but the CS coil has a solid plug through its bore, and the top and bottom limbs of the TF coils are supported by large, thick rings. The result is that for a given field on coil, the stress on the inboard of the TF legs are reduced (in comparison to ITER or our preferred reactor designs), so the thickness of the TF coil casing is reduced - allowing for the production of higher

fields before the cost-optimal field becomes stress-limited. We have proxied the effects of such support structures to the best of our ability within `PROCESS` by simulating fictitiously strong steels (chapter 7) which would have broadly the same effect of reducing the necessary TF casing thickness. A superior approach would be to explicitly model the support structure of the ARC reactor in a general tokamak. The costs could then be calculated directly without the need for a range as given in figure 7.1.

Additionally, all of the magnets we have modelled using the `PROCESS` code have been mono-material and ungraded. That is to say that the cable in a given winding pack is of a single superconducting material, and every cable is of the same dimension, with the same conduit thickness, regardless of position within the winding pack, the local field and local forces. For the reasons discussed in section 5.4.9 this is not the cost-optimal coil design: The cable critical current densities in the lower-field coil regions are greater than necessary and the conduit steel thickness is larger in the lower-force regions than necessary. Using graded coils would allow for further cost optimisation in both the reactor CS and TF coils.

The inclusion of graded coils would allow for the optimisation of the superconducting magnets in three primary ways: (1) The conduit steel thicknesses in the radial and toroidal directions could vary as a function of the local force field in the winding pack (e.g. make use of thinner cable conduits on the lower-field, out-board side of the winding pack, and thicker conduits on the inboard side). (2) The superconductor fraction could vary in order to maintain a constant critical current density under the changing field in the winding pack. (3) Different superconductors could be used in different field conditions (e.g. Nb-Ti could be used in the lower field regions, reducing the material cost of the coils - a common practice in smaller superconducting magnet systems).

Such a model must be at least 2 dimensional in the horizontal plane in order to accurately capture the field, stress and current profile within a real-world TF coil winding pack. Without these data, neither grading of the superconductor nor

grading the conduit casing thickness would be accurate. Such a 2D model would tie in well with an existing EUROfusion needs; which currently lacks a widely accessible and holistic 2D TF coil modelling tool. 1D, low resolution TF coil and winding pack models are produced by `PROCESS` and are verified after every confirmed run in 3D with `ANSYS`. This presents a significant bottleneck in the magnet design process. Each `PROCESS` output must be validated by a new hand-created 3D `ANSYS` model, only allowing for limited and slow iteration between `PROCESS` outputs and DEMO baselines. This 2D code would then be validated against `ANSYS` at conception, rather than after every code run. The model would also compliment the `BLUEPRINT` code [105] which already provides a 2 dimensional reactor build and TF coil shape optimisation.

The first step for the model would be to take user input or `PROCESS` generated coil and winding pack geometries and currents and (using `BLUEPRINT`) produce a 2D field and stress profile within the winding pack at the inboard mid-plane of a TF coil (taking into account both bursting and toppling forces). To model coil grading, the winding pack could then be segmented into a number of layers, and the superconducting and steel fractions of the cables within each layer would be optimised to yield (as close as possible) a uniform critical current density and stress for cables between layers. Users should have the power to choose superconductors for each layer, though the model should have default options for different operating conditions. The model should also have the capability to optimise the number of layers and superconductors of each layer to minimise the overall cost of the TF coil, coil size, coil field, etc. Naturally, this updated winding pack and graded coil model could and should be used when optimising spherical tokamak reactor designs as well.

This work would benefit greatly from collaboration with world-renowned fusion magnet labs that have produced designs of graded superconducting magnets for future fusion reactors. The Durham University superconductivity group already has strong ties with the EPFL superconductivity group [223, 237, 238] and Po-

litenico di Torino/ENEA [236] who have designed graded coils CS and TF coils respectively for EU-DEMO. Approaching them for a collaborative project would be a prudent first port of call.

It would also be beneficial to include an explicit remountable coil model in `PROCESS` and `BLUEPRINT`. All superconducting coils currently modelled in both codes are fixed, though for reasons given in section 6.2 it is almost certain that both commercial and pilot tokamak power plants must be built with remountable magnets. The `PROCESS` model would have to be fully integrated with the reactor build, electromagnetic, cryogenic, stress and cost models and the joints must be fully compatible with the winding pack architecture. The model should include the option to choose between proposed remountable joint options such as those proposed by MIT [264, 9] or Tohoku university [263]. New joint designs should be added as and when they are published in order to maintain a state-of-the-art model - collaboration with designers would be a prudent course of action. Remountable joints effectively split the TF coils into two or more sections. A clear further advancement of this model would be to include the option to use different superconductors for different inter-joint sections of the TF coil. For example, Nb-Ti could be used in the lower field outboard legs, whilst REBCO could be used on the higher field inboard legs reducing cost with respect to a fully REBCO magnet. Durham University has produced a patent for such magnet [239].

A final, highly optimistic, future work programme (far beyond what a single person could accomplish) would be to convince experts at the UK Atomic Energy Authority, EuroFusion and beyond of the necessity and urgency with which practical remountable coils should be designed and integrated into tokamak pilot plant and power plant designs. As argued in this thesis, commercial tokamaks must have remountable coils to avoid long periods of downtime for both routine maintenance or magnet replacement in the case of debilitating damage. There are a number of remountable joint designs, but scarce few have even reached the conceptual proof-of-concept prototyping phase. Certainly no tokamak scale remountable supercon-

ducting magnet prototypes have been built (unless such projects are kept behind closed doors). They may not be deemed necessary for the current generation of tokamaks, but the lack of published progress towards a remountable demonstration coil for a future pilot plant is disheartening - 2040 is not so long away! Significant resources should be put into designing and building remountable magnets, both from Nb-Ti and REBCO. The risk-elimination during commissioning and testing offered by Nb-Ti training magnets far outweighs the meagre increase in reactor cost (<10 %) required to construct and install them. In the author's opinion, if (when) remountable coils are used in tokamaks, also using Nb-Ti training coils seems a prudent choice... Fusion power must be reliable and consistent to adequately replace fossil fuels as the foundation of the global energy market - remountable coils (including training coils) greatly help make this so.

Bibliography

- [1] V. Masson-Delmotte, P. Zhai, A. Pirani, S. L. Connors *et al.*, “Climate change 2021: The physical science basis.” Intergovernmental panel on climate change, Report, 2021.
- [2] United Nations, “Ensure access to affordable, reliable, sustainable and modern energy for all,” 2021, <https://sdgs.un.org/goals/goal7>, Accessed 2021/09/12.
- [3] M. R. Gilbert, T. Eade, C. Bachmann, U. Fischer, and N. P. Taylor, “Activation, decay heat, and waste classification studies of the european DEMO concept,” *Nuclear Fusion*, vol. 57, no. 4, p. 046015, 2017.
- [4] A. J. Creely, M. J. Greenwald, S. B. Ballinger, D. Brunner *et al.*, “Overview of the SPARC tokamak,” *Journal of Plasma Physics*, vol. 86, no. 5, p. 865860502, 2020.
- [5] ITER Organization, “The ITER Tokamak,” 2021, <https://www.iter.org/mach>, Accessed 2021/05/14.
- [6] G. Federici, C. Bachmann, L. Barucca, W. Biel *et al.*, “DEMO design activity in europe: Progress and updates,” *Fusion Engineering and Design*, vol. 136, pp. 729–741, 2018.

- [7] K. Tobita, R. Hiwatari, Y. Sakamoto, Y. Someya *et al.*, “Japan’s efforts to develop the concept of JA DEMO during the past decade,” *Fusion Science and Technology*, vol. 75, no. 5, pp. 372–383, 2019.
- [8] K. Kim, K. Im, H. C. Kim, S. Oh *et al.*, “Design concept of k-DEMO for near-term implementation,” *Nuclear Fusion*, vol. 55, no. 5, p. 053027, 2015.
- [9] B. N. Sorbom, J. Ball, T. R. Palmer, F. J. Mangiarotti *et al.*, “ARC: A compact, high-field, fusion nuclear science facility and demonstration power plant with demountable magnets,” *Fusion Engineering and Design*, vol. 100, pp. 378–405, 2015.
- [10] G. Zhuang, G. Q. Li, J. Li, Y. X. Wan *et al.*, “Progress of the CFETR design,” *Nuclear Fusion*, vol. 59, no. 11, p. 112010, 2019.
- [11] A. Sykes, A. E. Costley, C. G. Windsor, O. Asunta *et al.*, “Compact fusion energy based on the spherical tokamak,” *Nuclear Fusion*, vol. 58, no. 1, p. 016039, 2018.
- [12] Commonwealth Fusion Systems, “Commonwealth fusion systems creates viable path to commercial fusion power with world’s strongest magnet,” 2021, <https://cfs.energy/news-and-media/cfs-commercial-fusion-power-with-hts-magnet>, Accessed 2021/09/12.
- [13] J. E. Menard, T. Brown, L. El-Guebaly, M. Boyer *et al.*, “Fusion nuclear science facilities and pilot plants based on the spherical tokamak,” *Nuclear Fusion*, vol. 56, no. 10, p. 106023, 2016.
- [14] M. R. Wade and J. A. Leuer, “Cost drivers for a tokamak-based compact pilot plant,” *Fusion Science and Technology*, vol. 77, no. 2, pp. 119–143, 2021.
- [15] National Academies of Sciences Engineering and Medicine, “Bringing fusion to the u.s. grid,” Report, 2021, <https://doi.org/10.17226/25991>, Accessed 2021/02/18.

- [16] G. Aubert, C. Berthier, F. Debray, M. Horvatic *et al.*, “The grenoble gigamr project,” *IEEE Transactions on Applied Superconductivity*, vol. 10, no. 1, pp. 732–735, 2000.
- [17] R. Aymar, P. Barabaschi, Y. Shimomura, and I. design team, “The iter design,” *Plasma Physics and Controlled Fusion*, vol. 44, no. 5, pp. 519–565, 2002.
- [18] J. Sapper, W. Gardebrecht, F. Kerl, and I. Schoenewolf, “The layout of the Wendelstein 7-X magnet,” *Fusion Engineering and Design*, vol. 58-59, pp. 237–240, 2001.
- [19] A. J. Wuis, B. Bordini, A. Ballarino, L. Oberli, and H. H. J. ten Kate, “Characterization of Nb₃Sn Rutherford cables for the LHC 11-T dipole magnet,” *IEEE Transactions on Applied Superconductivity*, vol. 24, no. 3, p. 5, 2014.
- [20] D. van Delft and P. Kes, “The discovery of superconductivity,” *Physics Today*, vol. 63, no. 9, pp. 38–43, 2010.
- [21] H. K. Onnes, K. Gavroglu, and Y. Goudaroulis, “Through measurement to knowledge : the selected papers of heike kamerlingh onnes, 1853-1926 : with a bibliography of works by heike kamerlingh onnes,” 1991, Conference Proceedings.
- [22] K. Tachikawa and P. J. Lee, *History of Nb₃Sn and Related A15 Wires*. National High Magnetic Field Laboratory, 2011, https://fs.magnet.fsu.edu/lee/superconductor-history_files/Centennial_Supplemental/11_3_Tachikawa+Lee-History_of_Nb3Sn_and_Related_A15_Wires.pdf.
- [23] P. J. Lee and B. Strauss, *Nb-Ti - from beginnings to perfection*. National High Magnetic Field Laboratory, 2012, https://fs.magnet.fsu.edu/lee/superconductor-history_files/Centennial_Supplemental/11_2_Nb-Ti_from_beginnings_to_perfection-fullreferences.pdf.

- [24] J. G. Bednorz and K. A. Muller, "Possible high-Tc superconductivity in the Ba-La-Cu-O system," *Zeitschrift Fur Physik B-Condensed Matter*, vol. 64, no. 2, pp. 189–193, 1986.
- [25] F. London and H. London, "The electromagnetic equations of the superconductor," *Proceedings of the Royal Society A*, vol. A149, pp. 71–88, 1935.
- [26] J. Bardeen, L. N. Cooper, and J. R. Schrieffer, "Theory of superconductivity," *Physical Review*, vol. 108, no. 5, pp. 1175–1204, 1957.
- [27] L. P. Gor'kov, "Microscopic derivation of the ginzburg-landau equations in the theory of superconductors," *Soviet Physics JETP*, vol. 9, no. 6, pp. 1364–1367, 1959.
- [28] Y. J. Uemura, "Condensation, excitation, pairing, and superfluid density in high-t-c superconductors: the magnetic resonance mode as a roton analogue and a possible spin-mediated pairing," *Journal of Physics-Condensed Matter*, vol. 16, no. 40, pp. S4515–S4540, 2004.
- [29] A. Bussmann-Holder and H. Keller, "High-temperature superconductors: underlying physics and applications," *Zeitschrift für Naturforschung B*, vol. 75, no. 1-2, pp. 3–14, 2020.
- [30] H. Fröhlich, "Theory of the superconducting state. i. the ground state at the absolute zero of temperature," *Physical Review*, vol. 79, no. 5, pp. 845–856, 1950.
- [31] D. R. Tilley and J. Tilley, *Microscopic Theory of Superconductivity*, 3rd ed. Bristol: IOP publishing Ltd., 1990.
- [32] E. Maxwell, "Isotope effect in the superconductivity of mercury," *Physical Review*, vol. 78, no. 4, p. 477, 1950.

- [33] V. L. Ginzburg and L. D. Landau, “On the theory of superconductivity,” *Zhurnal Eksperimentalnoj i Teoreticheskoj Fiziki*, vol. 20, pp. 1064–1082, 1950.
- [34] J. F. Annett, *Superconductivity, Superfluids and Condensates*. Oxford University Press, 2003.
- [35] D. R. Tilley and J. Tilley, *Ginzburg-Landau Theory*, 3rd ed. Bristol: IOP publishing Ltd., 1990, pp. 296–302.
- [36] W. Meissner and R. Ochsenfeld, “Ein neuer effekt bei eintritt der supraleitfähigkeit,” *Naturwissenschaften*, vol. 21, pp. 787–788, 1933.
- [37] A. A. Abrikosov, “On the magnetic properties of superconductors of the second group,” *Soviet Physics JETP*, vol. 5, no. 6, pp. 1174–1182, 1957.
- [38] W. H. Kleiner, L. M. Roth, and S. H. Autler, “Bulk solution of Ginzburg-Landau equations for type II superconductors: Upper critical field region,” *Physical Review*, vol. 133, no. 5A, pp. A1226–A1227, 1964.
- [39] M. Tinkham, *Magnetic Properties of Classic Type II Superconductors*, 2nd ed. New York: Dover Publications, 1996, pp. 149–154.
- [40] A. Rorheim, “Superconductor interactions with magnetic field,” 2020, https://commons.wikimedia.org/wiki/File:Superconductor_interactions_with_magnetic_field.png, Accessed 2021/04/28.
- [41] M. N. Wilson, *Superconducting Magnets*. Oxford, UK: Oxford University Press, 1986.
- [42] A. K. Jha, K. Matsumoto, T. Horide, S. Saini *et al.*, “Tailoring the vortex pinning strength of ybco thin films by systematic incorporation of hybrid artificial pinning centers,” *Superconductor Science & Technology*, vol. 28, no. 11, 2015.

- [43] D. X. Fischer, R. Prokopec, J. Emhofer, and M. Eisterer, “The effect of fast neutron irradiation on the superconducting properties of REBCO coated conductors with and without artificial pinning centers,” *Superconductor Science and Technology*, vol. 31, no. 4, p. 044006, 2018.
- [44] National High Magnetic Field Laboratory, “Engineering critical current density vs. applied field for superconductors available in long lengths,” 2017, https://nationalmaglab.org/images/magnet_development/asc/plots/JcChart092617.pdf, Accessed 2021/04/28.
- [45] P. Libeyre, J. L. Duchateau, B. Gravit, E. Tena *et al.*, “Pioneering superconducting magnets in large tokamaks: Evaluation after 16 years of operating experience in tore supra,” *Fusion Engineering and Design*, vol. 75-79, pp. 221–228, 2005.
- [46] J. Wei, W. G. Chen, W. Y. Wu, Y. N. Pan *et al.*, “The superconducting magnets for east tokamak,” *IEEE Transactions on Applied Superconductivity*, vol. 20, no. 3, pp. 556–559, 2010.
- [47] G. S. Lee, M. Kwon, C. J. Doh, B. G. Hong *et al.*, “Design and construction of the KSTAR tokamak,” *Nuclear Fusion*, vol. 41, no. 10, pp. 1515–1523, 2001.
- [48] H. Shirai, P. Barabaschi, and Y. Kamada, “Recent progress of the JT-60SA project,” *Nuclear Fusion*, vol. 57, no. 10, p. 102002, 2017.
- [49] R. Albanese, F. Crisanti, P. Martin, A. Pizzuto *et al.*, “Design review for the italian divertor tokamak test facility,” *Fusion Engineering and Design*, vol. 146, pp. 194–197, 2019.
- [50] F. Najmabadi, “Spherical torus concept as power plants—the ARIES-ST study,” *Fusion Engineering and Design*, vol. 65, no. 2, pp. 143–164, 2003.

- [51] E. Fauve, E. Monneret, T. Voigt, G. Vincent *et al.*, “ITER cryoplant infrastructures,” *IOP Conference Series: Materials Science and Engineering*, vol. 171, p. 012008, 2017.
- [52] L. D. Cooley, A. K. Ghosh, and R. M. Scanlan, “Costs of high-field superconducting strands for particle accelerator magnets,” *Superconductor Science and Technology*, vol. 18, no. 4, 2005.
- [53] S. B. L. Chislett-McDonald, Y. Tsui, E. Surrey, M. Kovari, and D. P. Hampshire, “The magnetic field, temperature, strain and angular dependence of the critical current density for Nb-Ti,” *Journal of Physics: Conference Series*, vol. 1559, p. 012063, 2020.
- [54] M. Sborchia, E. Barbero Soto, R. Batista, B. Bellesia *et al.*, “Overview of ITER magnet system and european contribution,” *IEEE/NPSS 24th Symposium on Fusion Engineering*, pp. 1–8, 2011.
- [55] S. Pradhan, Z. Khan, V. L. Tanna, A. N. Sharma *et al.*, “The first experiments in sst-1,” *Nuclear Fusion*, vol. 55, no. 10, p. 104009, 2015.
- [56] P. Bruzzone, A. Anghel, A. Fuchs, G. Pasztor *et al.*, “Upgrade of operating range for sultan test facility,” *IEEE Transactions on Applied Superconductivity*, vol. 12, no. 1, pp. 520–523, 2002.
- [57] X. Liu, F. Wu, Z. Wang, G. Li *et al.*, “Progress in the conceptual design of the CFETR toroidal field coil with rectangular conductors,” *Nuclear Fusion*, vol. 60, no. 4, p. 046032, 2020.
- [58] P. Bruzzone, “Review of design aspects for high current Nb₃Sn conductors,” *IEEE Transactions on Applied Superconductivity*, vol. 21, no. 3, pp. 2036–2041, 2011.
- [59] D. Uglietti, K. Sedlak, R. Wesche, P. Bruzzone *et al.*, “Progressing in cable-in-conduit for fusion magnets: from ITER to low cost, high performance

- DEMO,” *Superconductor Science and Technology*, vol. 31, no. 5, p. 055004, 2018.
- [60] T. Sekitani, N. Miura, S. Ikeda, Y. H. Matsuda, and Y. Shiohara, “Upper critical field for optimally-doped $\text{YBa}_2\text{Cu}_3\text{O}_7$,” *Physica B: Condensed Matter*, vol. 346–347, pp. 319–324, 2004.
- [61] P. Bruzzone, W. H. Fietz, M. V. Minervini, M. Novikov *et al.*, “High temperature superconductors for fusion magnets,” *Nuclear Fusion*, vol. 58, no. 10, p. 103001, 2018.
- [62] V. Braccini, A. Xu, J. Jaroszynski, Y. Xin *et al.*, “Properties of recent IbAd-MoCVD coated conductors relevant to their high field, low temperature magnet use,” *Superconductor Science and Technology*, vol. 24, no. 3, p. 9, 2011.
- [63] Fujikura Europe Ltd., “2G High Temperature Superconductor,” 2021, <https://www.fujikura.co.uk/products/energy-and-environment/2g-ybco-high-temperature-superconductors/>, Accessed 2021/04/28.
- [64] J. D. Weiss, T. Mulder, H. J. ten Kate, and D. C. Van der Laan, “Introduction of $\text{CORC}^{\text{®}}$ wires: highly flexible, round high-temperature superconducting wires for magnet and power transmission applications,” *Superconductor Science and Technology*, vol. 30, 2017.
- [65] G. Celentano, G. D. Marzi, F. Fabbri, L. Muzzi *et al.*, “Design of an industrially feasible twisted-stack HTS cable-in-conduit conductor for fusion application,” *IEEE Transactions on Applied Superconductivity*, vol. 24, no. 3, pp. 1–5, 2014.
- [66] Z. S. Hartwig, R. F. Vieira, B. N. Sorbom, R. A. Badcock *et al.*, “Viper: An industrially scalable high-current high temperature superconductor cable,” *Superconductor Science and Technology*, vol. 33, no. 11, p. 11LT01, 2020.

- [67] N. Bykovsky, D. Uglietti, R. Wesche, and P. Bruzzone, “Design of HTS fusion conductors for TF and CS coils,” *IEEE Transaction on applied superconductivity*, vol. 26, no. 4, p. 6600104, 2016.
- [68] M. J. Wolf, C. M. Bayer, W. H. Fietz, R. Heller *et al.*, “Toward a high-current conductor made of HTS crossconductor strands,” *IEEE Transactions on Applied Superconductivity*, vol. 26, no. 4, pp. 1–4, 2016.
- [69] L. L. Lucas and M. P. Unterweger, “Comprehensive review and critical evaluation of the half-life of tritium,” *Journal of Research of the National Institute of Standards and Technology*, vol. 105, no. 4, pp. 541–549, 2000.
- [70] World Nuclear Association, 2017, <https://world-nuclear.org/information-library/current-and-future-generation/lithium.aspx>, Accessed 2022/03/01.
- [71] K. Niu, *Nuclear Fusion*. Cambridge University Press, 2009.
- [72] S. Atzeni and J. Meyer-ter Vehn, *The Physics of inertial fusion*. Oxford University Press, 2004.
- [73] J. Wesson, *Tokamaks*. Oxford: Oxford University Press, 2011, vol. 149.
- [74] J. D. Lawson, “Some criteria for a power producing thermonuclear reactor,” *Proceedings of the Physical Society of London Section B*, vol. 70, no. 1, pp. 6–10, 1957.
- [75] H. Wilson, I. Chapman, T. Denton, W. Morris *et al.*, pp. 8–1–8–18, 2020.
- [76] F. F. Chen, *Introduction to Plasma Physics and Controlled Fusion*. Springer, 1984.
- [77] P. Titus, “Structural design of high field tokamaks,” Plasma Science and Fusion Centre, Massachusetts Institute of Technology, Report, 2003.
- [78] J. Milnes, N. B. Ayed, F. Dhalla, G. Fishpool *et al.*, “MAST upgrade – construction status,” *Fusion Engineering and Design*, vol. 96-97, pp. 42–47, 2015.

- [79] A. W. Leonard, “Edge-localized-modes in tokamaks,” *Physics of Plasmas*, vol. 21, no. 9, p. 090501, 2014.
- [80] D. N. Hill, “A review of ELMs in divertor tokamaks,” *Journal of Nuclear Materials*, vol. 241-243, pp. 182–198, 1997.
- [81] ITER Organization, “External heating systems,” 2021, <https://www.iter.org/mach/Heating>, Accessed 2021/05/24.
- [82] A. K. Ram and S. D. Schultz, “Excitation, propagation, and damping of electron Bernstein waves in tokamaks,” *Physics of Plasmas*, vol. 7, no. 10, pp. 4084–4094, 2000.
- [83] J. Urban, J. Decker, Y. Peysson, J. Preinhaelter *et al.*, “A survey of electron Bernstein wave heating and current drive potential for spherical tokamaks,” *Nuclear Fusion*, vol. 51, no. 8, p. 083050, 2011.
- [84] R. A. Pitts, X. Bonnin, F. Escourbiac, H. Frerichs *et al.*, “Physics basis for the first ITER tungsten divertor,” *Nuclear Materials and Energy*, vol. 20, p. 100696, 2019.
- [85] W. Morris, J. R. Harrison, A. Kirk, B. Lipschultz *et al.*, “MAST upgrade divertor facility: A test bed for novel divertor solutions,” *IEEE Transactions on Plasma Science*, vol. 46, no. 5, pp. 1217–1226, 2018.
- [86] G. Mazzitelli, R. Albanese, F. Crisanti, P. Martin *et al.*, “Role of Italian DTT in the power exhaust implementation strategy,” *Fusion Engineering and Design*, vol. 146, pp. 932–936, 2019.
- [87] P. C. Stangeby, “A tutorial on some basic aspects of divertor physics,” *Plasma Physics and Controlled Fusion*, vol. 42, no. 12B, pp. B271–B291, 2000.
- [88] S. Brezinsek, T. Loarer, V. Philipps, H. G. Esser *et al.*, “Fuel retention studies with the ITER-like wall in jet,” *Nuclear Fusion*, vol. 53, no. 8, p. 083023, 2013.

- [89] M. R. Gilbert, S. L. Dudarev, D. Nguyen-Manh, S. Zheng *et al.*, “Neutron-induced dpa, transmutations, gas production, and helium embrittlement of fusion materials,” *Journal of Nuclear Materials*, vol. 442, no. 1, Supplement 1, pp. S755–S760, 2013.
- [90] G. Federici, L. Boccaccini, F. Cismondi, M. Gasparotto *et al.*, “An overview of the eu breeding blanket design strategy as an integral part of the DEMO design effort,” *Fusion Engineering and Design*, vol. 141, pp. 30–42, 2019.
- [91] S. A. Humphry-Baker and G. D. W. Smith, “Shielding materials in the compact spherical tokamak,” *Philosophical Transactions of the Royal Society A: Mathematical, Physical and Engineering Sciences*, vol. 377, no. 2141, p. 20170443, 2019.
- [92] EURATOM, “JET joint undertaking,” ECSC/EEC/EURATOM, Report, 1982, <http://aei.pitt.edu/88591/1/1982.pdf>, Accessed 2021/06/14.
- [93] H. Zohm, “On the minimum size of demo,” *Fusion Science and Technology*, vol. 58, no. 2, pp. 613–624, 2010.
- [94] H. Zohm, “On the size of tokamak fusion power plants,” *Philosophical Transactions of the Royal Society A: Mathematical, Physical and Engineering Sciences*, vol. 377, no. 2141, p. 20170437, 2019.
- [95] P. C. de Vries, M. F. Johnson, B. Alper, P. Buratti *et al.*, “Survey of disruption causes at jet,” *Nuclear Fusion*, vol. 51, no. 5, p. 053018, 2011.
- [96] I. P. E. G. on, C. Plasma, MHD, Disruptions, and ITER Physics Basis Editors, “Chapter 3: Mhd stability, operational limits and disruptions,” *Nuclear Fusion*, vol. 39, no. 12, p. 2251, 1999.
- [97] M. Greenwald, “Density limits in toroidal plasmas,” 2001, <https://www-internal.psfc.mit.edu/g/papers/aps01.pdf>, Accessed 2021/03/03.

- [98] Q. Teng, D. P. Brennan, L. Delgado-Aparicio, D. A. Gates *et al.*, “A predictive model for the tokamak density limit,” *Nuclear Fusion*, vol. 56, no. 10, p. 106001, 2016.
- [99] D. C. McDonald, J. G. Cordey, K. Thomsen, O. J. W. F. Kardaun *et al.*, “Recent progress on the development and analysis of the ITPA global H-mode confinement database,” *Nuclear Fusion*, vol. 47, no. 3, p. 147, 2007.
- [100] M. Valovič, R. Akers, G. Cunningham, L. Garzotti *et al.*, “Scaling of H-mode energy confinement with i_p and b_t in the MAST spherical tokamak,” *Nuclear Fusion*, vol. 49, no. 7, 2009.
- [101] P. F. Buxton, J. W. Connor, A. E. Costley, M. P. Gryaznevich, and S. McNamara, “On the energy confinement time in spherical tokamaks: implications for the design of pilot plants and fusion reactors,” *Plasma Physics and Controlled Fusion*, vol. 61, no. 3, p. 035006, 2019.
- [102] M. R. Wade, M. Murakami, T. C. Luce, J. R. Ferron *et al.*, “Integrated, advanced tokamak operation on diii-d,” *Nuclear Fusion*, vol. 43, pp. 634–646, 2003.
- [103] A. C. C. Sips, “Advanced scenarios for ITER operation,” *Plasma Physics and Controlled Fusion*, vol. 47, no. 5A, p. A19, 2005.
- [104] S. M. Kaye, M. G. Bell, R. E. Bell, E. D. Fredrickson *et al.*, “Energy confinement scaling in the low aspect ratio national spherical torus experiment (NSTX),” *Nuclear Fusion*, vol. 46, no. 10, pp. 848–857, 2006.
- [105] M. Coleman and S. McIntosh, “Blueprint: A novel approach to fusion reactor design,” *Fusion Engineering and Design*, vol. 139, pp. 26–38, 2019.
- [106] M. Kovari, R. Kemp, H. Lux, P. Knight *et al.*, ““PROCESS”: A systems code for fusion power plants—part 1: Physics,” *Fusion Engineering and Design*, vol. 89, no. 12, pp. 3054–3069, 2014.

- [107] M. Kovari, F. Fox, C. Harrington, R. Kembleton *et al.*, ““PROCESS”: A systems code for fusion power plants – part 2: Engineering,” *Fusion Engineering and Design*, vol. 104, pp. 9–20, 2016.
- [108] J. Morris, N. Asakura, Y. Homma, K. Hoshino, and M. Kovari, “Comparison of the process systems code with the sonic divertor code,” *IEEE Transactions on Plasma Science*, vol. 48, no. 6, pp. 1799–1803, 2020.
- [109] J. Last, “Orthotropic properties of ITER TF winding (internal memorandum),” Culham Centre for Fusion Energy, Report, 2013/06/13 2013.
- [110] F. Warmer, C. D. Beidler, A. Dinklage, K. Egorov *et al.*, “Implementation and verification of a HELIAS module for the systems code PROCESS,” *Fusion Engineering and Design*, vol. 98-99, pp. 2227–2230, 2015.
- [111] S. I. Muldrew, F. Warmer, J. Lion, and H. Lux, “Design uncertainty for a helias 5-b stellarator fusion power plant,” *Fusion Engineering and Design*, p. 112708, 2021.
- [112] S. I. Muldrew, H. Lux, V. Menon, and R. Srinivasan, “Uncertainty analysis of an SST-2 fusion reactor design,” *Fusion Engineering and Design*, vol. 146, pp. 353–356, 2019.
- [113] J. Morris, V. Chan, J. Chen, S. Mao, and M. Y. Ye, “Validation and sensitivity of CFETR design using eu systems codes,” *Fusion Engineering and Design*, vol. 146, pp. 574–577, 2019.
- [114] R. Kemp, R. Wenninger, G. Federici, H. Reimerdes *et al.*, “Exploring a broad spectrum of design options for DEMO,” *Fusion Engineering and Design*, vol. 136, pp. 970–974, 2018.
- [115] P. J. Knight and M. D. Kovari, “A user guide to the PROCESS fusion reactor systems code,” Culham Centre For Fusion Energy, Report, 2016.

- [116] R. L. Crane, K. E. Hillstrom, and M. Minkoff, "Solution of the general non-linear programming problem with the subroutine vmcon," Argonne National Laboratory, Report, 1980.
- [117] G. Sanderson, "Meaning of the lagrange multiplier," 2016, <https://www.khanacademy.org/math/multivariable-calculus/applications-of-multivariable-derivatives/lagrange-multipliers-and-constrained-optimization/v/meaning-of-lagrange-multiplier>, Accessed 2021/06/30.
- [118] 2022, https://en.wikipedia.org/wiki/Lagrange_multiplier, Accessed 2022/03/17.
- [119] S. C. Schulte, T. L. Willke, and J. A. Young, "Fusion reactor design studies - standard accounts for cost estimates," U.S. Department of Energy, Report, 1978.
- [120] J. D. Galambos, L. J. Perkins, S. W. Haney, and J. Mandrekas, "Commercial tokamak reactor potential with advanced tokamak operation," *Nuclear Fusion*, vol. 35, no. 5, p. 551, 1995.
- [121] J. P. Holdren, D. H. Berwald, R. J. Budnitz, J. G. Crocker *et al.*, "Report of the senior committee on environmental, safety, and economic aspects of magnetic fusion energy," Report, 1989.
- [122] P. Christensen and L. R. Dysert, "Cost estimate classification system – as applied in engineering, procurement, and construction for the process industries," Report, 2005.
- [123] Federal Reserve Bank of St. Louis, "Producer price index by commodity: Metals and metal products: Iron and steel," 2021, <https://fred.stlouisfed.org/series/WPU101>, Accessed 2021/08/02.
- [124] "IHS- CERA US power plant costs," <https://ihsmarkit.com/info/cera/ihsindexes/index.html>, Accessed 2022/02/18.

- [125] J. Morris, R. Kemp, M. Kovari, J. Last, and P. Knight, “Implications of toroidal field coil stress limits on power plant design using PROCESS,” *Fusion Engineering and Design*, vol. 98-99, pp. 1118–1121, 2015.
- [126] A. Devred, I. Backbier, D. Bessette, G. Bevillard *et al.*, “Status of ITER conductor development and production,” *IEEE Transactions on Applied Superconductivity*, vol. 22, no. 3, p. 4804909, 2012.
- [127] T. Boutboul, P. Readman, E. Viladiu, M. Losasso *et al.*, “Status of the procurement of the european superconductors for the ITER magnets,” *IEEE Transactions on Applied Superconductivity*, vol. 24, no. 3, p. 4, 2014.
- [128] J. Minervini, “Superconducting magnet technology for fusion and large scale applications,” 2014.
- [129] S. Ejima, R. W. Callis, J. L. Luxon, R. D. Stambaugh *et al.*, “Volt-second analysis and consumption in doublet III plasmas,” *Nuclear Fusion*, vol. 22, no. 10, pp. 1313–1319, 1982.
- [130] M. S. Lubell, “Empirical scaling formulas for critical current and critical field for commercial Nbti,” *IEEE Transactions on Magnetics*, vol. 19, pp. 754–757, 1983.
- [131] M. J. Wolf, N. Bagrets, W. H. Fietz, C. Lange, and K. Weiss, “Critical current densities of 482 A/mm² in HTS crossconductors at 4.2 K and 12 T,” *IEEE Transactions on Applied Superconductivity*, vol. 28, no. 4, pp. 1–4, 2018.
- [132] P. J. Branch, Y. Tsui, K. Osamura, and D. P. Hampshire, “Weakly-emergent strain-dependent properties of high field superconductors,” *Nature Scientific Reports*, vol. 9, p. 13998, 2019.
- [133] P. Branch, K. Osamura, and D. Hampshire, “Weak emergence in the angular dependence of the critical current density of the high temperature superconductor coated conductor REBCO,” *Superconductor Science and Technology*, vol. 33, no. 10, p. 104006, 2020.

- [134] S. A. Keys and D. P. Hampshire, “A scaling law for the critical current density of weakly and strongly-coupled superconductors, used to parameterise data from a technological Nb₃Sn strand,” *Supercond. Sci. Technol.*, vol. 16, pp. 1097–108, 2003.
- [135] X. F. Lu, D. M. J. Taylor, and D. P. Hampshire, “Critical current scaling laws for advanced Nb₃Sn superconducting strands for fusion applications with six free parameters,” *Supercond. Sci. Technol.*, vol. 21, no. 10, p. 105016, 2008.
- [136] D. M. J. Taylor and D. P. Hampshire, “The scaling law for the strain dependence of the critical current density in Nb₃Sn superconducting wires,” *Superconductor Science and Technology*, vol. 18, pp. S241–S252, 2005.
- [137] D. Dew-Hughes, “Flux pinning mechanisms in type II superconductors,” *Philos. Mag.*, vol. 30, no. 2, pp. 293–305, 1974.
- [138] D. M. J. Taylor and D. P. Hampshire, *Superconductor Science and Technology*, vol. 18, pp. 356–368, 2005.
- [139] N. Chegour and D. P. Hampshire, “A probe for investigating the effect of magnetic field, temperature and strain on transport critical currents in superconducting tapes and wires,” *Review of Scientific Instruments*, vol. 71, p. 4521, 2000.
- [140] Y. Yamada and B. Marchionini, “High temperature superconductivity a roadmap for the electric power section,” International Energy Agency, Report, 2015, <https://euagenda.eu/upload/publications/untitled-94819-ea.pdf>, Accessed 2021/02/10.
- [141] L. Cooley and I. Pong, “Cost drivers for very high energy p-p collider magnet conductors,” 2016, https://indico.cern.ch/event/438866/contributions/1085142/attachments/1257973/1858756/Cost_drivers_for_VHEPP_magnet_conductors-v2.pdf,

- Accessed 2021/01/25 (presented at Future Circular Collider Week 2016, Rome).
- [142] T. S. Lee, I. Jenkins, E. Surrey, and D. P. Hampshire, “Optimal design of a toroidal field magnet system and cost of electricity implications for a tokamak using high temperature superconductors,” *Fusion Engineering and Design*, vol. 98-99, pp. 1072—1075, 2015.
- [143] P. Bruzzone, “Open issues and challenges for fusion magnets of future generations,” 2021, presented at Frontiers of Fusion 2021, University of York.
- [144] U.S. Bureau of labour statistics, “CPI inflation calculator,” 2021, https://www.bls.gov/data/inflation_calculator.htm, Accessed 2021/08/02.
- [145] T. Oishi, K. Yamazaki, H. Arimoto, K. Ban *et al.*, “Comparative study of cost models for tokamak DEMO fusion reactors,” *Plasma and Fusion Research*, vol. 7, p. 2405115, 2012.
- [146] “Final report of the ITER EDA,” IAEA, Report, 2001, IAEA/ITER EDA/DS/21.
- [147] M. Neil, Z. Jinxing, V. Christian, C. Valentina *et al.*, “Superconductors for fusion: a roadmap,” *Superconductor Science and Technology*, 2021.
- [148] R. J. Buttery, J. M. Park, J. T. McClenaghan, D. Weisberg *et al.*, “The advanced tokamak path to a compact net electric fusion pilot plant,” *Nuclear Fusion*, vol. 61, no. 4, p. 046028, 2021.
- [149] T. Goorley, M. James, T. Booth, F. Brown *et al.*, “Initial mcnp6 release overview,” *Nuclear Technology*, vol. 180, no. 3, pp. 298–315, 2012.
- [150] H. R. Wilson, J. W. Ahn, R. J. Akers, D. Applegate *et al.*, “Integrated plasma physics modelling for the culham steady state spherical tokamak fusion power plant,” *Nuclear Fusion*, vol. 44, no. 8, pp. 917–929, 2004.

- [151] M. Greenwald, D. Whyte, P. Bonoli, Z. Hartwig *et al.*, “The high-field path to practical fusion energy,” Massachusetts Institute of Technology, Report, 2018.
- [152] E. Bertolini, M. Buzio, A. Kaye, J. Last *et al.*, “Raising the JET toroidal field to 4 tesla,” JET Joint Undertaking, Report, 2000.
- [153] F. Romanelli, “Overview of the JET results,” *Nuclear Fusion*, vol. 55, p. 104001, 2015.
- [154] J. Paméla, E. R. Solano, and J. E. Contributors, “Overview of JET results,” *Nuclear Fusion*, vol. 43, no. 12, pp. 1540–1554, 2003.
- [155] “3. plant description: 3.1 magnets,” Japan Atomic Energy Agency, Report, 2007, http://www.jt60sa.org/pdfs/CDR/06-3.1_Magnets.pdf, Accessed 2021/05/24.
- [156] K. Kim, H. K. Park, K. R. Park, B. S. Lim *et al.*, “Status of the KSTAR superconducting magnet system development,” *Nuclear Fusion*, vol. 45, no. 8, pp. 783–789, 2005.
- [157] J. W. Ahn, H. S. Kim, Y. S. Park, L. Terzolo *et al.*, “Confinement and ELM characteristics of H-mode plasmas in KSTAR,” *Nuclear Fusion*, vol. 52, no. 11, p. 114001, 2012.
- [158] B. Shen, W. B. Xi, J. P. Qian, Y. W. Sun, and H. Y. Fan, “The magnetic field configuration measurement on east tokamak,” *Fusion Engineering and Design*, vol. 84, no. 1, pp. 19–23, 2009.
- [159] P. Weng, “Experimental advanced superconducting tokamak (east) design, fabrication and assembly,” 2005, https://fire.pppl.gov/sofe_05_weng.pdf, Accessed 2021/05/23.

- [160] Z. X. Liu, X. Gao, W. Y. Zhang, J. G. Li *et al.*, “ELMy H-mode confinement and threshold power by low hybrid wave on the east tokamak,” *Plasma Physics and Controlled Fusion*, vol. 54, no. 8, p. 085005, 2012.
- [161] C. Bourdelle, J. F. Artaud, V. Basiuk, M. Bécoulet *et al.*, “West physics basis,” *Nuclear Fusion*, vol. 55, no. 6, p. 063017, 2015.
- [162] J. L. Duchateau, S. Bremond, V. Lamaison, P. Prochet *et al.*, “The superconducting magnet system of tore supra: lessons learnt and perspectives for west steady state operation,” 2007/03/20 2017.
- [163] J. R. Harrison, R. J. Akers, S. Y. Allan, J. S. Allcock *et al.*, “Overview of new MAST physics in anticipation of first results from MAST upgrade,” *Nuclear Fusion*, vol. 59, no. 11, p. 112011, 2019.
- [164] D. Bora, “SST and ADITYA tokamak research in India,” *Brazilian Journal of Physics*, vol. 32, pp. 193–216, 2002.
- [165] Y. Saxena, “First experiments with SST-1 tokamak,” 2004, https://www.researchgate.net/publication/282251654_First_Experiments_with_SST-1_Tokamak_Presentation-IAEA04-F3-4Ra, Accessed 2021/05/15.
- [166] A. E. Costley and S. A. M. McNamara, “Fusion performance of spherical and conventional tokamaks: implications for compact pilot plants and reactors,” *Plasma Physics and Controlled Fusion*, vol. 63, no. 3, p. 035005, 2021.
- [167] M. Valovič, R. Akers, M. d. Bock, J. McCone *et al.*, “Collisionality and safety factor scalings of H-mode energy transport in the MAST spherical tokamak,” *Nuclear Fusion*, vol. 51, no. 7, p. 073045, 2011.
- [168] D. G. Whyte, J. Minervini, E. S. Marmor, M. J. Greenwald *et al.*, “Smaller and sooner: Exploiting high magnetic fields from new superconductors for a more attractive fusion energy development path,” *Journal of Fusion Energy*, vol. 35, pp. 41–53, 2016.

- [169] T. W. Strobridge, “Cryogenic refrigerators - an updated survey nbs report,” National Bureau of Standards, Report, 1974.
- [170] N. J. Simon, E. S. Drexler, and R. P. Reed, “Properties of copper and copper alloys at cryogenic temperatures,” *Nist Monograph 177*, 1992.
- [171] E. Chehura, S. J. Buggy, S. W. James, A. Johnstone *et al.*, “Multi-component strain development in superconducting magnet coils monitored using bragg grating sensors fabricated in highly linearly birefringent fibre,” *Smart Material Structures*, vol. 20, 2011.
- [172] A. Chiuchiolo, H. Bajas, M. Bajko, L. Bottura *et al.*, “Advances in fiber optic sensors technology development for temperature and strain measurements in superconducting magnets and devices,” *IEEE Transactions on Applied Superconductivity*, vol. 26, no. 4, pp. 1–5, 2016.
- [173] M. Takayasu, “Acoustic mems sensor array for quench detection of cicc superconducting cables,” *IEEE Transactions on Applied Superconductivity*, vol. 30, no. 4, pp. 1–5, 2020.
- [174] E. Ravaioli, D. Davis, M. Marchevsky, G. Sabbi *et al.*, “A new quench detection method for HTS magnets: stray-capacitance change monitoring,” *Physica Scripta*, no. 95, p. 015002, 2020.
- [175] F. Hernández, P. Pereslavitsev, Q. Kang, P. Norajitra *et al.*, “A new HCPB breeding blanket for the EU DEMO: Evolution, rationale and preliminary performances,” *Fusion Engineering and Design*, vol. 124, pp. 882–886, 2017.
- [176] J. Shimwell, M. Kovari, S. Lilley, S. Zheng *et al.*, “A parameter study of time-varying tritium production in solid-type breeder blankets,” *Fusion Engineering and Design*, vol. 104, pp. 34–39, 2016.
- [177] M. Kovari, M. Coleman, I. Cristescu, and R. Smith, “Tritium resources available for fusion reactors,” *Nuclear Fusion*, vol. 58, no. 2, p. 026010, 2017.

- [178] E. Martelli, A. Del Nevo, P. Arena, G. Bongiovì *et al.*, “Advancements in DEMO WCLL breeding blanket design and integration,” *International Journal of Energy Research*, vol. 42, no. 1, pp. 27–52, 2017.
- [179] A. Tassone, A. D. Nevo, P. Arena, G. Bongiovì *et al.*, “Recent progress in the WCLL breeding blanket design for the DEMO fusion reactor,” *IEEE Transactions on Plasma Science*, vol. 46, no. 5, pp. 1446–1457, 2018.
- [180] G. S. Xu, Q. P. Yuan, K. D. Li, L. Wang *et al.*, “Divertor impurity seeding with a new feedback control scheme for maintaining good core confinement in grassy-ELM H-mode regime with tungsten monoblock divertor in east,” *Nuclear Fusion*, vol. 60, no. 8, p. 086001, 2020.
- [181] M. R. K. Wigram, B. LaBombard, M. V. Umansky, A. Q. Kuang *et al.*, “Performance assessment of long-legged tightly-baffled divertor geometries in the ARC reactor concept,” *Nuclear Fusion*, vol. 59, no. 10, p. 106052, 2019.
- [182] M. V. Umansky, B. LaBombard, D. Brunner, M. E. Rensink *et al.*, “Attainment of a stable, fully detached plasma state in innovative divertor configurations,” *Physics of Plasmas*, vol. 24, no. 5, p. 056112, 2017.
- [183] D. D. Ryutov and V. A. Soukhanovskii, “The snowflake divertor,” *Physics of Plasmas*, vol. 22, no. 11, p. 110901, 2015.
- [184] R. Ambrosino, A. Castaldo, S. Ha, V. P. Loschiavo *et al.*, “Evaluation of feasibility and costs of alternative magnetic divertor configurations for demo,” *Fusion Engineering and Design*, vol. 146, pp. 2717–2720, 2019.
- [185] H. Reimerdes, R. Ambrosino, P. Innocente, A. Castaldo *et al.*, “Assessment of alternative divertor configurations as an exhaust solution for demo,” *Nuclear Fusion*, vol. 60, no. 6, p. 066030, 2020.

- [186] K. Lackner and H. Zohm, “Calculation of realistic snowflake equilibria for next-step devices,” *Fusion Science and Technology*, vol. 63, no. 1, pp. 43–48, 2013.
- [187] N. Asakura, K. Hoshino, H. Utoh, Y. Someya *et al.*, “Plasma exhaust and divertor studies in japan and europe broader approach, DEMO design activity,” *Fusion Engineering and Design*, vol. 136, pp. 1214–1220, 2018.
- [188] J. Narl Davidson, “Effect of toroidal field ripple on particle and energy transport in a tokamak,” *Nuclear Fusion*, vol. 16, no. 5, pp. 731–742, 1976.
- [189] K. Hamada, H. Nakajima, K. Kawano, K. Takano *et al.*, “Demonstration of full scale JJ1 and 316LN fabrication for ITER TF coil structure,” *Fusion Engineering and Design*, vol. 82, no. 5, pp. 1481–1486, 2007.
- [190] P. Titus, “Coil concepts for DEMO and next step reactors,” <https://nucleus.iaea.org/sites/fusionportal/Shared%20Documents/DEMO/2018/3/Titus.pdf>.
- [191] J. H. Schultz, T. Antaya, J. Feng, C. Y. Gung *et al.*, *The ITER Central Solenoid*, ser. 21st IEEE/NPSS Symposium on Fusion Engineering - SOFE 05. New York: Ieee, 2006.
- [192] T. Franke, E. Barbato, A. Cardinali, S. Ceccuzzi *et al.*, “Rf hcd systems for DEMO - challenges and opportunities,” *AIP Conference Proceedings*, vol. 1580, no. 1, pp. 207–210, 2014.
- [193] R. Raman and V. F. Shevchenko, “Solenoid-free plasma start-up in spherical tokamaks,” *Plasma Physics and Controlled Fusion*, vol. 56, no. 10, p. 103001, 2014.
- [194] R. Raman, T. R. Jarboe, B. A. Nelson, D. Mueller *et al.*, “Design details of the transient chi plasma start-up system on NSTX-U,” *IEEE Transactions on Plasma Science*, vol. 42, no. 8, pp. 2154–2160, 2014.

- [195] A. Sykes, R. J. Akers, L. C. Appel, E. R. Arends *et al.*, “First results from mast,” *Nuclear Fusion*, vol. 41, no. 10, pp. 1423–1433, 2001.
- [196] M. Inomoto, T. G. Watanabe, K. Gi, K. Yamasaki *et al.*, “Centre-solenoid-free merging start-up of spherical tokamak plasmas in utst,” *Nuclear Fusion*, vol. 55, no. 3, p. 033013, 2015.
- [197] K. J. Chung, Y. H. An, B. K. Jung, H. Y. Lee *et al.*, “Design features and commissioning of the versatile experiment spherical torus (vest) at seoul national university,” *Plasma Science and Technology*, vol. 15, no. 3, pp. 244–251, 2013.
- [198] M. P. Gryaznevich and A. Sykes, “Merging-compression formation of high temperature tokamak plasma,” *Nuclear Fusion*, vol. 57, no. 7, p. 072003, 2017.
- [199] M. Ushigome, S. Ide, S. Itoh, E. Jotaki *et al.*, “Development of completely solenoidless tokamak operation in jt-60u,” *Nuclear Fusion*, vol. 46, no. 2, pp. 207–213, 2006.
- [200] C. Darbos, M. Henderson, F. Albajar, T. Bigelow *et al.*, “ECRH system for ITER,” *AIP Conference Proceedings*, vol. 1187, no. 1, pp. 531–538, 2009.
- [201] R. S. Hemsworth, D. Boilson, P. Blatchford, M. D. Palma *et al.*, “Overview of the design of the ITER heating neutral beam injectors,” *New Journal of Physics*, vol. 19, no. 2, p. 025005, 2017.
- [202] B. Colling, “Blanket performance and radioactive waste of fusion reactors: A neutronics approach,” Thesis, Lancaster University, 2016.
- [203] P. Vontobel and S. Pelloni, “Jef/eff based nuclear data libraries,” Swiss Federal Institute for Reactor Research, Report, 1987.
- [204] “Evaluated nuclear data file (endf) retrieval & plotting,” 2019, <https://www.nndc.bnl.gov/sigma/>, accessed 2019/02/28.

- [205] H. W. Weber, “Radiation effects on superconducting fusion magnet components,” *International Journal of Modern Physics E*, vol. 20, no. 06, pp. 1325–1378, 2011.
- [206] L. S. Richard, R. Bonifetto, U. Bottero, A. Foussat *et al.*, “Analysis of the effects of the nuclear heat load on the ITER TF magnets temperature margin,” *IEEE Transactions on Applied Superconductivity*, vol. 24, no. 3, pp. 1–4, 2014.
- [207] T. Goorley, M. James, T. Booth, F. Brown *et al.*, “Features of mcnp6,” *Annals of Nuclear Energy*, vol. 87, pp. 772–783, 2016.
- [208] S. G. Mashnik, “Validation and verification of mcnp6 against intermediate and high-energy experimental data and results by other codes,” *The European Physical Journal Plus*, vol. 126, no. 5, p. 49, 2011.
- [209] M. R. Gilbert, S. L. Dudarev, S. Zheng, L. W. Packer, and J. C. Sublet, “An integrated model for materials in a fusion power plant: transmutation, gas production, and helium embrittlement under neutron irradiation,” *Nuclear Fusion*, vol. 52, no. 8, 2012.
- [210] V. P. Chakin, A. O. Posevin, and R. N. Latypov, “Radiation damage in beryllium at 70–440°C and neutron fluence $(0.3\text{--}18) \cdot 10^{22} \text{ cm}^2$ ($e_n > 0.1 \text{ MeV}$),” *Atomic Energy*, vol. 101, no. 4, pp. 743–749, 2006.
- [211] F. Hofmann, D. R. Mason, J. K. Eliason, A. A. Maznev *et al.*, “Non-contact measurement of thermal diffusivity in ion-implanted nuclear materials,” *Scientific Reports*, vol. 5, no. 1, p. 16042, 2015.
- [212] I. Newton, “Vii. scala graduum caloris,” *Philosophical Transactions of the Royal Society of London*, vol. 22, no. 270, pp. 824–829, 1701.
- [213] S. Varin, F. Bonne, C. Hoa, S. Nicollet *et al.*, “An update of dynamic thermal-hydraulic simulations of the JT-60SA toroidal field coil cooling loop for preparing plasma operation,” *Cryogenics*, vol. 109, p. 103092, 2020.

- [214] National Institute of Standards and Technology, “Thermophysical properties of fluid systems,” <https://webbook.nist.gov/chemistry/fluid/>, Accessed 2020/12/18.
- [215] J. P. Egan and R. W. Boom, *Measurement of the Electrical Resistivity and Thermal Conductivity of High Purity Aluminum in Magnetic Fields*. Boston, MA: Springer US, 1990, pp. 679–686.
- [216] F. R. Fickett, “Magnetoresistivity of copper and aluminum at cryogenic temperatures,” in *4th International Conference on Magnet Technology (MT-4)*, Y. Winterbottom, Ed., vol. C720919, Conference Proceedings, p. 539.
- [217] R. A. Slade, “Cable design in HTS tokamaks,” p. 29, 2019/08/09 2019, <https://patentimages.storage.googleapis.com/5a/a0/f8/fd75370480e502/US20190267171A1.pdf>, Accessed 2010/10/09.
- [218] W. T. Liu, X. H. Liu, Y. Feng, H. J. Xie *et al.*, “Development of fine filament NbTi superconducting strands for ITER,” *IEEE Transactions on Applied Superconductivity*, vol. 20, no. 3, pp. 1504–1506, 2010.
- [219] D. M. J. Taylor and D. P. Hampshire, “The scaling law for the strain dependence of the critical current density in Nb₃Sn superconducting wires,” *Superconductor Science and Technology*, vol. 18, pp. S241–S252, 2005.
- [220] N. Cheggour, L. F. Goodrich, T. C. Stauffer, J. D. Splett *et al.*, “Influence of Ti and Ta doping on the irreversibility strain limit of ternary Nb₃Sn superconducting wires made by the restacked-rod process,” *Superconductivity Science and Technology*, vol. 23, p. 052002, 2010.
- [221] S. Balachandran, C. Tarantini, P. J. Lee, F. Kametani *et al.*, “Beneficial influence of Hf and Zr additions to Nb₄at%Ta on the vortex pinning of Nb₃Sn with and without an O source,” *Superconductor Science and Technology*, vol. 32, no. 4, p. 044006, 2019.

- [222] P. Bruzzone, K. Sedlak, X. Sarasola, B. Stepanov *et al.*, “A prototype conductor by react & wind method for the EUROfusion DEMO TF coils,” *IEEE Transactions on Applied Superconductivity*, vol. 28, no. 3, pp. 1–5, 2018.
- [223] K. Sedlak, P. Bruzzone, X. Sarasola, B. Stepanov, and R. Wesche, “Design and r&d for the DEMO toroidal field coils based on Nb₃Sn react and wind method,” *IEEE Transactions on Applied Superconductivity*, vol. 27, no. 4, pp. 1–5, 2017.
- [224] K. Osamura, S. Machiya, and G. Nishijima, “Reversible stress and strain limits of the critical current of practical REBCO and BSCCO wires,” *Superconductor Science and Technology*, vol. 29, no. 9, p. 094003, 2016.
- [225] C. Barth, G. Mondonico, and C. Senatore, “Electro-mechanical properties of REBCO coated conductors from various industrial manufacturers at 77 k, self-field and 4.2 k, 19 t,” *Superconductor Science & Technology*, vol. 28, 2015.
- [226] H. Maeda and Y. Yanagisawa, “Recent developments in high-temperature superconducting magnet technology (review),” *IEEE Transactions on Applied Superconductivity*, vol. 24, no. 3, pp. 1–12, 2014.
- [227] C. Lacroix, J. Fournier-Lupien, K. McMeekin, and F. Sirois, “Normal zone propagation velocity in 2G HTS coated conductor with high interfacial resistance,” *IEEE Transactions on Applied Superconductivity*, vol. 23, no. 3, pp. 4 701 605–4 701 605, 2013.
- [228] M. Bonura and C. Senatore, “High-field thermal transport properties of REBCO coated conductors,” *Superconductor Science & Technology*, vol. 28, no. 2, p. 9, 2015.
- [229] T. Horiuchi, Y. Monju, and N. Nagai, “Transition temperatures and resistive critical fields of superconducting Ti-Nb-Zr-Ta alloys,” *Japan Institute of Metals*, vol. 37, pp. 882–887, 1973.

- [230] E. W. Collings, *Applied superconductivity, metallurgy, and physics of titanium alloys. Volume 1: fundamentals*. New York: Plenum Press, 1986.
- [231] M. Tinkham, *Introduction to Superconductivity*, 2nd ed. Singapore: McGraw-Hill Book Co., 1996.
- [232] A. Nijhuis, W. A. J. Wessel, H. G. Knoopers, Y. Ilyin *et al.*, “Compressive pre-strain in Nb₃Sn strand by steel tube and effect on the critical current measured on standard ITER barrel,” *IEEE Transactions on Applied Superconductivity*, vol. 15, no. 2, pp. 3466–3469, 2005.
- [233] A. Devred, I. Backbier, D. Bessette, G. Bevillard *et al.*, “Challenges and status of ITER conductor production,” *Superconductor Science & Technology*, vol. 27, no. 4, p. 39, 2014.
- [234] S. B. L. Chislett-McDonald, E. Surrey, and D. P. Hampshire, “Could high H98-factor commercial tokamak power plants use Nb-Ti toroidal field coils?” *IEEE Trans. Appl. Supercond.*, vol. 29, no. 5, pp. 4200–4208, 2019.
- [235] C. Sborchia, Y. Fu, R. Gallix, C. Jong *et al.*, “Design and specifications of the ITER TF coils,” *IEEE Transactions on Applied Superconductivity*, vol. 18, no. 2, pp. 463–466, 2008.
- [236] L. Savoldi, A. Brighenti, R. Bonifetto, V. Corato *et al.*, “Performance analysis of a graded winding pack design for the eu DEMO TF coil in normal and off-normal conditions,” *Fusion Engineering and Design*, vol. 124, pp. 45–48, 2017.
- [237] R. Wesche, X. Sarasola, O. Dicuonzo, I. Ivashov *et al.*, “Hybrid HTS-Nb₃Sn-NbTi DEMO CS coil design optimized for maximum magnetic flux generation,” *Fusion Engineering and Design*, vol. 14, pp. 10–13, 2018.
- [238] X. Sarasola, R. Wesche, I. Ivashov, K. Sedlak *et al.*, “Progress in the design of a hybrid HTS-Nb₃Sn-NbTi central solenoid for the eu demo,” *IEEE Transactions on Applied Superconductivity*, vol. 30, no. 4, pp. 1–5, 2020.

- [239] D. P. Hampshire, “Superconducting magnet for producing part of a substantially toroidal field,” Granted 2018, <https://dro.dur.ac.uk/26302/>, Accessed 2020/04/13.
- [240] D. C. Robinson, “The physics of spherical confinement systems,” *Plasma Physics and Controlled Fusion*, vol. 41, no. 3A, p. A143, 1999.
- [241] Y.-K. M. Peng, “The physics of spherical torus plasmas,” *Physics of Plasmas*, vol. 7, no. 5, pp. 1681–1692, 2000.
- [242] J. Friedberg, *Plasma Physics and Fusion Energy*, 1st ed. Cambridge University Press, 2007.
- [243] M. Windridge, “Smaller and quicker with spherical tokamaks and high-temperature superconductors,” *Philosophical Transactions of the Royal Society A: Mathematical, Physical and Engineering Sciences*, vol. 377, no. 2141, p. 20170438, 2019.
- [244] A. E. Costley, “Towards a compact spherical tokamak fusion pilot plant,” *Philosophical Transactions of the Royal Society A: Mathematical, Physical and Engineering Sciences*, vol. 377, no. 2141, p. 20170439, 2019.
- [245] G. Fishpool, J. Canik, G. Cunningham, J. Harrison *et al.*, “Mast-upgrade divertor facility and assessing performance of long-legged divertors,” *Journal of Nuclear Materials*, vol. 438, pp. S356–S359, 2013.
- [246] S. Joseph, “High strength, high conductivity copper alloys and electrical conductors made therefrom,” 2014/09/02 2014, <https://patentimages.storage.googleapis.com/67/a8/3b/3772c665b968f4/WO2012074572A1.pdf>, Accessed 2021/06/01.
- [247] J. D. Troxell, “Glidcop dispersion strengthened copper, potential application in fusion power generators,” in *IEEE Thirteenth Symposium on Fusion Engineering*, 1989, Conference Proceedings, pp. 761–765 vol.2.

- [248] F. U. Flores, D. N. Seidman, D. C. Dunand, and N. Q. Vo, “Development of high-strength and high-electrical-conductivity aluminum alloys for power transmission conductors,” in *Light Metals 2018*, O. Martin, Ed. Springer International Publishing, 2018, Conference Proceedings, pp. 247–251.
- [249] D. M. Meade, “Fire, a next step option for magnetic fusion,” *Fusion Engineering and Design*, vol. 63-64, pp. 531–540, 2002.
- [250] D. P. Hampshire, “A derivation of maxwell’s equations using the heaviside notation,” *Philosophical Transactions of the Royal Society A: Mathematical, Physical and Engineering Sciences*, vol. 376, no. 2134, p. 20170447, 2018.
- [251] J. Mlynář, “Focus on: Jet the european centre of fusion research,” EURATOM, Report, 2007, http://large.stanford.edu/courses/2011/ph241/kates-harbeck2/docs/Focus_on.pdf, Accessed 2021/06/12.
- [252] R. A. Matula, “Electrical resistivity of copper, gold, palladium and silver,” *Journal of Physical and Chemical Reference Data*, vol. 8, no. 4, pp. 1147–1297, 1979.
- [253] “How much power is needed to start the reactor and to keep it working?” 2020, accessed 2021/04/28.
- [254] N. Balshaw, “A collection of sensational technical ‘factoids’ for JET tour guides (internal document),” 2018.
- [255] V. Riccardo, T. C. Hender, P. J. Lomas, B. Alper *et al.*, “Analysis of jet halo currents,” *Plasma Physics and Controlled Fusion*, vol. 46, no. 6, pp. 925–934, 2004.
- [256] V. Riccardo, G. Arnoux, P. Cahyna, T. C. Hender *et al.*, “JET disruption studies in support of ITER,” *Plasma Physics and Controlled Fusion*, vol. 52, no. 12, p. 124018, 2010.

- [257] M. R. Gilbert, T. Eade, C. Bachmann, U. Fischer, and N. P. Taylor, “Waste assessment of european demo fusion reactor designs,” *Fusion Engineering and Design*, vol. 136, pp. 42–48, 2018.
- [258] M. S. Lubell and J. A. Clinard, “The iea large coil task test results in ifsmtf,” *IEEE Transactions on Magnetics*, vol. 24, no. 2, pp. 761–766, 1988.
- [259] International Atomic Energy Agency, “Radiological characterization of shutdown nuclear reactors for decommissioning purposes,” Report, 1998, https://www-pub.iaea.org/mtcd/publications/pdf/trs389_scr.pdf, Accessed 2021/03,02.
- [260] C. Damiani, J. Palmer, N. Takeda, C. Annino *et al.*, “Overview of the ITER remote maintenance design and of the development activities in europe,” *Fusion Engineering and Design*, vol. 136, pp. 1117–1124, 2018.
- [261] J. Keep, S. Wood, N. Gupta, M. Coleman, and A. Loving, “Remote handling of DEMO breeder blanket segments: Blanket transporter conceptual studies,” *Fusion Engineering and Design*, vol. 124, pp. 420–425, 2017.
- [262] J. Powell, S. Hsieh, G. Danby, P. Bezler *et al.*, “Deals: a demountable superconducting magnet system for fusion reactors,” *Cryogenics*, vol. 20, pp. 59–74, 1980.
- [263] H. Hashizume and S. Ito, “Design prospect of remountable high-temperature superconducting magnet,” *Fusion Engineering and Design*, vol. 89, pp. 2241–2245, 2014.
- [264] Z. S. Hartwig, C. B. Haakonsen, R. T. Mumgaard, and L. Bromberg, “An initial study of demountable high-temperature superconducting toroidal field magnets for the vulcan tokamak conceptual design,” *Fus. Eng. and Design*, vol. 87, p. 201, 2012.
- [265] F. J. Mangiarotti and J. V. Minervini, “Advances on the design of demountable toroidal field coils with REBCO superconductors for an ARIES-I class

- fusion reactor,” *IEEE Transactions on Applied Superconductivity*, vol. 25, no. 3, pp. 1–5, 2015.
- [266] J. Weiss, D. van der Laan, S. Allen, J. Holt *et al.*, “Development of low-resistance CORC-CICC joints for use in demountable magnets for fusion and their performance up to 10 kA within a background magnetic field of up to 8 T.” 2021, presented at EUCAS 2021, Moscow.
- [267] Y. Tsui, E. Surrey, and D. P. Hampshire, “Soldered joints - an essential component of demountable high temperature superconducting fusion magnets,” *Supercond. Sci. and Technology*, vol. 290, p. 075005, 2016.
- [268] N. Taylor, B. Merrill, L. Cadwallader, L. Di Pace *et al.*, “Materials-related issues in the safety and licensing of nuclear fusion facilities,” *Nuclear Fusion*, vol. 57, no. 9, p. 092003, 2017.
- [269] M. Jakobs, N. L. Cardozo, and R. Jaspers, “Fusion burn equilibria sensitive to the ratio between energy and helium transport,” *Nuclear Fusion*, vol. 54, no. 12, p. 122005, 2014.
- [270] A. Lustgarten and M. Kohut, “The great climate migration,” 2020, <https://www.nytimes.com/interactive/2020/07/23/magazine/climate-migration.html>, Accessed 2021/06/01.
- [271] A. J. McMichael and E. Lindgren, “Climate change: present and future risks to health, and necessary responses,” *Journal of Internal Medicine*, vol. 270, no. 5, pp. 401–413, 2011.
- [272] United Nations, “Paris agreement,” Report, 2015, https://unfccc.int/sites/default/files/english_paris_agreement.pdf, Accessed 2021/06/12.
- [273] B. Johnson, “PM Climate Ambition Summit opening remarks: 12 december 2020,” 2020, accessed 2021/06/01.

- [274] M. Shepherd, “UK net zero target,” 2020, <https://www.instituteforgovernment.org.uk/explainers/net-zero-target>, Accessed 2021/06/01.
- [275] M. Fedkin, “9.1. base load energy sustainability,” 2020, <https://www.education.psu.edu/eme807/node/667>, Accessed 2021/20/15.
- [276] C. D. Henning, “Synfuel production in nuclear reactors.”
- [277] “Necoc project aims to convert ambient co2 to industrially relevant carbon black,” *Additives for Polymers*, vol. 2020, no. 7, pp. 5–6, 2020.
- [278] EUROfusion, “The demonstration power plant: Demo,” 2020, <https://www.euro-fusion.org/programme/demo/>, Accessed 2021/06/01.
- [279] Bill & Melinda Gates Foundation, “Polio,” 2021, <https://www.gatesfoundation.org/our-work/programs/global-development/polio>, Accessed 2021/06/12.
- [280] D. J. C. MacKay, *Sustainable Energy - without the hot air*. Cambridge: UIT, 2008.
- [281] M. Carney, *Value(s) building a better world for all*. Penguin Random House Canada, 2021.
- [282] “John F. Kennedy moon speech - Rice Stadium,” 1962, <https://er.jsc.nasa.gov/seh/ricetalk.htm>, Accessed 2021/06/01.
- [283] B. Jenkin, N. de Bois, A. Cairns, M. Dugher *et al.*, “Public administration committee - twelfth report government and it- "a recipe for rip-offs": Time for a new approach,” 2011, <https://publications.parliament.uk/pa/cm201012/cmselect/cmpublicadm/715/71502.htm>, Accessed 2021/06/02.
- [284] D. Chassels, “Public administration written evidence submitted by david chassels (proc 6),” 2013, ht-

[tps://publications.parliament.uk/pa/cm201314/cmselect/cmpubadm/123/123vw09.htm](https://publications.parliament.uk/pa/cm201314/cmselect/cmpubadm/123/123vw09.htm), Accessed 2021/06/02.

- [285] IRENA(2021), *Renewable Power Generation Costs in 2020*. Abu Dhabi: International Renewable Energy Agency, 2021.
- [286] D. Uglietti, “A review of commercial high temperature superconducting materials for large magnets: from wires and tapes to cables and conductors,” *Superconductor Science and Technology*, vol. 32, no. 5, p. 053001, 2019.
- [287] International Energy Agency, “World energy outlook 2021,” International Energy Agency, Report, 2021, <https://www.iea.org/topics/world-energy-outlook>, Accessed 2021/20/15.

Example PROCESS Input File

```
*-----Constraint Equations-----*

icc = 1 * Beta
icc = 2 *Global power balance
icc = 5 * Density upper limit
icc = 8 * Neutron wall load upper limit
icc = 11 * Radial build
icc = 13 * Burn time lower limit
icc = 15 * L - H power threshold limit
icc = 16 * Net electric power lower limit
icc = 24 * Beta upper limit
icc = 26 * Central solenoid EOF current density upper limit
icc = 27 * Central solenoid BOP current density upper limit
icc = 30 * Injection power upper limit
icc = 31 * TF coil case stress upper limit
icc = 32 * TF coil conduit stress upper limit
icc = 33 * I_op / I_critical limit
icc = 34 * Dump voltage upper limit
icc = 35 * J_winding pack
icc = 56 * Pseparatrix
icc = 72 * CS Tresca stress limit

*-----Iteration Variables-----*

ixc = 1 *aspect ratio
aspect = 2.9418E+00 * Aspect ratio (iteration variable 1)

ixc = 2 * bt
bt = 4.8875E+00 * Toroidal field on axis (t) (iteration variable 2)

ixc = 3 * rmajor
rmajor = 6.1792E+00 * Plasma major radius (m) (iteration variable 3)
```

A. Example PROCESS Input File

```
ixc = 4 * te
te      = 1.0965E+01 * Volume averaged electron temperature (kev)

ixc = 5 * beta
beta    = 4.4046E-02 * Total plasma beta (iteration variable 5)

ixc = 6 * dene
dene    = 1.0695E+20 * Electron density (/m3) (iteration variable 6)

ixc = 9 * fdene
boundu(9) = 1.1
fdene   = 1.1000E+00 * F-value for density limit

*ixc = 10 *Hfactor
boundu(10) = 1.20
boundl(19) = 1.19
*hfact = 1.20E+00

ixc = 13 * tfcth
tfcth   = 0.661 * Inboard tf coil thickness; (centrepost for st) (m)

ixc = 14 * fwalld
fwalld  = 1.0735E-01 * F-value for maximum wall load

ixc = 16 * ohcth
ohcth   = 5.2844E-01 * Central solenoid thickness (m)

ixc = 18 * q
boundl(18) = 3.45
boundu(18) = 50.0
q       = 3.450E+00 * Safety factor 'near' plasma edge (iteration variable 18);

ixc = 25 * f-value for the net electrical power generated (MW)
fpnetel = 1.0000E+00

ixc = 29 * bore
bore    = 1.3123E+00 * Central solenoid inboard radius (m)

ixc = 36 * fbetatry
fbetatry = 6.0543E-01 * F-value for beta limit

ixc = 37 * coheof
boundl(37) = 1.9d+07
coheof   = 1.9000E+07 * Central solenoid overall current density at end of flat-top (a/m2)

ixc = 38 * fjohc
boundu(38) = 0.5
fjohc    = 1.3652E-01 * F-value for central solenoid current at end-of-flattop (nominally 0.25)
```

A. Example PROCESS Input File

```
ixc = 39 * fjohc0
boundu(39) = 0.5
fjohc0 = 1.4617E-01 * F-value for central solenoid current at beginning of pulse (nominally 0.25)

ixc = 41 * fcohbop
fcohbop = 1.0000E+00 * Ratio of central solenoid overall current density at

*ixc = 42 * gapoh
boundl(42) = 0.05
boundu(42) = 0.051
gapoh = 5.0000E-02 * Gap between central solenoid and tf coil (m)

ixc = 44 * fvsbrnni
fvsbrnni = 5.6502E-01 * Fraction of the plasma current produced by

ixc = 48 * fstrcase
fstrcase = 1.0000E+00 * F-value for tf coil case stress

ixc = 49 * fstrcond
fstrcond = 1.0000E+00 * F-value for tf coil conduit stress

ixc = 50 * fiooic
boundu(50) = 0.5
fiooic = 8.1304E-02 * F-value for tf coil operating current / critical CHANGED from 0.3978

ixc = 51 * fvdump
fvdump = 3.2748E-01 * F-value for dump voltage

ixc = 52 * vdalw
boundu(52) = 10.0
vdalw = 5.6239E+00 * Max voltage across tf coil during quench (kv)

ixc = 53 * fjprot
fjprot = 1.0000E+00 * F-value for tf coil winding pack current density

ixc = 56 * tdmptf
boundl(56) = 30
boundu(56) = 100.0
tdmptf = 3.1778E+01 * Dump time for tf coil (s)

ixc = 57 * thkcas
thkcas = 5.0000E-02 * Inboard tf coil case outer (non-plasma side) thickness (m)

ixc = 58 * thwcndut
thwcndut = 6.2524E-03 * Tf coil conduit case thickness (m)

*ixc = 59 * fcutfsu
*fcutfsu = 8.3398E-01 * Copper fraction of TF cable

*ixc = 61 * gapds
```

A. Example PROCESS Input File

```
boundl(61) = 0.01
gapds    = 1.0000E-02 * Gap between inboard vacuum vessel and tf coil (m)

ixc = 97 * fpsepr
boundu(97) = 0.8
fpsepr = 8.0000E-01

ixc = 103 * flhthresh
flhthresh = 1.7651E+00 * F-value for l-h power threshold

ixc = 112 * foh_stress, f-value for CS coil Tresca stress limit
foh_stress = 1.0000E+00

ixc = 116 * fradwall, f-value for radiation wall load limit
fradwall = 1.0000E+00

ixc = 122 * oh_steel_frac, fraction of steel in CS
oh_steel_frac = 7.1572E-01

ixc = 123 * fzeffmax, f-value for max Zeff
fzeffmax = 1.0000E+00

ixc = 131 * Argon impurity f-value
fimp(09) = 1.7728E-03

ixc = 140 * WP radial thickness
thkwp = 5.6856E-01

*-----Build Variables-----*

blnkith = 0.775 * Inboard blanket thickness (m); 0.775
blnkoth = 1.275 * Outboard blanket thickness (m); 1.275
ddwex   = 0.15 * Cryostat thickness (m)
ddwi    = 0.32 * Vacuum vessel thickness (tf coil / shield) (m)
gapomin = 0.20 * Minimum gap between outboard vacuum vessel and tf coil (m)
iohcl   = 1 * Switch for existence of central solenoid;
scrapli = 0.225 * Gap between plasma and first wall; inboard side (m)
scraplo = 0.225 * Gap between plasma and first wall; outboard side (m)
shldith = 0.25 * Inboard shield thickness (m) Initially 0.3
shldoth = 0.25 * Outboard shield thickness (m) Initially 0.8
shldtth = 0.30 * Upper/lower shield thickness (m);
vgap2   = 0.12 * Vertical gap between vacuum vessel and tf coil (m)
vgap    = 1.60 * Vertical gap between x-point and divertor (m)
vvblgap = 0.01 * Gap between vacuum vessel and blanket (m)
tftsgap = 0.01 * Minimum metal-to-metal gap between TF oil and thermal shield (m)

*-----Buildings Variables-----*
```

A. Example PROCESS Input File

```
*-----Constraint Variables-----*

bmxlim = 14.0 * Maximum peak toroidal field (t)
bigqmin = 10 * minimum big Q
ffuspow = 1 * F-value for maximum fusion power
fhldiv = 2.0e0 * F-value for divertor heat load
fpeakb = 9.2290d-1 * F-value for maximum toroidal field
fpinj = 1.0 * F-value for injection power
ftburn = 1.00e+00 * F-value for minimum burn time
pnetelin = 100.0 * Required net electric power (mw)
pseprmax = 25 * Maximum ratio of power crossing the separatrix to plasma major radius
psepbqarmax = 12 * Maximum ratio of psepb/qar
walalw = 10 * Allowable wall-load (mw/m2)

*-----Cost Variables-----*

output_costs = 1
cost_model = 3 * 0 = 1990 USD s/c in $/kg, 3 = 1990 USD s/c in $/kAm
abktflnc = 15 * Allowable first wall/blanket neutron
adivflnc = 25.0 * Allowable divertor heat fluence (mw-yr/m2)
cfactr = 0.75 * Total plant availability fraction;
dintrt = 0.00 * Diff between borrowing and saving interest rates
fcap0 = 1.15 * Average cost of money for construction of plant
fcap0cp = 1.06 * Average cost of money for replaceable components
fcontng = 0.15 * Project contingency factor
fcr0 = 0.065 * Fixed charge rate during construction
fkind = 0.65 * Multiplier for nth of a kind costs
iavail = 0 * Switch for plant availability model;
ifueltyp = 1 * Switch;
lsa = 2 * Level of safety assurance switch (generally; use 3 or 4);
ratecdol = 0.06 * Effective cost of money in constant dollars
tlife = 40 * Plant life (years)
ucblvd = 280.0 * Unit cost for blanket vanadium ($/kg)
ucdiv = 5.0d5 * Cost of divertor blade ($)
ucme = 3.0d8 * Unit cost of maintenance equipment ($/w**0;3)

*-----Current Drive Variables-----*

bscfmax = 0.99 * Maximum fraction of plasma current from bootstrap;
enbeam = 1000.0 * Neutral beam energy (kev) (iteration variable 19)
etanbi = 0.4 * Neutral beam wall plug to injector efficiency
feffcd = 1.0 * Current drive efficiency fudge factor (iteration variable 47)
frbeam = 1.0 * R_tangential / r_major for neutral beam injection

iefrf = 10 * Switch for current drive efficiency model;
gamma_ecrh = 0.3 * ECRH gamma_CD (user input)
etaech = 0.4 * ECRH wall-plug efficiency

irfcd = 1 * Switch for current drive calculation;
```

A. Example PROCESS Input File

```
pinjalw = 50. * Maximum allowable value for injected power (mw)

*-----Divertor Variables-----*

anginc = 0.175 * Angle of incidence of field line on plate (rad)
divdum = 1 * Switch for divertor zeff model; 0=calc; 1=input
divfix = 0.621 * Divertor structure vertical thickness (m)
hldivlim = 10 * Heat load limit (mw/m2)
ksic = 1.4 * Power fraction for outboard double-null scrape-off plasma
prnl = 0.4 * N-scrape-off / n-average plasma;
zeffdiv = 3.5 * Zeff in the divertor region (if divdum /= 0)

*-----Fwbs Variables-----*

denstl = 7800.0 * Density of steel (kg/m3)
emult = 1.18 * Energy multiplication in blanket and shield
fblss = 0.13 * Kit blanket model; steel fraction of breeding zone
fhole = 0.05 * Area fraction taken up by other holes (not used)
fblbe = 0.47 * Beryllium fraction of blanket by volume
fwclfr = 0.1 * First wall coolant fraction
vfshld = 0.60 * Coolant void fraction in shield
fblli2o = 0.07 * Lithium oxide fraction of blanket by volume
fbllipb = 0.00 * Lithium lead fraction of blanket by volume
fblvd = 0.00 * Vanadium fraction of blanket by volume
vfblkt = 0.10 * Coolant void fraction in blanket (blktmodel=0);

*-----Global Variables-----*

*-----Heat Transport Variables-----*

ipowerflow = 0 * Switch for power flow model;
primary_pumping = 3 * Switch for pumping power for primary coolant
etahtp = 0.87 * electrical efficiency of FW and blanket coolant pumps
etaiso = 0.9 * isentropic efficiency of FW and blanket coolant pumps
secondary_cycle = 2 * user input thermal-electric efficiency (etath)
iprimshld = 1 * switch for shield thermal power destiny: = 1 contributes to energy generation cycle
etath = 0.375D0 * thermal to electric conversion efficiency

iblanket = 3 * 1 = no TBR calculation HCPB, 3 = TBR calculation HCPB
iblanket_thickness = 1 * thin blanket

*-----Ife Variables-----*

*-----Impurity Radiation Module-----*

coreradius = 0.75 * Normalised radius defining the 'core' region
```

A. Example PROCESS Input File

```
coreradiationfraction = 0.6 * fraction of radiation from 'core' region that is subtracted from the loss power
fimp(1) = 1.0
fimp(2) = 0.1
fimp(3) = 0.0
fimp(4) = 0.0
fimp(5) = 0.0
fimp(6) = 0.0
fimp(7) = 0.0
fimp(8) = 0.0
*fimp(9) = 0.0016
fimp(10) = 0.0
fimp(11) = 0.0
fimp(12) = 0.0
fimp(13) = 0.0
fimp(14) = 5e-05
fimpvar = 0.0016 * Impurity fraction to be used as fimp(impvar)
impvar = 9 * Fimp element value to be varied if iteration

*-----Pf Power Variables-----*

*-----Pfcoil Variables-----*

cptdin = 4.22d4, 4.22d4, 4.22d4, 4.22d4, 4.3d4, 4.3d4, 4.3d4, 4.3d4, * Peak current per turn input for pf coil i (a)
ipfloc = 2,2,3,3 * Switch for locating scheme of pf coil group i;
ncls = 1,1,2,2, * Number of pf coils in group j
ngrp = 4 * Number of groups of pf coils;
ohghf = 0.9 * Central solenoid height / tf coil internal height
rjconpf = 1.1d7, 1.1d7, 6.d6, 6.d6, 8.d6, 8.0d6, 8.0d6, 8.0d6, * Average winding pack current density of pf coil i (a/m2)
rpf2 = -1.825 * Offset (m) of radial position of ipfloc=2 pf coils
zref(1) = 3.6
zref(2) = 1.2
zref(3) = 1.0
zref(4) = 2.8
zref(5) = 1.0
zref(6) = 1.0
zref(7) = 1.0
zref(8) = 1.0
alstroh = 6.6D8 * allowable stress on OH coil 6.6D8 nominally

*-----Physics Variables-----*

alphaj = 2.0 * Current profile index;
alphan = 1.0 * Density profile index
alphan = 1.45 * Temperature profile index
dnbeta = 3.0 * (troyon-like) coefficient for beta scaling; default of 3
fkzohm = 1.0245 * Zohm elongation scaling adjustment factor (ishape=2; 3)
gamma = 0.3 * Ejima coefficient for resistive startup v-s formula
ibss = 4 * Switch for bootstrap current scaling;
iculbl = 1 * Switch for beta limit scaling (constraint equation 24);
```

A. Example PROCESS Input File

```
icurr   = 4 * Switch for plasma current scaling to use; 4 for ITER, 2 for ST double null, 9 for ST from fiesta
idensl  = 7 * Switch for density limit to enforce (constraint equation 5);
ifalphap = 1 * Switch for fast alpha pressure calculation;
ifispact = 0 * Switch for neutronics calculations;
iinvqd  = 1 * Switch for inverse quadrature in l-mode scaling laws 5 and 9;
ipedestal = 1 * Switch for pedestal profiles;
itart   = 0 * Switch for spherical tokamak model (itart = 1 for ST)
neped   = 0.678e20 * Electron density of pedestal (/m3) (ipedestal=1)
nesep   = 0.2e20 * Electron density at separatrix (/m3) (ipedestal=1)
rhopedn = 0.94 * R/a of density pedestal (ipedestal=1)
rhopedt = 0.94 * R/a of temperature pedestal (ipedestal=1)
tbeta   = 2.0 * Temperature profile index beta (ipedestal=1)
teped   = 5.5 * Electron temperature of pedestal (kev) (ipedestal=1)
tesep   = 0.1 * Electron temperature at separatrix (kev) (ipedestal=1)
iprofile = 1 * Switch for current profile consistency;
isc     = 34 * Switch for energy confinement time scaling law
ishape  = 2 * Switch for plasma cross-sectional shape calculation;
kappa   = 1.700 * Plasma separatrix elongation (calculated if ishape > 0)
q0      = 1.0 * Safety factor on axis
ralpne  = 0.1 * Thermal alpha density / electron density (iteration variable 109)
I_single_null = 1 * Switch for single null 1 / double null plasma 0;
ssync   = 0.6 * Synchrotron wall reflectivity factor
triang  = 0.7 * Plasma separatrix triangularity (calculated if ishape=1; 3 or 4)

maxradwallload = 0.5 * Maximum permitted radiation wall load (MW/m2)
peakfactrad = 2.00 * peaking factor for radiation wall load

*-----Pulse Variables-----*

lpulse   = 1 * Switch for reactor model; 1 for pulsed, 0 for steady state

*-----Rfp Variables-----*

*-----Stellarator Variables-----*

*-----Times Variables-----*

tburn    = 1.0d6 * Burn time (s) (calculated if lpulse=1)

*-----Vacuum Variables-----*

*-----Tfcoil Variables-----*

casthi   = 0.07 * Inboard tf coil case inner (plasma side) thickness (m)
casths   = 0.05 * Inboard tf coil sidewall case thickness (m)
cpttf    = 10e+04 * Tf coil current per turn (a);
ripmax   = 0.6 * Maximum allowable toroidal field ripple amplitude (nominally 0.6)
tdmptf   = 30.0 * Dump time for tf coil (s)

n_tf     = 18 * Number of tf coils (default = 50 for stellarators)
```

A. Example PROCESS Input File

```
alstrtf = 6.6D8 * allowable von Mises stress in TF coil structural material (Pa )

thicndut = 1.5d-3 * Conduit insulation thickness (m)
tinstf   = 0.008 * Ground insulation thickness surrounding winding pack (m)
tmargin  = 1.7 * Minimum allowable temperature margin (cs and tf coils) (k) This doesnt matter as I've set a current limit rather
vftf     = 0.20 * Coolant fraction of tfc 'cable' (itfsup=1); or of tfc leg (itfsup=0)
i_tf_sup = 1 * magnet type, 1 for superconductor, 0 for (water cooled)

*-----Quick Access Switches-----*

isumatpf = 7 * Switch for superconductor material in pf coils; (3 = NbTi, 6 = GL_nbti in ASC2018) ( 7 = GL_nbti in SBLCM_develop)
isumatoh = 8 * same numbering as isumatpf
i_tf_sc_mat = 8 *switch for TF coil superconductor material (1 = Nb3Sn 3 = NbTi 5 = WST 7 = YBCO, 8 = GL_nbti in ASC18) ( 7 = GL_
tftmp    = 4.5 * Peak helium coolant temperature in tf coils (k) nominally 4.75
iblanket = 3 * 1 = no TBR calculation HCPB, 3 = TBR calculation HCPB
iblanket_thickness = 1 * thin blanket
tbrnmn   = 7200 * Minimum burn time (s)
i_cs_stress = 1
i_tf_bucking = 3 *reduces cost significantly
iprecomp = 0 * required with above

*-----Scan Module-----*

isweep = 1
nsweep = 4* 1 aspect, 28 bt, 4 Hfactor, 54 b_crit_upper_nbti
sweep = 3.7369E+00, 3.7,3.8,3.9
sweep = 1.2,1.15,1.14,1.13,1.12,1.11,1.1,1.05,1.0

*-----Numerics-----*

ioptimz = 1 * for optimisation VMCON only
minmax  = 7 * Switch for figure-of-merit (1 = radius 6 = CoE 7 = capital investment, 17 net electrical output)
epsvmc  = 1.0e-6 * Error tolerance for vmcon
```

Example PROCESS Output File

Summary

```
*****
***** PROCESS *****
***** Power Reactor Optimisation Code *****
*****

Program : process.exe
Version : 1.0.17   Release Date :: 2020-02-25
Tag No.  : 1.0.17-310-gfb5772e code contains untracked changes
Branch   : Roadmap
Git log  : plot proc_v2 change,
Date/time : 16 Apr 2021 15:14:07 +01:00(hh:mm) UTC
User     : schislet
Computer : freia026
Directory : /home/schislet/local_dev/bin
Input    : IN.DAT
Run title : TF coil testing
Run type  : Reactor concept design: Pulsed tokamak model, (c) CCFE

*****

Equality constraints : 19
Inequality constraints : 00
Total constraints : 19
Iteration variables : 36
Max iterations : 200
Figure of merit : +07 -- minimise capital cost.
Convergence parameter : 1.00E-03

*****
```

B. Example PROCESS Output File Summary

(Please include this header in any models, presentations and papers based on these results)

Quantities listed in standard row format are labelled as follows in columns 112-114:

ITV : Active iteration variable (in any output blocks)

OP : Calculated output quantity

Unlabelled quantities in standard row format are generally inputs

Note that calculated quantities may be trivially rescaled from inputs, or equal to bounds which are input.

**** Scan point 1 of 1: Confinement_H_factor, hfact = 1.200E+00 ****

***** Numerics *****

PROCESS has performed a VMCON (optimisation) run.

and found a feasible set of parameters.

VMCON error flag	(ifail)	1
Number of iteration variables	(nvar)	36
Number of constraints (total)	(neqns+nineqns)	19
Optimisation switch	(ioptimz)	1
Figure of merit switch	(minmax)	7
Square root of the sum of squares of the constraint residuals	(sqsumsq)	2.476E-04 OP
VMCON convergence parameter	(convergence_parameter)	4.243E-05 OP
Number of VMCON iterations	(nviter)	11 OP

PROCESS has successfully optimised the iteration variables to minimise the figure of merit CAPITAL COST.

Certain operating limits have been reached,

as shown by the following iteration variables that are

at or near to the edge of their prescribed range :

fdene	=	1.1000E+00	is at or above its upper bound:	1.1000E+00
q	=	3.4500E+00	is at or below its lower bound:	3.4500E+00
fpnetel	=	1.0000E+00	is at or above its upper bound:	1.0000E+00
coeof	=	1.9000E+07	is at or below its lower bound:	1.9000E+07
fstrcase	=	1.0000E+00	is at or above its upper bound:	1.0000E+00
fjprot	=	1.0000E+00	is at or above its upper bound:	1.0000E+00
tdmptf	=	3.0000E+01	is at or below its lower bound:	3.0000E+01
fpsepr	=	8.0000E-01	is at or above its upper bound:	8.0000E-01
fzeffmax	=	1.0000E+00	is at or above its upper bound:	1.0000E+00
fradwall	=	1.0000E+00	is at or above its upper bound:	1.0000E+00
foh_stress	=	1.0000E+00	is at or above its upper bound:	1.0000E+00

The solution vector is comprised as follows :

final	final /
-------	---------

B. Example PROCESS Output File Summary

i		value	initial
1	aspect	3.1469E+00	1.0697
2	bt	5.3570E+00	1.0961
3	rmajor	6.7503E+00	1.0924
4	te	1.0605E+01	0.9672
5	beta	3.1175E-02	0.7078
6	dene	9.0720E+19	0.8482
7	fdene	1.1000E+00	1.0000
8	tfcth	6.6100E-01	1.0000
9	fwalld	8.0588E-02	0.7507
10	ohcth	6.1735E-01	1.1682
11	q	3.4500E+00	1.0000
12	fnetel	1.0000E+00	1.0000
13	bore	1.7577E+00	1.3394
14	fbetatry	4.8920E-01	0.8080
15	coheof	1.9000E+07	1.0000
16	fjohc	2.2635E-01	1.6580
17	fjohc0	1.3726E-01	0.9390
18	fcobop	7.3211E-01	0.7321
19	fvsbrnni	6.0217E-01	1.0658
20	fstrcase	1.0000E+00	1.0000
21	fstrcond	9.6460E-01	0.9646
22	fiooic	8.1112E-02	0.9976
23	fvdump	3.7729E-01	1.1521
24	vdalw	6.4793E+00	1.1521
25	fjprot	1.0000E+00	1.0000
26	tdmptf	3.0000E+01	1.0000
27	thkcas	5.1969E-02	1.0394
28	thwcdut	7.1694E-03	1.1467
29	fpsepr	8.0000E-01	1.0000
30	flhthresh	1.7682E+00	1.0018
31	fzeffmax	1.0000E+00	1.0000
32	fradwall	1.0000E+00	1.0000
33	oh_steel_frac	8.0375E-01	1.1230
34	foh_stress	1.0000E+00	1.0000
35	fimp(09)	8.0171E-05	0.0452
36	thkwp	5.5088E-01	0.9689

The following equality constraint residues should be close to zero :

	physical constraint	constraint residue	normalised residue
1	Beta consistency = 3.1175E-02	2.0064E-09	-6.4360E-08
2	Global power balance consistency = 2.1028E-01 MW/m3	1.3131E-08 MW/m3	-6.2445E-08
3	Density upper limit < 1.0322E+20 /m3	7.1118E+12 /m3	6.8896E-08
4	Neutron wall load upper limit < 8.0588E-01 MW/m2	4.8905E-08 MW/m2	6.0685E-08
5	Radial build consistency = 6.7503E+00 m	-6.1889E-08 m	9.1683E-09
6	Burn time lower limit > 7.2000E+03 sec	4.0445E-01 sec	-5.6173E-05

B. Example PROCESS Output File Summary

7	L-H power threshold limit	>	7.6351E+01 MW	2.8771E-05 MW	-3.7683E-07
8	Net electric power lower limit	>	1.0000E+02 MW	2.4326E-02 MW	2.4326E-04
9	Beta upper limit	<	5.6886E-02	2.5063E-09	4.4058E-08
10	CS coil EOF current density limit	<	8.3940E+07 A/m2	-1.4353E+02 A/m2	-1.7099E-06
11	CS coil BOP current density limit	<	1.0134E+08 A/m2	-1.4245E+02 A/m2	-1.4056E-06
12	Injection power upper limit	<	5.0000E+01 MW	-4.8840E-06 MW	9.7679E-08
13	TF coil case stress upper limit	<	6.6000E+08 Pa	-1.5322E+02 Pa	-2.3215E-07
14	TF coil conduit stress upper lim	<	6.6000E+08 Pa	-1.8523E+02 Pa	-2.8065E-07
15	I _{op} / I _{critical} (TF coil)	<	2.8368E+08 A/m2	2.9296E+00 A/m2	-1.2732E-07
16	Dump voltage upper limit	<	6.4793E+00 V	4.0347E+00 V	1.5690E-06
17	J _{winding pack} /J _{protection} limit	<	2.3010E+07 A/m2	0.0000E+00 A/m2	-8.2165E-08
18	Psep / R upper limit	<	2.5000E+01 MW/m	-7.1057E-06 MW/m	3.5528E-07
19	CS Tresca stress limit	<	6.6000E+08 Pa	-1.3282E+02 Pa	-2.0125E-07

***** Final Feasible Point *****

***** Power Reactor Costs (1990 US\$) *****

First wall / blanket life (years)	(fwbllife)	24.817
Divertor life (years)	(divlife.)	9.549
Cost of electricity (m\$/kWh)	(coe)	547.243

Power Generation Costs :

	Annual Costs, M\$	COE, m\$/kWh
Capital Investment	219.11	421.42
Operation & Maintenance	19.86	38.20
Decommissioning Fund	1.85	3.56
Fuel Charge Breakdown		
Blanket & first wall	35.18	67.67
Divertors	6.08	11.70
Centrepost (TART only)	0.00	0.00
Auxiliary Heating	1.01	1.94
Actual Fuel	0.29	0.55
Waste Disposal	1.14	2.19
Total Fuel Cost	43.70	84.06
Total Cost	284.53	547.24

***** Replaceable Components Direct Capital Cost *****

First wall direct capital cost (M\$)	(fwallcst)	62.791
Blanket direct capital cost (M\$)	(blkcst)	277.191
Divertor direct capital cost (M\$)	(divcst)	32.821
Plasma heating/CD system cap cost (M\$)		9.750
Fraction of CD cost --> fuel cost	(fcdfuel)	0.100

B. Example PROCESS Output File Summary

***** Detailed Costings (1990 US\$) *****

Acc.22 multiplier for Nth of a kind	(fkind)	6.500E-01
Level of Safety Assurance	(lsa)	2

***** Structures and Site Facilities *****

Breakdown of the costs of various buildings and land

(c21)	Total account 21 cost (M\$)	488.28
-------	-----------------------------	--------

***** Reactor Systems *****

Breakdown of the costs of the divertor, first wall, blanket, shield and their support structures

(c221)	Total account 221 cost (M\$)	38.59
--------	------------------------------	-------

***** Magnets *****

Break down of the costs of the TF, CS and PF coils, including the conductor, winding, assembly and their support structures

(c222)	Total account 222 cost (M\$)	557.19
--------	------------------------------	--------

***** Power Injection *****

Breakdown of the costs of the ECRH, lower hybrid and neutral beam systems

(c223)	Total account 223 cost (M\$)	87.75
--------	------------------------------	-------

***** Vacuum Systems *****

Costs of the vacuum pumps, ducts, valves, shielding and instrumentation

(c224)	Total account 224 cost (M\$)	16.19
--------	------------------------------	-------

***** Power Conditioning *****

Costs of the TF, CS and PF coil power supplies, breakers, dump resistors, instrumentation and bussing

(c225)	Total account 225 cost (M\$)	81.65
--------	------------------------------	-------

***** Heat Transport System *****

Costs of the cryogenic system, and cooling systems for the blanket, first wall and divertor including piping and heat exchangers

(c226)	Total account 226 cost (M\$)	129.92
--------	------------------------------	--------

B. Example PROCESS Output File Summary

***** Fuel Handling System *****		
Costs of the fuel system, processing, ventilation and atmospheric recovery systems		
(c227)	Total account 227 cost (M\$)	119.56
***** Instrumentation and Control *****		
(c228)	Instrumentation and control cost (M\$)	97.50
***** Maintenance Equipment *****		
(c229)	Maintenance equipment cost (M\$)	195.00
***** Total Account 22 Cost *****		
(c22)	Total account 22 cost (M\$)	1323.35
***** Turbine Plant Equipment *****		
(c23)	Turbine plant equipment cost (M\$)	99.43
***** Electric Plant Equipment *****		
Costs of the switchyard, transformers, back-up systems and low voltage equipment		
(c24)	Total account 24 cost (M\$)	32.19
***** Miscellaneous Plant Equipment *****		
(c25)	Miscellaneous plant equipment cost (M\$)	22.12
***** Heat Rejection System *****		
(c26)	Heat rejection system cost (M\$)	25.05
***** Plant Direct Cost *****		
(cdirt)	Plant direct cost (M\$)	1990.42
***** Reactor Core Cost *****		
(crctcore)	Reactor core cost (M\$)	683.53
***** Indirect Cost *****		
(c9)	Indirect cost (M\$)	558.51
***** Total Contingency *****		

B. Example PROCESS Output File Summary

Effective charge, plasma profile model. Pedestal density, temperature and height.
Electron temperature and density at separatrix, comparison with limits.

Density Limit using different models :

Density limits as specified using various models e.g. ITER models I and II, Greenwald model etc.

Fuel Constituents :

Deuterium and tritium fractions

Fusion Power :

Total fusion power, D-T, D-D and D-He3 fusion powers, alpha, neutron and charged particle power.
Total power deposited in plasma

Radiation Power (excluding SOL):

Bremsstrahlung and synchrotron radiation powers. Core edge and total radiation. Core and scrape off layer radiation fractions. Maximum and nominal radiation wall load and mean neutron wall load. Power incident on the various divertor targets. Ohmic heating power, fraction of alpha power to ions and electrons. Power into divertor zone. P_{sep} / R ratio, $P_{sep} Bt / qAR$ ratio. L-H mode transition power via various scaling laws.

Confinement :

Confinement time scaling law. Global thermal energy, ion energy and electron energy confinement times. Triple product, transport power loss. Alpha particle confinement time. Total energy confinement time including radiation loss

Dimensionless plasma parameters

Normalized plasma pressure beta, normalised ion Larmour radius, normalised collisionality, volume measure of plasma elongation.

Plasma Volt-second Requirements :

Total volt-second requirements, inductive volt-seconds, start-up and flat-top resistive volt-seconds. Bootstrap fraction via various scaling laws. Diamagnetic fraction, Pfirsch-Schlueter fraction. Loop voltage during plasma burn, plasma resistance and inductance. Coefficient for saw-tooth effects on volt-second requirements.

Fuelling :

Fueling and burn-up rates and burn-up fraction.

***** Energy confinement times, and required H-factors : *****

Plasma energy confinement times via various scaling laws, and the required H-factors for power balance from those laws.

B. Example PROCESS Output File Summary

***** Current Drive System *****

Current drive wall plug and coupling efficiencies. Injected power. Bootstrap fraction, inductive fraction.
Total flux swing capability of CS and PF coils. Required flux swing during start-up, available flux swing during burn.

***** Times *****

CS current ramp time, plasma current ramp-up time, heating time, burn time, reset to zero CS current time,
time between pulses, total plant cycle time.

***** Radial Build *****

Radial thicknesses of components from the inner bore of the CS coil to the outer leg of the TF coil

***** Vertical Build *****

Vertical thicknesses of components from the bottom of the TF coil, to the top of the TF coil

***** Divertor build and plasma position *****

Divertor configuration. Positions of plasma top and centre and X-point (radial and vertical). Plasma lower
triangularity, plasma lower triangularity,
plasma elongation. TF coil vertical offset. Positions of the divertor plates and strike points

***** TF coils *****

TF coil stresses (radial, toroidal, vertical, Von-Mises and Tresca). Maximum radial deflection at the mid-plane.
TF coil support architecture and superconductor model. TF coil geometry, radii, thicknesses, heights and shape.
TF coil, winding pack and cable dimensions, masses and material fractions. Nominal and peak fields on the
conductor, critical and operating current densities and currents in the winding pack and cables. Number of turns in
the winding pack. Field ripple. Radial build of the winding pack. Quench voltage and relaxation time.
Vacuum vessel stress due to quench.

***** Central Solenoid and PF Coils *****

CS and PF coil stresses (hoop, axial and Tresca), coil geometry, radii, thicknesses, heights and shape. TF coil,
winding pack and cable dimensions, masses and material fractions. Peak fields, operating and critical
current densities. Peak fields, operating and critical current densities at beginning of pulse and end of flat-top.
Number of turns in the winding pack.

***** Volt Second Consumption *****

Volt-second consumption breakdown during start-up and burn on each PF coil and the CS coil. Currents in each coil
(broken down into equilibrium field and CS field balancing) at initialisation, beginning-of-pulse,
end-of-ramp, beginning-of-flat-top, end-of-flat-top and end-of-pulse. Current evolution in the plasma at
initialisation, beginning-of-pulse, end-of-ramp, beginning-of-flat-top, end-of-flat-top and end-of-pulse.

***** Support Structure *****

B. Example PROCESS Output File Summary

PF and CS coil gravity support and inter-coil support structure masses. Mass of cooled components.

***** PF Coil Inductances *****

PF, CS and plasma inductance evolution at initialisation, beginning-of-pulse, end-of-ramp, beginning-of-flat-top, end-of-flat-top and end-of-pulse.

***** Pumping for primary coolant (helium) *****

Pressure drop in FW and blanket coolant. Fraction of FW and blanket thermal power required for pumping.
Total power absorbed by FW & blanket. Inlet and outlet temperature of FW & blanket coolant pump.
Mechanical pumping power for FW, blanket, divertor, shield and vacuum vessel cooling loops

***** First wall and blanket : CCFE HCPB model *****

Blanket material composition by volume. Component volumes and masses. Nuclear heating in TF and PF coil, blanket, shield and divertor. Number of inboard and outboard blanket modules. Blanket pumps isentropic efficiency.
First wall and blanket coolant pressures. Tritium breeding ratio (during pulse and 5 year time averaged)

***** Superconducting TF Coil Power Conversion *****

TF coil cable operating current-per-turn. Number of TF coils. Quench voltage. TF coil inductance and resistance.
TF coil charging time. Number of circuit breakers and dump resistors. Dump resistor resistances.
Dump resistor energy and power. Power supply voltage and current. TF coil resistive and inductive power.
Aluminium bus current density and cross section. TF coil power conversion floor space. AC inductive and steady state power demand.

***** PF Coils and Central Solenoid: Power and Energy *****

Number of PF coil circuits. Sum of PF power supply ratings. Total PF coil circuit bus length. Total PF coil bus resistive power. Total PF coil resistive power. Maximum PF coil voltage. Efficiency of transfer of PF stored energy into or out of storage. Maximum stored energy in poloidal field. Energy stored in poloidal magnetic field as a function of time.

***** Vacuum System *****

Pumpdown to base pressure: First wall outgassing rate, total outgassing load, base pressure required, required N2 pump speed. Pumpdown between burns: plasma chamber volume, chamber pressure before and after burn, required D-T pump speed. Helium Ash Removal: divertor chamber gas pressure, He gas fraction in divertor chamber, required helium pump speed. D-T Removal at Fuelling Rate: D-T fuelling rate, required D-T pump speed.
Number of pump ducts, duct diameter, passage length, passage diameter.

***** Plant Buildings System *****

Volume and floor area of reactor building, maintenance building, workshop building, tritium building, electrical building, control building, cryogenics building, administration building, shops volume.

***** Electric Power Requirements *****

B. Example PROCESS Output File Summary

Base electricity load and electricity loads for divertor coils, cryoplant, primary coolant pump, TF, CS and PF power supplies plasma heating power supply, tritium processing, and vacuum pumps. Total pulsed power and total base power required at all times.

***** Cryogenics *****

Conduction, radiation and nuclear heat loads on cryogenic components. Resistive losses in current leads. Total heat to remove at cryogenic temperatures. Cryogenic components and coolant temperature, cryoplant efficiency. Total electric power required by cryoplant.

***** Plant Power / Heat Transport Balance *****

Neutron power multiplication in blanket, divertor area fraction of whole toroid surface, H/CD apparatus + diagnostics area fraction, first wall area fraction. Mechanical and electrical pumping power for FW, blanket and divertor cooling loop including heat exchanger. Efficiency of coolant pumps and power conversion cycle. Fraction of high-grade thermal power to divertor. Heat removal from cryogenic plant, reactor facilities, injection power, tritium plant, vacuum pumps. Coolant pumping efficiency losses.

Power Balance across separatrix :

Transport power loss from confinement time scaling law, radiation power from plasma core. Alpha power deposited in plasma, power from D-D and D-He charged particles, injected power, total power across separatrix.

Power Balance for Reactor - Summary :

Fusion power, power from energy multiplication in the blanket, injected power, ohmic power, power deposited in primary coolant by pump. Heat extracted from first wall, blanket, shield and divertor. Nuclear and photon lost to H/CD system.

Electrical Power Balance :

Net electric power output, electric power for H/CD system, coolant pumps, vacuum pumps, tritium plant, cryoplant, TF coils, PF coils, other systems gross electric power.

Power balance for power plant :

Fusion power, power from energy multiplication in blanket and shield, net electrical output, heat rejected by main power conversion circuit, heat rejected by other cooling circuits.

Plant efficiency measures :

Net electric power to total nuclear power ratio. Net electric power to total fusion power ratio.
Gross electric power to high-grade heat ratio

Time dependent power usage

***** Errors and Warnings *****

B. Example PROCESS Output File Summary

Any level 3 errors that caused the PROCESS run to exit, or any level 2 or 1 warnings that the user may wish to review.

***** End of PROCESS Output *****

Colophon

This thesis is based on a template developed by Alex Blair, Matthew Townson and Andrew Reeves. It was typeset with $\text{\LaTeX}2_{\epsilon}$. It was created using the *memoir* package, maintained by Lars Madsen, with the *madsen* chapter style. The font used is Latin Modern, derived from fonts designed by Donald E. Knuth.